Investigation and Optimisation of a Plasma Cathode Electron Beam Gun for Material Processing Applications

Thesis submitted for the degree of
Doctor of Philosophy
at Brunel University London

by

Sofia del Pozo Rodriguez
Department of Electronic and Computer Engineering
College of Engineering, Design and Physical Sciences
Brunel University London

30th September 2016

Investigation and Optimisation of a Plasma Cathode Electron Beam Gun for Material Processing Applications

Sofia del Pozo Rodriguez

Abstract

This thesis describes design, development and testing work on a plasma cathode electron beam gun as well as plasma diagnosis experiments and Electron Beam (EB) current measurements carried out with the aim of maximising the power of the EB extracted and optimising the electron beam gun system for material processing applications. The elements which influence EB gun design are described and put into practice in a thermionic EB gun case study.

The relevant principles of plasma EB gun systems, such low-temperature, low-pressure, RF excitation, are described along with the test rigs developed to investigate different plasma cathode configurations. The first experimental setup was for optical spectroscopy measurements of the light emitted from the plasma and the second included current measurements from EBs generated at –30 and –60 kV as well as the spectroscopic measurements.

Comparison of EB current measurements with different plasma cathode configurations and correlation with spectroscopic measurements are presented. The maximum current extracted from the Radiofrequency (RF) gun was 38 mA at –60 kV using a hollow cathode geometry and permanent magnets for electron confinement. The RF gun was compared to a Direct Current (DC) gun which generated higher currents. This was reflected in the spectra which indicated a higher ionisation level than in the RF plasma.

Simulation work carried out using Opera-2d to model beam trajectories indicated that the beam shape is largely influenced by the plasma boundary. Particle In Cell (PIC) simulations of a parallel plate RF plasma cathode demonstrated that higher excitation frequencies produced higher ionisation, however the RF sheaths were larger and thus the current extracted may be limited in practice due to fewer electrons being available near the aperture. The sheath thickness decreased in the simulations as the discharge gap was increased. RF plasma also produced larger currents from larger plasma chambers.

Contents

Glossary

2D	Two dimensions
Argon I	Excited argon
Argon II	Ionised argon
CCP	Capacitively Coupled Plasma
DC	Direct Current
EB	Electron Beam
EEDF	Electron Energy Distribution Function
EEPF	Electron Energy Probability Function
FEA	Finite Element Analysis
HV	High Voltage
ICP	Inductively Coupled Plasma
LTE	Local Thermodynamic Equilibrium
MC	Monte Carlo
MFP	Mean Free Path
OES	Optical Emission Spectroscopy
PECVD	Plasma Enhanced Chemical Vapour Deposition
PIC	Particle In Cell
PSU	Power Supply Unit
RF	Radiofrequency

Declaration

I hereby declare that no part of this thesis has been previously submitted to this or any other university as part of the requirements for a higher degree. The work described herein was conducted solely by the undersigned except for those colleagues and others acknowledged in the text.

Sofia del Pozo Rodriguez

30th September 2016

Dedication

To Consuelo, Monica, Doroteo and others who supported me during this journey.

Acknowledgements

I would like to express my gratitude for my supervisor at Brunel University London, Dr. David Ryan Smith and for my supervisor at TWI, Colin Ribton, for their guidance, motivation, positive attitude, and being available to give me wise advice when I needed.

I would like to acknowledge the financial support received from TWI Ltd. and for allowing this experience. Special thanks to my manager at the EB team, Mike Nunn for his support during these years. I would like to extend my thanks to the colleagues at the EB and Friction team, as well as other departments in TWI who spent a bit of their time with me and from which I learnt many things.

I also would like to thank Professor Balachandran for his advice from the start to the end of this work and for his help with my thesis and PhD structure.

Thanks to Alexander Beniyash and Nils Murray from the Institut für Werkstoffkunde, Leibniz University, Hanover, for their time and useful discussions and for giving me the opportunity of carrying out some of my measurements at their laboratory.

Thanks to my family for their support and thanks to my flatmates for keeping me company during some of the long writing sessions.

Chapter 1 : Introduction

This chapter provides the context for the presented thesis work and describes the research goals, contributions to knowledge made by the work and gives an overview of the thesis structure.

1.1. Conventional Electron Gun Limitations

Electron beam (EB) guns generate a high energy beam of electrons that can be used to melt metal and have been used for a long time in material processing applications such as welding of thick-section metals, cutting and more recently additive layer manufacturing. EB guns offer advantages over lasers in additive manufacturing such as a faster building speed as a result of their ability to melt thicker layers of material. Figure 1.1 shows titanium aluminide turbine blades by Avio (part of GE Aviation) (left) and a hip implant in titanium (right) both made with Arcam EB powder bed additive manufacturing machines.

Figure 1.1 - Additive manufactured titanium parts using an EB gun integrated in a powder bed system (Arcam AB 2016)

Conventional electron guns use a heated filament with a low work function – typically tungsten (W), lanthanum hexaboride (LaB_6) or cerium hexaboride (CeB_6) – as the electron source. As a result, the electron beam quality is affected by the limited lifetime of the filament, which wears during the manufacturing process as a result of erosion and evaporation. Figure 1.2 (left) shows a diagram of a conventional EB gun, using a tungsten filament as the cathode to generate an electron beam. The cathode is usually heated up directly by a Direct Current (DC), which gives some of the electrons in the cathode sufficient energy to overcome the potential barrier at the surface of the filament and escape. The electric field beyond the surface then accelerates the electrons and directs their trajectories to form a beam. The system is in a vacuum to avoid oxidation and burning of the filament and collisions of the accelerated electrons in the beam with other particles in the chamber.

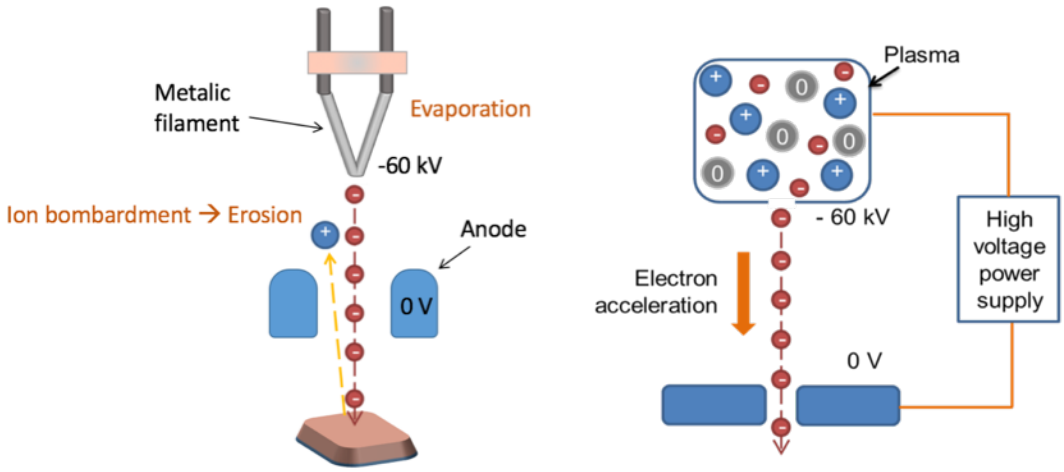

Figure 1.2 - Diagram of a thermionic cathode electron beam gun system (left) and plasma cathode electron gun system (right)

This thesis focuses on the next generation of electron beam guns that offers an alternative to thermionic cathodes: a plasma cathode EB gun that provides a solution to the main problems of material processing electron guns. Figure 1.2 (right) shows a diagram of a plasma cathode gun. The plasma is generated by applying energy to the plasma chamber. In the presented thesis, the energy is applied in the form of radiofrequency (RF) power. A high electric field in front of the plasma chamber then extracts the electrons from it and forms a beam of electrons, which can be used to melt

and process metal. Table 1.1 presents a summary of advantages and limitations of thermionic and plasma cathode electron guns.

Table 1.1 - Comparison of thermionic and plasma cathodes

	Thermionic cathode	**Plasma cathode**
Lifetime	Limited by evaporation and erosion	Unaffected by evaporation and erosion
Vacuum	Limited to high vacuum	Wider range only limited by HV breakdown
Power control	Third electrode is used introducing beam aberration	RF modulation can be used so that power can be controlled keeping beam shape
Beam pulsing	Complex and expensive	Readily possible by control of RF signal

Work carried out by the Jet Propulsion Laboratory (JPL) for NASA looked at the limitations and advantages of hollow cathodes, many of which were also true for the plasma cathode of the RF gun designed and optimised in this thesis work. Electron beams generated from the JPL hollow cathodes were used in Hall thrusters for ionisation of the propellant and for ion beam neutralisation (Goebel, Katz 2008).

Research has been carried out on DC plasmas as electron sources for EB guns (Oks 2006), however, there has been very little investigation into RF plasma cathodes and the plasma parameters and their relation to the electron beam quality and power produced. In addition, RF plasma cathode guns could bring advantages over DC plasma cathode guns such as the capability to readily pulse the beam. Thus, the aim of this thesis work was to investigate this gap in knowledge and ultimately use the findings to optimise plasma cathode electron guns for material processing applications.

1.2. Research Goals

The focus of this thesis was to investigate plasma cathodes in EB guns for material processing applications and optimise them for maximum electron beam power.
The objectives set to achieve the above were:

- To identify the design parameters and operating conditions that are critical to electron emissivity and that govern the quality and characteristics of electron beams extracted from a plasma.
- To optimise the design of an RF plasma cathode electron gun.
- To measure and characterise the performance of a plasma cathode gun through plasma diagnosis techniques and EB current measurements.

Different plasma chamber geometries were designed and manufactured as part of this work. The designs were assessed for different plasma parameters (i.e. pressure, excitation power) through measurements on the plasma gun using two experimental setups. The first set of measurements looked at the plasma generated in a plasma chamber inside the vacuum chamber of the EB gun system, without generating an EB. An optical spectrometer and optical fibre were used pointing at the plasma chamber aperture, in the plasma chamber direction.

The second experimental setup added a high voltage (HV) power supply unit (PSU) to extract electron beams from the plasma cathode at –30 kV and –60 kV into the vacuum chamber. The EB current extracted was collected in a Faraday cup and compared to the spectra of the plasma from which it had been generated. The effect of ring magnets for magnetic confinement was also investigated in both of the experimental setups.

Additionally, simulation work was carried out to justify the results from the experience in the laboratory. Finite element model simulations of the electric field in the gun and trajectory plotting of beamlets from the cathode were used to understand the shape and characteristics of beams generated from a curved plasma boundary, which were observed to be affected largely by the plasma parameters instead of by the gun electrodes, in contrast to what happens with thermionic electron guns. Particle in cell (PIC) simulations were also used in this work to simulate a simplified version of the plasma cathode chamber. These simulations helped to understand the effect of the plasma sheaths, which were found to be a critical component in the system for the amount of EB current extracted.

The plasma cathode gun was integrated into a 3D printer. The electron beams that were generated in the experimental setup were reproduced in this system.

1.3. Contributions to Knowledge

1. A comparison of the spectra measurements ratios at the key plasma parameters of pressure, excitation power, geometry, DC vs. RF excitation as well as the relationship of those ratios with the EB current measurements has been presented. A correlation of emission from plasmas with key parameters and optical spectroscopy has been carried out for the first time to the best of the author's knowledge.
2. An investigation of a DC plasma cathode and comparison to an RF plasma cathode has been carried out for the first time to the best of the author's knowledge.
3. Optimisation (design and development) through experimental trials and modelling of an RF excited plasma cathode to produce sufficient EB current from the plasma cathode EB gun for material processing applications.

1.4. Thesis Organisation

This thesis is split into eight chapters. Following this introduction, Chapter 2 gives an overview of EB gun technology. The chapter also describes the design parameters that govern conventional thermionic guns, the expressions to define the quality of the electron beams generated, and the main material processing applications of electron guns.

Chapter 3 is a case study of a thermionic electron gun design which was for an application requiring an electron beam to be injected into a microwave plasma as part of an on-board modular system developed to convert ship fume pollutants into less damaging substances. An finite element analysis (FEA) modelling program was used to design the EB gun electrodes which were manufactured and tested afterwards to

generate the required beam power and shape. The aim of this chapter was to gain an understanding of thermionic electron gun design and limitations.

Chapter 4 reviews relevant work on plasma emission and plasma diagnostics at similar operating conditions. The type of plasma cathode used in this work is a low-temperature, low-pressure, RF excited plasma cathode design. Description of other plasma cathode guns available in the literature is also included.

Chapter 5 describes the experimental setups used in the experimental work carried out. Chapter 6 presents the experimental results from the RF plasma cathode gun, as well as from a DC plasma cathode gun. The results include EB current measurements and spectroscopic measurements.

Chapter 7 describes the simulation work. The first section of the simulations chapter includes a FEA model to look at the EB trajectories generated. The second section gives an overview of the PIC simulations results of the RF plasma chamber.

Finally, Chapter 8 summarises the conclusions drawn from this thesis work and suggests future work lines to follow.

1.5. Publications

Some of the results included in this thesis work have been published and references are given below. The chapter numbers where the material from each publication appears is given next to each reference.

DEL POZO, S., RIBTON, C.N. and SMITH, D.R., 2014. A Novel RF Excited Plasma Cathode Electron Beam Gun Design. *Electron Devices, IEEE Transactions on,* **61**(6), pp. 1890-1894. **[Chapters 5 & 6]**

DEL POZO, S., RIBTON, C. and SMITH, D.R., 2014a. Characterisation of an RF excited argon plasma cathode electron beam gun, *Vacuum Electron Sources Conference (IVESC), 2014 Tenth International* 2014a, pp. 1-2. **[Chapters 5 & 6]**

DEL POZO, S., RIBTON, C.N. and SMITH, D.R., 2014b. Spectroscopic characterization of a novel RF excited plasma cathode electron beam gun design, *Vacuum Electronics Conference, IEEE International* 2014b, pp. 169-170. **[Chapters 5 & 6]**

DEL POZO, S., RIBTON, C.N. and SMITH, D.R., 2014. Spectroscopic Characterisation of a Novel RF Excited Plasma Cathode Electron Beam Gun Design, *41st Institute of Physics (IOP) Plasma Physics Conference. London, UK* **[Chapters 5 & 6]**

RIBTON, C., DEL POZO, S. and SMITH, D.R., 2015. *Characterisation of a Novel Electron Beam Gun Design with a Radio Frequency Excited Plasma Cathode.* 1056/2015. **[Chapters 5 & 6]**

A publication on the last results is under preparation in collaboration with the Institut für Werkstoffkunde, Leibniz University, Hanover. **[Chapters 6 & 7]**

Chapter 2 : The Conventional Electron Beam Gun

In this chapter the basic components of a conventional electron beam gun are described. The fundamental principles regarding the design of conventional electron beam guns for material processing applications are summarised. Published work on electron guns is reviewed to gain an understanding of the main parameters that affect electron gun design and the limitations for the designer.

2.1. Introduction

Electron beams were first investigated by Thompson at the end of the 19th century (Thomson 1897). The first record of the concept of using the power of electron beams for deliberately melting metals, such as tantalum powder, was from von Pirani in his patent of 1907 (Von Pirani 1907), inventing electron beam refining of metals (Schultz 1994, Eichmeier, Thumm 2008). The principles of electron emission and acceleration in electric fields were investigated by Langmuir, Child, Dushman and Richardson in the period 1900 to 1920. The science developed at this time is still used today in the design of electron guns. Examples of charged particle beam applications (mainly electron beams) in the period 1920 – 1940 were cathode ray tubes for early television, X-ray tubes for medical examination and charged-particle accelerators for scientific instruments (Molokovskiy, Sushkov 2005).

In the 1950's some other applications for electron beams such as microwave tubes (klystrons, travelling-wave tubes and other high frequency vacuum electronic devices) emerged. Most of the electron gun development up to this time was for vacuum electronic devices for applications in radio and radar systems.

In 1953 K.H. Steigerwald invented the electron beam drilling and welding process using a focal Wehnelt design. Following this, significant developments in the electron beam technology for material processing took place. These included electron beam welding,

melting and refining of metals later in the 50´s (Molokovskiy, Sushkov 2005, Schultz 1994). The expansion of applications for the technology was stimulated mainly by the requirements of industries such as automotive (rapid welding for mass production), aerospace and nuclear power plants (precision welding of highly reactive metals such as titanium and zirconium alloys in a vacuum chamber) (Molokovskiy, Sushkov 2005).

There was a need for all these beam applications to develop optical systems to optimise the beams produced. These would allow the beam to be focussed to an intense spot at long range, but also as the motion of charge particles is affected by the space charge fields, the gun electric field distribution was modified to counter this effect and maintain a beam focusable to an intense spot at high beam currents.

Pierce was the first one to publish his monograph on electron beam gun design based on this theory (Pierce 1954). Magnetic lenses were developed to allow the beam to be focused at the work piece. In 1927 J. Bush developed a formula to calculate the focal length of a magnetic lens after calculating the electron beam trajectories in an axially symmetrical magnetic field. This was used by Liebmann (Pierce 1954, Liebmann 1955a, Liebmann, Grad 1951, Liebmann 1955b) and others in developing high quality lenses that enabled the development of the electron microscope and electron beam processing systems. Pierce and Wehnelt, in particular, developed the underlying science and design methodologies for high power electron beams of the type useful for material processing applications. The principles and laws that they investigated will be summarised in the following subsections.

In more recent times the use of computer simulation software to allow accurate modelling of the electron gun and electron optical systems has been a key enabling factor in the development of higher power electron beam systems. Section 2.8 describes a number of software packages that are available today for the electron gun designer.

This chapter describes how conventional electron beam guns operate and gives details on the main components and basic electron physics involved. Further details on this subject can be found in Schultz (1994), (Pierce 1954). There are a number of issues to

be considered in the design of electron guns and this section gives an overview of the important design rules.

2.2. The Principal Components of an Electron Gun

Electron guns are used in a wide number of different applications and devices in industry. The beam power produced and requirements for other electron beam attributes vary depending on each specific application. However, the generic configuration of the main components of most electron gun designs is illustrated in Figure 2.1. The key components of an electron gun are:

- The cathode and anode
- The bias electrode
- The vacuum system
- The X-ray biological shielding

These components are described in more detail in the following subsections.

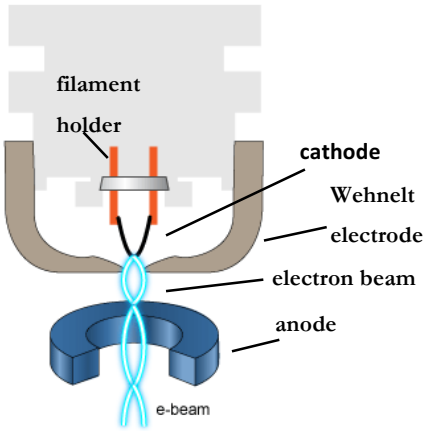

Figure 2.1 - Diagram showing main components of a conventional electron gun: cathode, anode and Wehnelt electrode. Modified from (Australian Microscopy and Microanalysis Research Facility 2014)

Beam power in an electron beam gun is given by the product of the electron beam current and the accelerating voltage applied to extract the electrons:

$$\text{Power (W)} = \text{Voltage (kV)} \cdot \text{Current (mA)}$$

Other parameters that characterise the quality of electron beams are emittance and brightness and these will be described further in this chapter.

2.3. The Cathode and the Anode

The cathode is the source of electrons in the electron gun and for materials processing it should be able to produce a high current electron beam (Schultz 1994), in the range 0.5 mA to 1 A. The most commonly employed cathodes in material processing electron guns are thermionic cathodes.

The anode is at ground potential and electrons leaving the cathode, which is held at a high voltage of typically –30 to –150 kV, are accelerated in the electric field towards it. The anode has a hole in the middle and the electrons pass through it when they are fully accelerated.

The cathode is an important part of the electron gun, and it has a strong influence on the properties of the beam produced. A good understanding of the cathode electron emission properties is necessary to allow investigation of electron gun designs. The following sub sections give the key principles of cathode operation.

2.3.1. Thermionic Emission

Thermionic emission in materials is achieved by heating up the material until the kinetic energy of some of the electrons within it is increased sufficiently to overcome the potential barrier at the emitter surface. Oscilloscopes, travelling wave tubes, display monitors, vacuum display devices, and vacuum tubes all use a thermionic cathode as electron source (Eichmeier, Thumm 2008).

Thermionic emission is governed by the Richardson-Dushman law, which calculates the current density J for a cathode in a high strength electric field as follows (Richardson 1916):

$$J = AT^2 e^{-\frac{e\phi}{kT}}$$

where J is the cathode emission current density in A/cm^2, T is absolute temperature of the emitting surface in K, e is the electronic charge in Coulombs, k is Boltzmann's constant; $k = 1.3806504\times10^{-23}$ Joule/K, ϕ is the work function in eV and it can be

expressed as $\phi = \phi_w - \phi_{qt}$; where ϕ_w is theoretical work function of the material and ϕ_{qt} is correction factor for quantum tunnelling (Tuohimaa 2008):

$$\phi_{qt}[\text{eV}] = 0.012\sqrt{E_K[\text{kV/cm}]}$$

As seen from the Richardson-Dushman law, current density obtained from a cathode surface as a result of thermionic emission is dependent om the work function of the surface. The lower the work function, the lower the energy an electron needs to leave the material surface, thus the lower the temperature the cathode must be at to give a required current density. Table 2.1 shows the work function for commonly used thermionic materials.

Table 2.1 - Work function for commonly used thermionic materials

Element	W	LaB_6	CeB_6	Ta
Work function [eV]	4.52	2.69	2.65	4.1

A is the emission constant for the surface in A/cm^2K^2 theoretically derived as:

$$A = \frac{4\pi mek^2}{h^3}$$

where h is Planck's constant, m is the mass of the electron, A is a theoretical constant (of ~120×10^4 A/m^2K^2), but from experiment varies depending on the material and surface characteristics, such as roughness and crystal orientation (Goebel, Katz 2008).

There are some properties inherent to thermionic emission that will affect the design of electron guns (Gewartowski, Watson 1965):

- The emitted electrons have a range of initial velocities when they are emitted that should be taken into account in the design as it affects the electron trajectories.
- Thermionic cathode surface material determines the maximum emission density.

As seen from Richardson-Dushman law, a high temperature is needed to get a high emission from the cathode, and emission is related to temperature. The heating power required to achieve high electron currents is dependent on the dimensions, shape and material of the cathode. Figure 2.2 shows the emission current density curves for

typically used thermionic cathode materials such as tungsten, tantalum and LaB_6. Figure 2.3 and Figure 2.4 show some examples of cathode designs.

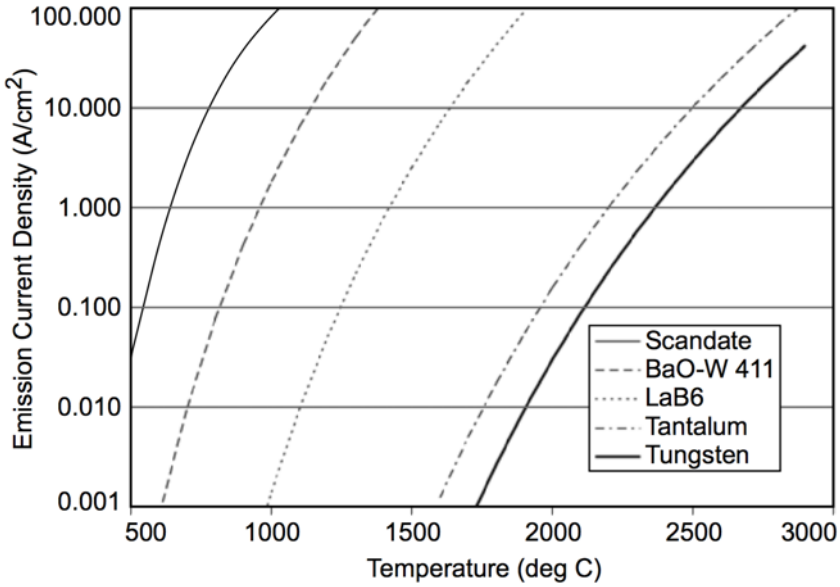

Figure 2.2 - Emission current density from metals used as cathode materials (Goebel, Katz 2008)

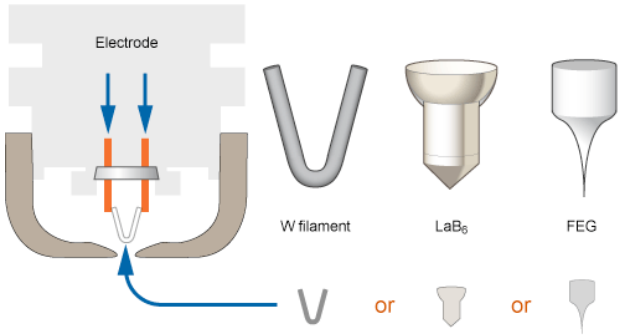

Figure 2.3 - Main cathode materials and shapes in electron guns showing a tungsten filament, a lanthanum hexaboride button and a field emission cathode (Australian Microscopy and Microanalysis Research Facility 2014)

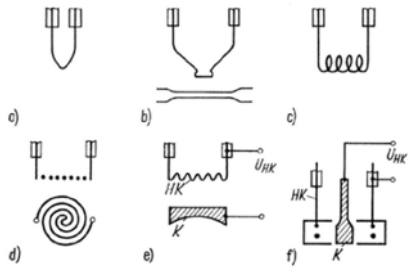

Figure 2.4 - Cathode designs: a) hair pin filament, b) back-bombarded cathode, c) coiled filament, d) pancake coil filament, e) back-bombarded shaped cathode, f) inductively heated cathode rod (Schultz 1994)

There are other excitation mechanisms that lead to electron emission such as incident electrons (secondary emission), photons striking a surface (photoemission), or application of a high electric field on the cathode surface, called field emission or the Schottky effect (Gewartowski, Watson 1965). These mechanisms are not employed in material processing equipment as they yield lower currents and insufficient processing power in the beam.

2.3.2. Cathode Heating

There are several ways to heat the cathode. Some systems include a primary cathode to which the current is applied and a secondary cathode that is heated through back bombardment by an electron beam from the primary cathode. In other cases, a high frequency generator is used to inductively heat the cathode.

The simplest and most widely used cathode heating method is to directly heat the cathode by a current. The peak energy of the electrons in the cathode is increased as the temperature goes up. Some of these electrons gain sufficient energy to overcome the potential barrier at the surface (given by the work function of the material) and escape. If there was no applied electric field, coulomb forces would accelerate the electrons back to the surface. However, in the case of an electron gun, the electric field beyond the surface accelerates the electrons and directs their trajectories to form a beam. In Chapter 3 these concepts are put into practice and a case study of the design process and test of an electron gun system using a tungsten filament design that is directly heated by a current is described.

2.3.3. Lifetime of the Cathode

The lifetime of the cathode is limited due to vaporisation (Schultz 1994) and erosion. The lifetime of the cathode will depend on the evaporation rate of the material at the operating temperature, and on the level of vacuum (Fiksel et al. 1996, Iiyoshi et al. 1996, Howard et al. 1927). For example, for tungsten, the evaporation rate at an emission current density of 10 A/cm^2 is approximately 10^{-3} mm/h (Schiller et al. 1982).

Cathode lifetime is also limited by erosion (Sanderson 1978), which is significant, particularly in materials processing applications due to ion bombardment coming from the EB melt pool at the work piece. This occurs because of ion generation where the beam fuses and vaporises the work piece. Positive ions are accelerated towards the cathode by the field in the gun, impact upon the cathode and cause vaporisation of material at the surface.

2.4. The Bias Electrode

This section describes the main types of electron guns attending at the bias electrode. The concept of perveance is also introduced.

2.4.1. Diode Guns – Cathode and Anode

The simplest electron beam gun consists of a cathode surrounded by an electrode at the same potential and an anode. The beam current is controlled by varying the cathode temperature. This type of configuration is known as a diode system. Although no differential voltage is applied between the gun electrode and cathode in a diode, the shape of the electrode surrounding the cathode and the shape and spacing of the anode have a strong influence on the beam trajectories and therefore the beam properties, such as the maximum beam power and intensity.

2.4.2. Triode Guns – Third Electrode

The most common means of controlling the electron beam current is by using a bias electrode for modulating the beam power. The beam current is controlled by variation of the potential (bias supply) applied to a third electrode (Molokovskiy, Sushkov 2005).

This third electrode is variously known as the grid cup, control electrode, bias electrode or Wehnelt cylinder. The bias supply is floating at near to the cathode potential, and it is used for controlling the electric field at the surface of the cathode, thereby controlling the emission density, according to Child's law.

A triode system allows an improved beam quality when using a heated ribbon cathode when compared with a diode system. This is because in a diode system there is no means of preventing electron emission from the filament edges and legs, and these electrons tend to have trajectories that are non-laminar with the rest of the beam, causing the beam brightness to be reduced. Figure 2.5 shows a diagram of a triode gun:

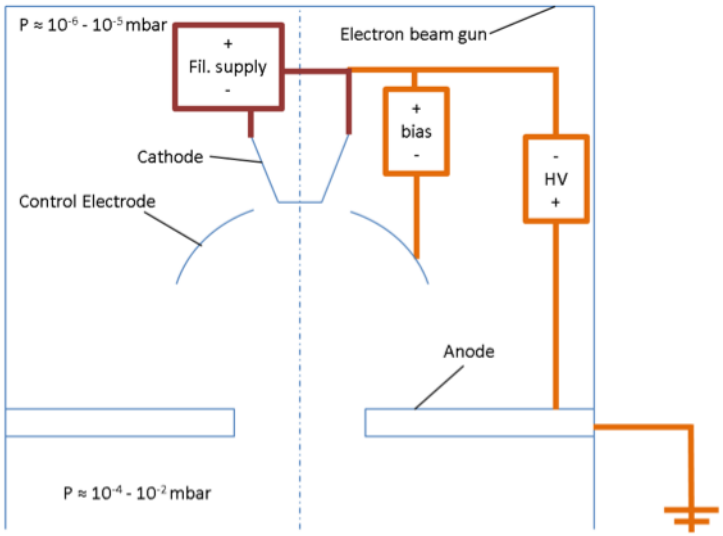

Figure 2.5 - Diagram of a triode electron beam gun

2.4.3. Pierce – Type Gun

As the beam current produced is increased, the electric field is modified by the charge density. This in turn affects the electron trajectories, generally causing the beam to diverge. The field can cause emission to be reduced and the electron beam to be aberrated. Charge density is greatest close to the cathode, where the beam is at low velocity, and it is here where space charge can have the most effect on the beam. This happens for high perveance guns. Perveance is an important gun parameter used to

assess the ability of a gun to produce beam current at a specific voltage (Molokovskiy, Sushkov 2005). It is given by the expression:

$$P = \frac{I}{V^{\frac{3}{2}}}$$

where I is beam current in A and V is the accelerating potential in V. The perveance is dependent upon on the gun geometry (Weon, Je 2005, Steckelmacher 1996). According to (Friedel, Felba 1994), from experiments and computations, space-charge effects become appreciable at perveance values P $\geq 0.1\ \mu A/V^{\frac{3}{2}}$. Perveance values of the installations of charge particle beam technology are in the range 0.01 – 20 $\mu A/V^{\frac{3}{2}}$. Perveance values lower than 0.05 $\mu A/V^{\frac{3}{2}}$ indicate that the effect of the space charge on the electron path is minimal.

The Pierce type gun design is intended to form a convergent beam compression. A Pierce type triode gun geometry can be used to compensate for the spreading effect of the space charge in the beam, by applying a convergent electric field. There is a coefficient of compression (C) which is given by the beam current density J divided by the cathode current density J_c. Perveance of up to $1\ \mu A/V^{\frac{3}{2}}$ can be achieved with the Pierce type gun desingn (Molokovskiy, Sushkov 2005).

2.5. Electron Optics / Focusing System

Beam guidance systems are used to get the desired shape of the beam, i.e. with a defined diameter, current density and specified power density (Schiller et al. 1982).

2.5.1. Focusing Lens

A mainly axially directed magnetic field, produced by a DC current applied through a solenoid coil, can be used to focus the electrons without changing their speed. The radially directed part of the field as the beam enters the lens causes the electron trajectories to rotate around the axis according to the Lorentz force law. As the electrons enter the more axially directed field at the centre of the lens, the Lorentz force is directed radially inward causing the trajectories to converge to a focus point that can be several hundred millimetres outside of the region of the lens. These magnetic lenses

consist of a ring with a large number of windings of copper wire shrouded by a high permeability iron casing (Schultz 1994) (See Figure 2.6). The shroud enhances, contains and localises the lens magnetic field, avoiding interference from ferritic objects nearby.

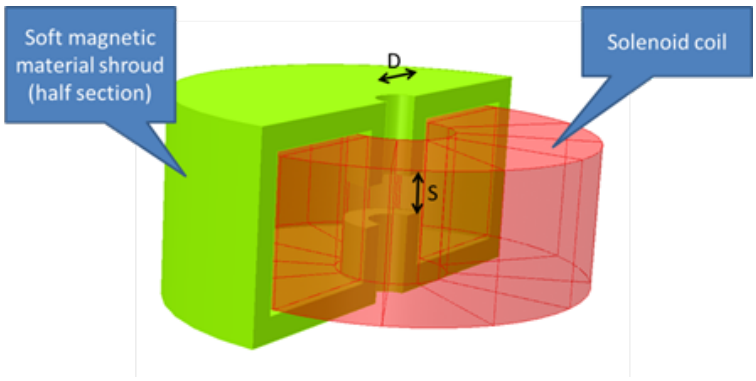

Figure 2.6 - Electromagnetic lens showing pole piece gap (S) and lens bore (D)

The focusing system is governed by the physical rules equivalent to a lens used to focus a beam of light (Schultz 1994):

$$\frac{1}{f} = \frac{1}{u} + \frac{1}{v}$$

where: f is focal length, u is "object" distance and v is "image" distance shown in Figure 2.7:

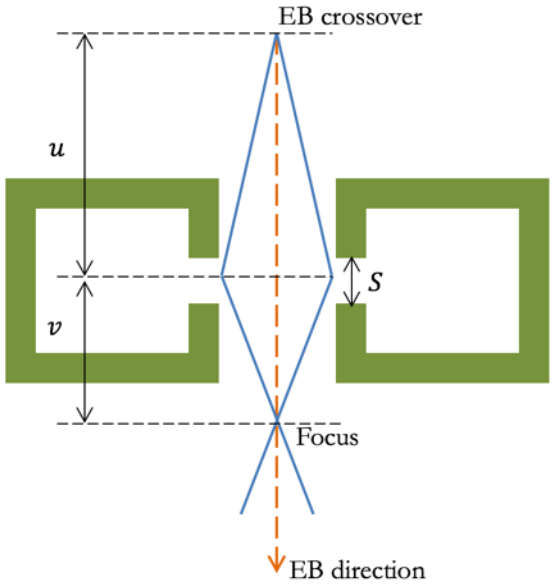

Figure 2.7 - Focal length in electromagnetic lens

The focal length of a lens is determined by the bore and pole piece gap (D and S in Figure 2.6), the coil excitation and the beam acceleration potential An empirical formula for calculating the lens geometry and the excitation required for a magnetic lens is given by Liebmann (Liebmann 1955a):

$$f \approx \frac{24\,(S+D)V_r}{(N \cdot I)^2}$$

where V_r is relativistically corrected voltage:

$$V_r = V\left(1 + \left(\frac{V}{1022000}\right)\right)$$

where V is the accelerating voltage [V], S is the lens shroud pole piece gap [mm], D is the internal bore of the lens shroud [mm], N is the number of turns in the coil, I is the current through the coil [A]. *S*, *D* are chosen such that the bore of the lens is many times bigger than the beam diameter (to reduce spherical aberration) and to fit with mechanical constraints, and then *NI* (ampere turns) are calculated.

In most electron beam applications the optical system has the aim of focusing the beam to a small spot or to obtain a small beam cross section (Molokovskiy, Sushkov 2005). This is the case with welding or additive manufacturing with metal. In other cases electron optics are not required, and an example of this is given in chapter 3, in which the electron gun is used to generate a beam that needs to be spread over a large area.

2.5.2. Deflection Coils

Deflection coils are used to move the beam away from its normal axis by applying a magnetic field transverse to the beam axis (Schultz 1994). The simplest deflection systems are either electrostatic or magnetic two- pole elements. Usually they are mounted in the gun column after the focusing lens. Figure 2.8 shows one form of a deflection system, called a bucking coil winding, with four coils wound on a single core. The deflection angle will be determined by the high voltage applied in the gun and the strength of the magnetic field generated by the deflection system.

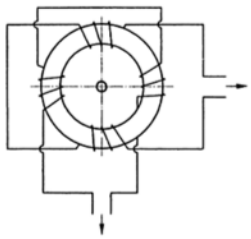

Figure 2.8 - A beam deflection system (Schultz 1994)

2.6. Vacuum System

Vacuum is necessary in the electron gun system to avoid collisions of electrons with particles in the air, to avoid oxygen contamination of the hot cathode, and to keep electrical insulation between the anode, cathode, and control electrode, i.e. avoiding ionisation due to the electric field strength and subsequent electrical breakdown (Schultz 1994). The pressure in the gun column is of the order of 10^{-5} mbar. A typical vacuum system for an electron gun has two separately pumped sections - the volume where the high voltage electrodes are mounted, and the working chamber containing the electron lens and the work piece. The working chamber is typically at a pressure between 10^{-2} mbar and 10^{-5} mbar. Generally, a typical vacuum system will have a rotary vane pump that is started to get to a coarse vacuum level (of the order of 10^{-2} mbar) and then a turbo pump would be started to get to the high vacuum levels (around 10^{-5} – 10^{-6} mbar) (Harris 1989). The two pumps are commonly cascaded, so that the rotary vane pump initially pumps the gun enclosure through the turbo, but ultimately provides becomes a backing pump for the turbo molecular pump, as this requires a backing pressure of the order of 10^{-2} mbar. There are different surface interactions and outgassing that contribute to the vacuum pumps load (Harris 1989). Programmable logic controllers are often used to automate the vacuum process and avoid damaging the pumps through incorrect sequencing, e.g. venting when the turbo molecular pump is at high speed.

2.7. X-Ray Biological Shield

Electron beam guns for material processing applications are generally operated at 30 – 150 kV accelerating voltage. At this high voltage, X-rays will be produced by Bremsstrahlung radiation as the electrons impact on electrodes or the workpiece surface

(ref) and suitable biological shielding is mandatory. Radiological quantities and units are shown below in Table 2.2 (Wrixon 2008).

Table 2.2 - Radiological quantities and units

Quantity	**Absorbed Dose**	**Dose Equivalent**	**Effective Dose Equivalent**
Unit	Gray (Gy)	Sievert (Sv) = Gy × R_{WT}	Sievert (Sv) = Sv × T_{WT}

Where R_{WT} is Radiation Weighting Factor (1 for X-rays); T_{WT} is Tissue Weighting Factor (1 for whole body total, see Table 2.3 for a certain tissue or organ).

Table 2.3 - Tissue weighting factors

Target tissue or organ	**Tissue weighting factor T_{WT}**
Gonads	0.2
Bone Marrow (Red)	0.12
Colon	0.12
Lung	0.12
Stomach	0.12
Bladder	0.05
Breast	0.05
Liver	0.05
Oesophagus	0.05
Thyroid	0.05
Skin	0.01
Bone surface	0.01
Remainder	0.05
Whole Body Total	**1**

The International Commission on Radiological Protection (ICRP) has set the following limits on exposure to ionising radiation (Wrixon 2008):

- General public – not more than 1 mSv per year
- Occupational effective dose should not exceed 20 mSv per year, averaged over 5 years (dose should not exceed 50 mSv in any year)

In order to provide adequate X-Ray shielding for an electron gun system, a British Standard is available to allow calculation for a range of X-ray sources (British Standards Institution 1971).

2.8. Quality of Electron Beams

This section describes the main parameters that are used to measure the quality of electron beams.

2.8.1. Electron Beam Brightness

Brightness B is given by the current density J per steradian:

$$B = \frac{J}{solid\ angle}$$

Another form for beam brightness is determined as:

$$B = \frac{I}{\pi r^2 \Omega}$$

where I is beam current, πr^2 is beam cross section (area) and Ω is the solid angle of the electron beam (Molokovskiy, Sushkov 2005). Brightness is calculated at a point in a given direction (Worster 1969). In other words, it can be defined as the amount of current that can be focused into a beam diameter from a particular solid angle of the electron beam (Eichmeier, Thumm 2008).

A high brightness electron beam will have a high current density and / or parallel electron trajectories (Humphries 2013). Langmuir (1937) and Pierce (1949) investigated electron beam brightness and assumed that the velocity distribution of the emitted electrons is semi-Maxwellian (this is a reasonable approximation for thermionic emission without electric field at the cathode) (Worster 1969):

$$B = \frac{JeV}{\pi kT}$$

The intensity J can be found experimentally by measuring the beam current and diameter, or by knowing the emission area at the cathode, and the total emission current. Brightness is conserved along the beam if the electrons are not accelerated i.e. after the anode. Lenses will reduce brightness due to aberration, but with some

attention to lens designs; their aberration effect on brightness will be insignificant for materials processing electron gun systems.

(Worster 1969) showed that the axial electron beam brightness, which is the brightness on the axis in the direction of the axis, in a cylindrically symmetric system, can be simplified to the following expression involving the average tangential and normal energies at the cathode, which correspond to the energy spread $E_{thermal}$ due to the cathode temperature and the energy given by an accelerating field E_{accel} respectivelly:

$$E_{thermal} = kT = \frac{1}{2}mv_x^2$$

$$E_{accel} = eV = \frac{1}{2}mv_y^2$$

Thus, the following can be calculated:

$$\frac{v_x^2}{v_y^2} = \frac{\frac{2kT}{m}}{\frac{2eV}{m}}$$

Assuming the worst case – when all the thermal velocity of the electron is transverse to the acceleration direction, the minimum beam half angle would be: $\sqrt{\frac{kT}{eV}}$

Therefore if the beam solid angle is small it approximates to: $\frac{\pi kT}{eV}$

Langmuir law: $\frac{B}{J} = \frac{eV}{\pi kT}$

From the equations above, the maximum brightness is calculated as:

$$B = \frac{J}{solid\ angle} = J\frac{1}{\pi}\frac{eV}{kT}\ [\mathrm{A/steradian/m^2}] \qquad [3]$$

$$J = B \times \alpha^2\pi = I/A$$

$$I = B \times \alpha^2\pi \times \pi r_{beam}^2;$$

$$r_{beam} = \sqrt{\frac{I}{B \times \alpha^2 \times \pi^2}};$$

$$d_{beam} = \sqrt{\frac{4 \times I}{B \times \alpha^2 \times \pi^2}}$$

Therefore, if brightness is assumed to not change along the beam, the minimum diameter of the beam can be calculated at the work piece.

$$\frac{B}{J} = \frac{1}{\pi}\left(\frac{eV}{E_t} + \frac{E_n}{E_t}\right)$$

where: E_n*is* normal energy and E_t *i*s tangential energy.

At points of high potential the dependence on the average normal energy is negligible. Brightness is conserved along the beam if the electrons are not accelerated, i.e. after the anode. Lenses will reduce brightness due to aberration, but with only slight attention to lens designs; their aberration effect on brightness will be insignificant for materials processing electron gun systems.

2.8.2. Space Charge

Space charge is a field produced by the density of electrons in front of the cathode surface. It can be described as a self-field of the beam (Stupakov, Huang 2008), which affects electron trajectories addition to the field from the accelerating voltage. This self-field can cause emission to be reduced and the electron beam to be aberrated. Charge density is greatest close to the cathode, where the beam is at low velocity, and it is here where space charge can have the most effect on the beam. Space charge affects electron beam brightness.

As the high voltage is applied, this cloud of electrons appears in front of the cathode and generates a current flow in the space, causing the radial potential distribution to change (Schiller et al. 1982). There is a limit in the maximum current that can be drawn from the cathode due to the space charge effect. This limitation is given by the Child-Langmuir's law, which calculates the space-charge limited current density for a parallel plate accelerator as follows (Child 1911):

$$J_{CL} = \frac{4}{9}\varepsilon_0\left(\frac{2e}{m_e}\right)^{\frac{1}{2}}\frac{V_0^{\frac{3}{2}}}{d^2}$$

J_{CL} is the space charge limited current density, ϵ_0 is permittivity of free-space, e is the charge of the electron [C], m_e is mass of electron, V_0 is the acceleration voltage applied, d is the gap distance (Tuohimaa 2008).

"The Child-Langmuir law shows that the space-charge limited current is proportional to the voltage raised to 3/2 power. This relationship between the current and the voltage is valid for all cathode–anode geometries and we can write I=pV3/2, where the constant p, called the perveance, only depends on the form of the electrodes (in the nonrelativistic limit). The classical scaling of the limiting current to the 3/2 power of gap voltage is widely used in the fields of high-current emission diodes, vacuum microelectronics, high-power microwave sources, accelerator physics, and sheath physics" (Weon, Je 2005).

Classical Child-Langmuir relation:

$I = pV^{\frac{3}{2}}$

where p is perveance.

2.8.3. Beam Perveance

The previous section described the Child-Langmuir law, which showed that the space-charge limited current is proportional to the accelerating voltage to the 3/2 power. This relationship can be applied for all cathode-anode geometries (Weon, Je 2005) and can be described as $I = pV^{\frac{3}{2}}$. The constant p is perveance, which gives a measure of how much space charge affects the the beam (Lawson 1988) and it is only dependent on the geometry of the electrodes (Weon, Je 2005, Steckelmacher 1996). Beam perveance is an important gun parameter used to assess the ability of a gun to produce beam current at a specific voltage (Molokovskiy, Sushkov 2005). It is given by the expression: $P = \frac{I}{V^{\frac{3}{2}}}$, which shows that beam perveance P is proportional to beam current I [A] and to the inverse of the $\frac{3}{2}$ power of the accelerating potential V [V]. Typically a beam current will start to be space-charge limited from perveance values $p \geq 0.1\ \mu A/V^{\frac{3}{2}}$. Minimum space-charge effects on the electron path would be given at perveance values lower than $0.05\ \mu A/V^{\frac{3}{2}}$ (Friedel, Felba 1994).

2.8.4. Beam Emittance

Another measure of the quality of an electron beam is beam emittance. This is a measure of how laminar or parallel a beam is (Tuohimaa 2008). Figure 2.9 shows particle trajectories in a laminar beam. Laminar beams are defined by the following conditions (Humphries 2013):

1) "All particles at a position have identical transverse velocities". Thus the electron trajectories will not cross each other except at the axis.
2) "The magnitude of the transverse particle velocity is linearly proportional to the displacement from the axis of beam symmetry".

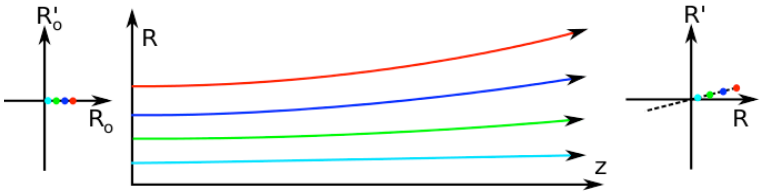

Figure 2.9 - Laminar beam where space charge dominates (Barnard 2014)

Thus, a beam will be focusable to a single point if the electron trajectories never cross each other – i.e. it will appear to have been emitted from a single point - such beams are laminar. However, aberration due to electron optics and thermal velocity spread will cause the beam trajectories to be non-laminar and their focus to become more diffuse. In this case, electrons are emitted from each point in different directions and therefore their paths do not intersect at a point on the image (Friedel, Felba 1994). In order to measure the degree of non-laminar flow in a beam, the notion of emittance has been introduced.

The emittance of a beam is determined as a phase ellipse area A divided by π (Friedel, Felba 1994):

$$\varepsilon = \frac{A}{\pi}\ [\pi\ \mathrm{m\ rad}]$$

Brightness, as described before in section 2.8.1, is defined as the maximum focused power flux of a beam and it can be quantified as a function of emittance. If the emittance remains constant, the beam brightness is also a conserved quantity. For

isotropic beams with average emittance ε the following approximation for Brightness can be applied (Humphries 2013):

$$B = \frac{I}{\pi^2 \varepsilon^2} \ [\mathrm{A/m^2 rad^{\,2}}]$$

2.8.5. Beam Aberration

Aberrations appear in electron optics systems. "In particular, gun aberration, lead to crossing of beam trajectories"(Molokovskiy, Sushkov 2005). Aberration can be classified as follows (Tuohimaa 2008):

- Axial aberration – either spherical or chromatic.

This normally has the highest influence on the beam quality. The spot size enlargement (at focus) due to spherical aberration is (Tuohimaa 2008):

$d_s = \frac{1}{4} C_s \theta^3$; with $C_s$aberration coefficient and θ focusing angle

The spot size enlargement due to chromatic aberration is:

$d_c = \frac{1}{4} C_c \frac{\Delta V}{V} \theta$; with $C_c$aberration coefficient, $\frac{\Delta V}{V}$ monochromacity of the beam, and θ focusing angle

- Off-axis aberration – astigmatism

Stigmator coils are used for compensating electrical and magnetic interferences that cause this phenomenon. They use magnetic fields to squeeze the beam shape in cross section to minimise astigmatism.

- Field aberration – field curvature, distortion

Modelling software is used to optimise the geometry shape for the required beam current and accelerating potential.

Brightness is given by the current density J per steradian:

$B = \frac{J}{solid\ angle}$ [A/cm^{2}steradian]

Brightness is conserved along the beam if the electrons are not accelerated i.e. after the anode. Lenses will reduce brightness due to aberration, but with only slight attention to lens designs, their aberration effect on brightness will be insignificant.

The total spot size is the sum (in quadrature) of these aberrations and is given by the following equation, taking into account aberration disks (d_C, d_S) and brightness limitations:

$$d_{total} = \sqrt{d_B^2 + d_c^2 + d_s^2}$$

2.9. Electron Beam Gun Modelling Software

The advent of powerful computing capability in the past two decades has allowed electron gun design to make use of simulation software to investigate cathode and electrode geometries, and to model cathode emission to a good degree of accuracy. Finite element analysis software packages are often used in the design and optimisation of electron guns and calculating the trajectories of the electron beams generated. There are a number of software packages available and in this section a sample of these has been reviewed made up of the following:

- Opera
- Charged Particle Optics
- Beam Optics Analyser
- EGUN

This list is not exhaustive, but is representative of the range of software available. All software generally will solve the geometry as an electrostatic problem to determine the field amplitude and direction distributed across the gun. It will then plot a set of beamlet trajectories through the field, and will then calculate how the space charge produced by the beam modifies the electric fields, re-plot the trajectories and recalculate the fields iteratively until some convergence criteria is met.

2.9.1. Opera Vector Fields

In the work described in this thesis Opera-2d and Opera-3d versions were used. 2D modelling software is typically used in electron gun simulations as geometries are axisymmetric and it allows solving complex problems in a short time. A practical example is given in Chapter 3 of this thesis, in which Opera-2d is used to simulate a triode electron beam gun design that is manufactured and tested. The 3D version of Opera is used when there is not axial symmetry.

Opera-2d simulation software

Opera-2d uses finite element analysis for solving electromagnetic and electrostatic problems in two dimensions with either xy symmetry or axisymmetry. The field equations used in the analysis are based on the Poisson's equation in two dimensions, and the modification of this by space charge (Opera 2012).The software comprises the pre and post processor and the solver modules:

- Pre and Post-Processor

In the pre-processor, the geometry of the 2D model is defined by the user in different regions. A grid of points and construction lines can be defined as drawing aids. Then the material properties, element size and distribution for the mesh are set for each of the regions. These can be modified, copied, moved or grouped.

For magnetic regions BH data should be defined for non-linear materials. For electrostatic regions the permittivity is usually defined to be linear with electric field where required for electron gun analysis. The boundaries of the problem can be defined in various ways to enable symmetry or to define the potential along a boundary. The regions and mesh data are checked to be consistent. Then the mesh is generated and all the nodes and elements are created. After this, the type of analysis is chosen and run. Command files can be used in the process.

Once the model has been analysed, the post-processor allows display of results in various ways: Fields at a point, at a line, around a circular arc, contour and vector maps.

Particle trajectories can be calculated for the results obtained and intersections with a line can be obtained. Then these can be displayed or graphed.

Magnetostatic and electrostatic field analysis

Static Field (ST) Analysis Program - This program is used for solving time invariant magnetic or electric fields problems, with either linear or nonlinear material permeability or permittivity. Information such as if the solution is linear or nonlinear, mesh refinement and scale factor should be defined.

Space Charge Beam (SP) - This analysis solves time invariant electric fields models taking into account the effects of space charge created by beams of charged particles (Opera 2012). At least one emitter should be defined in the SP Beam analysis. The emitter represents the cathode which is used in the real electron beam gun; and therefore, the dimensions and material details should be input to the software.

2.9.2. Other Software Packages for Electron Gun Modelling

- **Charged Particle Optics (CPO)**

CPO uses the Boundary Element Method to solve 2D and 3D electrostatic problems. CPO 2D is used to model systems with axial or planar symmetry whereas the 3D version can be used for systems with no symmetry (CPO Ltd 2015). The main features of this package are:

  - The geometry of the electrodes is defined by coordinates (r,z) or (x,z) in the 2D version and (x,y,z) in the 3D version.
  - The electrodes are defined as thin sheets of charge, with no nodal points in the space that the electrodes enclose.
  - Space charge cells can be added to the space through which the beam passes so that mesh points are used for space charge calculations.

- **Beam Optics Analyser (BOA)**

BOA is a 3D particle simulation code that uses finite element analysis combined with user-controlled meshing (Calabazas Creek Research 2010). It is used to simulate

electron guns, collectors and charged particle devices. The code solves 3D electrostatic and nonlinear magnetostatic problems.

- 3D complex structures can be modelled and geometries can be imported from commercial solid modelling programs
- Space charge and self magnetic fields are modelled
- Multiple emitters are available

2.10. Electron Gun Applications

Electron gun systems consist of electron gun electrodes, vacuum chamber and pumps, X-ray shielding, power supplies and control systems. Figure 2.10 presents a diagram of an EB system and main elements. However, some features such as the power of the generated electron beam and the size of pumps will be different depending on the application. Electron beam welding, additive manufacturing, surface texturing, cutting and fume treatment are the most relevant applications for the type of electron gun investigated in this thesis work. This subsection will review these processes and their typical power values and vacuum levels.

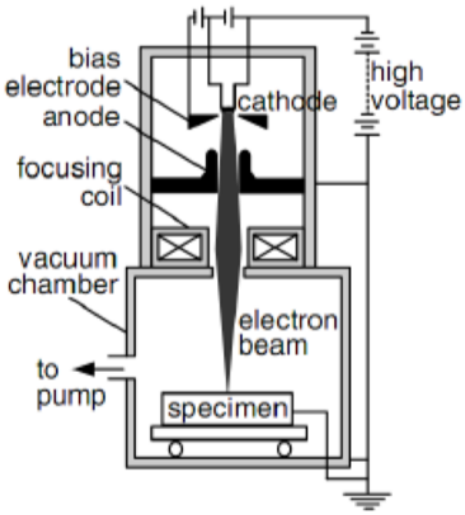

Figure 2.10 - EB welding system (Kou 2003)

2.10.1. Electron Beam Welding (EBW)

EBW is a fusion welding process in which the electron beam penetrates the material and creates a "keyhole" in the workpiece (Schultz 1994). As a result, deep and narrow

welds can be made. The kinetic energy of the electron beam is turned into heat when applied to the work pieces so that these are melted locally to the beam and joined together. It is also an automatic process and allows fast, clean and precise welding of thick sections. Even though it is a fusion process, the distortion in the welded joint is very low as a result of the deep penetration in the material and narrow welds. Thus, EBW is used in industries that require very high quality standards such as automotive and aerospace (Serles 2015). Figure 2.11 shows a diagram of an electron beam and the keyhole on the work piece.

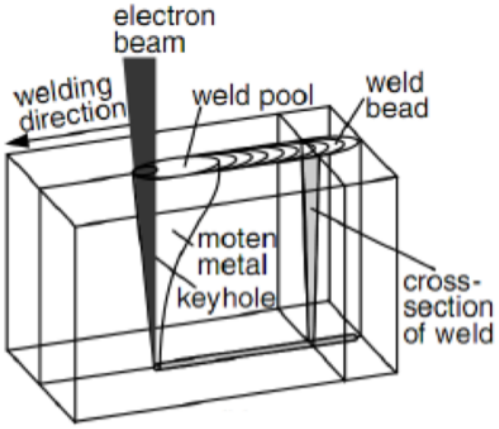

Figure 2.11 - EB keyhole (Kou 2003)

Conventional welding as described in the previous sections is carried out in a vacuum chamber, which provides a clean environment for the weld. Other electron beam welding process variants include out-of-chamber EB welding and local vacuum welding with a sliding vacuum chamber that moves along the welded joint. Figure 2.12 shows the local vacuum EB welding system developed in TWI Ltd. welding a 1300 mm linear seam in 60 mm thick steel that was completed in 6 minutes. High vacuum levels of around 10^{-4} mbar are achieved for in-chamber welding and only coarse vacuum can be reached in the out-of-chamber and local vacuum systems (10^{-2} mbar in the case of this last one).

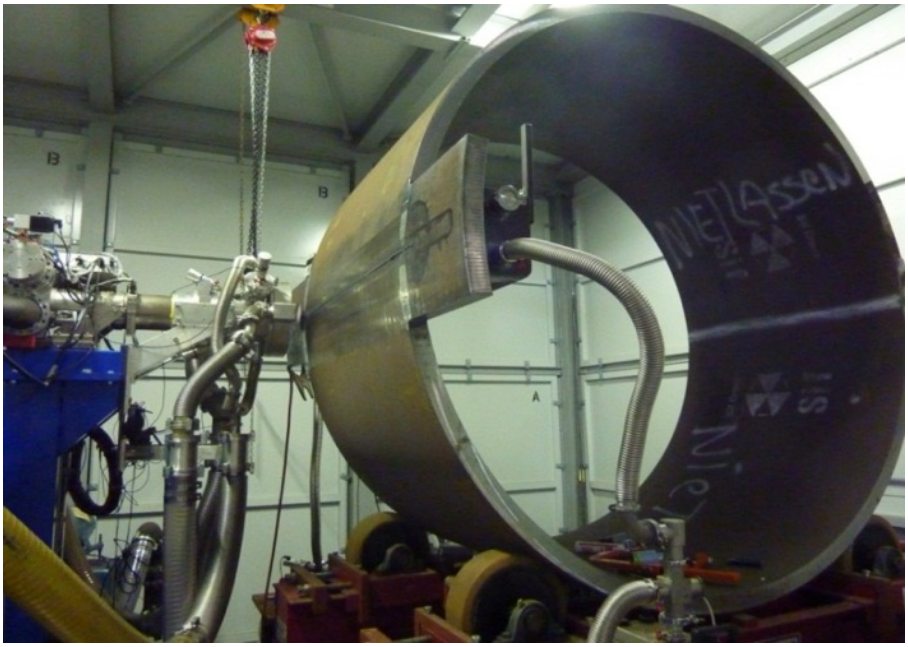

Figure 2.12 - Local vacuum EB welding with sliding seal (TWI Ltd.)

Electron guns can be classified depending on their power range (TWI Ltd.):

- Very high power guns from 100 kW to 5 MW operating at 40 kV to 150 kV are widely used for melting and vacuum refining of metals.
- High power guns from 15 kW up to 100 kW and 60 kV to 150 kV electron guns are used for welding of thick section material (up to 250 mm penetration in steel) while keeping a stable electron beam. This high power is typically used in the energy sector and nuclear waste encapsulation. Figure 2.13 shows an EB welded gear cluster as example of application in EB welding at high power in which the fusion zone is localised to the weld.

Figure 2.13 - Example of an EB welded gear cluster

- Medium power guns from 60 kV to 150 kV, and 3 kW to 15 kW electron guns are widely used for welding of metal sections with a penetration that ranges from 1 to 20 mm, surface texturing, curing of surface coatings and additive

manufacturing using a powder bed. The industries that use medium power are mainly automotive, medical and aerospace.

- Low power guns (<3 kW) are used to produce very intense beams focused to a very small spot (20 μm). These systems typically use an accelerating potential of less than 60 kV. They have found some applications in the medical and electronic industries.

2.10.2. Electron Beam Additive Manufacturing (EBAM) or Electron Beam Melting (EBM)

3D printing of objects in metal has brought great advantages in manufacturing as it has enabled making complex parts inexpensively, "complexity comes for free", and saving in raw material. This is very beneficial with parts made of high cost materials such as titanium alloy used for parts in the medical and aerospace industries. Other materials suitable for EBM include: stainless steels, Inconel, tantalum and tungsten (Sciaky Inc. 2015). Electron guns are integrated into these systems as the source of heat for melting the metal. There are two main variants of EB additive manufacturing:

1) Metal powder bed – Figure 2.14 shows the additive manufacturing technology in which an EB is used to selectively melt the surface of a metal powder bed and form a 2D layer of the final object. The powder bed is then lowered and a layer of powder is spread across the bed selective melting is carried out by the beam for the next layer. This operation is consecutively repeated and objects are made layer by layer (Attar 2011).

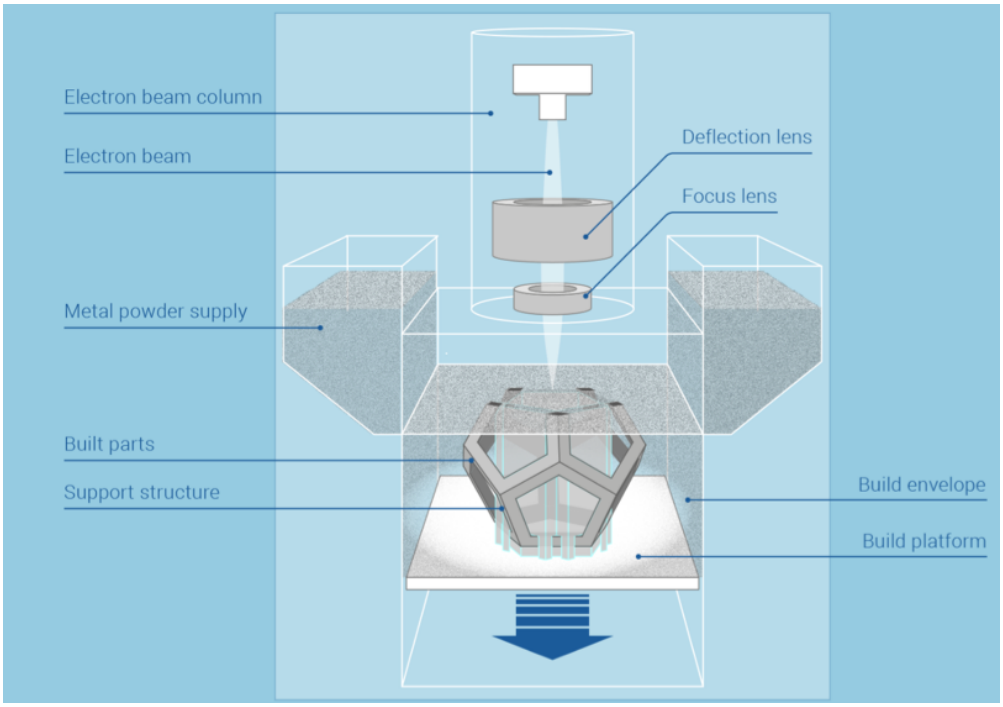

Figure 2.14 - Electron beam gun system for additive manufacturing in powder bed (Additively 2016)

2) Wire feed – The material from a wire feedstock is deposited layer by layer by applying the heat of the EB. The layers are thicker than in the metal powder beds so the objects are made faster, but the surface produced can be rough. Finish machining is needed to get the final object (Sciaky Inc. 2015).

Figure 2.15 - Additive manufacturing using wire feed in titanium (Sciaky Inc. 2015)

2.10.3. Surface Modification

Electron guns can be also used for surface modification of metals. The electron beam is deflected rapidly over the metal surface to displace material in a controlled manner and make texture features (protrusions and cavities) on the surface (Tavakoli et al. 2007). The voltage used is about 150 kV at a low power of about 2 kW. By accurately controlling beam parameters (beam acceleration potential, beam current and focus) a wide variety of features can be made. Figure 2.16 shows an example of surface modification in titanium alloy. Some of the applications include surface modification of medical implants (such as titanium hip implants) so their surface has a texture as similar as possible to bone tissue. The fact that the process is done in vacuum is also beneficial for medial parts as it keeps a clean environment. Heat exchangers are another application.

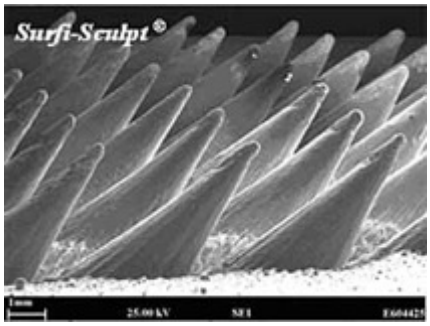

Figure 2.16 - Surface modification in titanium alloy using Surfi-Sculpt process (Dance, Buxton 2007)

2.10.4. Cutting/Machining

This is an emerging technology where finely focussed electron beams are being investigated for applications in cutting and machining, where in the last two decades laser processing has dominated. Electron beam cutting and machining offers a higher rate of material ablation and rapid beam movement using magnetic deflection systems.

2.10.5. Competitive Technologies – Laser Beams

Laser beams share a number of material processing applications with EB, such as welding, additive manufacturing, surface modification and cutting. Moreover, both are

thermal processes. However, electron beam processes use electrical energy to generate high energy electrons and laser beam processes use high energy coherent photons for material processing (IIT Kharagpur 2009). Thus each of the processes has different advantages and limitations.

Laser beams can be easily focused using optical lenses achieving a very high power in a very small spot. This is very beneficial for some machining applications such as metal cutting or drilling of holes. Another advantage of lasers is that they can be pulsed which is a great advantage in applications where the beam needs to be switched on and off rapidly. An example of this is powder bed additive manufacturing as the beam is moved to different positions on the powder bed.

The main limitations of laser beams is their penetration capability in the target material. The energy of the photons in the laser beam only is applied in a thin layer of the surface of the metal. This limits the speed for building objects in additive manufacturing applications and the speed for cutting. In contrast, electron beams can penetrate in the material, which allows melting thicker layers and processing the material faster. However, beam pulsing in conventional electron guns (with a thermionic cathode) is complex if compared with laser pulsing. This will be discussed later as this limitation can be eliminated if using electron sources other than thermionic cathodes, i.e. plasma cathodes.

2.11. Other Electron Sources

In this section, other ways to generate a beam of electrons are reviewed.

2.11.1. Field Emitted Electrons

Thermionic cathode electron guns are the most common type used but there are other electron sources such as field electron emission or cold cathode. In this type of electron gun a very high electric field is applied to the cathode surface to generate the electrons. The cathode has a field emitting tip which is usually tungsten and has a strong curvature in order to get high field strengths with low voltages.

2.11.2. Plasma Cathodes

Plasma cathode are the main focus of this thesis and will be discussed in more detail in Chapter 4. Plasma EB sources offer solutions to the main problems with conventional electron beam guns, which use a thermionic cathode. Cathode wear from thermal cycling or ion bombardment is eliminated. EB power can be controlled by RF power modulation, which avoids the need for a grid electrode, and as a result reduces beam aberration. Plasma cathodes have shown to be capable of generating high emission densities and can be used in low vacuum environments without damaging the cathode or electron source (Oks 2006). This technology has generated interest from various sectors of industry including additive manufacturing where rapid printing would be possible due to the high power provided by the electron beam, and at the same time fast beam pulsing can control material melting. Plasma cathodes will be further described and detailed in later chapters.

2.12. Summary

A review of the main components and important parameters in electron gun design has been presented. The principles and laws governing electron gun performance have been reviewed.

Details about the main applications of electron guns for processing have been given. Electron beam processing was compared to another thermal processing technology, laser beam processing. Laser processing has been shown to have some advantages compared to electron beam processing and different limitations depending on the material processing application considered. Benefits of plasma cathodes were introduced. Plasma cathodes will be described in more detail in the following chapter, as plasma cathode electron guns are the focus of this work.

Chapter 3 : Case Study "A Thermionic Electron Gun Design"

This chapter describes the design, development and testing of an electron gun used in a non-thermal plasma reactor (NTPR). This work was part of the FP7 European project "Diesel Engine Emission Control" (DEECON) (Balachandran et al. 2014). The principles reviewed in Chapter 2 and the main parameters involved with electron beam (EB) gun design were put into practice in this work. This chapter concludes showing that the simulation work used for the design optimisation and the real beam measurements in the final system were in agreement.

3.1. Introduction

Air pollutants generated by the engines of sea fairing cargo ships produce at least 15 % of the World's NOx, between 2.5 – 4 % of greenhouse gases, 5 % black carbon (BC) and between 3 – 7 % of global SO_2 output (Neef 2009). These hazardous components have long term damaging effects on the environment and are harmful for the health of people, particularly those living in coastal areas. The global fleet will increase by 35% over the next five years and 60% by 2020. International and national regulations have been established in order to limit ship emissions. As a result, according to legislation, in forthcoming years new ships must be designed, and existing ships must be retrofitted, with systems to reduce emissions.

Current solutions include using lighter fuels, which are more environmental friendly. However, fuel switching only reduces SOx emissions and it is ineffective in the reduction of submicron and nanoparticles. Available on-board cleaning technologies are based on adaptations of existing systems used in power plants or industry. These solutions are efficient in SOx abatement but have lower efficiency with NOx and do

not work for reducing Particulate Matter (PM), CO, CO_2 and Volatile Organic Components (VOC) emissions (Jaworek et al. 2014).

A new technology is needed to address the lack of suitable fume scrubbers. The solution proposed by DEECON for the control of marine emissions was an innovative on-board after-treatment system for reduction of PM, SOx, NOx, CO and VOC emission (Jaworeke 2014). This technology was developed as an integrated system approach using an electrostatic seawater scrubber (ESWS), a non-thermal plasma reactor, state of the art selective catalytic reduction, and an ESWS wash water treatment unit. The NTPR combined electron injection and microwave power to generate a non-thermal plasma for VOC, NOx and SO_2 abatement (Balachandran 2014). The work described in this chapter concerns the design, development and testing of the electron beam gun system used for the electron injection in the NTPR.

3.2. Requirements

The NTPR design consists of a set of magnetrons that produce microwave (MW) emission to generate a non-thermal plasma in the reaction chamber, through which the exhaust gases from a marine diesel engine are passed. The energetic electrons generated by the EB gun system are injected into the reaction chamber increasing the plasma energy. Molecular excitation, ionisation and dissociation occur as a result of the incident high energy electrons and the exhaust gas is converted into different components with much lower concentration of NOx, SO_2 and VOC (Balachandran et al. 2014). Figure 3.1 shows a diagram of the NTPR system (Manivannan et al. 2014).

As seen in Chapter 2 a nozzle system and differential pumping is typically used in conventional EB systems for material processing when the beam is required to be employed at pressures higher than those required in the EB itself. Differential pumping requires very large pumps as gas constantly leaks into the gun column, but one of the DEECON NTPR requirements was reduced pump sizes. An electron beam window was needed between the EB system and the reaction chamber, allowing electrons to pass through into the reaction chamber but preventing ingress of gas into the gun. Thus, only the EB gun enclosure would be pumped down. A second reason for a

window was to avoid contamination of the anode and grid cup electrodes and the cathode in the EB gun.

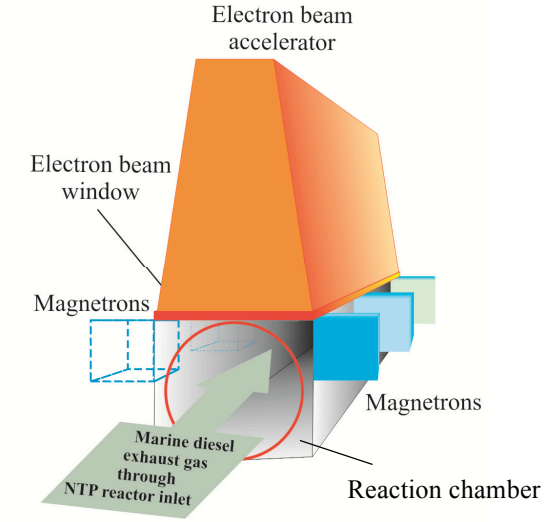

Figure 3.1 - Integrated NTPR with MW and EB (Balachandran et al. 2014)

The EB gun system requirements for the NTPR processes were:

- To produce a minimum beam current of 35 mA (limited to 4 mA for laboratory scale trials) – required to produce the plasma ionisation.
- To use a maximum acceleration potential of 60 kV – required as higher acceleration potential would require more X-ray shielding.
- To pass the beam through a window of a certain diameter in a way that the beam can be spread over the maximum area and at the same time is kept within the window – required as transmission losses cause window heating and heat dissipation limits the maximum beam intensity that can be dealt with.
- To operate the gun with a 1100 V bias supply and 15 A filament – this constraint was imposed by the available commercial high voltage power supplies.

To meet the requirements above the objectives set for this work were:

1. To design and develop a 60 kV triode EB gun capable of producing 35 mA minimum current and to be switched off at 1100 V bias voltage, with a filament current of up to 15 A.
2. To design the electron optics to focus the beam through a window measuring 10×10 mm and to fit into an existing gun housing, within weight limitations suitable for the application.

3. To demonstrate that the 60 kV triode EB gun designed is capable of producing 35 mA minimum current, switches off at 1100 V bias voltage and that the design is flexible to generate beams as low as 4 mA needed for laboratory scale while still satisfying the rest of the requirements.
4. To demonstrate that the beam diameter matches the window area over the working range of beam current.

3.3. Design and Test of The Electron Gun System

This section describes the design process followed to produce an electron gun that satisfied the specifications of the NTPR. A 60 kV EB gun system was designed to meet the requirements for the DEECON project. Figure 3.2 illustrates the process followed to carry out the work described in this chapter. After discussion and collation of the requirements with the project team at Brunel University London, an electron gun was designed. An existing housing, HV socket and filament holder were procured from an EB gun supplier. The design of the gun electrodes was carried out through a trial and error process using a finite element modelling software package. Once a design was found that satisfied the requirements, this was transferred into a mechanical model, engineering drawings were produced and the gun was manufactured. Following this the EB gun was mounted onto a chamber and was commissioned. The beam was measured and the results were compared with predictions from the modelling software and the requirements.

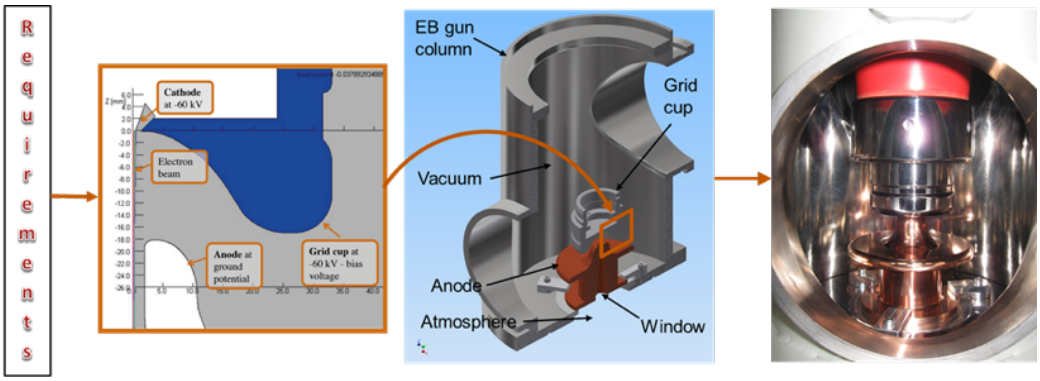

Figure 3.2 - Design, development, test and measurement process of the EB gun system

The cathode in this application is a tungsten (W) filament ($\phi_w = 4.52$ eV). As can be seen from Richardson-Duschman's law, the emission current is exponentially proportional to the temperature. The filament was heated by supplying a current through the filament.

3.3.1. Beam Power Requirement

2d finite element (FE) analysis software for solving axisymmetric electrostatic and electromagnetic problems (Opera-2d) was used in the design and optimisation of the grid cup and anode electrode geometries. Opera-2d has been described in more detail in Chapter 2. Different geometries at 60 kV accelerating potential were analysed until the power requirements were reached. The minimum current needed according to the NTPR requirements was 35 mA, thus the power requirement is:

$$Power(\text{kW}) = accelerating\ voltage\ (\text{kV}) \times current\ (\text{A})$$
$$Power(\text{kW}) = 60\ (\text{kV}) \times 35\ (\text{mA}) = 2.1\ \text{kW}$$

Figure 3.3 shows the EB gun geometry defined in the Opera pre-processor 2D model with the different regions and units in mm. Grid cup, cathode and anode were drawn with boundary conditions to define scalar potentials. HV cable and insulator were added to the model to allow investigation of the electric field on the surface of the insulator, to mitigate against electrical discharges in this area. In Figure 3.3 the voltages for each of the regions were indicated, and in Figure 3.4 the voltages are illustrated in a colour map.

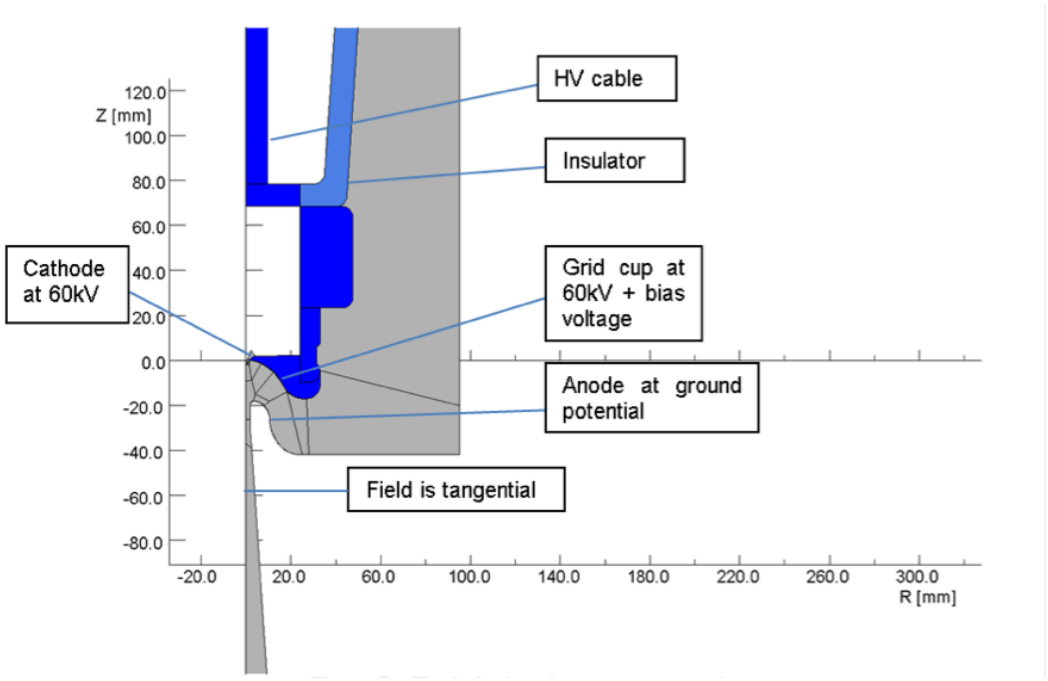

Figure 3.3 - Final electron beam gun model geometry

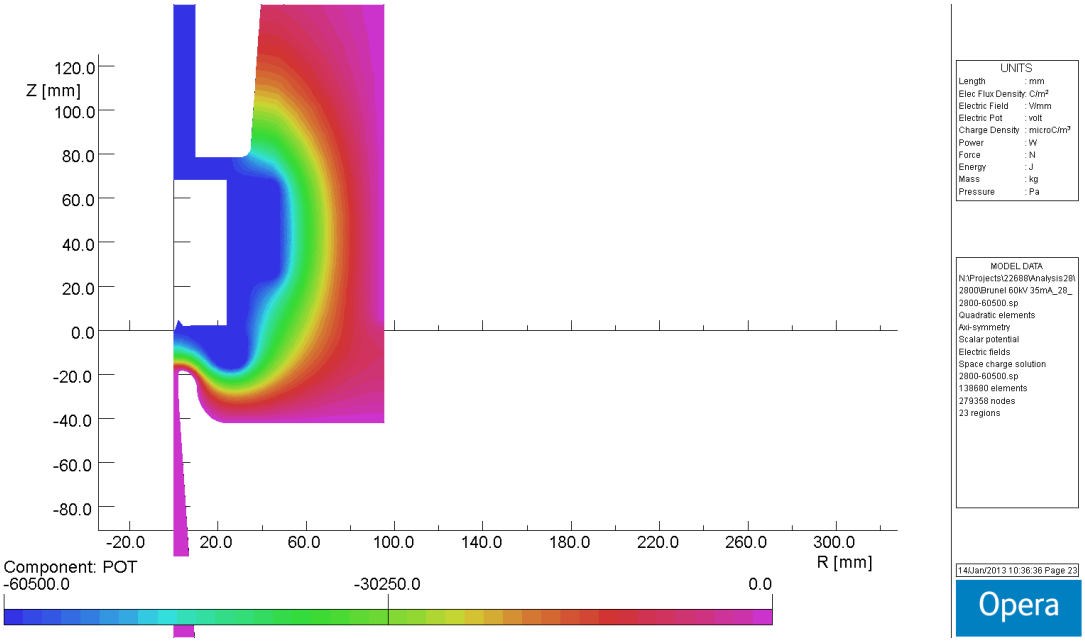

Figure 3.4 - Colour map showing potential distribution

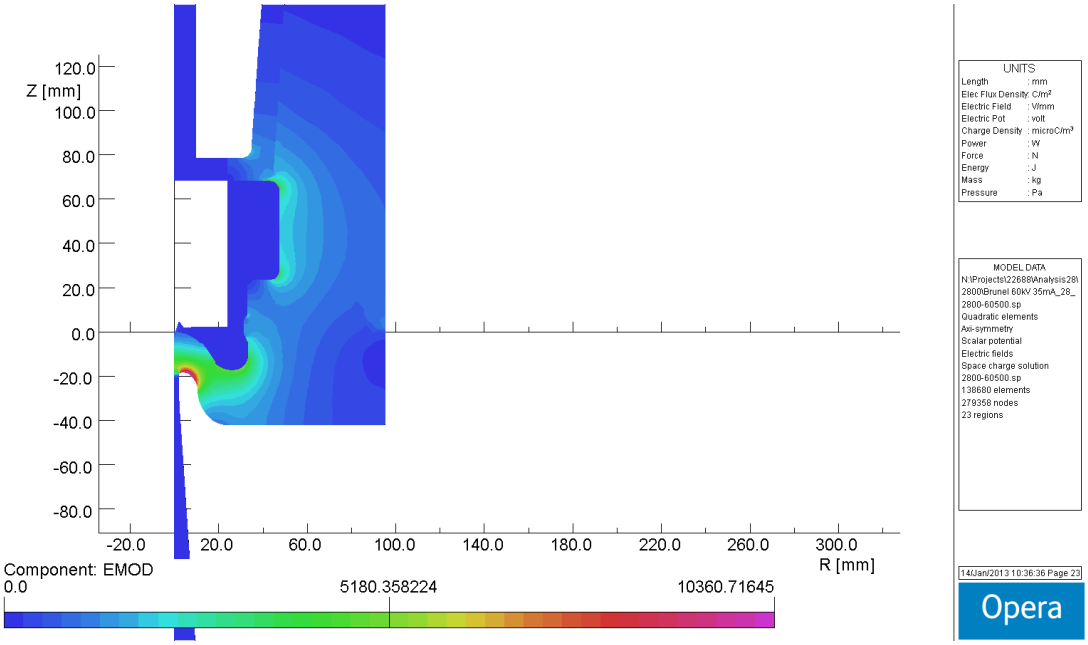

Figure 3.5 - Colour map showing electric field strength (Emod) in V/mm

A space charge (SP) beam analysis was set with an emitter type defined by the Langmuir-Fry equations (Opera 2012). The emitter parameters were:

- Particle mass = 1 electron
- Charge = -1 (particle type is electron)
- Maximum ray spacing [length units] = 1
- Temperature [K] = 2300 to 2800
- Work function [eV] = 4.52 (for Tungsten ribbon filament)
- Emission constant [A/cm^2K^2] = 120

After the preliminary analysis the following observations were made:

- Changing the grid cup from a spherical to a parabolic shape has a strong effect on the shape of the beam. The grid cup was designed to be parabolic in order to concentrate the beam in a diameter not bigger than the drift tube in the anode.
- As the cathode temperature was increased, the current density of the beam increased, and so did the beam diameter, reducing clearance between beam and drift tube. The drift tube diameter was also increased to a minimum of 4mm in order to leave enough clearance for the beam.

- Reducing the distance between cathode and anode from 18mm to 16mm did not increase the maximum current produced as this was at the thermal emission limit.

3.3.2. Design to Minimise Potential Stresses

The geometry of the electrodes was modified to minimise potential stresses. The electric field strength (V/mm) was displayed in a colour map in order to identify the high voltage stress regions. The radius at top of the anode was increased so that the potential stress was reduced, as dictated by Gauss's Law (citation):

$$E = \frac{q}{4\pi\varepsilon_0 R^2}$$

The grid cup edges were smoothed and potential stress was reduced in this region to reduce the risk of voltage breakdown. The density of elements was increased in critical regions (top of anode), in order to avoid error in the finite element analysis calculations. The final shape, optimised for low voltage stress, is presented in Figure 3.5. The maximum voltage stress is about 10 kV/mm on the tip of the anode, which is an acceptable value to avoid high voltage breakdown in the vacuum chamber.

3.3.3. Bias Voltage Requirement

The beam current should be switched off at 1000 to 1100 V bias voltage between the filament (at –60 kV) and the grid cup, as the selected electron gun power supply (HiTek EB4000) has a –10 to –1100 V grid bias supply. The grid cup hole diameter was reduced in order to switch off the current at the maximum bias available. As a result, the distance between the cathode (at –60 kV) and the grid cup electrode (at up to –61.1 kV) was made very small, but this introduced risk of electrical break down across this gap. This would lead to uncontrolled surges in beam current that could be detrimental to the system. It was observed that reducing this distance did not have a major effect upon the bias voltage required to switch off the beam current. Therefore, the distance was left at 1 mm.

The anode was moved away from the cathode. At 18 mm distance from the anode tip to the cathode surface the current is switched off at the desired bias voltage, and the maximum beam power that can be produced and the low stress potential features are retained.

3.3.4. Final Design Analysis Over Full Range of Temperatures and Bias Voltages

Once the geometry was designed for the main conditions described above, space charge analyses over the full range of cathode temperatures and bias voltages were performed with the aid of scripts (command files) and the following sweep parameters:

- Cathode temperature: 2300 to 2800 K (50 K steps).
- Bias voltage: 0 to 1100 V (25 V steps).

With the results obtained, the peaking curves of the gun were plotted:

- Beam current/Temperature for a fixed bias.
- Beam current/Bias voltage for a fixed temperature (See Figure 3.18).

From the peaking curves, the operating point for the gun can be observed at the desired temperature. A triode is normally operated in the knee of the curve (in the beam current-temperature graph). From Figure 3.6 it can be seen that below the knee the beam current is dependent on cathode temperature. At temperatures higher than at the knee point, the beam current increases very little as the emission is space charge limited. Beam current emission from the legs of the filament starts to take place at bias voltages below 425 V, and increases as the bias is reduced, as illustrated in Figure 3.6.

a)

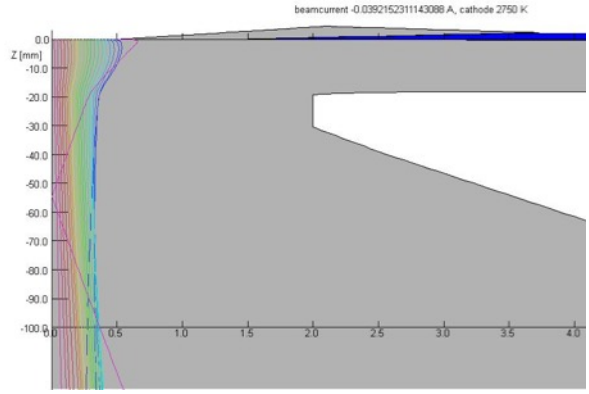

b)

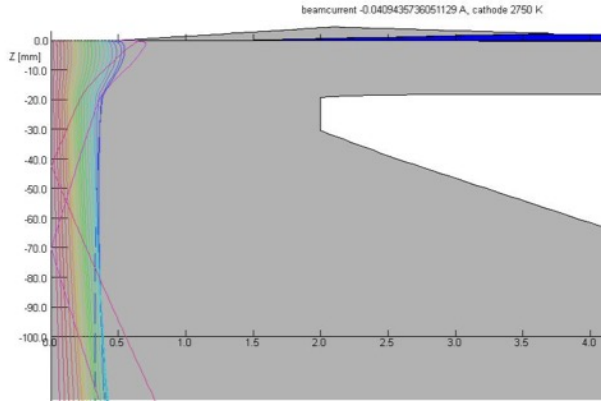

c)

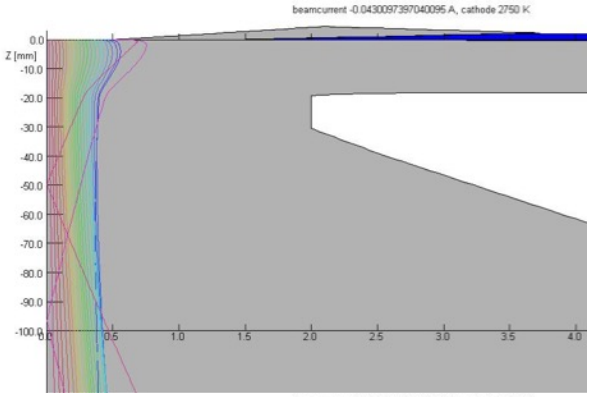

d)

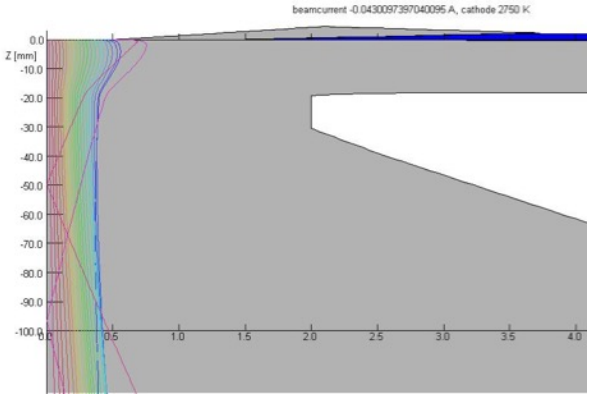

Figure 3.6 - Beam current trajectories with increasing emission from the filament legs at: a) 475 V; b) 450 V; c) 425 V; d) 400 V bias voltage

3.3.5. Beam Quality Analysis

The figure of merit used in electron beam guns for beam quality analysis is brightness. High brightness is achieved when all the electrons are apparently originating from the same point and poor brightness if they are coming from different points. This is important as when the beam has to be focused, the brighter the beam is, the smaller the focused spot will be. In this application some spreading of the beam across the transmission window is required, so it has been more relevant to look at the beam profile at the window position.

As seen before in Chapter 2, the maximum emission possible is given by the Richardson – Duschman's law (Richardson 1913). At the temperature selected (2750 K) the maximum current density is:

$$J_0 = 4.724\ \mathrm{A/cm^2}$$

The tungsten ribbon filament has a 50 μm thickness and 1 mm^2 front face. Then, for 1mm diameter cathode emitting surface, the maximum current will be:

$$I_{max} = \frac{4.724A}{100mm^2} \cdot (\pi 0.5^2) = 0.036816\ \mathrm{A}$$

The maximum brightness is given by the maximum current density per minimum solid angle:

$$B = \frac{J}{solid\ angle}$$

Another command-file was used to obtain the brightness of the beam as well as other parameters for each of the temperatures and bias voltages analysed before. The beamlets calculated by the SP solver and stored in track files are intersected by a line and for each of the beamlets the values for velocity and position are stored as well as the beamlet current and total beam current. From these parameters, the basic characteristics of the complete beam were calculated: angular divergence, current weighted average source position, mean source radius and beam brightness.

As shown seen in Chapter 2, the maximum possible brightness takes into account thermal velocity spread (in calculations) to calculate the minimum solid angle; however, no thermal velocity spread was considered in the emitter model. Thus, the brightness

values obtained by the software for a highly optimised geometry could be higher than those predicted by the thermal velocity spread calculations. In this case, further refining of the model to improve beam brightness to a higher value than this target will not produce a brighter beam in practice.

Emission from the filament legs usually causes the brightness of the beam to be low as the beamlets are not laminar. However, since the beam was required to be spread over the area of the window material, this fact was not critical in this particular application.

3.3.6. Optics Design

A magnetic lens was selected as a convenient means to focus the beam allowing the spot diameter at the window to be varied. Magnetic lenses obey the same Newtonian rule as light lenses. As the object distance (*u*) to the lens plane is defined by the trajectories of the beam from the gun, and the image distance (*v*) is the distance of the window from the lens plane, the focal length of the lens can be calculated as seen in Chapter 2.

The Liebmann formula (Liebmann 1955) gives an empirical means of estimating the lens geometry and the excitation required for a magnetic lens:

$$f = \frac{24 \cdot (S + D) \cdot V_r}{(N \cdot I)^2}$$

where V_r is relativistically corrected voltage $V_r = V \cdot \left(1 + \left(\frac{V}{1022000}\right)\right)$,$V$ is accelerating voltage [V], S is pole piece gap [mm], D is lens bore [mm], N is number of turns in coil, I is current in coil [A]. *S* and *D* are chosen (See Figure 3.7) such that the bore of the lens is many times bigger than the beam diameter (to reduce spherical aberration) and to fit with mechanical constraints, and then *NI* (ampere turns) are calculated:

a. For practicality, the current density in the coil cross section should not exceed 0.7 A/mm2, as at higher values active cooling of the coil is required – for example water cooled hollow conductors.
b. The actual number of turns of a commercially available wire can be calculated from look up tables, and then the required current to achieve the focal length can be deduced.

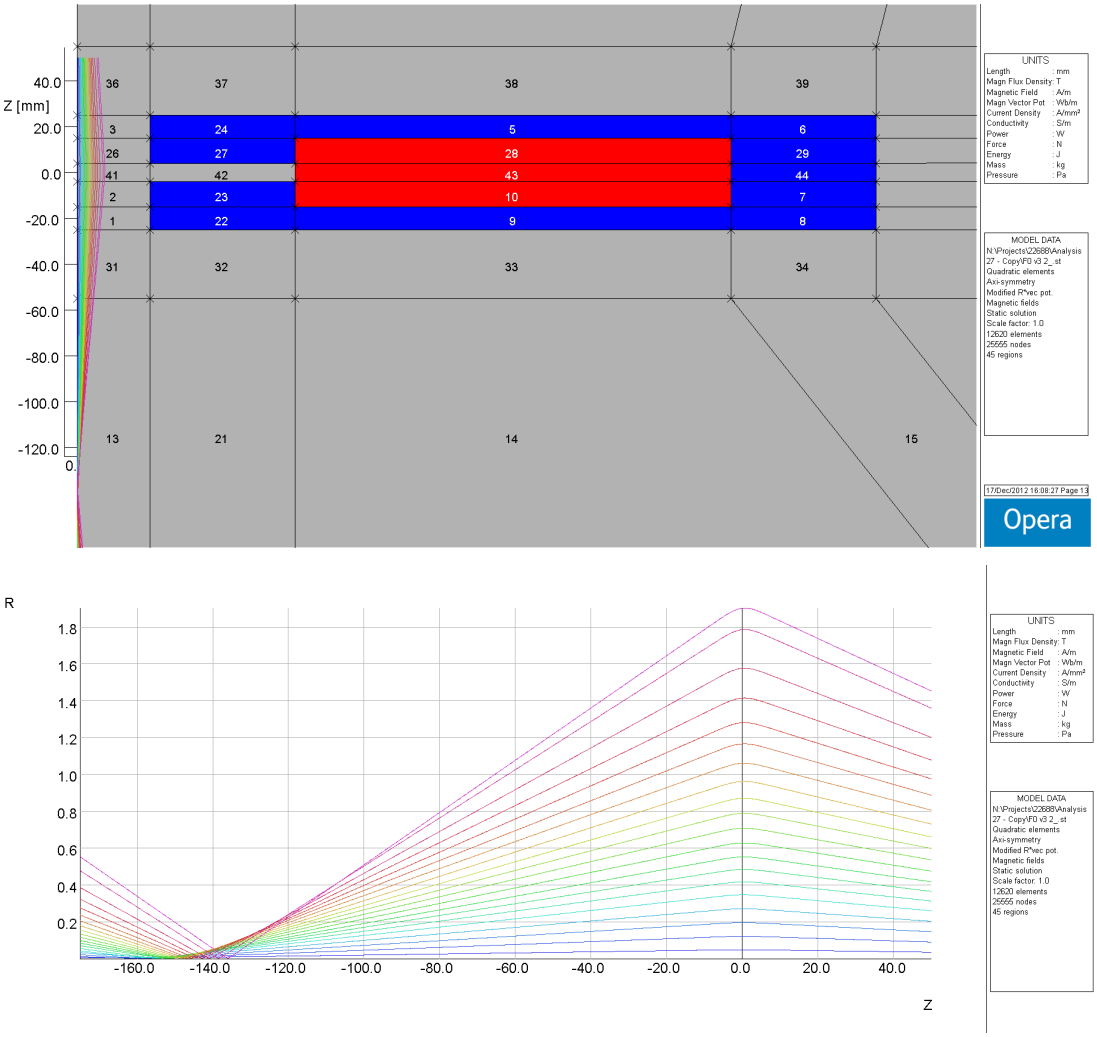

Figure 3.7 - Opera-2d model for lens (top) and graph of the focused beam (bottom) NB electrons travelling from right to left in the lower figure

The lens was modelled separately in Opera-2d, and an ST analysis was run. (This analysis solves for magneto-static fields but does not take into account space charge. Once the beam is accelerated to –60 kV space charge does not play a significant role in the beam characteristics) (Anderson et al. 2002). The beam trajectories previously generated and stored from the triode gun model were introduced, with the aid of a command file, into the lens model and compared with the calculations. Figure 3.7 shows the 2D model in Opera and a graph with the focused beam.

Second, the beam was required to be spread in the window, so that the heat load is shared over the area. Although this could be achieved by focussing the beam at a shorter working distance so that it crossed over and spread, the lens added weight and

complexity. Therefore, in the final design the focusing lens was not used, although the design could be useful if there were changes in requirements, e.g. window size. Small deflection coils can be used to spread the beam if the beam diameters generated by the gun are not big enough.

3.3.7. Shielding Calculations

The following calculations were carried out using BS 4094. Part 2 (British Standards Institution 1971):

Flux per milliamp and minute produced by a certain high voltage at 1 m is taken from Figure 3 in BS 4094, Part 2. For a 60 kV voltage:

$$(Flux/mA)/min = \ 0.027\ (Roentgens/mA)/min = \frac{0.027\ R}{mA \cdot min}$$

Since the maximum possible current is 100 mA, the radiation per hour is calculated for this current:

$$radiation\ at\ 1m = \frac{0.027\ R}{mA \cdot \frac{1}{60} hours} \cdot\ 100\ mA = 162\ Rad/\ hour$$

The exposure-rate at a distance y is obtained using the inverse square law (British Standards Institution 1971). Thus, radiation at 0.5 m (distance from shield to source):

$$radiation\ at\ 0.5\ \mathrm{m} = \frac{162\ \frac{\mathrm{Rad}}{\mathrm{hour}}}{y^2} = 648\ \frac{\mathrm{Rad}}{\mathrm{hour}} = 6.48 \cdot 10^5\ \frac{\mathrm{mRad}}{\mathrm{hour}}$$

As seen in section 2.5, allowable dose is 1 mSv per annum. Assuming that the equipment is run for 1000 hours per year:

$$1\ \mathrm{Sv} = 100\ \mathrm{Rem}$$

$$allowable\ dose = 0.1\ \frac{\mathrm{mRem}}{\mathrm{hour}}$$

Attenuation coefficient is:

$$Attenuation\ required = \frac{radiation\ at\ shielding\ distance}{allowable\ dose} = \frac{6.48 \cdot 10^5 \frac{mRad}{hour}}{0.1 \frac{mRem}{hour}}$$

$$= 6.48 \cdot 10^6$$

$$Transmission\ factor\ required = \frac{1}{Attenuation} = 1.54 \cdot 10^{-7}$$

The thickness of lead required is calculated in half-value or tenth-value thicknesses (radiation is reduced by half or tenth respectively):

$$no.half - value\ thicknesses = \frac{Log(attenuation)}{Log(2)} = 22.6$$

$$no.tenth - value\ thicknesses = Log(attenuation) = 6.8$$

Total shield lead thickness will be:

$$Total\ shield\ lead\ tickness = no.half\ thicknesses \cdot half\ thickness$$

$$= no.tenth\ thicknesses \cdot tenth\ thickness$$

Half-thickness and tenth thickness values for lead were interpolated from the data in Table 6, Appendix 3 (British Standards Institution, 1971):

$$Total\ shield\ lead\ thickness = 22.6 \cdot 0.11 = 6.8 \cdot 0.37 = 2.5\ \text{mm}$$

For a steel shielding and 60 kV voltage, the lead equivalence is given in Table 1 (British Standards Institution 1971), 0.39 mm thickness of Pb is equivalent to 2 mm steel thickness. Therefore, for 2.5 mm lead thickness:

$$Total\ shield\ steel\ thickness \cong 13\ \text{mm}$$

3.3.8. Electron Penetration Range Calculations for Electron Window

Brunel University London, as coordinator of the DEECON project, selected silicon nitrade as the material for the electron window as it has a low atomic number and therefore has a low absorption of electrons. The window had to be assessed for the following:

- Transmission efficiency – Part of the power will be lost as the beam passes through the window. The distance from surface the window surface is called the electron range. A first calculation for the electron interaction range gives an idea of the power loss (Schiller et al. 1982):

$$\delta = 2.6\times10^{-17}\frac{V^2}{\rho}$$

Where ρ is the density of the material [$\mathrm{Kg/mm^3}$], V is the high voltage of the gun [V], δ is the depth of electron penetration [$\mu\mathrm{m}$]

For Si_3N_4 window material $\rho = 3.44\times10^{-6}\ \mathrm{Kg/mm^3}$:

$\delta = 27.2\ \mu\mathrm{m}$

Which means that the thickness of the window should be far smaller than 27.2 μm, as almost all the power will be lost at this distance. Losses in a 3 μm thickness window can be estimated to be approximately 10%.

- Pressure – A 3 μm thickness window would be able to stand the pressure differential, according to advice received by Brunel University London from the material supplier.
- Heat and Contamination – further assessments should be carried out to evaluate these conditions. Air will be introduced through a channel between the glass and metal walls of the chamber. By keeping the air velocity higher than the velocity in the plasma chamber, contamination of the window will be avoided. Moreover, it acts as a cooling system for the heat load on the window.

3.3.9. Experimental Prototype

The modelling work predicted that the EB gun designed was capable of providing at least 35mA beam current. Technical drawings for the components designed were produced and sent for manufacture both in TWI and outside. Other elements such as pumps and power supplies were purchased. Once all the parts arrived, the electron beam gun system was put together and switched on in TWI.

Probing work was carried out to characterise the beam produced from the gun. This section describes the different elements of the system developed.

- **Cathode, grid cup and anode electrodes**

Figure 3.8 is a 3D CAD-model half-section of the final design showing grid cup and anode electrodes assembled in the upper gun column.

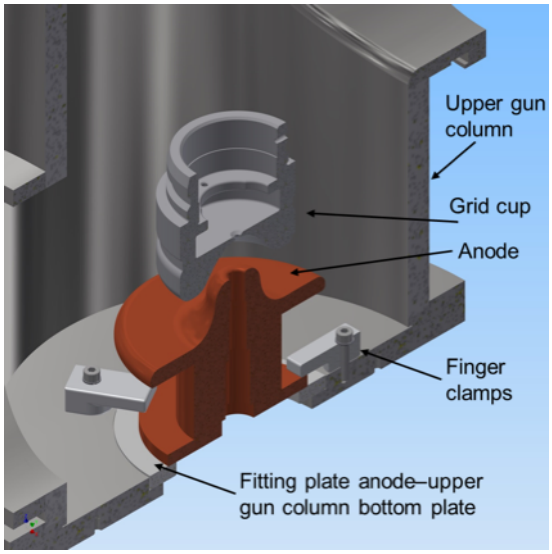

Figure 3.8 - 3D CAD model half-section in Inventor

The cathode (tungsten filament) is at –60 kV and it is important that it is placed in the centre and at the right distance from the anode and grid cup. In the electron gun design application presented in this chapter, there is no work piece and a window isolates the plasma chamber; therefore, there will be no ion bombardment from the ions released from the metal. Thus the cathode life will be limited mainly by evaporation of the material. For tungsten, the evaporation rate at an emission current density of 10 A/cm^2 is approximately 10^{-3} mm/h (Schiller et al. 1982).

Figure 3.9 shows the tungsten filament in the filament holder. The grid cup is at –60 kV plus bias voltage and the anode is at 0 V, ground potential.

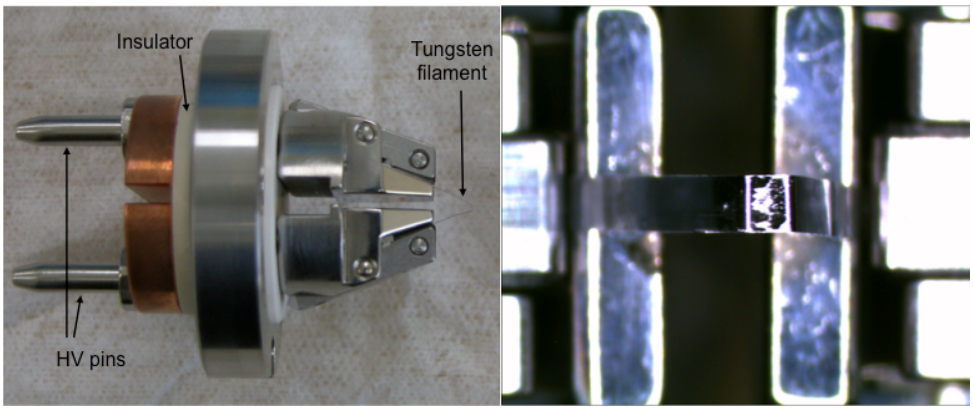

Figure 3.9 - Filament in filament holder side view (left) and top view in microscope (right)

The front face of the grid cup was designed from the simulation work carried out in Opera-2d, however design for manufacturing and assembly also played a vital role in this work. The grid cup was designed so that it fits the locking ring mechanism of the insulator by which it is held, as well as having the right features to accommodate the filament holder assembly. Figure 3.10 shows the grid cup and filament holder assembly.

Figure 3.10 - Filament holder assembly and grid cup (top), and the filament holder accommodated in the grid cup (bottom)

Special attention was paid to the dimensions and tolerances of the grid cup hole, which is very close to the filament and thus highly influences the beam quality; as well as to the face of the grid cup where the filament holder sits (called DATUM in the grid cup drawing). These dimensions are important since they affect directly the position of the filament and therefore the beam characteristics. Discussions with the technicians were necessary in order to find out about the tolerances that can be achieved with the technology, budget, materials and time available to keep the important features of the design from the simulation work in Opera-2d. Important dimensions were given tolerances as low as 0.01 mm, such as the grid cup hole.

Grid cup and anode design were constrained in size by the space available in the gun column since both of the parts had to be accessed from one of the holes at the gun column side. When the tungsten filament needs to be changed, the anode should be taken out first to then get to the grid cup, which accommodates the filament holder assembly. Figure 3.11 is a sketch showing the anode path. It demonstrates that the clearance for the anode inside the gun column housing is enough to take it out through the 151 mm diameter hole on the side.

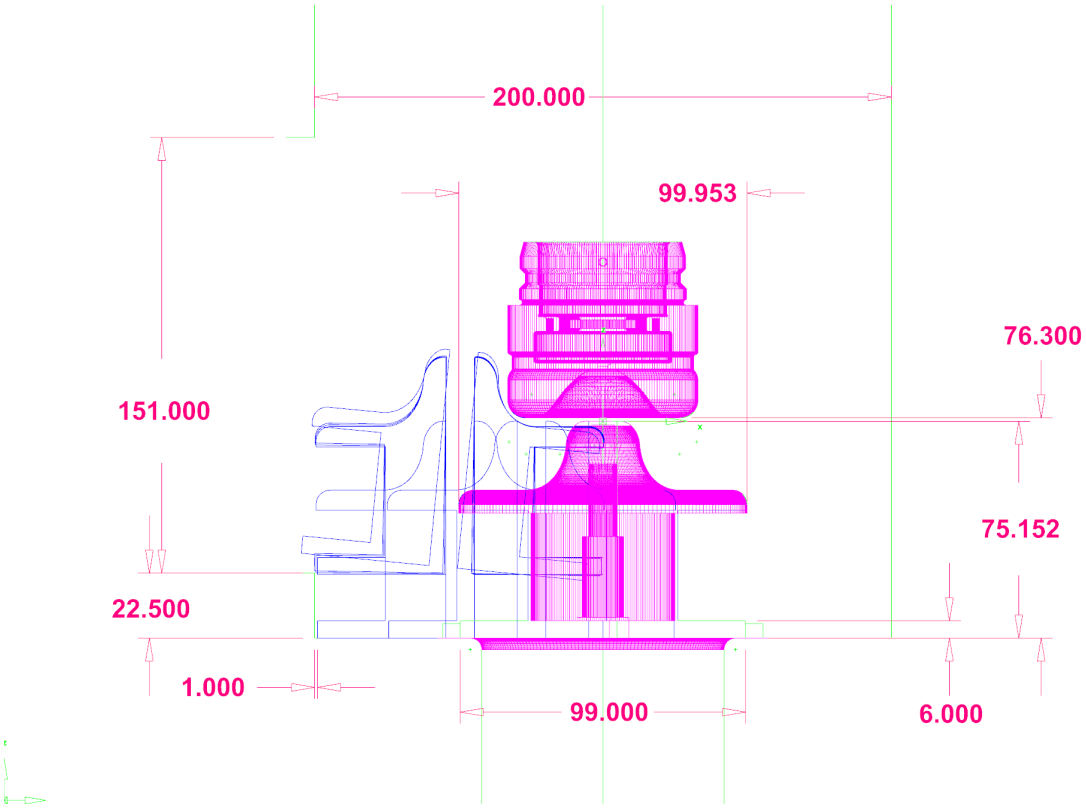

Figure 3.11 - Relevant dimensions (all in mm) in anode and grid cup design

The anode was manufactured in TWI and it was made from a copper block. Figure 3.12 summarises the process:

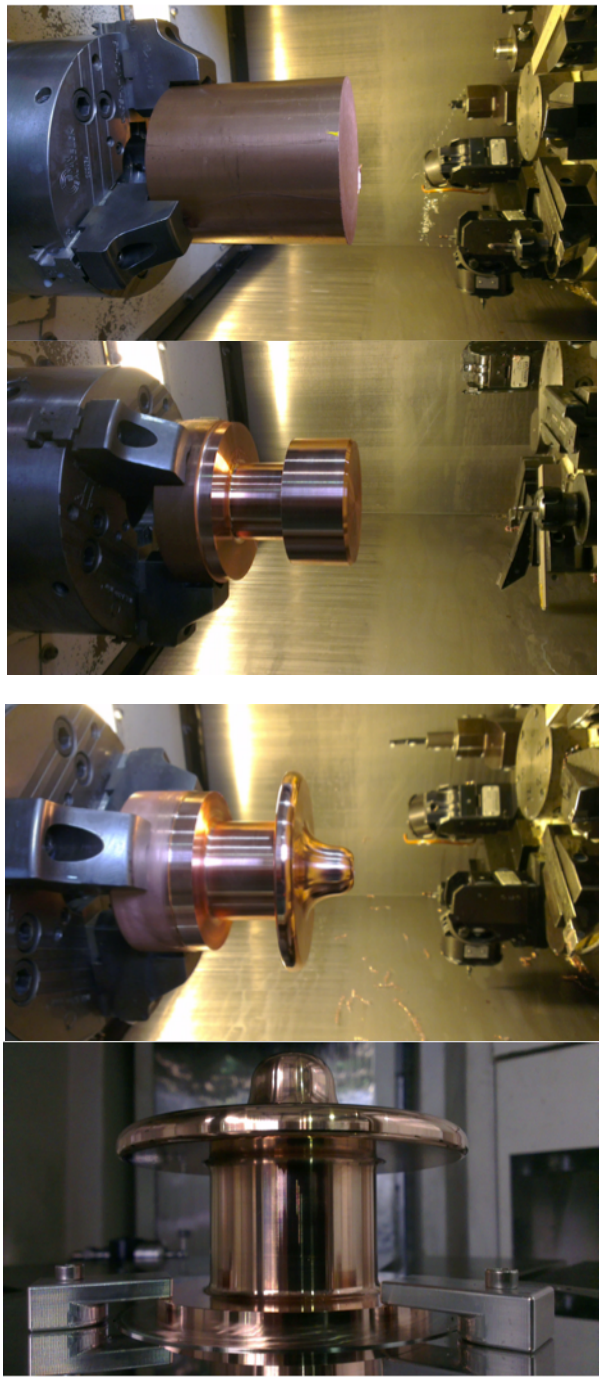

Figure 3.12 - Anode manufacturing process from the design derived from simulation work

In order to get the filament both in the middle and at the right distance from the grid cup, a jig for positioning it was designed. Figure 3.13 shows the filament jig designed and evidence of improvement in the position on using the jig can be observed.

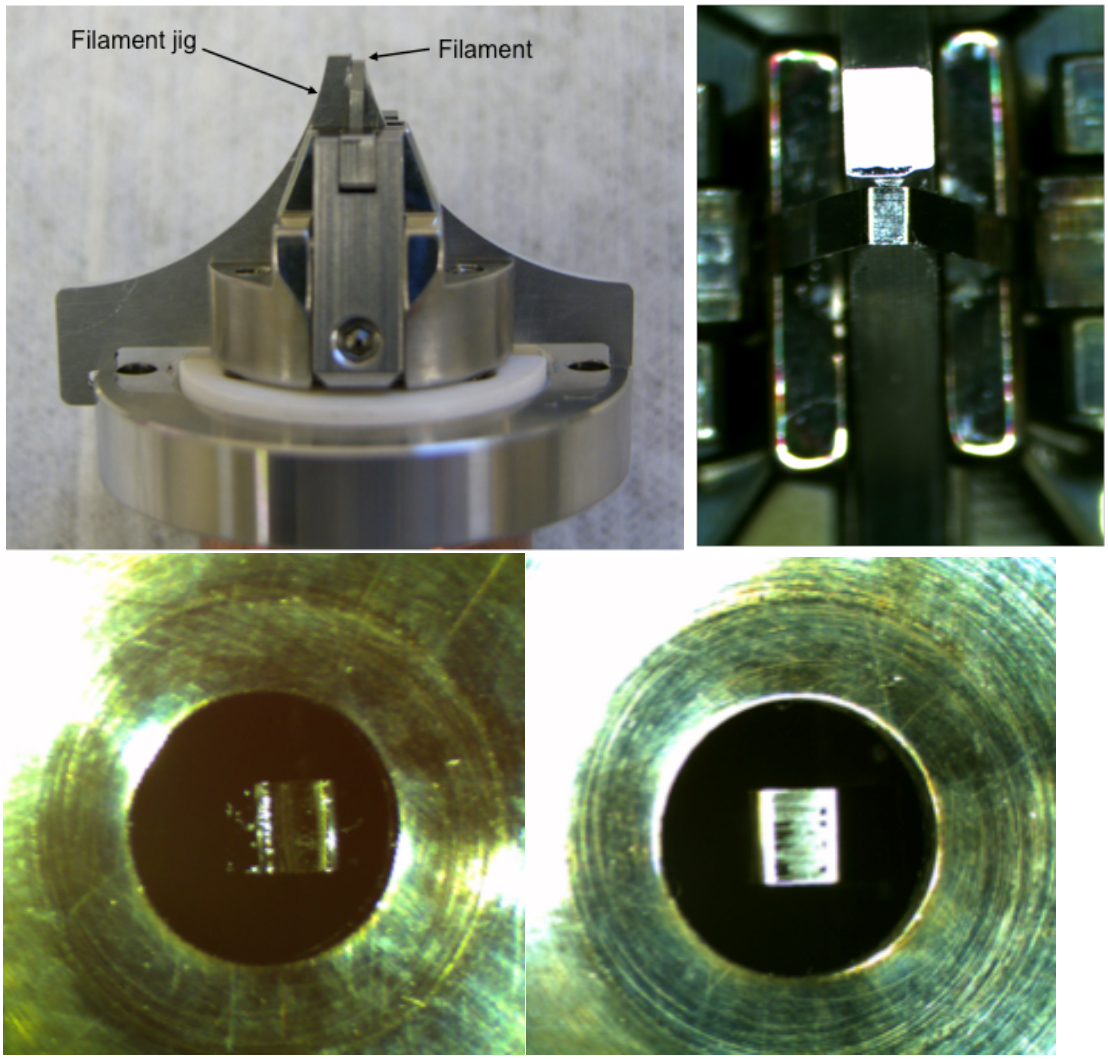

Figure 3.13 - Filament in grid cup off-centre (left) and filament in centre after using jig for positioning (right)

The improvement when positioning the filament in the centre is visible in the pictures above. The height was also measured several times using a height gauge. The result was that the filament was placed in the right position at the first attempt.

Three finger clamps were designed and manufactured to hold the anode in position on the bottom plate of the column. A fitting plate had to be designed and manufactured in

order to fit the anode on the upper gun column bottom plate. Another fitting plate was manufactured to fit the upper gun column onto the working chamber in which the electron beam was to be projected. Drawing of finger clamps and modifications made on fitting plates are in Appendix A4. The system was assembled and the manufactured parts were put together with the existing parts. The system was assembled successfully and no further modifications were needed on the parts designed. Figure 3.14 shows an overall picture of the upper gun column and work chamber.

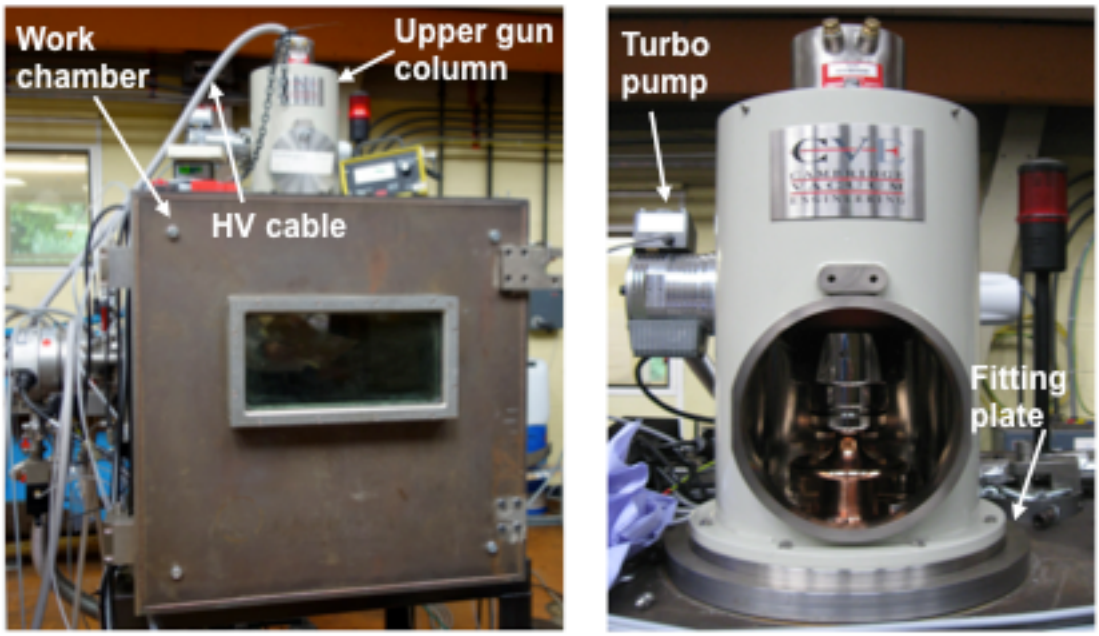

Figure 3.14 - EB gun system showing upper gun column on working chamber where the probing for beam characterisation was carried out

- **Pumping system**

The pumping system consists of a turbo-molecular (add turbo main details) pump and a backing pump (a single-phase XDS dry pump). The pumps are controlled by a TAG (Turbo and active gauge) controller. A vacuum gauge (non-magnetic type to avoid the magnetic field affect the beam quality), was used to monitor the upper column pressure, which value is displayed in the controller screen. All the parts were purchased from Edwards.

Figure 3.15 shows the pumping system configuration of the EB gun. This was the simplest configuration that could be made with the elements available. Other

configurations are possible, but note that the turbo pump should be always connected between the chamber and the baking pump, so that the gun column volume is pumped down first by the backing pump through the turbo and then, when the pressure reaches 1mbar the turbo is started by the controller to allow it to reach a vacuum level in the order of 10^{-5} mbar to 10^{-6} mbar.

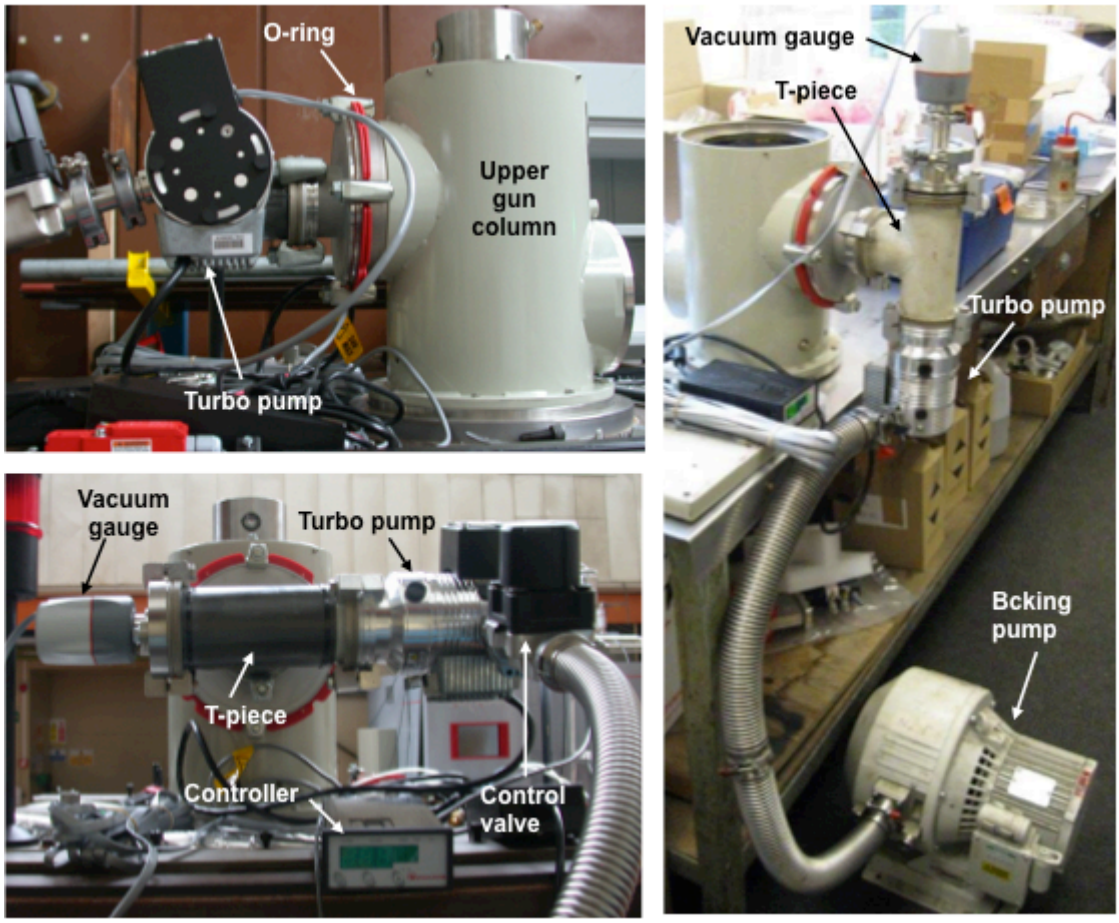

Figure 3.15 - Main parts in pumping system

O-rings are required in each of the joints for vacuum sealing. These were purchased with the needed diameters. The turbo pump should not be connected directly to the output of the chamber, since it does not stop the X-ray radiation. A 'T' piece with the right thickness and material, lead in this case, should be used. Further information about X-ray shielding calculations was given in the design section above. This configuration will be enough to pump down the 10 l volume of the gun column in about 1 h. This time could be higher if the chamber has been open and some vapours are trapped inside. An electron window should be used between the upper gun column and work

chamber. Otherwise, additional and more powerful pumps would be needed due to the volume to pump down being greater.

A manual control valve is used for controlling the flow of air through the turbo pump. The valve should be closed before venting the volume, until the turbo pump has stopped spinning. The speed of the turbo pump can be visualised in the controller screen (in % of the maximum speed).

- **Electrical system**

For running the EB gun system the following elements were connected:

- HV power supply unit (PSU) EB4000 Hi-Tek.
- Auxiliary PSU - which provides both filament and grid bias voltage.
- PLC and user interface – A control panel from another system was adapted to be used for controlling and monitoring the EB gun parameters.

3.3.10. Testing of the EB gun system: Results and discussion

This work presents the practical results obtained and comparison with the simulation work. There are three main sets of data: peaking curves, probing results and pyrometer data; as well as pictures of the tests.

Some adjustments had to be done on the user interface and controls in order to be able to use the Hi-Tek PSU units. Radiation dosimeters were used to keep records of the counts (us) per hour registered at the beginning and end of each test.

- **Peaking curves**

Peaking curves represent the beam current that is produced by an electron beam as the bias voltage is changed at a certain filament current / temperature. In the modelling work from Opera-2d the temperature is the parameter used to model the thermionic emitter, whereas in practice, the filament temperature is controlled by the filament current applied. As a result, it would be necessary to estimate the temperature

equivalent for each filament current in order to compare real results and simulation results.

Figure 3.16, shows the peaking curves obtained in a first test carried out with the EB gun designed for DEECON.

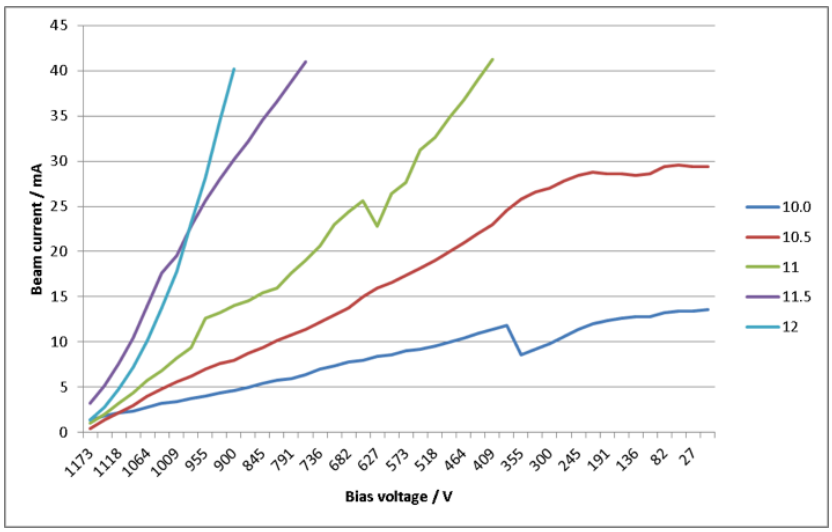

Figure 3.16 - First test peaking curves

It can be observed that the curves have some steps. This is due to the HV PSU continuously tripping off. Thus, the PSU should be brought to high voltages (few kilo Volts over the voltage at which the test is to be performed) before carrying out the tests. This is the case in Figure 3.17, which shows a comparison of two separated sets of peaking curves from the data taken in the laboratory with the DEECON gun.

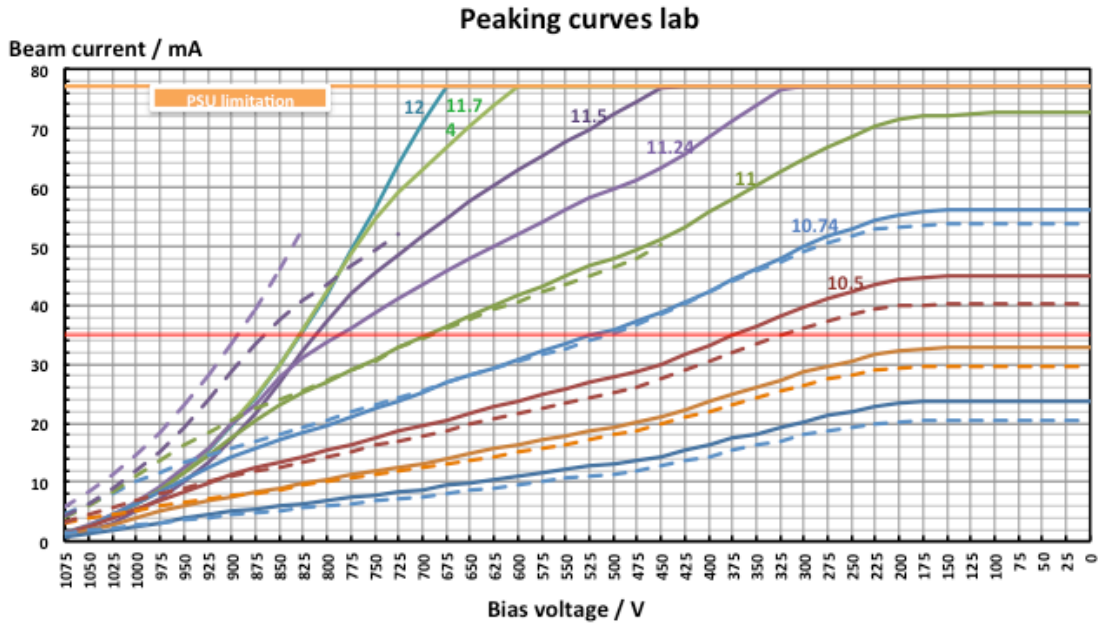

Figure 3.17 - Peaking curves starting from higher filament current (continuous line) and from lower filament current (discontinuous line)

The continuous lines being for a test started at the lowest filament current (10 A) and then progressing in 0.25 A steps up to 12 A, whereas the discontinuous lines present the peaking curves in a test started from the highest filament current (12 A) to the lowest. The graph shows that even though the filament current is kept constant, the time this current is applied affects the filament temperature and thus the electron emission. For curves corresponding to middle filament current valued the beam currents obtained at both tests match fairly well, due to the filament is been heated during roughly the same amount of time.

However, this difference variance of temperature does not have an important effect in the overall results, and does not make any difference in meeting the beam and power requirements for this work. As observed in the graph, the required 35 mA can be achieved when the filament is heated up with filament currents equal or higher than 10.5 A. The 5 mA required for lab scale can be achieved with temperatures as low as 10 A.

Figure 3.18 presents the peaking curves obtained from the simulation work:

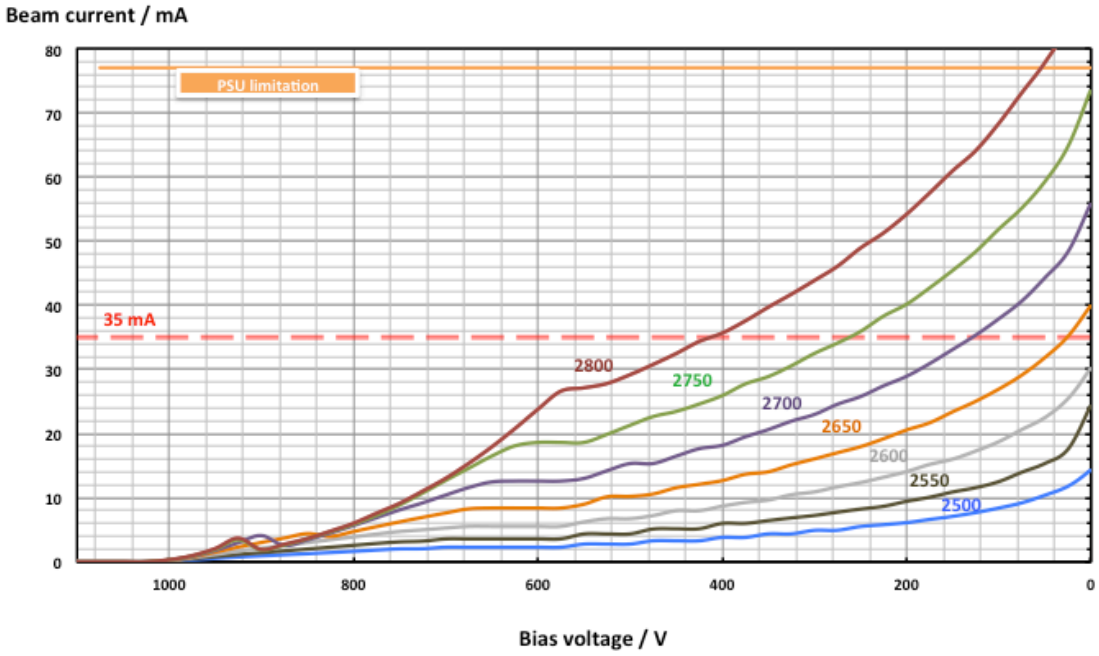

Figure 3.18 - Peaking curves from simulation work in Opera-2d

From the graph above, the 35 mA current required can be provided at filament temperatures of 2650 K and higher. The 5 mA required for lab scale can be reached at any of the filament temperature modelled. However, it can be observed that the model does not perfectly match the real results obtained in the laboratory. Various factors interfere in the modelling work:

- Emission from legs of the filament. Temperature gradient of the filament in reality is no properly reflected in the model.
- Front face of the filament is an approximation. Filament front face is modelled as a circular face due to the two dimensional software used, when in reality it is a square face.
- Mesh type and number of elements. Number of elements was increased in the most critical areas such as cathode and surroundings when possible, since this increases considerably the solving time.
- Type of emitter model chosen and its parameters. Langmuir-Fry model was chosen, which is the most appropriate for triode EB guns. For this type of model, the sampling distance can make a difference in the results. Therefore, the model was run with different sampling distances to estimate the most accurate one. The solution converges at sampling distances lower than 0.1.

- Richardson constant and work function assumed for Tungsten. The parameters chosen for a tungsten filament emitter were: Richardson constant is $A = 60.2$ Acm^2K^2 and Work function is $\varphi = 4.5\text{-}4.56$ eV (Lassner, Schubert 1999)

In order to better understand and relate modelling with real results, other tests were carried out. The filament temperature was measured at the filament currents selected for the lab test.

- **Probing**

The probe consists on a rotating arm with two tungsten wires at one end (Figure 3.19). The arm is made spin by a motor and the wires are at two different heights, separated 29 mm from each other. The probe is placed into the work chamber at one side of the beam and at the right distance so that the wires cut the full beam area in each lap. The current collected by the wire is visualised in an oscilloscope, so that the beam profile can be observed and the beam diameter estimated.

Figure 3.19 - Rotating probe

Probe set up is shown in Figure 3.20. Beam current distribution was collected at four different intersection heights (a and b) and probe at 90 and 0 degrees as shown below:

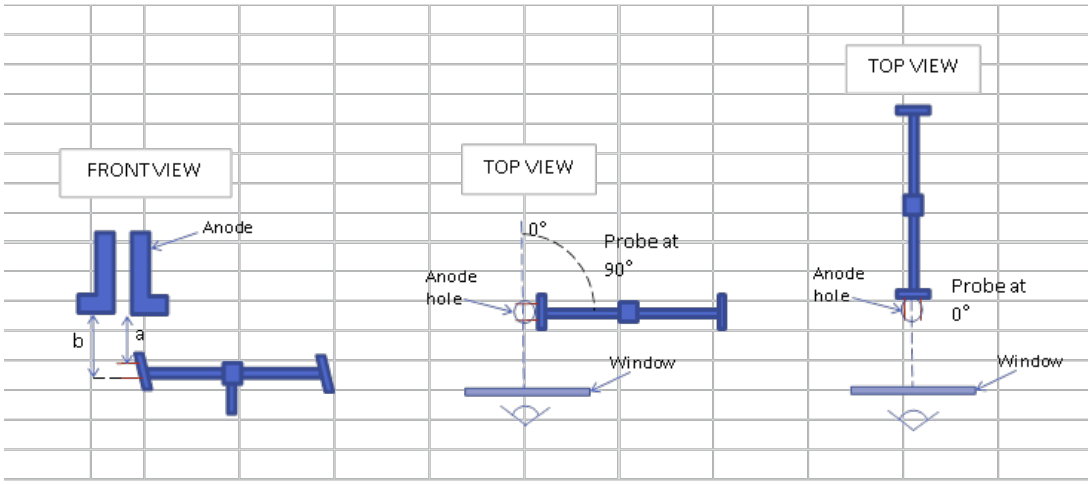

Figure 3.20 - Probe set up from view and top view at a) 90° and b) 0° angles

Figure 3.21 shows the two pulses that are obtained corresponding at each of the tungsten wires at two different intersection heights. The diameter of the beam (mm) can then be estimated from the time of the pulse and knowing that the distance swept between wires is 30 mm in 0.65 ms.

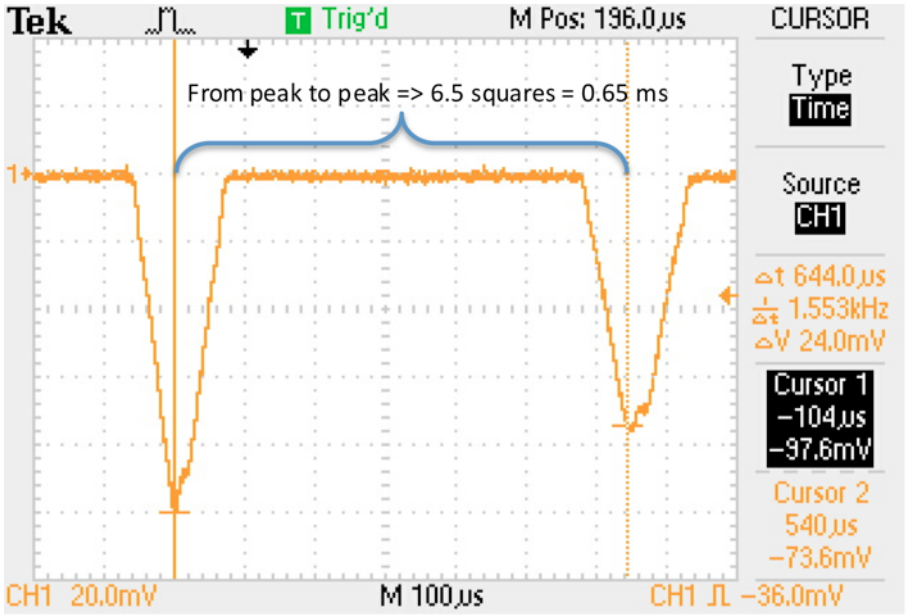

Figure 3.21 - Probe on the side (90°); 11 A filament current; 2 mA beam current; pulse 1 at 75 mm from anode base and pulse 2 at 104 mm

Figure 3.22 and Figure 3.23 present beam diameter-beam current graphs for different filament currents applied. D1 is diameter estimated from data taken with the probe at

90° and D2 is at 0°. The diameters were projected back and calculated to know the beam diameter at the window height, i.e. for the intersected at the anode base (ha).

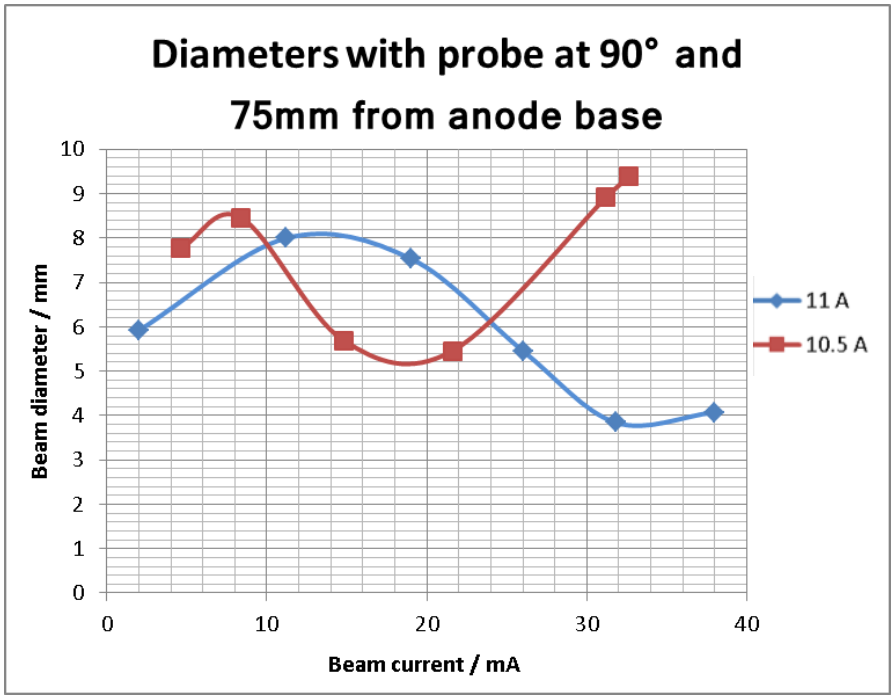

Figure 3.22 - Beam diameters with probe at 90° (from real results)

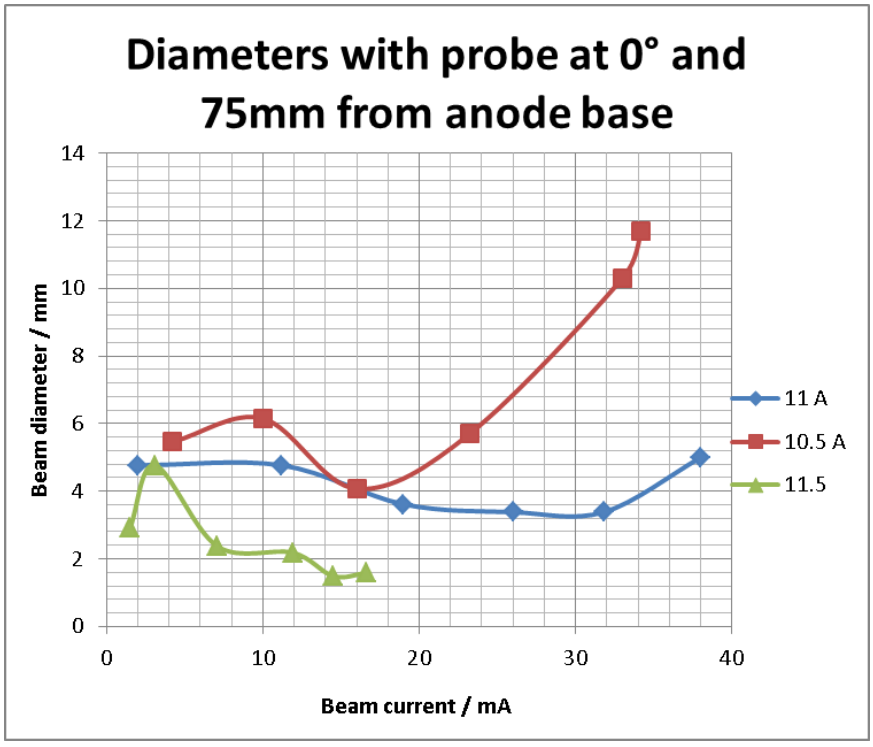

Figure 3.23 - Beam diameters with probe at 0° (from real results)

The shape of the beam changes over the power range. The beam changes from elliptical shape to rectangular and the beam diameter decreases when the crossover takes place in front of the filament face (at more than 2-3 mm distance). Finally, the diameter increases one last time. This process can be seen both in the pictures taken from the beam projected in a tile during one of the tests, in the beam profiles obtained with the probe and in the simulation work. Figure 3.24 below shows the diameters of the beam obtained in the simulations in Opera-2d:

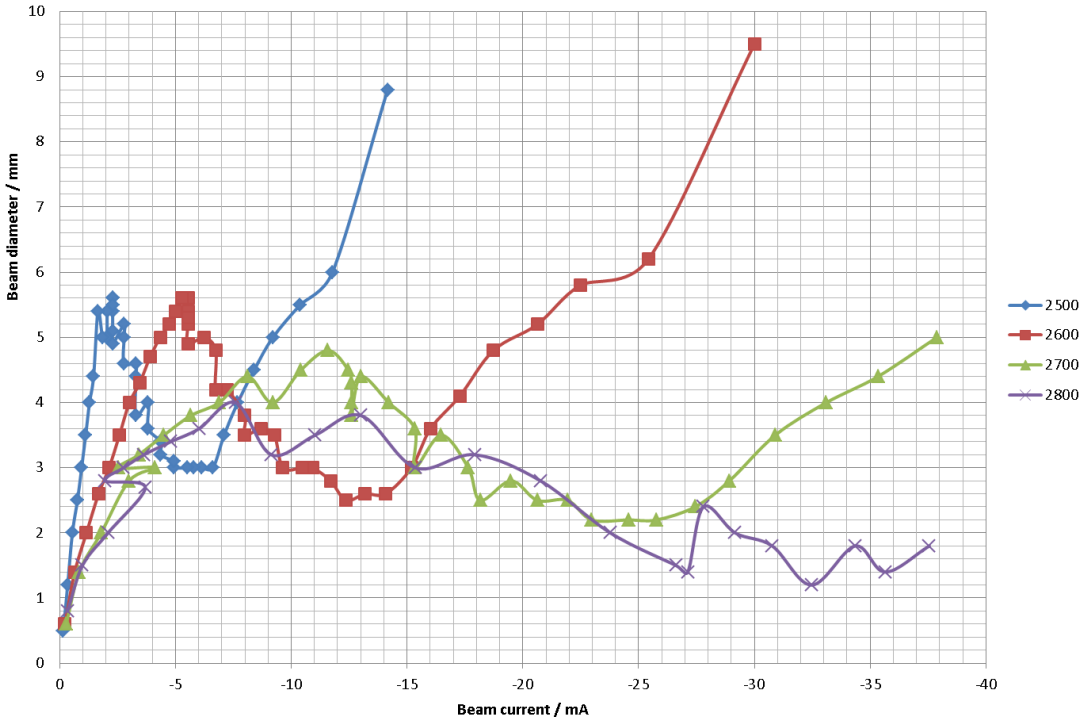

Figure 3.24 - Beam diameters (in simulation) over beam current range at different filament temperatures. The data is from the modelling work of the designed EB electrodes in Opera-2d

As seen in the real results, first the diameter increases as the beam current does. Then the beam diameter decreases as it progresses to the point of crossover. After the crossover the beam diameter starts increasing again. This behaviour in the beam diameter can be observed at all of the filament currents / temperatures. The difference in each curve is that the beam diameter follows this pattern in a shorter range of beam current at lower filament current/temperature and over a longer range at higher filament currents.

Current distribution should be looked at when the size and position of the window is chosen. Figure 3.25 to Figure 3.30 show a comparison of beam current distributions at 2750 K filament temperature in the simulation work and at 11 A filament current applied in the lab results.

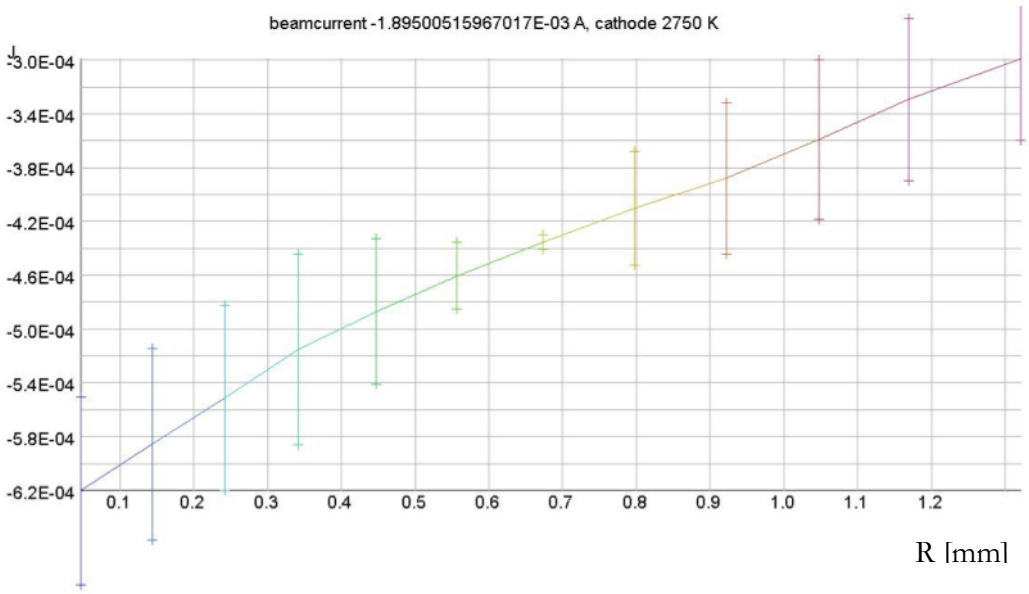

Figure 3.25 - Beam radius at 2 mA filament current and 2750 K filament temperature

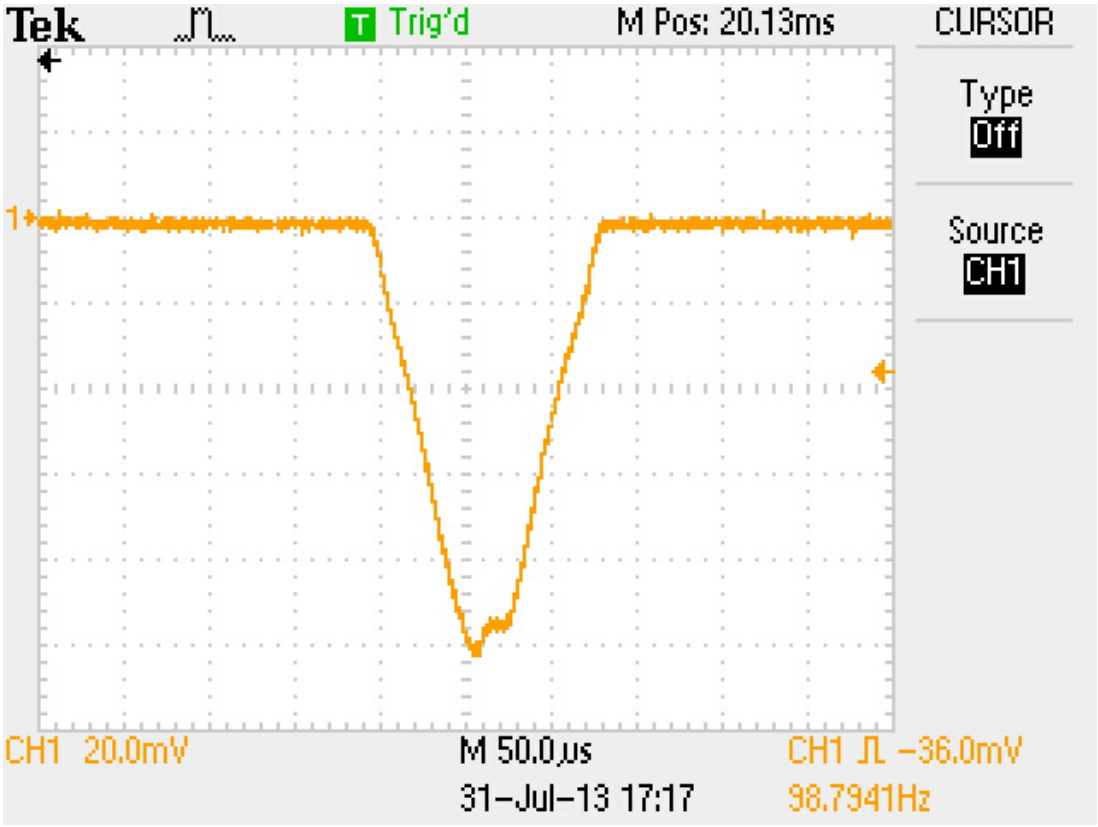

Figure 3.26 - Beam diameter with probe on the side (90 degrees), for 2 mA beam current and 11 A filament current

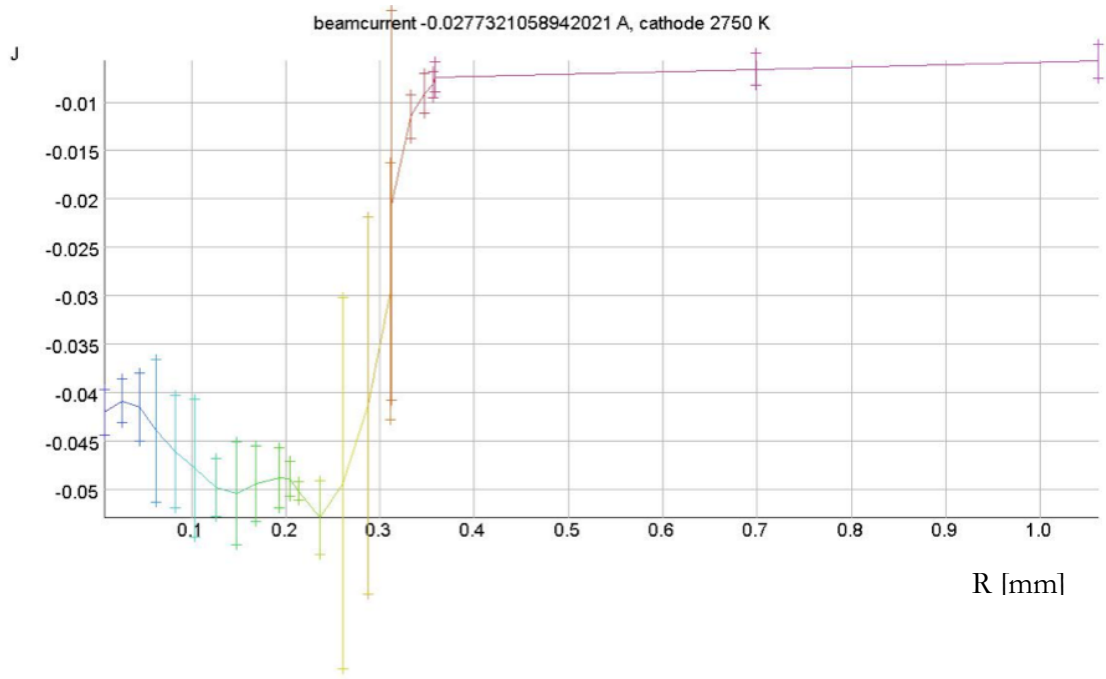

Figure 3.27 - Beam radius at 27 mA beam current and 2750 K filament temperature

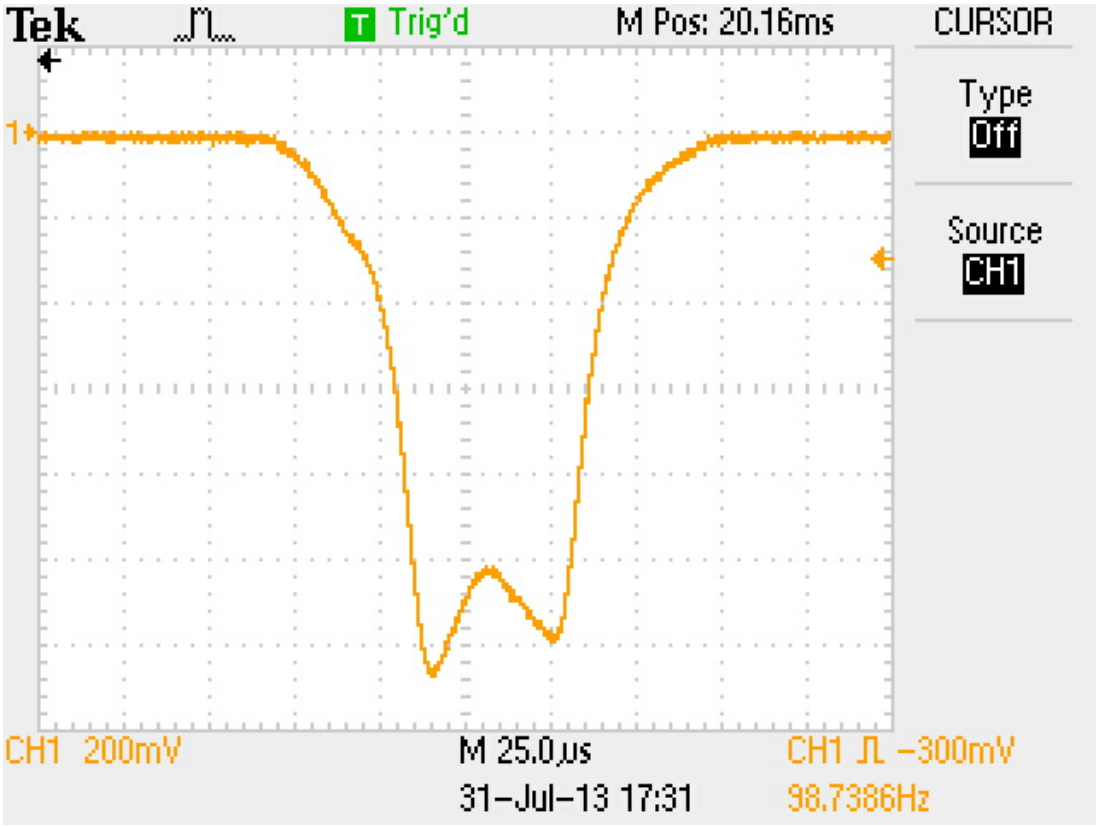

Figure 3.28 - Beam diameter with probe on the side (90°), for 26 mA beam current and at 11 A filament current

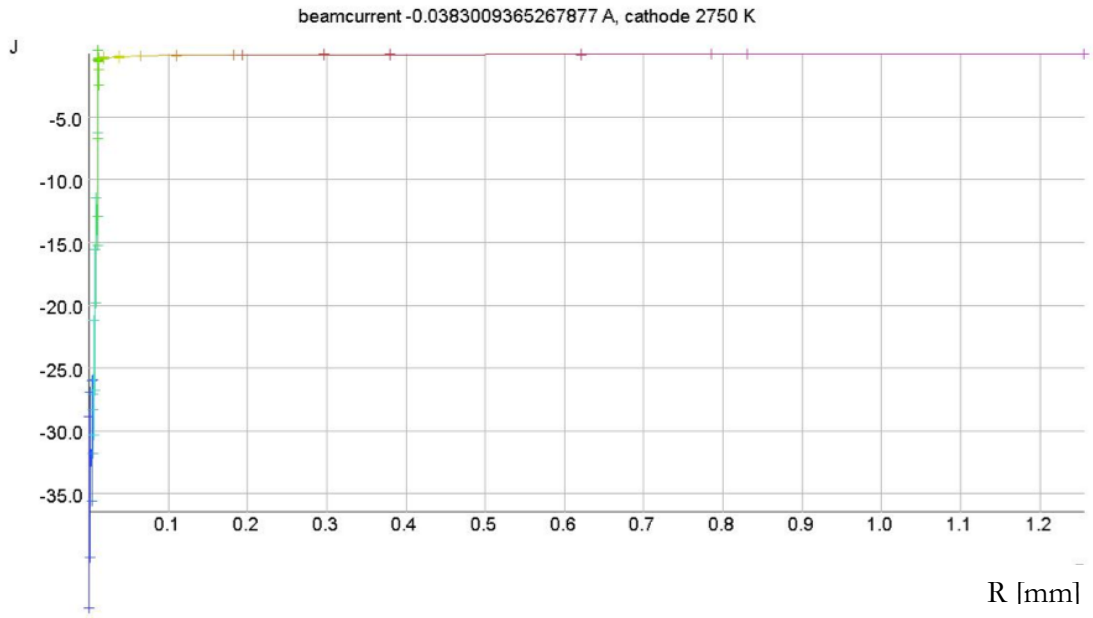

Figure 3.29 - Beam radius at 38 mA filament current and 2750 K filament temperature

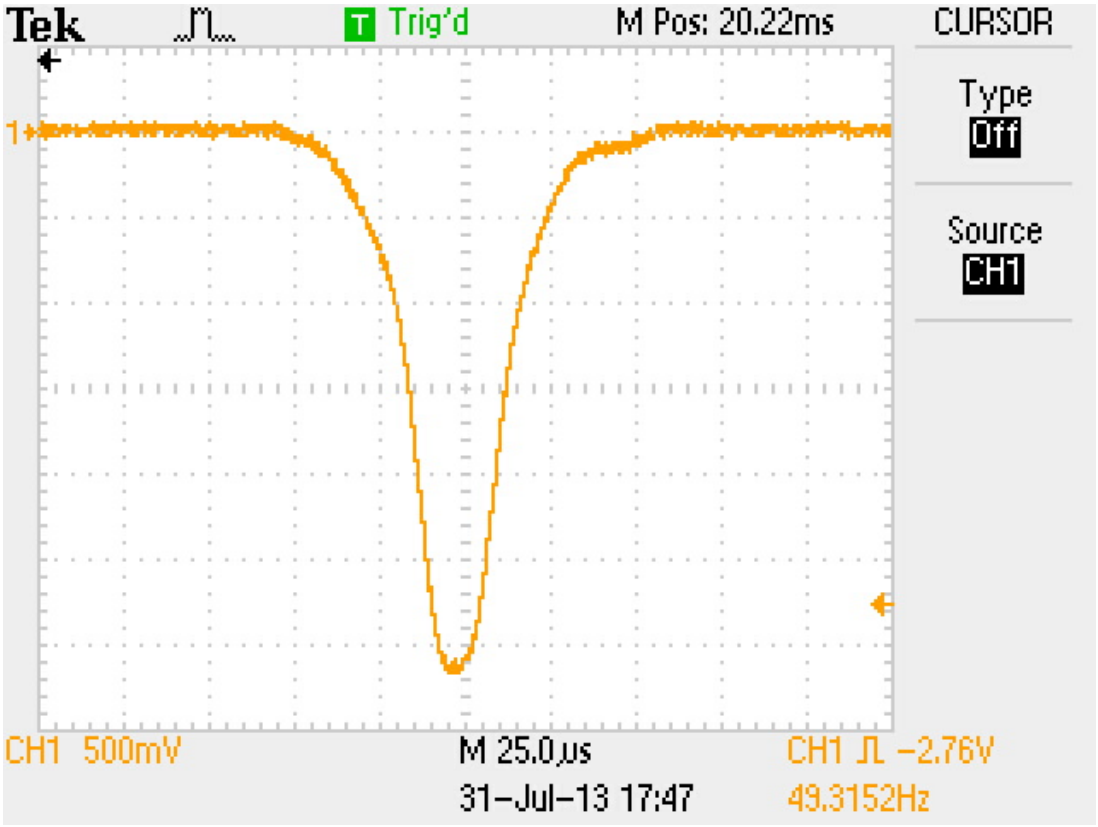

Figure 3.30 - Beam diameter with probe on the side (90°), for 38 mA beam current and at 11 A filament current

Therefore Figure 3.25 to Figure 3.30 show that real results keep similarities in shape with the results from simulations at same beam currents.

Figure 3.31 shows the beam shape of the beam projected on a tile placed at the bottom of the work chamber. As can be seen, the beam shape follows the pattern observed in the previous results. The beam goes from an elliptical shape to then a more rectangular shape due to the crossover in front of the cathode.

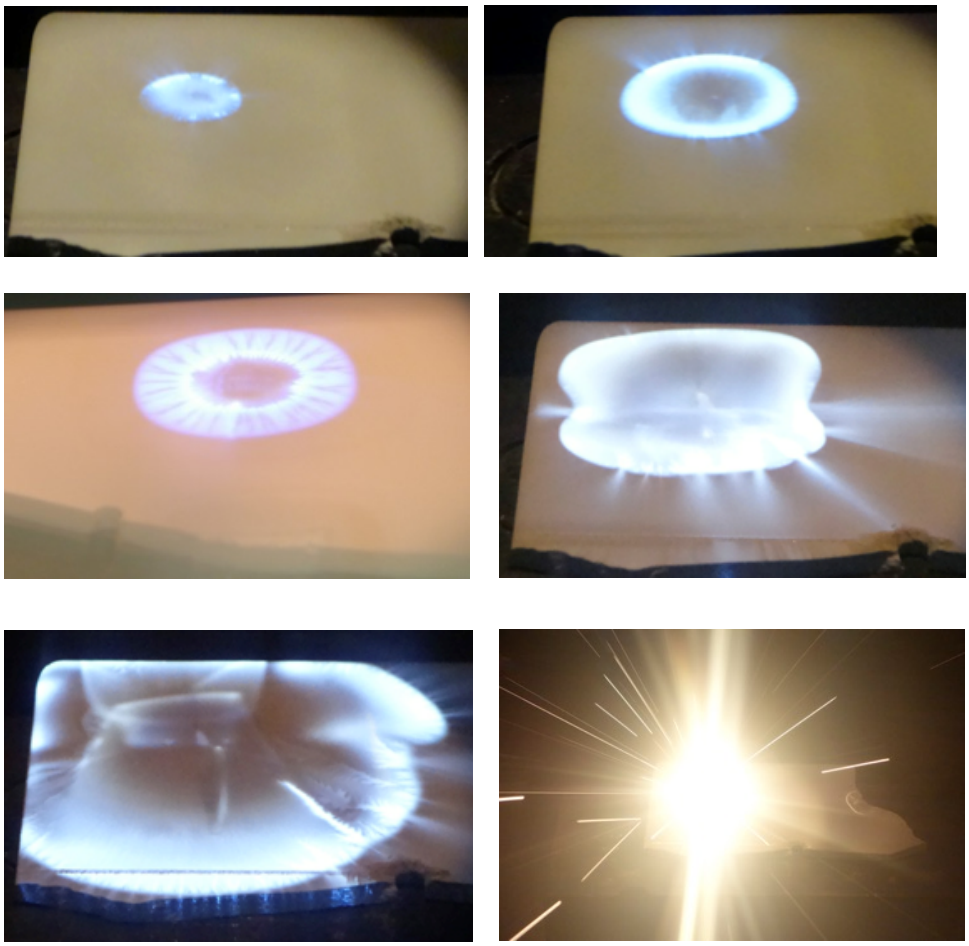

Figure 3.31 - Beam projected on a tile showing beam shape pattern at low beam currents and low filament current

Figure 3.32 shows the beam profile of the beam generated by the DEECON EB gun when tested in the work chamber. Argon gas was introduced in order to make the beam react and glow, making it visible.

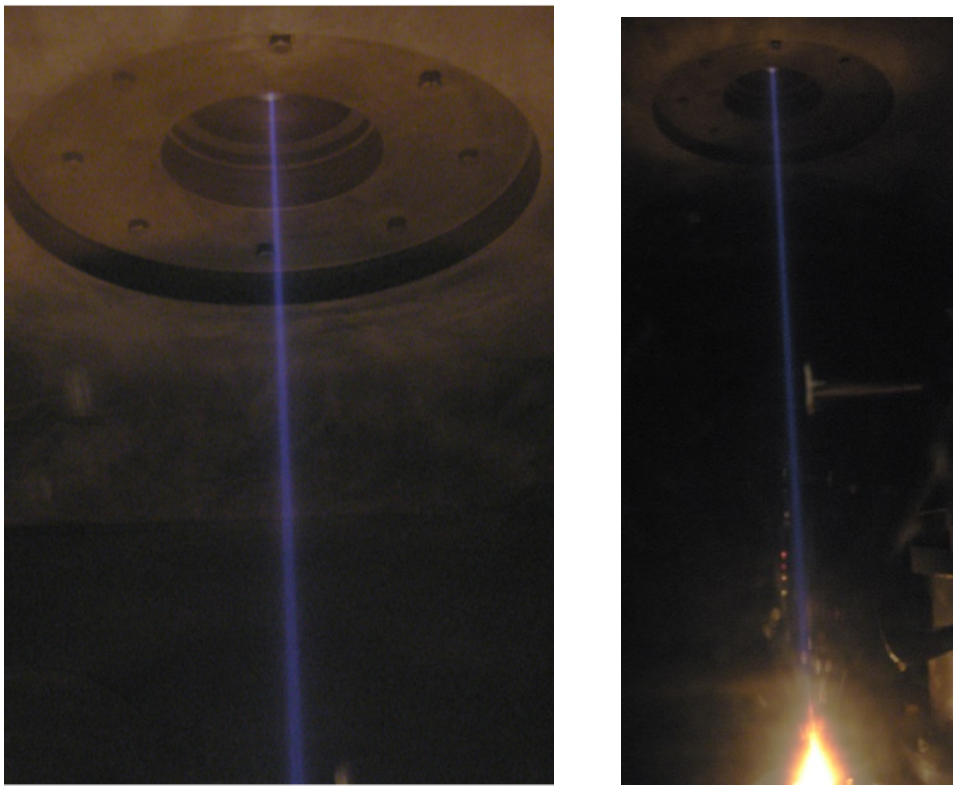

Figure 3.32 - Electron beam generated by DEECON EB gun glowing in the chamber

- **Pyrometer**

An infrared thermometer measures surface temperature by using an optical-electronic sensor which measures infrared/ heat radiation emitted from that surface. In this work an IR thermometer was used to measure the surface temperature of the tungsten ribbon filament. The device used is a High-Performance Infrared Thermometer, with the following specifications:

- Model: MM1MH
- Temperature range: 650 to 3000 °C
- Optical resolution: 300:1
- Spectral response: 1µm
- Time response: 1 ms
- Focus range: 300 mm to 2200 mm
- Smallest spot size: 1 mm @ 300 mm

The set up for the test is shown in Figure 3.33. The tungsten filament is in a vacuum inside the gun column chamber. The 10 l volume of the column is pumped down by a backing pump through a turbo-molecular pump. The upper gun column was separated from the EB gun system in order to be able to look at the tungsten filament without using a mirror which would affect the Transmission value. The pyrometer sensor was placed perpendicular to the face of the filament for the best performance, up to 30° good performance can be achieved.

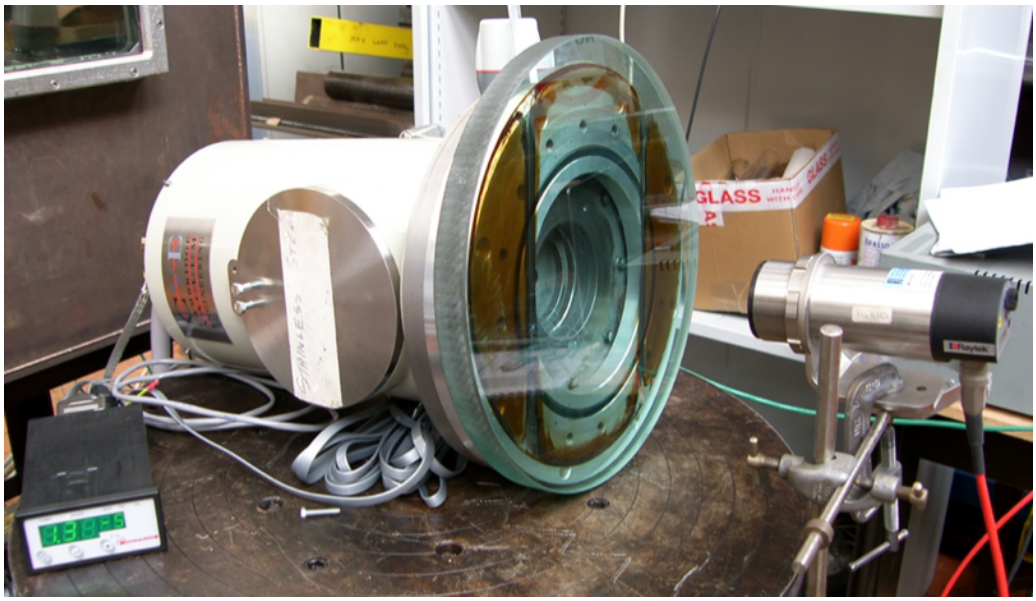

Figure 3.33 - Probe setup

The main parameters to take into account in the test are:

- Focal distance – Distance from target to sensor.

The target has to fill completely the measurement spot. The front face of the tungsten filament is a 1×1 mm square. The distance from the sensor to the target was set to be optimum at 1mm spot size. When looking at the optical resolution (Figure 3.34), the optimum focal distance for a 1 mm spot size is 300 mm. Thus the pyrometer was placed at 300 mm from the front face of the filament.

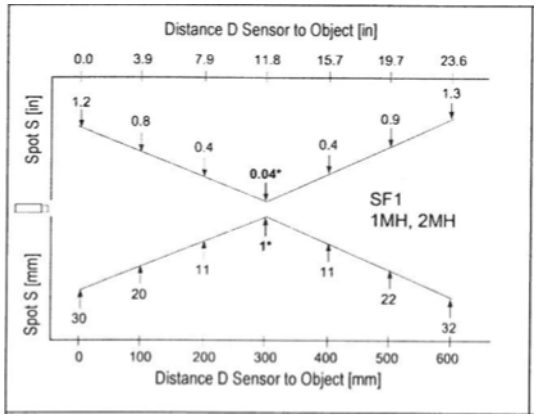

Figure 3.34 - Optical diagram for 1MH, 2MH sensors and standard focus SF1

- Emissivity – The emissivity of the object's surface is quantified with a value within 0 to 1 and indicates its ability to absorb and emit infrared energy (Raytek Corporation 2007). (Dependence of intensity of infrared/heat radiation – material)

A number of parameters can affect the emissivity of a material such as temperature, angle of measurement, geometry, thickness, surface quality, spectral range of measurement, transmission (Raytek Corporation 2007). Figure 3.35 shows the front face of the filament after running the gun for the tests. It can be observed that the surface quality and thickness of the front face of the filament is not uniform, and thus emissivity value varies in this small area. Moreover, the filament is bended and it might not be parallel to the optical sensor in all the points of its front face. Typical emissivity value for Tungsten for a 1 μm wavelength pyrometer is 0.35-0.4 (Raytek Corporation 2007). In this work readings were taken at E = 0.1, 0.35 and 0.4, at each filament current and T value.

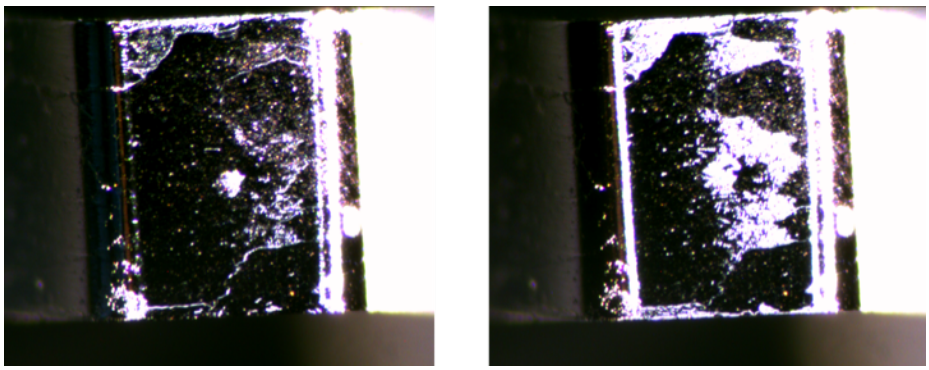

Figure 3.35 - Front face of tungsten filament after being heated up by a direct current in vacuum

- Transmission coefficient or Transmittance – Since the filament has to be kept in a vacuum in order to heat it up to the high temperatures required without melting it, a window has to be put between the pyrometer and the target. The transmission value of the window was estimated both empirically and theoretically.

Calibration was carried out by using an "industrial drier" as the one shown in Figure 3.36 and taking temperature readings when looking at it with and without the glass window. The transmission value obtained is 0.85.

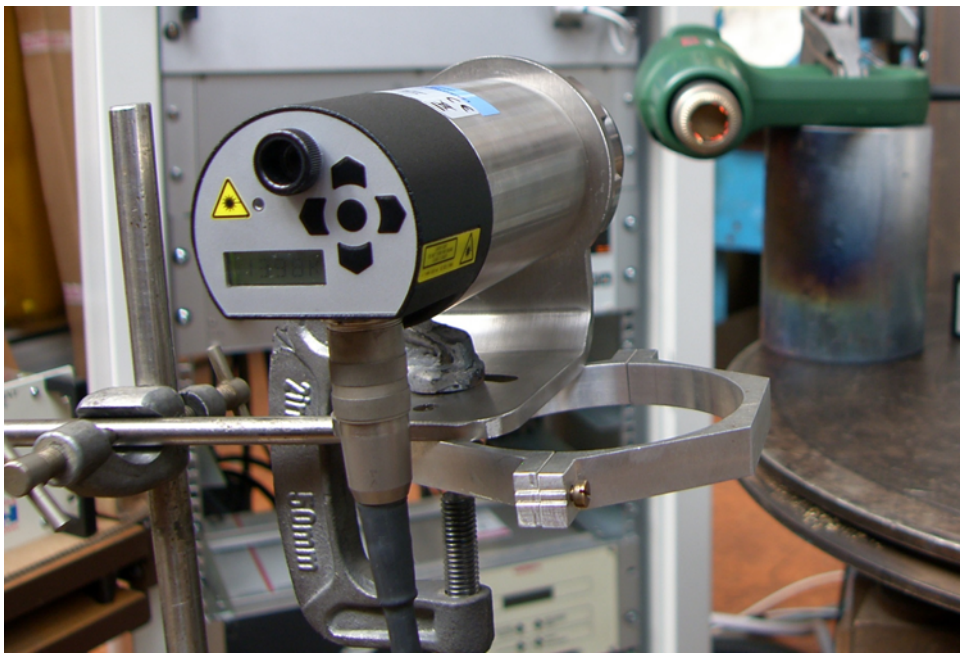

Figure 3.36 - IR thermometer calibration

The window used is a soda-lime glass and Figure 3.37 presents the transmission curve for this type of glass. For a 1 μm wavelength the transmission is 80%. In this work, temperature readings were taken at 80% and 85% transmission.

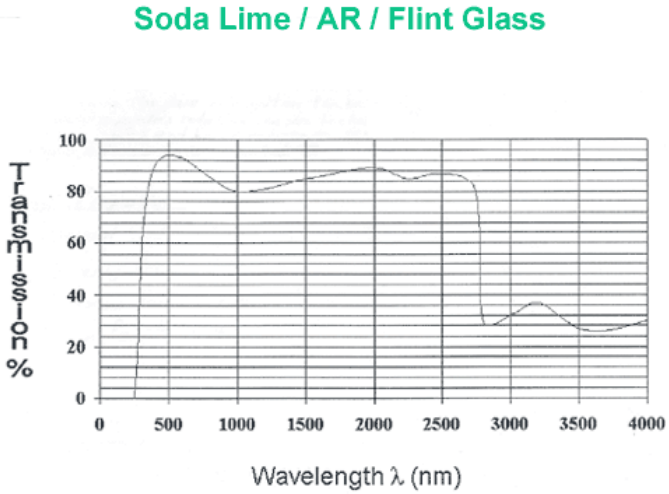

Figure 3.37 - Soda-lime glass transmission curves

Figures 6.9 to 6.11 shows that the temperature measured on the filament surface face keeps a linear relationship with filament currents applied.

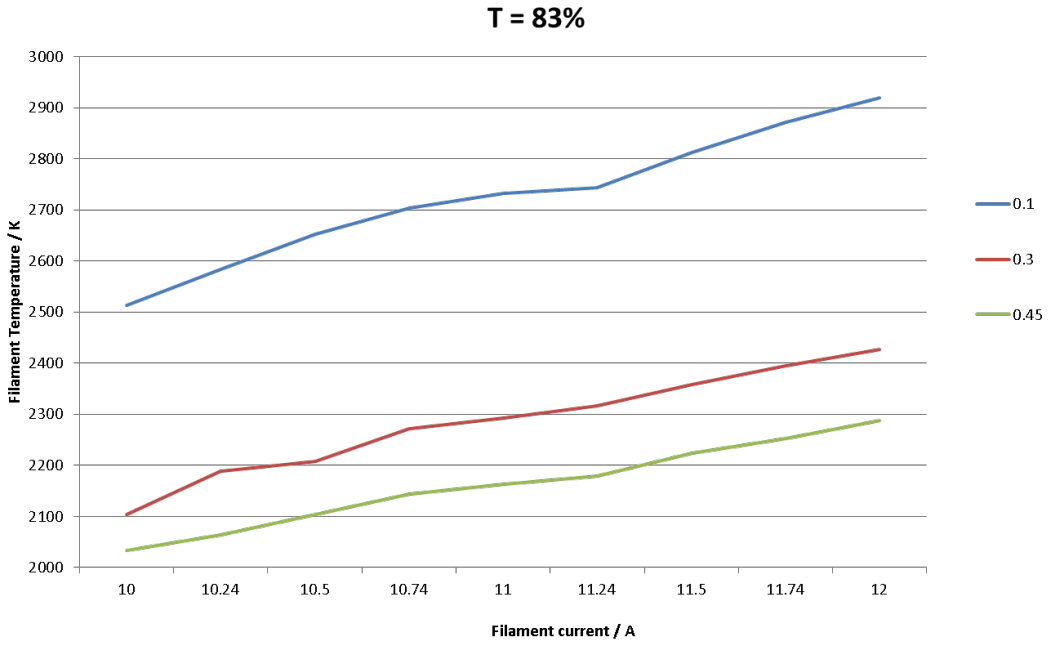

Figure 3.38 - Graph T/filament current at T = 83% T and E = 0.1, 0.3, 0.4

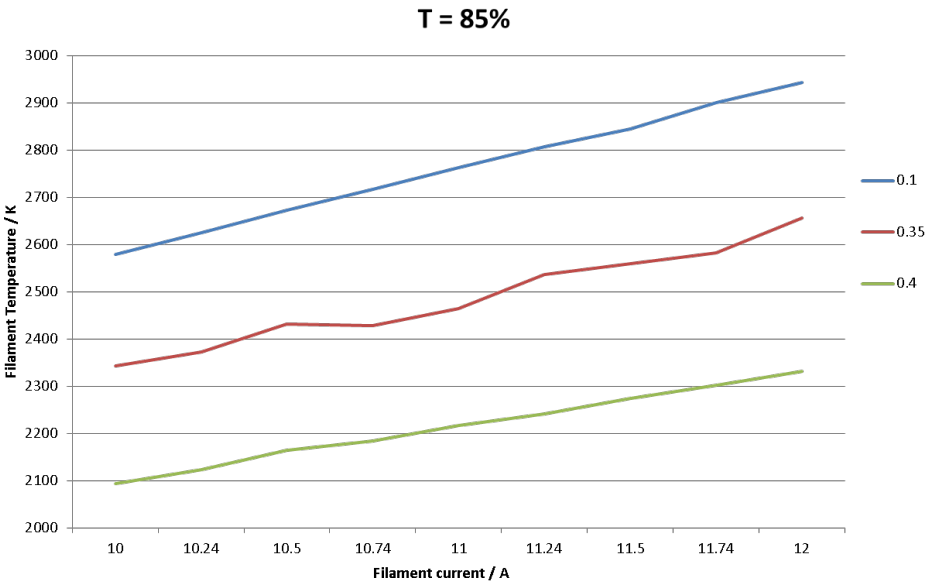

Figure 3.39 - Graph T/filament current at T = 85% and E = 0.1, 0.35, 0.4

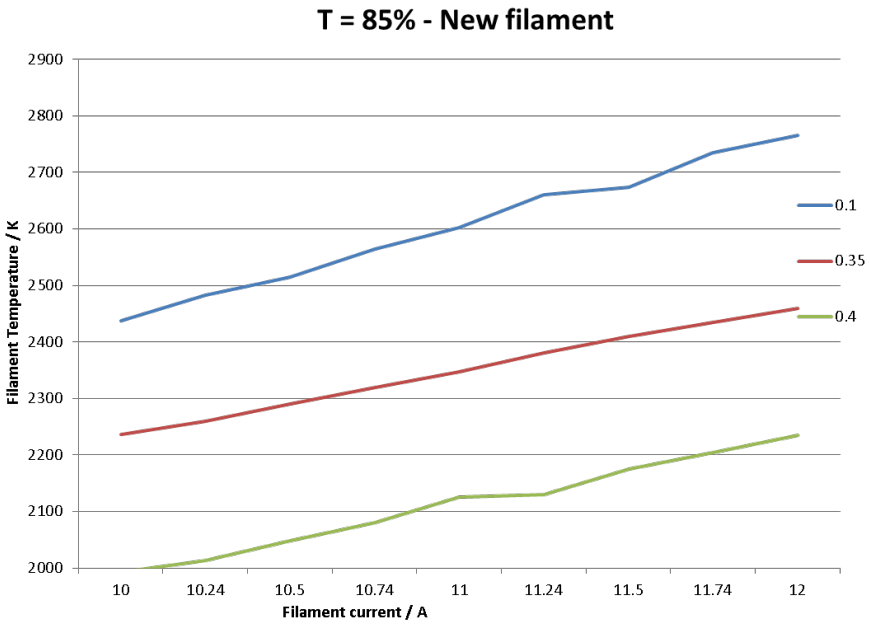

Figure 3.40 - Graph new filament T/filament current at T = 85% and E = 0.1, 0.35, 0.4

3.4. Summary

An EB gun system has been designed for 60 kV to provide a minimum of 35 mA beam current. Both modelling work and real results predict that a maximum power of 4.2 kW is achievable (70 mA maximum beam current).

The EB gun was optimised to switch off the beam current at 1100 V bias voltage, as required by the selected grid bias supply, and this has been achieved with the simulation results and demonstrated with real results.

The geometry and distances between key elements such as cathode, anode and grid cup electrode were optimised for avoiding high voltage stresses and voltage breakdown, as well as satisfying tolerance values achievable, space available and vacuum features to allow pumping down of the gun column in a reasonable time.

Probing work demonstrates that the gun is capable of producing the minimum power required at different beam diameters that can be chosen by modifying the filament current. This is convenient for this work as the window size has not been determined.
A flexible EB gun design has been provided for this application where beam current and diameter can be chosen by changing filament current and controlling bias voltage. 5 mA required for laboratory scale can be provided at different filament currents and beam diameters.

The requirements have been satisfied as well as leaving flexibility in the performance. This is ideal for this work as the optimum beam power and beam diameter for the DEECON project has not been determined yet.

Chapter 4 : Plasma as an Electron Source

In this chapter the fundamental principles, concepts and laws that govern low temperature plasmas that are relevant to this thesis work are described. A brief description of plasma diagnosis methods is given and the chosen techniques for the experiments carried out are described. Various plasma cathode electron guns are described.

4.1. Introduction

"There cannot be doubt that plasmas matter" (IOP 2013). If enough energy is applied to a solid, this becomes a liquid. If a liquid is energised enough it will form a gas. If sufficient energy is applied to a gas, the atoms in it collide with each other and decompose into freely moving electrons and ions, it becomes the "fourth state of matter", which is plasma (Lieberman, Lichtenberg 1994). The degree of plasma ionisation, which can range from 100% to 10^{-4} to 10^{-6}% (Bogaerts et al. 2002), needs to be high enough so that the system presents the characteristics of a plasma that are not observed in the other states of matter: plasma systems have high electrical and thermal conductivity, they form laminar regions of high ion concentration, they have high particle diffusion, transmit electromagnetic and mechanical waves and emit radiation (Olschewski 2015).

The cathode is the most important component in electron guns that affects the electron beam quality and power. The electron gun that was developed in this work used a plasma cathode, thus the study of plasma used as an electron source was essential. This section reviews the relevant literature on low temperature, low-pressure plasmas with the objective of extracting the required information to understand and design plasma cathode guns.

4.2. Plasma Cathode EB Guns

The focus of this thesis work is to investigate a plasma cathode and optimise the design of the plasma chamber in order to increase the EB current extracted. This section describes the main parts of a plasma cathode gun.

4.2.1. Plasma Cathode Gun Components

Even though thermionic cathodes are the most commonly used electron source in electron guns, plasma cathodes bring extra advantages that make them attractive over conventional electron guns (Goebel, Watkins 2000).

A plasma cathode gun system consists of two main parts: a plasma chamber (plasma cathode) and an electron extraction/acceleration stage. The current density of the electron beam generated will depend on the plasma parameters such as density and temperature and on the electric field of the extractor/accelerator (Oks, Schanin 1999). Thus, both parts of the system should be studied to optimise the electron gun system and maximise electron beam power. The electron beam acceleration part has been described already for thermionic guns in Chapter 2, and is not repeated here as that part of the plasma cathode system is similar as for conventional guns, whereas the study of the plasma cathode and its optimisation is detailed in this section.

- **Plasma chamber**

Figure 4.1 is a simplified diagram of a plasma cathode electron source. The configuration of the electrodes depends upon the electrical coupling method - for CCP the electrodes are within the plasma chamber. Once the gas is fed at low pressure in the plasma chamber, a plasma is generated by applying an electrical signal The electrons break away from the atoms and start moving freely together with the other species in the plasma chamber, mainly neutral atoms (grey), positive ions (blue). Depending on the electron beam requirements, different ways to excite the plasma can be used: vacuum arcs, constricted gaseous arcs, hollow cathode glows, penning discharges and magnetron discharges (Oks, Schanin 1999). The cathode consists of a low-pressure and low-temperature plasma. A typical pressure in the plasma chamber is 10^{-2} mbar.

- **Electron acceleration**

Just as with conventional electron guns, a high voltage is applied between the cathode and the anode (at ground potential, 0 V in the diagram). The high voltage electric field accelerates the electrons towards the anode and makes them into a beam of electrons. High electron beam powers can be achieved, so that the electron beams generated from plasma cathodes can be used for material processing applications. A typical pressure in the electron acceleration region of a plasma gun is $<10^{-3}$ mbar.

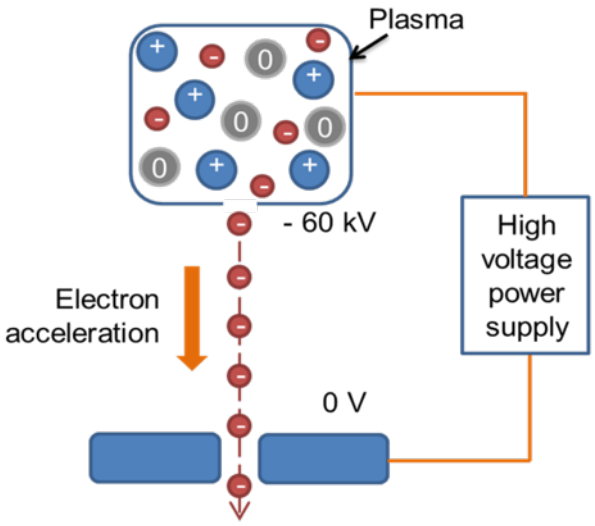

Figure 4.1 - Plasma cathode electron beam source

The plasma chamber geometry influences the electron beam characteristics. Low pressures in the plasma chamber are usually employed in order to avoid gas leakage into the acceleration gap that could cause high voltage breakdown. For CCPs, long electrode gaps are then required, as dictated by Paschen law. Typical values in a plasma cathode gun are less than 0.1 mbar gas pressure for electrode gaps in the order or higher than 0.1 m (Koval et al. 1992).

Hollow cathodes are commonly used in the plasma discharge chamber to improve the efficiency of electron densities. Hollow cathodes can be used in DC discharges as well as in RF discharges. Both forms of hollow cathodes will be detailed later in this section.

The EB current is emitted from an aperture at the side of the plasma chamber facing the acceleration gap. The EB current emitted from the plasma cathode is usually a

fraction of the discharge current, thus high discharge currents will be needed to obtain high EB currents (Koval et al. 1992). High current EBs are desired in the material processing applications of the RF plasma cathode gun that is concerned in this work. The aperture has an emission current density, similar to or greater than a thermionic cathode: "The maximum current density that can be extracted from a plasma is about 100 A/cm^2, which is at least one order of magnitude higher than in thermionic guns" (Oks, Schanin 1999).

4.2.2. Plasma Cathode Advantages

- **Cathode lifetime and consistency**

In conventional guns, cathode lifetime is limited due to material evaporation (Richardson 1913, Iiyoshi et al. 1996, Howard et al. 1927) and erosion. Erosion is mainly caused by ion bombardment when the beam is thermally processing material (Sanderson 1978, Goebel, Watkins 2000). As the cathode is gradually wearing from the beginning to the end of its life, this changes the beam characteristics (e.g. intensity and focus position) and introduces quality degradation to the processing. This leads to inconsistencies in the material processing, such as welding, cutting or additive manufacturing.

Plasma cathodes avoid problems caused by cathode wearing as the electrons are extracted from an ionised gas instead of an emissive surface. This allows the EB parameters to be stable over a long time (Belyuk et al. 2001) giving improved reproducibility compared to thermionic guns (Koval et al. 1992).

- **Operation in coarse vacuum**

Plasma cathode electron sources allow generation of electron beams (continuous and pulsed) in coarse vacuum pressures, e.g. 0.01 to 1 mbar, which widens the number of applications and possibilities of electron guns (Oks 2015). High voltage and currents can be obtained in a low vacuum of order 10^{-3} mbar (Kang et al. 2015), instead of the 10^{-5} to 10^{-6} mbar pressure in thermionic guns required to prevent chemical degradation

of the hot cathode. However, there are still limitations on the vacuum level for operating the gun to avoid high voltage breakdown in the acceleration gap.

- **No need for grid electrode**

A grid cup electrode is used in triode guns to control beam power, however it changes beam shape over the power range and introduces beam aberration. Plasma cathode electron guns do not require a third electrode for controlling the beam power, avoiding this aberration. They can be operated as diodes where the beam power is controlled by the plasma parameters. This allows generation of both focused beams with high power densities and large cross section beams at high currents (Koval et al. 1992).

- **Beam pulsing**

In thermionic guns the beam can only be pulsed slowly due to the thermal inertia of the cathode (Goebel, Watkins 2000). In diode guns pulsing is of the order of 100 ms whereas in triode guns beam pulsing requires complex electronics for control of the grid electrode voltage and pulsing transition times below 1ms are not generally available in material processing applications.

The plasma parameters can be rapidly modulated - allowing the plasma diode gun to rapidly change the beam current. RF excited plasma cathode guns (Ribton, Sanderson 2015), like the design investigated in this, allow rapid beam pulsing (below 1 μs) without the requirement of complex and expensive electronics.

- **Disadvantages plasma emitters/electron temperature in plasma cathodes**

Electrons from thermionic cathodes are at a lower temperature than plasma cathode electrons (Oks, Schanin 1999). In low pressure plasma discharges, electrons may be at temperatures higher than 3-5 eV (Oks, Schanin 1999). This affects directly the thermal velocity spread of the EB and as a result will limit the beam brightness, as described previously in this report, to a lower level with plasma electron emitters compared to thermionic emitters. Thus there are limitations in the electron current density of focused beams, however this can be compensated by higher emissivity of plasmas compared to thermionic cathodes (Oks, Schanin 1999).

In addition to this, electrons from plasma emitters have higher mobility and are emitted from an emission boundary that varies. This may lead to differences in the electron optics design as the plasma parameters vary over the beam current range.

4.3. What Is Plasma?

- "Plasmas are ionised gases in which long-range electrical and magnetic interactions involving charged particles dominate over collisions between neutral species." (IOP 2013)
- "Plasma is an ionised gas containing freely and randomly moving electrons and ions." (Chabert, Braithwaite 2011).
- Plasma is "a large collection of approximately equal numbers of positively and negatively charged particles." (Shohet 2012).

As deduced from the statements above, plasma consists of ions, neutral atoms or molecules and electrons. In addition, plasmas have quasi-neutral net charge and are characterised by the particle density $n_e \approx n_i \approx n$ particles/m^3 (Lieberman, Lichtenberg 1994).

Plasmas can be classified depending on their density and electron energy or temperature. Figure 4.2 shows a diagram of the very different types of plasma that exist. Energy and electron temperature are usually given in electron-volts:

$$1\ \text{eV} = 1.6\times10^{-19}\ \text{J}$$

$$T_e(volts) = \frac{kT_e(kelvins)}{e}$$

where $k = 1.38\times10^{-23}\ \text{J/K}$ is Boltzmann´s constant

Thus: $1\ \text{V} = 11605\ \text{K}$

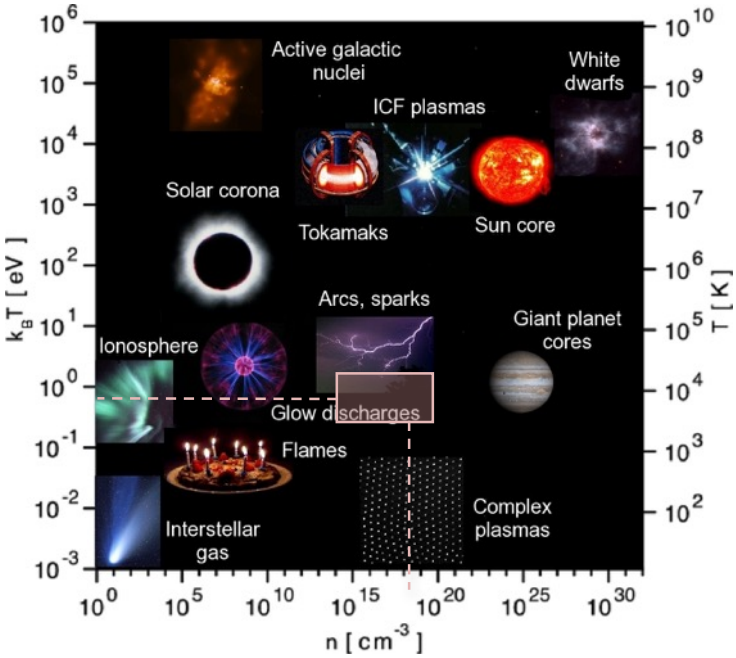

Figure 4.2 - Energy / plasma density diagram of the plasma state (NOVA Admin 2013) and modification of it showing typical electron density and temperature values for a low temperature, low pressure plasma as the type in this work

As seen in Figure 4.2, plasmas can have a wide range of densities (about 32 different orders of magnitude as seen in the graph) and temperatures (9 orders of magnitude). Plasmas over these ranges will act in very different ways.

Plasmas can be classified as thermal (or high temperature) plasmas, which are at around 4,000 K to 20,000 K (Lieberman, Lichtenberg 1994), and non-thermal plasmas (or low temperature plasmas), which are the type most relevant to electron beam sources for materials processing equipment. Both high temperature and low temperature plasmas can be found in space (astro-plasmas) as well as on earth (laboratory plasmas) (Bogaerts et al. 2002). Examples of astro-plasmas are the sun (high temperature) and interstellar gases (low temperature), while examples of plasmas on earth would be a nuclear fusion reactor (thermal plasma) and a plasma lamp (non-thermal plasma).

Typical values for gas discharges are 10^{-2} m length, 10^{18} m^{-3} particle density and 2 eV electron temperature. Examples of hot plasmas could be solar corona with length scales of the order of 10^{8} m, particle density of 10^{13} m^{-3} and electron temperatures of the order

of 10^2 eV; or a fusion reactor with plasma length of around 2 m, particle density of 10^{20} m^{-3} and electron temperatures of the order of 10^4 eV (Goldston, Rutherford 1995). Another example of a plasma in near thermal-equilibrium with all species close to about 10000 K are the arcs produced in lightning and arcs used by torches for welding and cutting (Chabert, Braithwaite 2011).

This work focuses on a plasma cathode, which belongs to the category of low-temperature and low-pressure plasmas. In low temperature plasmas the ionisation is very low, thus the percentage of electrons and ions compared to the number of neutrals is very low, for example 0.1% to 2%. In the low-temperature plasmas field, there are multiple and new applications that have emerged in the last decade, which have generated a lot of interest in this field.

Table 4.1 shows the macroscopic parameters that define a plasma system. These are described in more detail in this chapter.

Table 4.1 - Macroscopic parameters in a plasma system

Particle	Number density	Mass	Charge	Drift velocity	Temperature
e	n_e	m_e	$-e$	$\vec{v}$	T_e
ion	n_i	m_i	$z_i e$	$\overrightarrow{v_i}$	T_i
neutral	n_n	$m_n \sim m_i$	0	0	T_n

4.3.1. Temperature

Low temperature plasmas are weakly ionised and are not in thermal equilibrium. Weakly ionised plasmas (Lieberman, Lichtenberg 1994) have the following characteristics:

1) They are electrically generated and sustained. The most typical methods will be described in the "Plasma generation" section.
2) Collisions of charged species with neutrals are important
3) There are important losses at the boundaries
4) "Ionisation of neutrals sustains the plasma in the steady state"

5) There is not thermal equilibrium of ions and electrons, as the electrical discharge mostly heats up the electrons and the ions efficiently exchange energy when they collide with the neutral particles. Thus, $T_e \gg T_i$

The fractional ionisation of a plasma x_{iz} is (Lieberman, Lichtenberg 1994):

$$x_{\mathrm{iz}} = \frac{n_{\mathrm{i}}}{n_{\mathrm{g}} + n_{\mathrm{i}}}$$

Where n_{g} is the neutral gas density. x_{iz} will be near unity for fully ionised plasmas and $x_{\mathrm{iz}} << 1$ for weakly ionised plasmas. The weakest plasmas have values of $x_{\mathrm{iz}} \sim 0.001$. In low temperature plasmas around 1% of the species are electrons. Thus, the overall plasma temperature can be approximated to be the temperature of the neutral particles and ions. Low temperature plasmas can be classified into two subgroups:

- Local thermal equilibrium (LTE) – there are localised areas in the plasma where thermal equilibrium of ions and electrons exists. Usually this low temperature plasma type is at high pressure (around atmospheric pressure). As the pressure is high, the number of electron collisions is high (the mean free path is short for the electrode gap length), which leads to efficient energy exchange. As a result, the applications for this type of plasma are usually at gas temperatures higher than room temperature such as cutting, spraying and welding (Bogaerts et al. 2002).
- Non-LTE – the different species are at different temperatures, with the electron temperatures being a lot higher than the ions and other species. Generally, this type of low temperature plasma occurs at low pressure (typical values are 10^{-2} - 10^{-1} mbar). This is most relevant to the plasma cathode investigated in this work. As a result of the low pressures (the collisional mean free path is long compared to the electrode gap), the number of collisions is low and so is the energy transferred by collisions. Thus, the gas temperature of this type of plasma is low (room temperature or less) and the practical applications are ones that require a high electron temperature process at low gas temperature. Examples of applications are: etching, deposition of thin layers, sputtering and ion implantation.

In general terms, this classification is related to the pressure of the low temperature plasma, although there are exceptions to this. The exceptions appear at very small electrode gaps, such as with dielectric barrier discharges and atmospheric glow discharges. So actually the classification into LTE or non-LTE is related to the product pd given by the Pachen law (where p is the plasma pressure and d is the electrode gap). There is a long list of industrial applications of low temperature plasmas including light generation (plasma lamps), plasma etching in microelectronics, plasma enhanced chemical vapour deposition (PECVD), surface sterilisation, plasma spraying on artificial hips and wound healing in plasma medicine (Von Keudell 2013). As it has been discussed above, plasmas can also exist at a variety of pressures. In the next section this will be discussed.

4.3.2. Electron Energy Distribution Function (EEDF)

As seen above, in low temperature plasmas the species (neutral atoms, ions and electrons mainly in atomic gases) are not in thermal equilibrium and in non-LTE the electrons are at a much higher temperature than the other species. In addition to this, the electrons do not usually have the same electron temperature. Instead, there is a distribution function of energies (temperatures) of electrons: Electron energy distribution function (EEDF). The EEDF gives the most complete and universal information on the plasma electron characteristics in any plasma (Godyak, Demidov 2011, Godyak et al. 1992).

The typical electron distribution in a weakly ionised plasma is presented in Figure 4.3. This graph indicates the number of electrons per unit volume at each energy level (electron temperature). T_e is the temperature of the bulk electrons and it is lower than $\mathcal{E}_{diss}$ and $\mathcal{E}_{ion}$, which are dissociation (in molecular gases) and ionisation energies respectively. As a result, the electrons capable of causing ionisation are those at the high-energy tail of the distribution (Lieberman, Lichtenberg 1994).

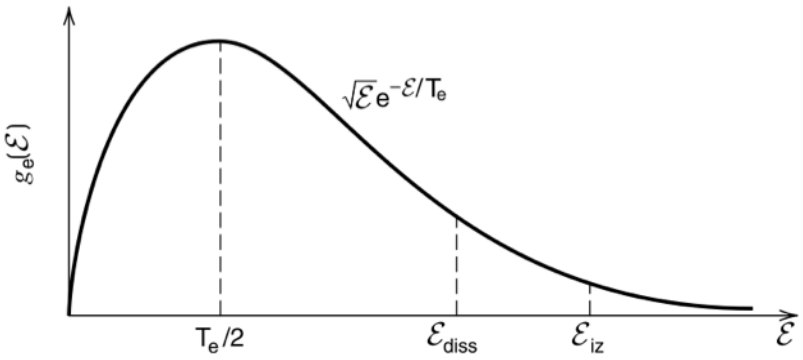

Figure 4.3 - Weakly ionised plasma electron energy distribution function (Lieberman, Lichtenberg 1994)

A Maxwell-Boltzmann distribution is used to describe plasmas in which the electrons are in thermal equilibrium with the ions and atoms in the gas. This distribution assumes that electron-electron collisions are relevant and that elastic collision frequency is constant. Maxwellian distribution is assumed in classical diagnosis techniques, which will be discussed later in this work. A Maxwell-Boltzmann energy distribution might be the case in a high density low pressure plasma plasma (Turner 2012), but it is usually only an approximation in low temperature, low pressure plasmas.

A closer approximation for low pressure plasmas (non-LTE) is the Druyvesteyn distribution function. This distribution has a higher average electron energy. Moreover, the number of electrons in the high energy tail of the Druyvesteyn distribution is higher than in the Maxwellian distribution, thus the ionisation rate is predicted to be higher. Both Maxwellian and Druyvesteyn distributions are shown in Figure 4.4 for three different average electron energies.

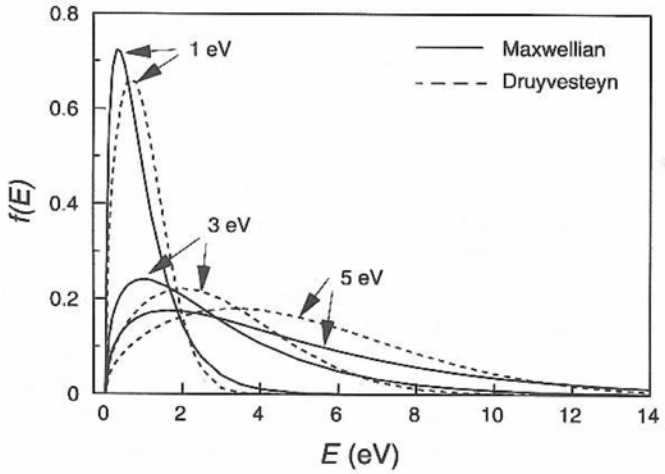

Figure 4.4 - Electron energy distribution according to Druyvesteyn and Maxwell for 1 eV, 3 eV and 5 eV average electron energies (Druyvesteyn, Penning 1940)

The distributions presented above are only approximations in the case of low- pressure plasmas, in which electrons are not in thermal equilibrium with the other species in the plasma but are at much higher temperatures ($T_e \gg T_i, T_g$). The electron energy distribution function in low pressure plasmas can take many different shapes, such as curves with bumps, holes or super-thermal tails (Turner 2015, Godyak, Piejak 1990, Godyak et al. 1992, Godyak 2011b, Godyak 2011a, Godyak, Alexandrovich 2015, Godyak et al. 1991). The TWI RF plasma cathode is a capacitively coupled plasma at low pressure. This type of plasma discharge and its EEDF will be discussed later in this chapter.

4.3.3. Pressure

Plasma pressure is another key parameter that dictates the behaviour of plasma. In plasma cathode electron guns, the plasma also influences the quality and characteristics of the beam extracted. As has been mentioned before, the type of plasma used in the TWI RF plasma cathode is at low pressure. This means that there is not thermal equilibrium between species and that electron temperature is a lot higher than the ions and overall gas temperature. Figure 4.5 shows temperature vs. pressure graph with electron and gas temperature (T_e and T_g) in plasmas.

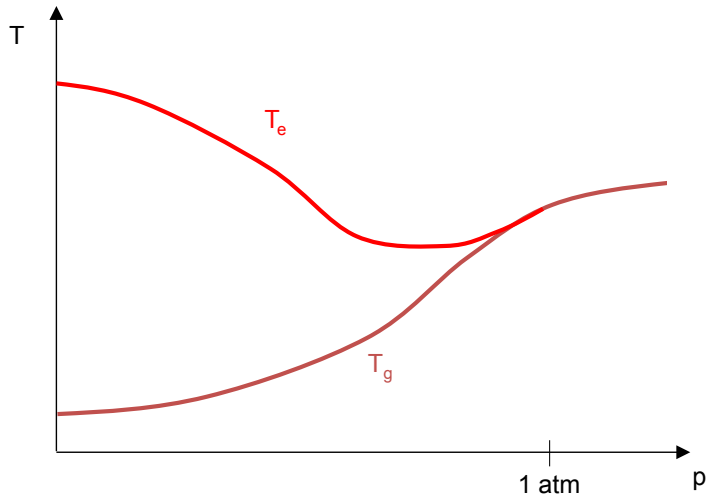

Figure 4.5 - Plasma temperature and pressure (Von Keudell 2013)

Low-pressure plasmas are those in the 10^{-3} to 1 mbar range and are characterised by $T_e \approx 1 - 10\,V$ and $T_i << T_e$, particle density of $n \approx 10^8 - 10^{13}\ \mathrm{cm}^{-3}$ and a Debye length of less than 1 cm (Lieberman, Lichtenberg 1994), see section 4.2.4.

Plasmas at low pressure tend to occupy all the volume of the container, in contrast to atmospheric pressure plasmas, as the mean free path of the electrons is at least comparable to the container dimensions. The plasma bulk is electrically quasineutral whereas the limit regions with the walls are positively charged. These limit regions are the sheaths of the plasma and are described in the following subsection. Low temperature plasmas are easily generated at big scales by electric discharges, in the glow discharge regime (Chabert, Braithwaite 2011).

In contrast, higher-pressure discharges, such as dielectric barrier discharges at atmospheric pressure, form streamers, as shown in Figure 4.6. In this type of discharge the plasma does not usually fill the complete volume of the chamber and filamentation occurs in which higher electron density thin regions appear across the electrode gap. Filamentation is essentially the generation of ionised tracks in the gas where the discharge current is carried predominantly. It can only occur at relatively high pressures where the mean free path of the electrons is short.

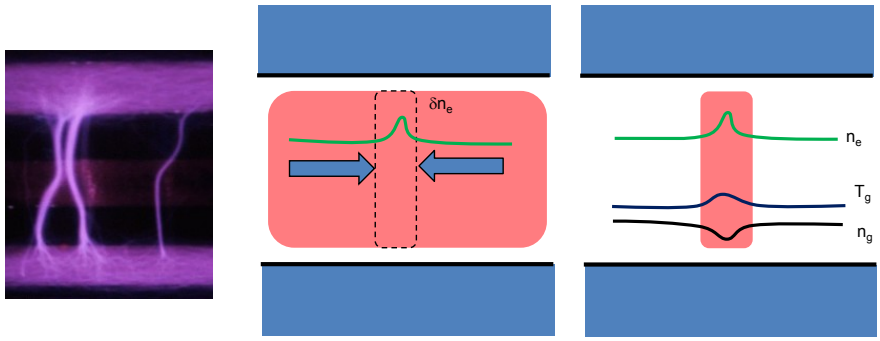

Figure 4.6 - High pressure discharge showing formation of streamers (Von Keudell 2013)

4.3.4. Plasma Sheaths

Plasmas are quasineutral or very close to being electrically neutral, i.e. they have approximately the same amount of negative charge from electrons and as positive charge from ions. Before the formation of the sheaths, the potential across the plasma chamber is zero everywhere. Thus, due to the electron thermal velocity being larger than the ions, the electrons are lost to the walls faster. This leaves a positively charged area next to the walls, which sets up the sheaths (Lieberman, Lichtenberg 1994).

Sheaths are the positively charged boundary region of the plasma at the limits with the walls (grounded) of its container. Figure 4.7 shows the electron and ion densities in the plasma bulk and sheaths after the sheaths formation. Φ is the plasma potential, Vp is the potential in the plasma bulk, s is the sheaths thickness, and E is the electric field in the sheaths.

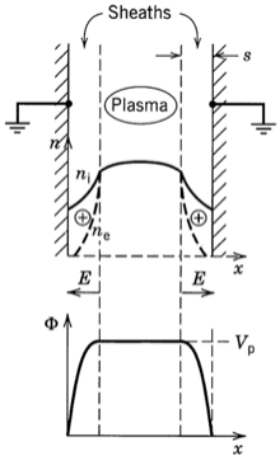

Figure 4.7 - Sheaths in an electric discharge (Lieberman 2003)

The positive potential at the plasma bulk Vp drops to zero next to the walls. The strong electric field next to the walls makes the electrons entering the sheaths being accelerated back towards the plasma bulk (Lieberman, Lichtenberg 1994).

The thickness of the sheaths is important in this work, as the application requires extraction of electrons from the plasma. The thinner the sheaths are, the closer the higher density region is to the accelerating potential for electron extraction. An RF simulation was carried out and preliminary results showing the thickness of the sheaths will be shown in Chapter 7.

4.3.5. Other Important Parameters

- Mean free path λ_m

The mean free path is the average distance between collision events (Buckman 2014) or distance an electron covers between two collisions:

$$\lambda_m = \frac{1}{\sqrt{2} n \sigma}$$

where n is the particle density and σ is the collision cross section of the particle.
It is dependent on particle size and cross section and as a result, larger molecules will have shorter mean free path.

- Cross section $\sigma(v_R)$(Boffard et al. 2004)

Cross section $\sigma(v_R)$ is the fundamental parameter that characterises a collision; where v_R is the relative velocity between the particles before the collision.

- Debye length λ_D

The Debye length is the most important length scale in a plasma and it can be calculated as follows (Lieberman, Lichtenberg 1994).

$$\lambda_D = \sqrt{\frac{\epsilon_0 T_e}{n_0 e^2}}$$

where: ϵ_0 is the relative permeability, T_e is the electron temperature (eV), n_0 is the electron density and e is the electron charge.

The Debye length can also be calculated as (Chabert, Braithwaite 2011):
$\lambda_D = \frac{v_e}{\omega_{pe}}$; where $v_e = (kT_e/m_e)^{1/2}$ is the electron thermal speed, and ω_{pe} is the electron plasma frequency.

The Debye length is the range over which an electron interacts with the fields of individual charges. Beyond the Debye length, the fields of individual charges are effectively screened from each other by the plasma. The plasma investigated in this thesis work should be bigger than Debye length so the effects of mutual/individual charges can be ignored.

Hollow cathodes and low-pressure discharges which are the types of plasma concerned in this work have a Debye length between 10^{-4} to 10^{-2} cm, as indicated from Figure 4.8. Diagonal lines indicate the Debye length in cm.

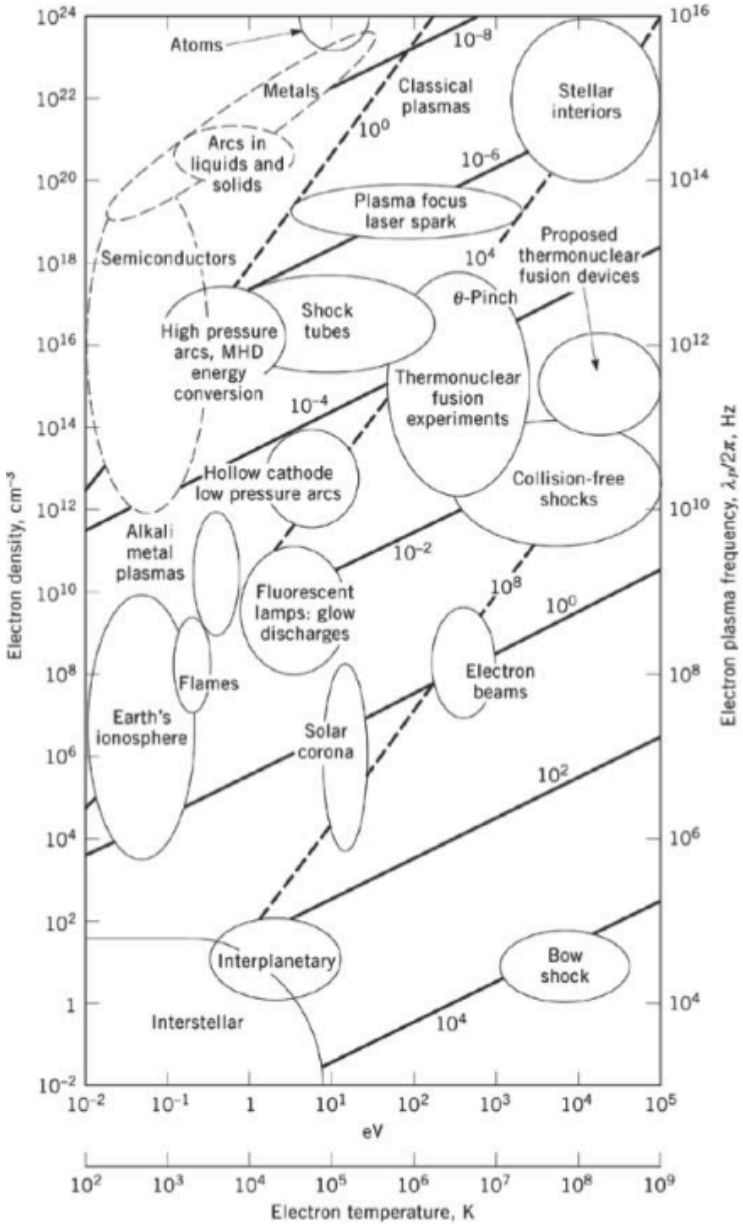

Figure 4.8 - Plasma types in function of the electron density and temperature regions (Chen, Smith 1984)

- Plasma frequency ω_p (characteristic frequency)

The plasma frequency is the natural frequency of oscillation of the plasma:

$$\omega_p = \sqrt[2]{\frac{n_0 e^2}{m\epsilon_0}} \approx 50\, n_0^{\frac{1}{2}};$$

where: ϵ_0 is the free space permittivity.

This quantity depends on electron density, a plasma of higher electron density will have a space oscillation of larger frequency whereas, a plasma of low density will have a space charge oscillation of lower frequency.

4.3.6. Atomic Collisions

Valence electrons determine the inelastic processes that can occur (Lieberman, Lichtenberg 1994). The TWI plasma cathode uses a plasma generated with argon, thus only atomic collisions need to be considered as the dominant processes in the type of discharge in this work.

The electron collisions that occur with this noble gas are the following: Inelastic collisions (in can be ionisation and excitation and there is electrons exchange), and elastic collisions (there is only change of momentum):

Ionisation: $e + Ar \rightarrow Ar^+ + 2e$

Excitation: $e + Ar \rightarrow e + Ar^* \rightarrow e + Ar + photon$

Elastic scattering: $e + Ar \rightarrow e + Ar$

If we consider Maxwellian electrons, when there is a collision with an argon atom, the rate of increase in the electron density:

$$\frac{dn_e}{dt} = \nu n_e = K n_g n_e$$

where ν is the collisional frequency [s^{-1}], $K(T_e)$ is the rate coefficient [m^3/s] and n_g is the argon density. Rate coefficient $K(T_e)$ is the average of cross section σ [m^2] for a process, over the normalised energy distribution $K(T_e) = \int_0^\infty \mathcal{E}\sigma(\mathcal{E})f(\mathcal{E})d\mathcal{E}$ (integral of the product of the energy, cross section and normalised energy distribution) (Buckman 2014). Figure 4.9 shows the electron-argon coefficients assuming a Maxwellian distribution: $K(T_e) = \langle \sigma v \rangle_{Maxwellian}$ (Lieberman 2003).

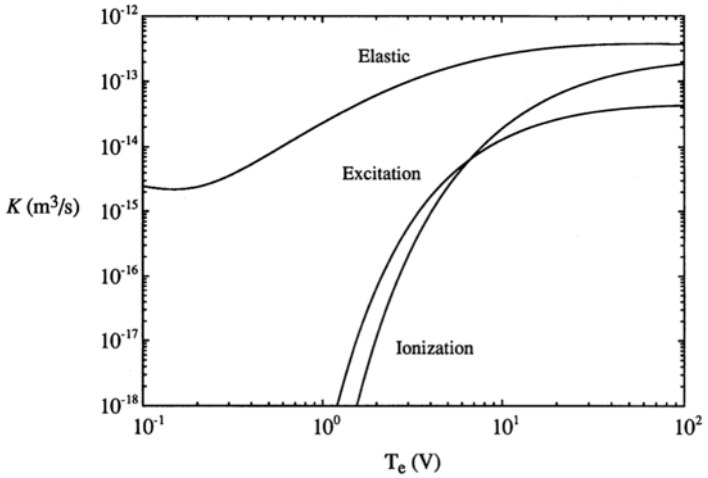

Figure 4.9 - Electron-argon rate coefficients for the different collision processes (Lieberman 2003)

The ion collisions that occur with argon are the following:

Elastic scattering: $Ar^+ + Ar \rightarrow Ar^+ + Ar$

Charge transfer: $Ar^+ + Ar \rightarrow Ar + Ar^+$

The important plasma parameters and their typical values for the cathode low temperature and low pressure plasma are summarised in Table 4.2:

Table 4.2 - Plasma parameters for a low temperature and low pressure plasma (Lieberman 2003)

Parameter	**Typical values for low temperature, low pressure plasma**
Electron temperature T_e	1 - 10 eV (2 - 5 eV in plasma bulk)
Ion temperature T_i	0.026 V (max. a few times room temperature in the bulk) $T_e/2$ (at the sheath edge)
Pressure	(1 mTorr – 1 Torr) 10^{-3} - 1 mbar
Plasma density n_e	10^8 - 10^{13} cm^{-3}
Degree of ionisation	10^{-6} - 10^{-4} %
Debye length λ_D	~10^{-4} m
Frequency	DC – 100 MHz

4.4. Plasma Models

There are different plasma models that can be used to describe plasma discharge behaviour. A combination of models can be also used in hybrid models (Bogaerts, Gijbels 2002).

4.4.1. Analytical Model

Analytical models give a fast and simple approximation of the plasma behaviour by solving a set of equations. However these have validity over limited plasma conditions (Bogaerts 2015).

A Single-particle motion model considers the response of an equilibrium plasma to a localised charge. This model analyses motion of individual charged particles in electric and magnetic fields and collisions of particles are not taken into account (Goldston, Rutherford 1995).

4.4.2. 0D Chemical Kinetic Model (Global Model)

The global model solves the rate balance equations for all the species taking into account the production and losses by chemical reactions. Global models can be used for simple models of low and intermediate pressure plasmas and are fast to solve. The global model looks in detail at the plasma chemistry, and can have surface interactions and time dependence (Turner 2012). However, it can only be taken as an approximation as the global model assumes that the species energy lost in collisions is equivalent to the energy that the species gain from the electric field (Bogaerts 2015). The limitations of this model are that it assumes spatial uniformity and a particular EEDF which is not always the case, particularly in low pressure plasmas.

4.4.3. Fluid Model

Fluid models of a gas discharge considers plasma as an "electrically conducting fluid" (Goldston, Rutherford 1995). The transport of the species (mainly electrons and ions) is described by solving the Boltzmann transport equation. The continuity equation, momentum density equation (usually approximated by the drift-diffusion) and energy

density equation (mainly for electrons) are derived for the plasma system. Each of these equations contains transport coefficients or rate coefficients (Alves 2015).

The inputs for fluid models of gas discharge are the transport coefficients and rate coefficients, which depend on the EEDF (Alves 2015). In most cases, the EEDF is not Maxwelliam and can vary considerably depending on the plasma parameters as it has been described earlier in this chapter. The EEDF and electron coefficients can be derived from the collisional cross-section data by solving the Boltzmann equation (Alves 2015). This model is also an approximation, as it assumes equilibrium with the electric field, which is not accurate in some cases (Bogaerts, Gijbels 2002).

4.4.4. Collisional-Radiative Model

Collisional-Radiative (CR) models are a special type of fluid model which takes into account radiation from excited states. CR models are usually applied to atoms and ions in excited levels (Bogaerts, Gijbels 2002) and derive the continuity/balance equation for each level.

4.4.5. Non-Equilibrium Boltzmann Equation Model

This model solves the Boltzmann transport equation and gives an accurate description of the plasma behaviour, including non-equilibrium plasma behaviour. However, it is mathematically complex and becomes very complicated if the model has more than one dimension.

4.4.6. Monte Carlo Simulations

Monte Carlo (MC) simulations describe plasma at a microscopic level, simulating each particle in a statistical way. This can take a lot of time for the large number of particles that are present in a plasma and for the statistics to be consistent.

MC simulations are accurate and can be used for non-equilibrium plasmas while being mathematically simple. They can be used to simulate all the species, however it takes long calculation times (specially for slow moving species) and it is not self-consistent as it needs a certain electric field input value. MC simulations are mainly used in hybrid

models to simulate the electrons or species with an specific behaviour while the other species are simulated by other less time-consuming model (Bogaerts 2015).

4.4.7. Particle In Cell Model

Particle In Cell (PIC) models simulate plasma particles by using superparticles or macroparticles, which are formed by several real plasma particles (Bogaerts 2015). Partice in Cell models are often used in combination with MC simulations in order to reduce the simulation time. These models combine MC simulations for ions and electrons with the Poisson equation for a self-consistent electric field (Pal 2015). However, the simulation time can be still long, this introduces the need for hybrid models, explained below.

4.4.8. Hybrid Model

A combination of different models is convenient in plasmas that are not in thermal equilibrium. In this way, some species can be modelled as fluids and other as particles. An example of hybrid model in a non-equilibrium (e.g. a low pressure noble gas discharge) plasma would use a combination of Monte Carlo for fast electrons, which are not in thermal equilibrium; a fluid model for slow species which are considered to be in equilibrium such as ions in the plasma bulk and neutrals, and a collisional-radiative model for excited atoms (Bogaerts 2015).

As it has been described, each model has advantages and disadvantages for the application and the species modelled. Using hybrid models allows taken the particular advantages of a model in each of the species. Hybrid models are accurate and self-consistent while keeping reduced calculation time.

The selection of the appropriate model will depend on the application. In general, fluid models (1D and 2D) and kinetic models (0D) give detailed information on the plasma chemistry. Hybrid PIC models have been already used to simulate plasma cathode electron guns. An example is presented in Figure 4.10, which shows a 2D diagram of the geometry and results of the plasma density calculated. The model is a 3D electrostatic kinetic PIC simulation of a hollow cathode plasma (pseudo spark

discharge) electron gun using the simulation code "VORPAL". It was used to compare the plasma behaviour when changing the extraction aperture hole size. The findings showed that "decreasing the aperture size from 8 to 3 mm increases the discharge current, the electron confinement time and the plasma density" (Pal 2015).

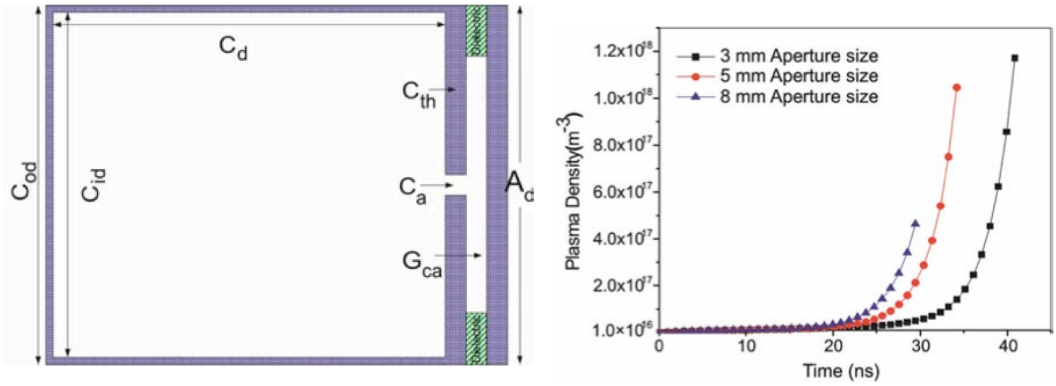

Figure 4.10 - 2D diagram of the plasma cathode gun geometry (left) and plasma densities calculated at different aperture sizes as a function of time (right) simulated in a 3D PIC model (Pal 2015)

This type of simulation is useful for the plasma cathode gun. VSim combines PIC and fluid models and uses the code VORPAL, which allows to simulate 1D, 2D and 3D systems (Pal 2015). VSim has been developed and validated by Tech-X. Another example of simulation work carried out with VSim is the NASA xenon ion thruster (NEXT) discharge chamber (Tech-X Corporation 2015). The plasma processes occurring in the discharge chamber (hollow cathode) were modelled: primary electron emission, neutral sources, static magnetic fields generated by permanent magnets and solving of the electrostatic fields every time step. The simulation results were compared and they were in agreement with the experimental plasma measurements done in a NEXT ion thruster (Tech-X Corporation 2015).

The type of results obtained in the example above are very relevant for the plasma cathode gun, as it has been observed from experiments the aperture size affects the electron beam current extracted from the plasma (del Pozo et al. 2014a). The hole size has been increased and tested experimentally and the EB current keeps increasing with it. It would be useful to simulate the TWI radio frequency excited plasma cathode gun in future work at different aperture sizes and find the optimum size.

There are many simulation software packages available. For the low temperature and low pressure plasmas of interest the most suitable model is one that simulates collisions. Computation efficiency can be increased by modelling the neutral particles as a fluid. VSIM (Tech-X Corporation 2016) was chosen for the work presented in this thesis. This software uses a particle in cell method (Pal 2015). The plasma cathode concerned in this work uses mainly argon. Sometimes other noble gases were used such as neon and krypton. Thus only atomic collisions need be considered and the important processes in noble gases discharges such as argon will be looked at. There is extensive literature on molecular collisions and the dissociation, recombination and other processes that occur in molecular gases that will not be described in this work. The VSIM software is able to simulate all of the relevant collisions for the plasma used in this work (mainly ionisation, excitation, elastic scattering), and interactions of electrons with the plasma container walls.

4.5. Plasma Generation

This section describes the main plasma excitation methods, including DC and RF discharges.

4.5.1. Electron Avalanche – Plasma Formation and Sustaining Plasma

The most commonly used plasma generation method in the non-thermal and low-pressure plasma region is produced by applying an electrical discharge or glow discharge (Conrads, Schmidt 2000). The plasma fills all the volume of the container, with the bulk of electrons and ions at near electrical neutrality occupying most of the volume and a positively charged region at the limits with the walls which are the sheaths of the plasma. DC glow discharges can be continuous wave or pulsed. Low-pressure glow discharges are the most common type in industrial applications.

Glow discharges also can be generated by an RF electric signal. Figure 4.11 shows a diagram of a capacitive discharge. This section will focus on DC glow discharges, RF capacitive and inductive discharges (1-500 MHz) and microwave discharges (0.5-10 GHz). These are most often used in processing chambers of sizes in the range 0.1 m to

1 m (Lieberman 2003). Other plasma generation methods are barrier discharges usually for high pressure plasmas and beam induced plasmas (Conrads, Schmidt 2000).

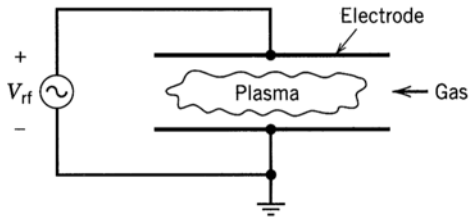

Figure 4.11 - RF capacitive discharge diagram (Lieberman 2003)

There is a wide range of industrial applications such as etching and deposition. These processes benefit from the high temperature electrons while being a low temperature process. There are non-thermal processes happening at an atomic scale.

4.5.2. DC Discharges

DC glow discharges at low pressure are one of the most common types of plasma discharge. Figure 4.12 shows the characteristic regions that appear in this type of discharge. The positive column length can be varied by increasing the distance between the electrodes (while keeping pressure and voltage drop the same). The other regions would keep their size and intensity unless gas, pressure or voltage drop are varied (Lieberman, Lichtenberg 1994).

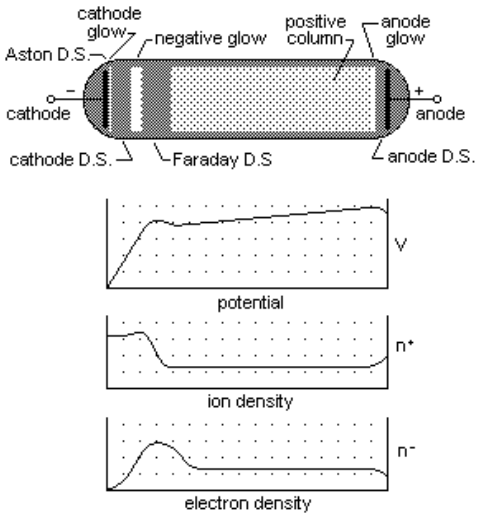

Figure 4.12 - DC glow discharge regions (Lieberman, Lichtenberg 1994)

4.5.3. RF Discharges: Capacitive or Inductive

Even though the RF frequency range extends from 1 to 500 MHz, RF discharges are usually operated at 13.56 MHz. At these frequencies, only the electrons are able to respond instantaneously to fields, while the ions, being a lot heavier, can only respond to time-averaged fields (Chabert, Braithwaite 2011).

There are various ways to generate an RF discharge. Figure 4.13 shows the most commonly used RF discharges. The capacitively coupled plasma (CCP) discharge consists of two parallel plates which are driven at the RF signal. The inductively coupled plasma (ICP) discharge consists of an inductor loop that magnetically couples to the plasma.

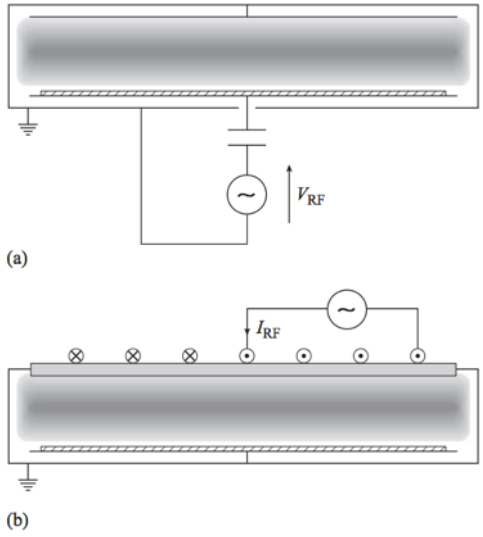

Figure 4.13 - RF plasma generation: (a) Capacitive discharge, (b) Inductive discharge (Chabert, Braithwaite 2011)

4.5.4. RF CCP Discharges

Capacitively coupled RF discharge parameters are typically (Goedheer 2000):

$$n_e = 10^{15} - 10^{17}\ \mathrm{m}^{-3}$$

$$T_e = 1 - 4\ \mathrm{eV}$$

There is an amount of energy required to strike the plasma. Figure 4.14 illustrates Paschen law in RF discharges. The graph shows that the voltage breakdown in an RF discharge is a function of the plasma/gas pressure p and the electrode gap.

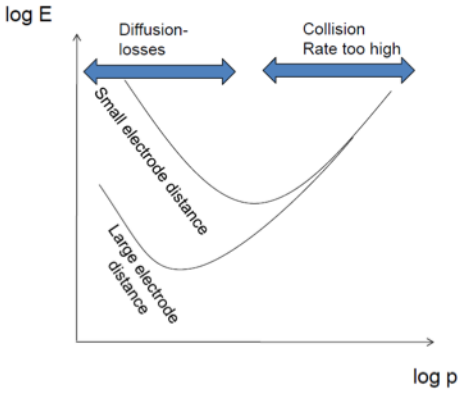

Figure 4.14 - Paschen curve for RF voltages

High voltage is often required to provide the initial discharge, but after this the voltage can be dropped by an order of magnitude to sustain the plasma. Once the plasma has been generated the discharge can be maintained applying less energy, as a result of the electron heating mechanisms that occur.

There are four main electron heating mechanisms or ways to transfer energy from the electric fields to the plasma that can occur (Lieberman, Lichtenberg 1994): Ohmic heating, stochastic heating, resonant wave-particle interaction heating, and secondary electron emission heating.

An RF capacitively coupled discharge can be distinguished by two electron heating mechanisms (Lieberman 2007):

- Ohmic (collisional) heating from plasma resistivity – this is given by the electron and neutral particles collisions. This mechanism for ionisation occurs within the plasma bulk .
- Stochastic (collisionless) heating of electrons from momentum transfer – this takes place as a result of the high voltage moving capacitive sheaths (Gozadinos et al. 2001). The energy is transferred to the plasma on reflection from the oscillating sheaths (Goedde et al. 1988).

In high frequency discharges (>50 MHz) the electron motion is shown to be stochastic. This heating mechanism seems to dominate over bulk plasma heating for sustaining this type of plasma (Goedde et al. 1988).

Measuring the electric parameters of the plasma allows information such as electron density or sheath width to be obtained. In low pressure RF discharges, the dominant heating mechanism is stochastic RF power dissipation (Godyak et al. 1991). Thus this needs to be taken into account in the RF equivalent circuit of the model used. The equivalent RF discharge plasma circuit shown in Figure 4.15 was taken from Schneider and modified (Godyak et al. 1991) to add stochastic heating. The circuit consists of two circuits in series: the plasma bulk and the sheaths. The plasma bulk part is represented by the resistance from stochastic heating R_{st}, the plasma resistance due to electron collisions with gas atoms R_v, the inductance from the electron inertia in the RF field L_o, and the capacitance C_o from the displacement current through the plasma body. The sheaths circuit consists of the ion acceleration losses R'_{sh} and the capacitance C'_{sh} within the sheaths width.

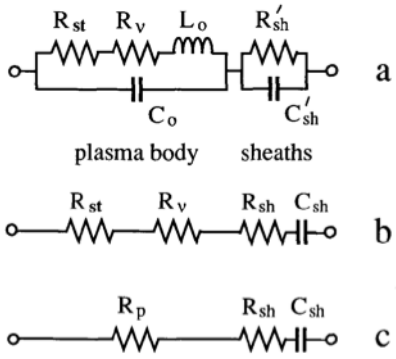

Figure 4.15 - Equivalent circuits of an RF discharge a) and simplifications b) and c) (Godyak et al. 1991)

4.5.5. Electron Energy Distribution Functions in Low Pressure RF Discharges

Electron energy distribution functions in low pressure RF discharges rarely follow a Maxwellian distribution. In some cases, the measured distribution can be approximated as a sum of two Maxwellian distributions. This is the case in Figure 4.16, where the EEPF (electron energy probability function) is approximated as a sum of two Maxwellian distributions with average electron temperatures T_1 and T_2 (Godyak et al. 1992).

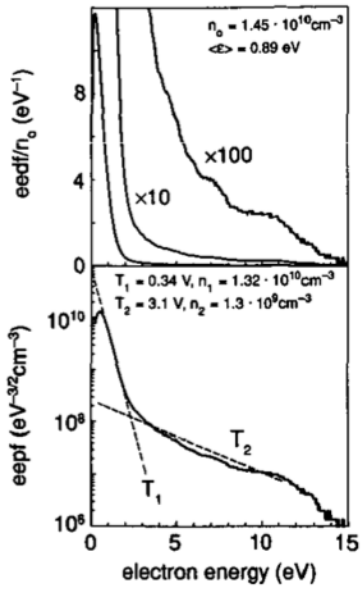

Figure 4.16 - EEDF and EEPF of an argon RF discharge at 13.56 MHz (Godyak et al. 1992)

Simulations and experimental work have shown that increasing the excitation frequency above 13.54 MHz and up to 120 MHz (very high frequency) provides higher density plasmas. However, uniformities appear in large area capacitive discharges (Perret et al. 2003). Significant effects can be appreciated when the wavelength is less than 2 times the electrode size. Even though the free space wavelengths are usually bigger than the electrodes size (5m at 60 MHz, 3.6 m at 84 MHz), the wavelength in the presence of plasma is shorter (Perret et al. 2003). An approximation of the wavelength in the presence of plasma is given by (Lieberman et al. 2002):

$$\lambda = \lambda_0 \left(1 + \frac{\Delta}{s}\right)^{-\frac{1}{2}} \leq \lambda_0$$

where $\Delta = min(d, \delta)$, d is half of the plasma thickness between the sheaths, δ is the plasma skin depth, and s is the sheath size.

A common use of RF CCP is plasma deposition. Figure 4.17 shows a diagram of a device for plasma deposition applications where an RF CCP is used. The main parts of this device are an RF function generator, RF amplifier, matching network for tuning the circuit to the resonant frequency and reducing the reflected power, low pressure plasma chamber, and discharge electrodes. The same main components are used in RF CCP

devices for other applications, and these are also the main components of the plasma chamber used as a cathode in this work. More details will be given in the following chapters.

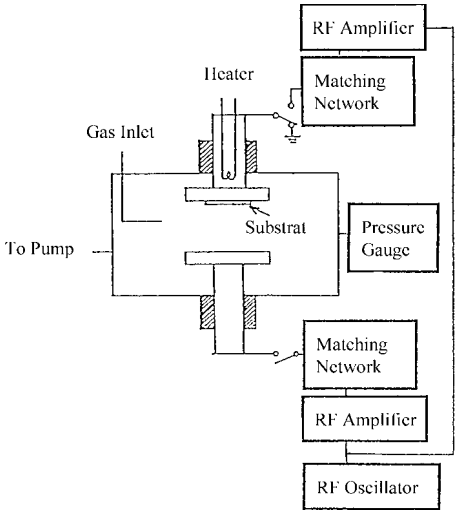

Figure 4.17 - Schematic diagram of a RF CCP discharge device for plasma deposition (Conrads, Schmidt 2000)

4.6. Plasma Diagnosis Tools for Low Temperature Plasmas

The different plasma diagnosis methods can be classified as electrical and optical techniques. The technique will be chosen depending on several factors, such as the type of plasma (this work is focused on low temperature, low pressure plasmas), the plasma parameters required to be extracted (electron densities and temperature), and the time and economic resources available.

The selected technique should be appropriate to measure low pressure non-equilibrium gas discharge, which are in the following ranges (Godyak 2011b, Godyak 2011a, Godyak, Demidov 2011):

- Gas pressure: 10^{-3} mbar to 10^{-1} mbar.
- Mean electron energy $< \varepsilon >$: between fraction and tens eV.
- Plasma density n_e : $10^6 - 10^{14}$ cm^{-3}.

CCP plasmas are one of the most common methods of plasma generation used in industrial applications. The diagnosis techniques used to characterise this type of

plasmas are based on probes, optical techniques and mass spectrometry mainly (Liu et al. 2012).

4.6.1. Plasma Spectroscopy

Plasma spectroscopy is a well establish method in the astrophysics and plasma physics fields. It allows real-time measurements and uses a non-intrusive and, at the same time, a simple and robust experimental setup (Fantz 2006).

Atoms and ions emit radiation when transitions of electrons occur between the various energy levels (Hutchinson 2005). Plasma spectroscopy uses the light emitted (passive method) or absorbed (active method) in these electron transitions to characterise a plasma. The radiation is emitted in the form of narrow lines that correspond to each electron transition that occurs between energy levels in the ion or atom. These are the "spectral lines" and together form the spectra of a plasma. This information is unique for each type of plasma, e.g. it is the fingerprint of a plasma. When a transition occurs, energy is emitted in form of photons in a certain wavelength:

$$E = \frac{h \times c}{\lambda}$$

where E is photon energy or energy emitted in a transition, h is the Plank constant, c is the speed of light and λ is the emitted light wavelength.

The amount of photon energy and the wavelength at which it is emitted is unique for each transition, so that by measuring the intensity of the light emitted with a certain photon energy, information about the plasma can be obtained. Figure 4.18 shows the information that is contained in a spectra line of a plasma. The intensity of the line gives information about how often this transition is occurring, and this can be related to the plasma parameters of neutrals, electrons and ions (density and temperature), the line width gives information about temperature and electron density, and the wavelength gives an indication of which transitions are happening.

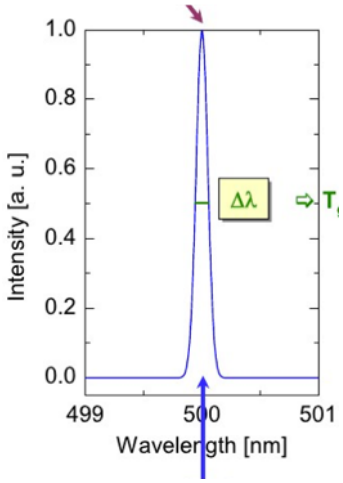

Figure 4.18 - Information in the plasma spectra lines (Fantz 2006)

Einstein coefficients

Between two energy levels (i, j) an electron can do three possible radiative transitions (Hutchinson 2005). The probabilities for each of these transitions to occur are given by the Einstein coefficients:

- A_{ij} – Spontaneous transition probability. Probability per unit time of this transition to occur. (Upper level *i* to lower level *j*).
- $B_{ji}\rho(\nu_{ij})$ – Probability of absorption per unit time. An atom with electron in the lower level may absorb a photon by a transition to the upper level.
- $B_{ij}\rho(\nu_{ij})$ – Probability of induced decay from E_i to E_j due to the presence of radiation per unit time.
- $\rho(\nu)$ – The energy density per unit frequency of electromagnetic radiation at the atom.

Spectrometers

The instrument used to measure the intensity of the light emitted or absorbed is the spectrometer. There are different types of spectrometers depending on:

- Time resolution.
- Spatial resolution.
- Intensity.
- Spectral resolution.

Different types of spectrometer will be chosen depending on the application. They can be classified as shown in Table 4.3 below (Schulz-von der Gathen 2013):

Table 4.3 - Classification of Optical Spectrometers

Type	Technique	Wavelength resolution	Cost/ Complexity	Measurement
Survey spectrometer	Line monitoring	1-2 nm	Pocket size, inexpensive	Simple ΔT Poor Δλ
1 m spectrometer	Common technique	20 pm	Good optics	Poor ΔT, Δλ, Δx Flexible rel. Int
Echelle spectrometer	Absolute values	1-2 pm	High resolution, expensive	Line shift Line profile

A fundamental characteristic of spectrometers is whether they are measuring emitted light, or measuring the absorption of light. Figure 4.19 shows a comparison of an emission spectra (left) and absorption spectra (right):

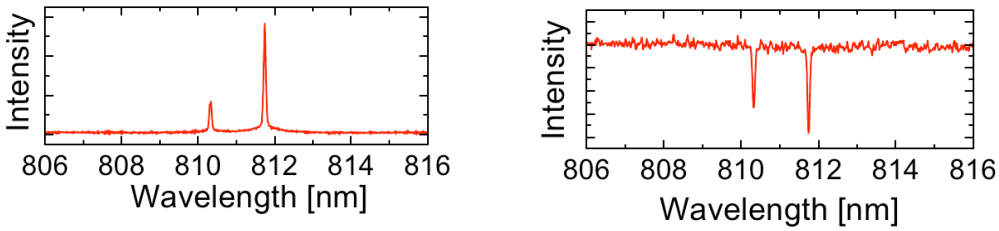

Figure 4.19 - Emission (left) and absorption (right) spectra of a plasma (Schulz-von der Gathen 2013)

Laser absorption spectroscopy uses the absorption spectra of the light that is absorbed when energy (usually from a laser) is applied to the plasma. The equipment used for this spectroscopy technique needs to be set up very accurately and is expensive.

Optical emission spectroscopy (OES) uses the information in the emission spectra. The equipment needed is less expensive and easier to set up. Calibration must be carried out by looking at the emission spectra from a 'black body' source of known temperature. Once the spectral data has been obtained, spectra databases such as that of the National Institute of Standards and Technology (NIST ASD Team et al. 2013) can be used to identify characteristic lines and compare the spectra with that from known plasma conditions.

Spectrometer calibration

Figure 4.20 presents the calibrated (top) and non calibrated (middle) curves of a black body, used for relative intensity calibration of an optical spectrometer.

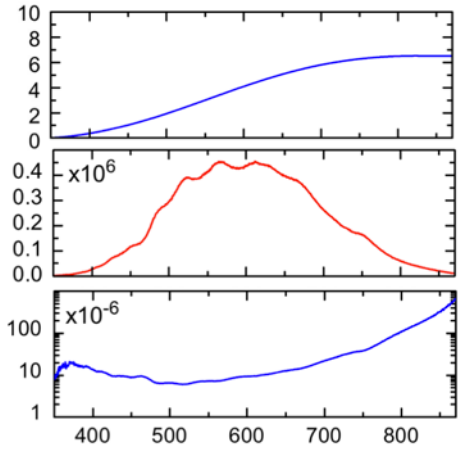

Figure 4.20 - Spectrometer calibration with dark body (Schulz-von der Gathen 2013)

A relative intensity calibration was carried out with the optical spectrometer used in this work. This will be described further in the following chapter.

4.6.2. Line Ratio Method

Particle densities can be determined by the line ratio method which uses the information contained in the spectra of the plasma. The line ratio method is useful as it does not rely upon measuring the absolute level of light intensity, but instead looks at the ratio of the intensity of one line to another. This enables, for example, derivation of rate coefficients of ionisation relative to the excitation of neutrals by rationing the relevant spectral line intensities (Zhu et al. 2009).

There are different models that can be used to calculate plasma parameters such as electron density and temperature from the spectra lines. Zhu and Pu classify the diagnosis techniques depending on the plasma pressure and density ranges. Figure 4.21 shows four main models used in low temperature, argon plasmas: corona model used in the *C*-region, *L* for the low pressure region, *H* for the high pressure region and *B* for the Boltmann-plot method region (Zhu, Pu 2010):

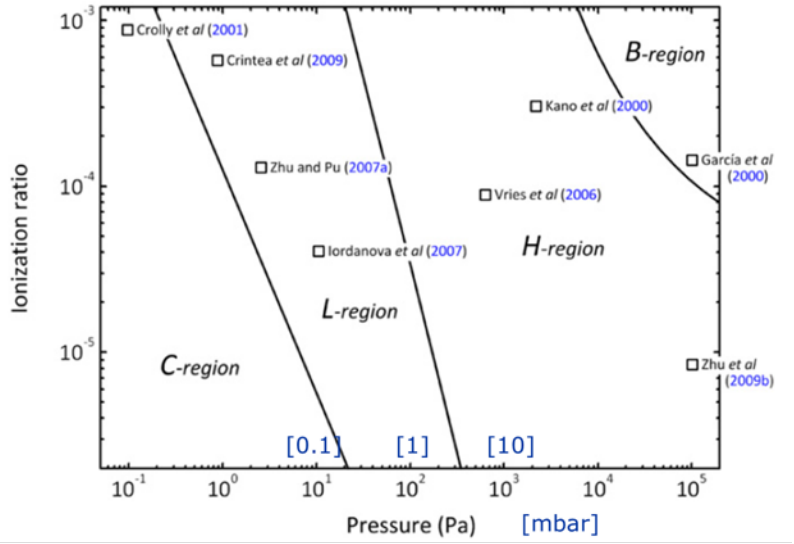

Figure 4.21 - Low temperature plasma Line Ratio models (modified) (Zhu, Pu 2010)

4.6.3. Other Diagnosis Tools

Plasma diagnosis tools for low temperature plasmas were reviewed.

- **Langmuir Probe**

The Langmuir probe, when introduced in a plasma, measures the species by intercepting the particles in their trajectory, as a result the assumption of equilibrium in its vicinity is not accurate. This introduces interferences to the measurements and a level of error. If the probe is biased negative with respect to the plasma, few electrons will be able to reach it and a sheath region with lower concentration of electrons will form around the probe. As a result the plasma bulk electrons will be still close to electrical charge equilibrium but the measurement would underestimate the electron density. The population of ions will also decrease around the vicinity of the probe but not as much as the electrons (Goldston, Rutherford 1995).

- **Power Dissipation**

Measuring the power dissipated by the plasma allows estimating important plasma parameters such as electron densities. In the case of RF excited plasmas, such as the plasma cathode investigated with this work, the dissipated power can be measured by

using a commercial thermal power meter. The probes for measuring voltage and current are connected between the power amplifier and the matching network in order to avoid changing the impedance of the setup which would have an influence on the coupling of the plasma. The power dissipated by the plasma (P_{diss}) is estimated by measuring the power with a gas flow (P_{on}) minus the power without a gas flow (P_{off}) (Hofmann et al. 2011):

$$P_{diss}(I_{rms}) = P_{on}(I_{rms}) - P_{off}(I_{rms})$$

where I_{rms} is the root mean square current. The results of the dissipated power measured in a helium plasma are presented in Figure 4.22 as a function of the root mean square current.

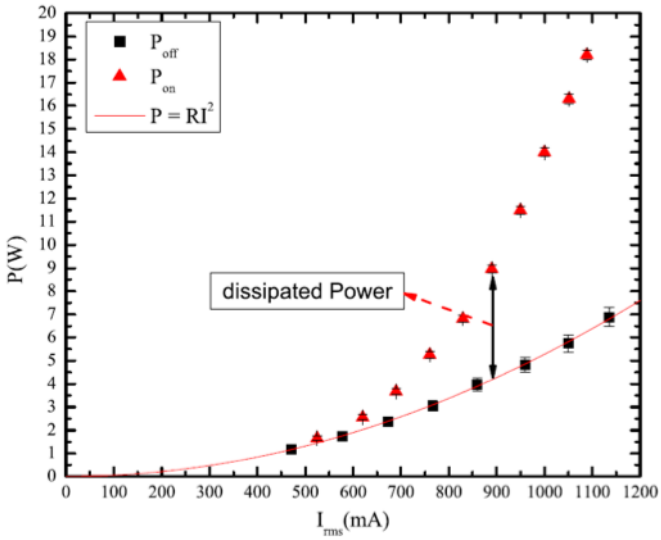

Figure 4.22 - Dissipated power as a function of the root square mean current in a helium plasma (Hofmann et al. 2011)

However, usually RF excited plasma chambers have a matching circuit connected to them in order to match the plasma at the resonant frequency so that the delivered power is maximised and reflected power is minimum. Thus, if the power dissipated by the plasma is small compared to the power dissipated by the matching circuit (which is usually the case), the power dissipated by the matching network cannot be neglected and this makes this method complicated to use (Hofmann et al. 2011).

4.7. Hollow Cathodes

The electrodes in the discharge chamber can vary in their geometry shape. From flat electrodes to hollow cathodes the plasma cathode properties are different and the use of a particular design will depend on the application. In related research, experiments have been carried out using both flat electrode designs and later hollow cathode geometry designs. Various plasma cathode electron gun designs using a hollow cathode are reviewed later in this section.

In general terms, hollow cathode geometries allow higher electron beam currents at a given voltage than a similar discharge with flat electrodes as a result of the hollow cathode effect (HCE) (Kolobov, Metel 2015). A typical hollow cathode geometry is a hollow cylinder with an aperture in one of its faces (Oks 2006). Hollow cathode glow discharges provide a simpler solution than other types of hollow cathode discharges such as Penning and magnetron discharges.

Figure 4.23 shows a diagram of a typical hollow cathode geometry and key dimensions that play an important role in the HCE. The discharge is applied between electrodes A and C.

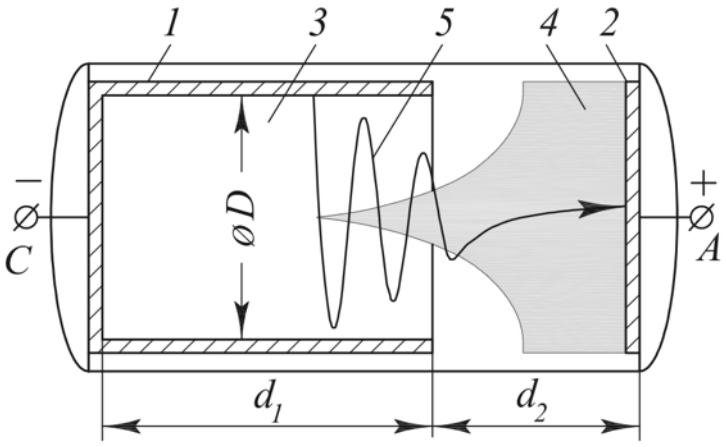

Figure 4.23 - Diagram of a hollow cathode (Kolobov, Metel 2015) showing: hollow cathode (1), anode (2), cathode sheath (3), plasma (4), and electrons oscillation path (5)

The optimum ratio of the cavity length d_1 to the cavity diameter $\emptyset D$ is $d_1/\emptyset D \approx 7-10$ (Oks 2006). The electrons mean free paths need to be bigger than the characteristic dimensions of the hollow cathode cavity for the HCE to occur (Oks 2006).

The HCE generates an exponential production of electrons. There are two main reasons why this occurs:

1) The geometry of the hollow cathode reduces the number of charged particles lost. The electrons oscillate inside the cavity and are not lost to the walls, so that their energy is spent in excitation and ionisation of the atoms (Bugaev et al. 2003).
2) The oscillations of electrons produce more ionisation and secondary electrons, however these secondary electrons are mostly generated at energies in the low energy part of the distribution, and do not have sufficient energy to further ionise atoms. However, the difference with flat electrode geometries is that those low energy electrons are generated in the sheath, thus they are accelerated by the intense sheath field and become capable of generating more secondary electrons (Bugaev et al. 2003).

- **DC plasma cathode electron gun with bias/auxiliary voltage**

There are different variations of electron gun designs using hollow cathodes depending on the application. Figure 4.24 shows a hollow cathode electron gun design that uses a hollow electrode Penning discharge chamber to create more efficient plasma density with a non-uniform plasma (Oks 2006), due to the geometry and the presence of a localised axial magnetic field. The discharge chamber consists of three electrodes: a cylindrical hollow cathode (1), anode (2), and auxiliary electrode (4). A permanent magnet (3) inducing a magnetic field of 0.06 - 0.08 T is used to confine the electrons at the end of the discharge chamber. Gas is feed at around 0.01 to 0.1 mbar pressure and a 350 - 450 V voltage discharge is used to generate a plasma. A high voltage is applied between the auxiliary electrode and the accelerating electrode (6) to extract an electron beam current through the aperture (5).

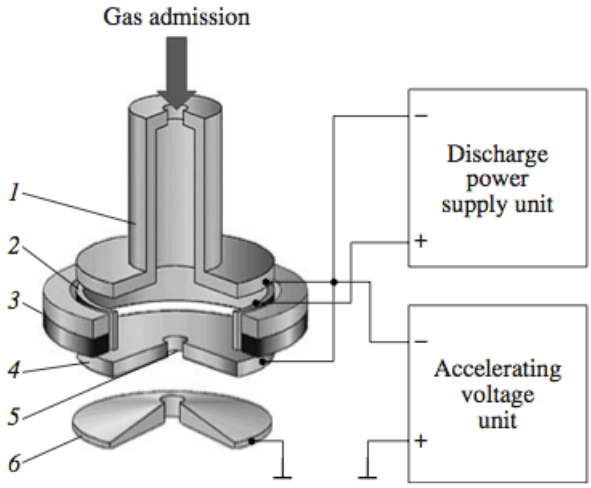

Figure 4.24 - DC plasma cathode electron source with auxiliary electrode (Kornilov et al. 2009)

With this design the high density plasma is kept only where it is needed: at the end of the plasma chamber, close to the accelerating region where the electrons are extracted. Thus the high density plasma is limited to a small region of the plasma chamber, and so is the heat load generated from it.

- **Plasma cathode electron gun with cooling system**

Figure 4.25 presents a diagram in part section of the discharge chamber in a plasma emitter electron source with cooling system. At high discharge currents the discharge electrodes will heat up but the cooling system in this design allows the operation of the cathode for prolonged periods (Belyuk et al. 2001). This electron gun design is used for welding applications (Volkov et al. 2001). The diagram shows high voltage ceramic insulator (1) with ring electrode (2) and anode assembly (3). The anode assembly consists of cermet insulators (4) welded to the anode of the discharge chamber (5). The discharge is generated in the hollow cathode (6) which is inserted in the central cermet insulator. A set of two cooling elements (7) are inside the other two cermet insulators. The electrons are extracted from the aperture in the cathode (8). Magnets (9) are used to keep a magnetic field of 0.01 T in the discharge chamber (Bugaev et al. 2003).

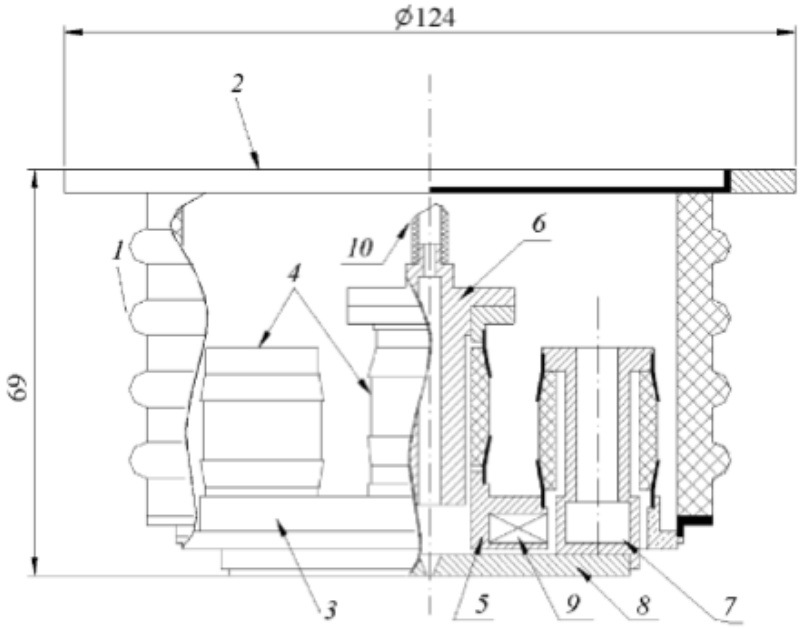

Figure 4.25 - DC excited, plasma-emitted electron source (Volkov et al. 2001)

Unlike the previous electron gun design described which was intended to reduce heat lost to the gun by having a non-uniform distributed plasma density, this electron gun generates a uniform plasma across all the chamber. Thus, instead of avoiding heating of the electrodes when the electron gun is generating high currents, more extensive thermal management must be used to enable dissipation of the heat load.

- **A high current, low pressure plasma cathode electron (Goebel, Watkins 2000).**

Figure 4.26 shows a diagram of the plasma discharge electron gun developed at Hughes Research Laboratories. The plasma is operated at low pressure (around 10^{-2} mbar) and the electron beams produced are up to 1 kA at 200 kV.

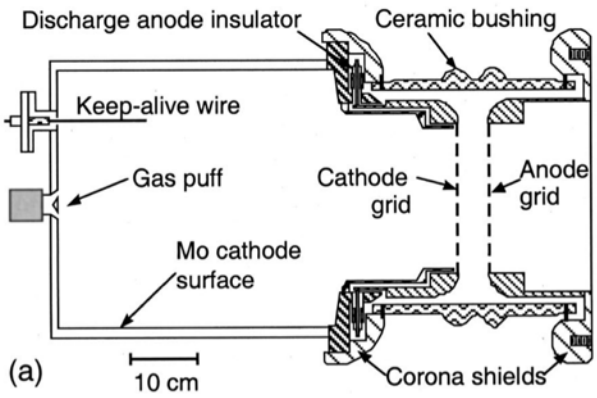

Figure 4.26 - Diagram of the discharge chamber for a high current, low pressure plasma cathode electron gun developed by Hughes research (Goebel, Watkins 2000)

This design used a gas-puff system in order to temporarily raise the plasma chamber pressure high enough to strike a plasma, and at the same time maintaining a low pressure in the accelerating region of the gun. However, the gas-puff system limits the pulse time of the beams generated to 100 μs.

In order to solve this problem the glow-discharge plasma generator was substituted by a "low-pressure thermionic discharge in a magnetic multipole confinement chamber" (Goebel, Watkins 2000). Figure 4.27 shows a diagram of this design, which generates high current beams from a plasma cathode at pressures as low as 10^{-4} mbar. This electron gun design produced beams of up to 200 A at up to 120 kV and allowed a pulse repetition frequency as high as 1.5 kHz. The beam current generated was up to 30 times higher than with the puffer design, and the pressure of the plasma cathode was 10-50 times lower (Goebel, Watkins 2000).

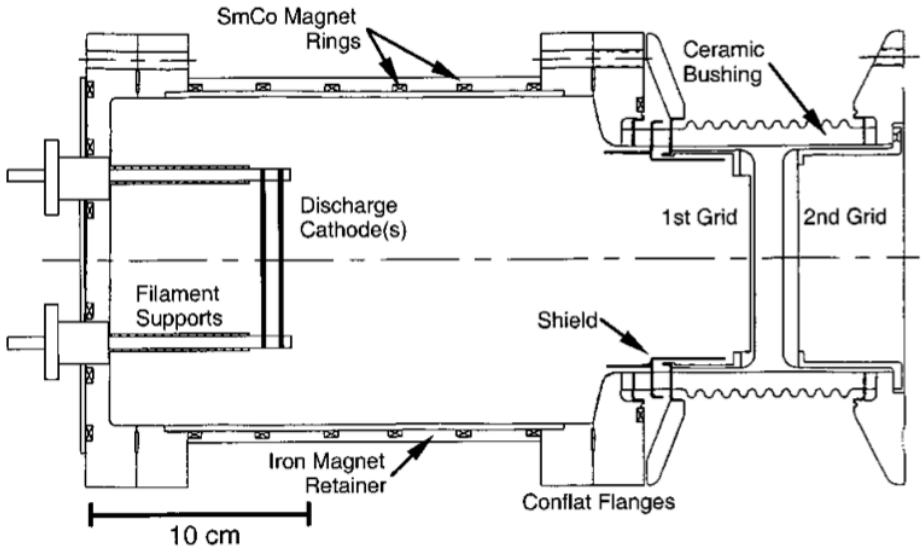

Figure 4.27 - Diagram of a plasma cathode gun with a thermionic discharge and magnets for electron confinement (Goebel, Watkins 2000)

There are key parameters in this design that are also of importance in the plasma cathode design investigated in related work at TWI:

- Low pressures are needed for keeping low pressure in the acceleration region.
- Higher pressures are needed at the time to strike a plasma, however if that pressure is kept during the operation of the electron gun this may cause high voltage breakdown in the acceleration region. On the other hand, if a puffer is used, pulsing at less than 100 μs is not possible. This may not be a limitation in the applications for the electron gun investigated in related work at TWI (Ribton et al. 2015), which is for material processing where switching times of the order of μs is considered rapid pulsing.
- The gas used in the discharge is xenon. Lighter gases allow the ions to have higher mobility, however, it also means that the ionisation cross section is lower. Thus, the type of gas used also has an influence on the ionisation level.

Hollow cathode discharges can be operated both in pulsed or continuous mode. A primary anode biased with a DC accelerating potential is used to control the electron emission without stopping the discharge. Details on this design from NRL, which has produced beams of up to 80 mA are given by (Cothran et al. 2015).

4.8. RF Excited Plasma Cathode Guns

An RF signal can also be used for generating a plasma, as is the case in the plasma cathode gun to be investigated in related work at TWI. The design of the RF plasma cathode electron gun (del Pozo et al. 2014a, del Pozo et al. 2014b) will be described in this section.

The benefits of RF excited plasma cathodes are that modulation of the RF signal can be used for current modulation of the electron beam or rapid switching of the beam, which can be very useful for some material processing applications. For example, in EB additive manufacturing this feature is beneficial as it would allow the beam to be rapidly switched off whilst being moved from one place to another in the powder bed, avoiding unwanted melting or charging of the powder.

Figure 4.28 shows a diagram of an RF excited plasma electron source. The plasma is generated with a 13.56 MHz frequency from argon flowing at 15 sccm (Longmier et al. 2006).

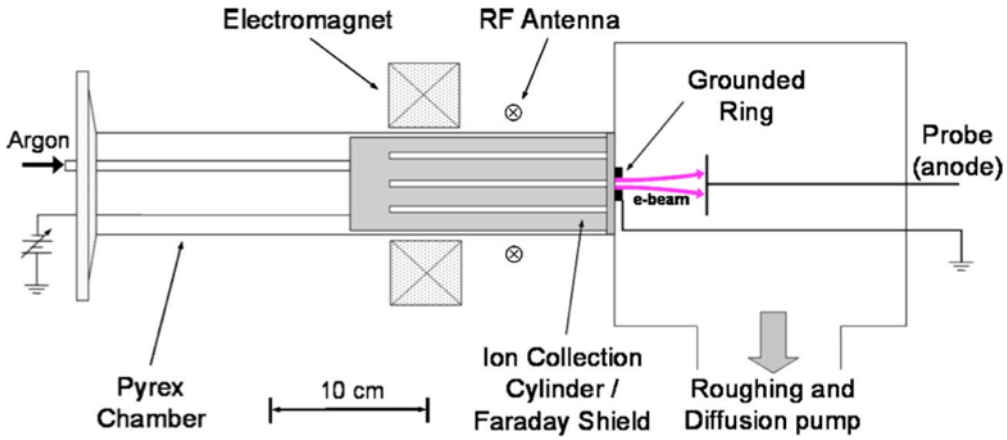

Figure 4.28 - Diagram of the non-ambipolar RF excited electron source (Longmier et al. 2006)

In their experiments, plasma density increases with RF power. The plasma electron density is 3×10^{12} cm^{-3}. In the plasma cathode gun investigated in this work, an increase of electron beam current with RF power was also observed in the experimental work.

4.9. Plasma Confinement

The first effect of a magnetic field on a plasma is that it makes the electrons and ions oscillate in orbits around the magnetic field lines (Hutchinson 2005). The radius of the oscillation r is termed the Larmor radius:

$$r = \frac{mv}{eB}$$

Where m is the particle (electron or ion) mass, v is its velocity, e is the particle charge and B is the magnitude of the magnetic field. As the Larmour radius is a lot larger for ions in a plasma as their momentum is much higher, the effect of the magnetic field is stronger on the electrons while the ions will be almost unaffected.

4.10. Industrial Applications of Plasma Cathode Electron Guns

Plasmas are used as particle sources, either for generating electron beams or ion beams such as plasma cathodes used for ion thrusters (Goebel, Katz 2008, Goebel, Watkins 2000). Applications of hollow cathodes include light sources, high power electric switches and electron sources. Applications for electron beams generated from plasmas include those applications for thermionic electron guns (reviewed in Chapter 2) such as welding, cutting and electron beam melting. Ion sources are used for other applications such as deposition of coatings, medical applications or ion propulsion.

Welding is one of the most used applications of plasma electron guns (Bugaev et al. 2003). This is used for sealing fuel encapsulations of nuclear power stations (Volkov et al. 2001). A plasma cathode diode for metal surface modification (Kang et al. 2015) is another more recent application in which the application benefits from the availability of operating at low vacuum.

4.11. Summary

In this chapter plasmas and their fundamental parameters have been introduced. The most common diagnosis methods have been described, with emphasis in the methods used in low temperature, low pressure plasmas as this is the type of plasma of the plasma cathode in this work. There are very different types of plasmas depending on the plasma density, pressure, temperature, size, excitation source or any other of the

characteristic parameters of a plasma. Thus, the plasma chamber and plasma system needs to be designed for the particular application that will be used for.

Optical emission spectroscopy has been selected as the diagnosis method for the low temperature plasma investigated in this work. Advantages of this widely known technique are its simplicity, and non-intrusive and easy to use setup. However, interpretation of the data obtained from the emission spectra is complex as low temperature low pressure plasmas are not in thermal equilibrium. There are other methods and the most relevant are briefly described.

Thermionic cathode electron beam guns are widely used for material processing equipment. However, cathode life is limited due to material evaporation and erosion. This can be avoided by using plasma as the cathode or electron source. Additionally, in RF excited plasma guns pulsing can be used to control the EB power by modulation of the RF signal. Pulsing in RF plasma guns is over 10 times faster than with conventional guns, which is very beneficial for materials processing applications, e.g. additive manufacturing of objects in metal.

In summary, there is no evidence that plasma cathode guns have any significant limitations compared to thermionic electron guns. In contrast, plasma sources provide solutions to the main problems with conventional guns. This includes operation in a coarse vacuum environment, long lifetime and high reliability, as maintenance from thermionic cathode problems is eliminated (Bugaev et al. 2003).

Chapter 5 : Experimental Setup and Design Process

This chapter describes the design and development of the RF plasma cathode gun and the experimental test rigs used to investigate it.

5.1. Introduction

A separate experimental rig was developed to focus on the characterisation of the plasma. A second experimental rig was developed with this work to carry out spectroscopic measurements on the plasma while a beam current was extracted from it. Both experimental rigs and the plasma parameters that govern beam quality are described in this chapter.

5.2. RF Plasma Gun Design Description

The plasma EB gun consisted of a plasma chamber used as a cathode or electron source, an RF plasma generation unit, and an electron acceleration unit for extracting the electrons from the plasma chamber and accelerating them to form a beam. Some of the parts in the EB gun system were modified while this thesis work was carried out such as the gas feed system and the plasma chamber geometry. These modifications will be specified later in this chapter. The main elements in the plasma gun system (plasma chamber, plasma generation unit and electron extraction unit) remained the same. Figure 5.1 shows a schematic diagram of the plasma EB gun system from the patent (Ribton, Sanderson 2015).

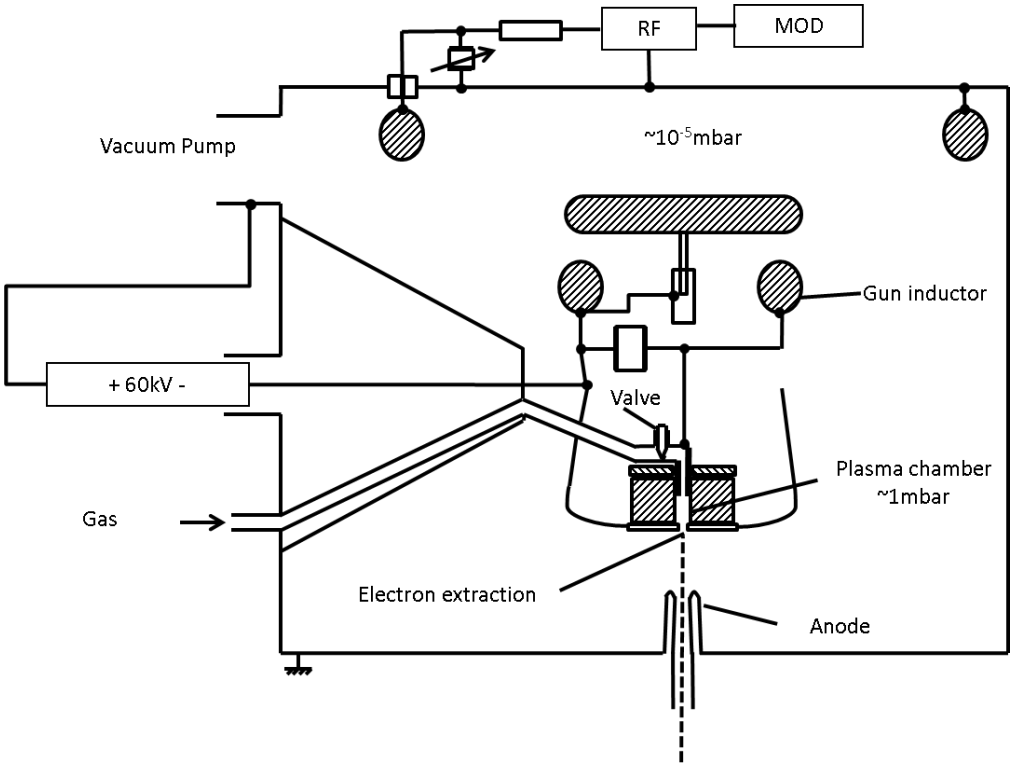

Figure 5.1 - Schematic cross-section of the plasma cathode EB gun design in the vacuum chamber. Modified from (Ribton, Sanderson 2015)

Figure 5.2 is a circuit schematic of the plasma EB gun showing the plasma chamber (12) and the vacuum chamber (8). The plasma generation unit comprised an RF function generator and RF amplifier (5) which were used to apply RF power to the plasma chamber through a resonant circuit. The plasma chamber was fed with gas, typically argon, and was maintained at a pressure where the gas readily breaks down. The resonant circuit consisted of RC1 and RC2, which were tuned at the same frequency and were configured as parallel LC circuits. Both the first antenna (10) and the second antenna (11) were single turn inductors. The quality factor of the coupled resonant circuits was high enough (at least 500) so that the voltage of the induced RF signal was substantially higher than the output voltage on RC1. The values of the parallel capacitors were chosen so that the system was at its resonant frequency. This resonant frequency of the gun could be changed by finely tuning its inductance. The power was applied to the transmitter circuit (RC1). The RF current through the first antenna (10) induced a voltage in the second antenna (11) of the receiver circuit (RC2). The plasma chamber (1) had an inlet (2) for the ingress of gas (G), a hollow electrode (3) and a diaphragm plate with an aperture (4). RC2 was connected to the plasma chamber

electrodes 3 and 4 (lines i and ii respectively). When RF power was applied, plasma was generated in the plasma chamber, where the gas was at a pressure of ~0.1 mbar. The plasma chamber contributed to the capacitance of the second resonant circuit. When a plasma was excited within the chamber, the loading of the secondary circuit increased and this lowered the circuit's Q-factor, lowering the plasma voltage but making more current available for sustaining the plasma (Ribton, Sanderson 2015).

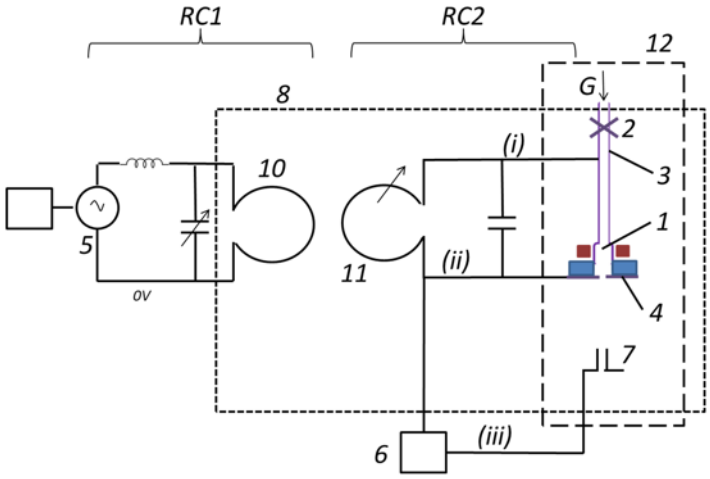

Figure 5.2 - Circuit schematic of the plasma gun system showing primary (RC1) and secondary (RC2) (Ribton, Sanderson 2015)

The electron extraction unit consisted of a DC power source (6) applying a high voltage between the plasma chamber and an anode (7) on lines (ii) and (iii) respectively. The electrons in the plasma chamber were accelerated and extracted through (4) to form a powerful beam that was used for processing metal. The vacuum chamber (8) was at a pressure of 10^{-5} mbar in order to maintain electrical isolation between the electrodes.

5.3. Vacuum System and Plasma Chamber Pressure Measurement

A diagram of the vacuum system in the EB generation experiments is presented in Figure 5.3.

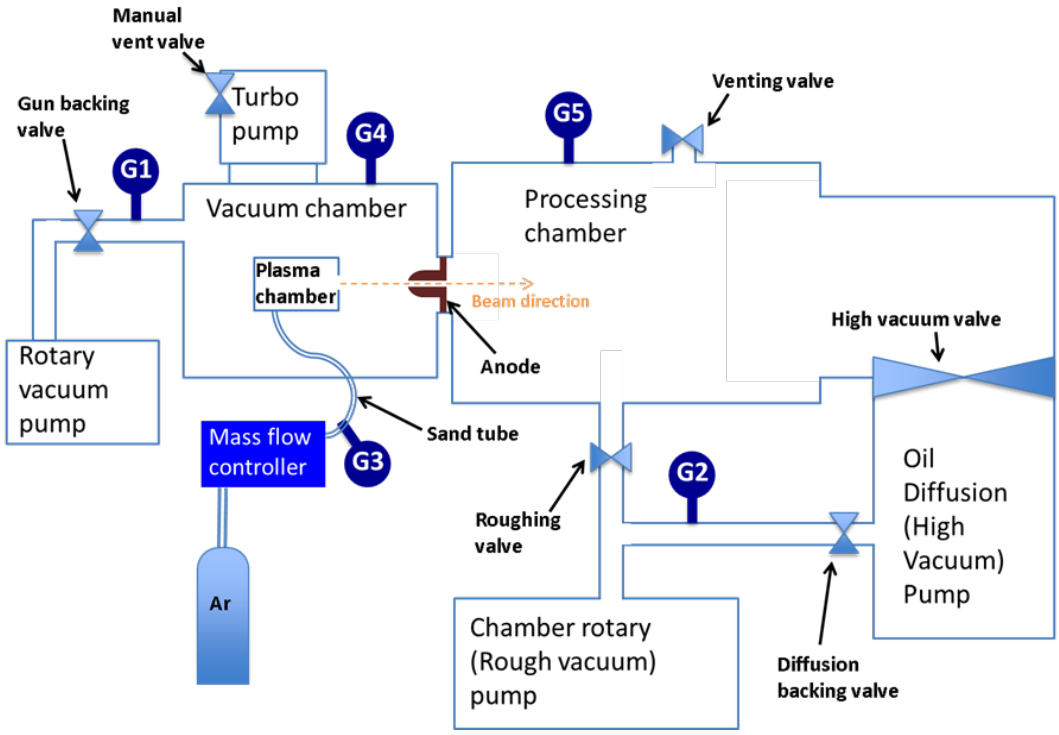

Figure 5.3 - Diagram of the electron beam gun system EB6

As seen in Figure 5.3 the vacuum system had several chambers and made use of differential pumping to keep the gun chamber at the lowest pressure possible (10^{-6} - 10^{-5} mbar). The pressure was monitored at different points in the system with gauges G1 to G5 (in Figure 5.3):

- G1 – Gun backing pressure (~10^{-2} mbar)
- G2 – Diffusion pump line pressure (~10^{-2} mbar)
- G3 – Foreline pressure at output of mass flow controller (0.2 to 0.8 bar)
- G4 – Gun vacuum chamber pressure (10^{-5} mbar to 10^{-4} mbar)
- G5 – Processing chamber pressure (10^{-4} mbar)

Following Paschen's law (Paschen 1889); plasma will most readily strike at the appropriate conditions given by the product of pressure and discharge gap (pd), thus the vacuum system had different pressure regions in order to keep the plasma only in the plasma chamber. Plasma had to be avoided in the vacuum chamber (which would have caused arcs from the HV to ground) and in the foreline gas pipe that was used to feed the gas into the plasma chamber. In order to meet these requirements, the vacuum chamber operated at the lower *pd* end of the Paschen curve, whereas the mass flow

controller side operated at the higher end of the Paschen curve. Figure 5.4 shows a diagram of the different chambers and pressure regions of operation.

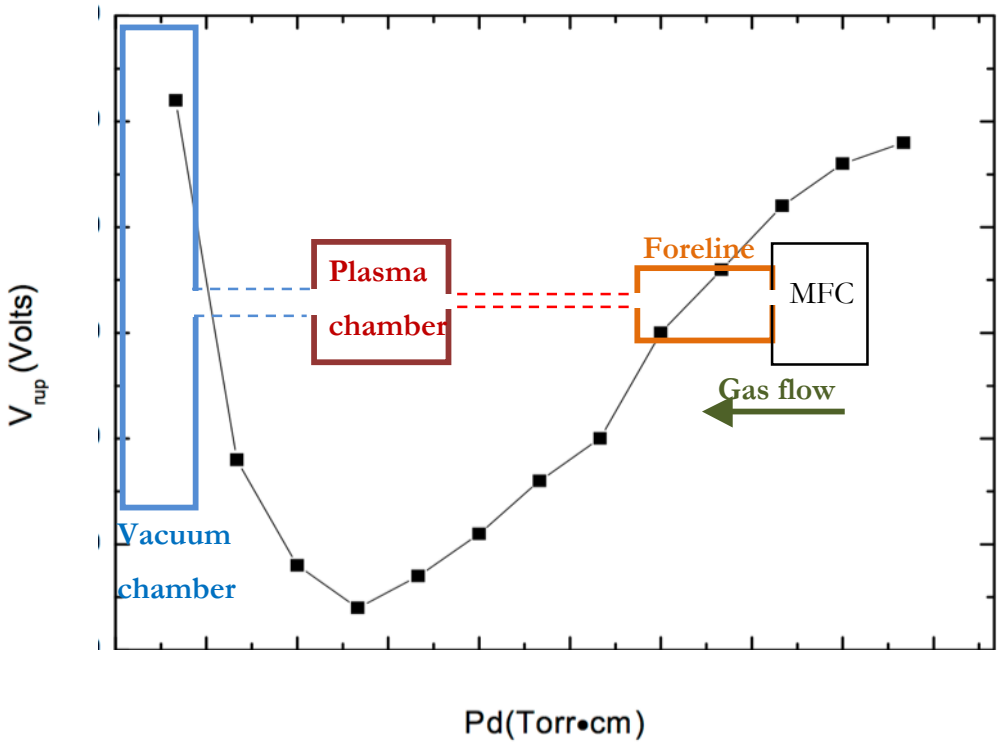

Figure 5.4 - Paschen's curve obtained varying the distance between copper electrodes. Modified from (Torres et al. 2012)

At steady state, the pressure in the vacuum chamber was dependent upon the gas flow rate and the chamber pump speed, while the pressure in the plasma chamber was dependent upon the gas flow rate and the diaphragm aperture diameter. When a needle valve was used the pressure in the foreline was dependent upon the gas flow rate and the needle valve setting.

There were some modifications carried out in the plasma gun body to make the system more reliable, with a more accurate, fast and easy pressure control:

→ A first design used a needle valve to keep over atmospheric pressure in the foreline while dropping the pressure in the plasma chamber. This design had a very slow response and long waiting times (over 30 minutes) were required for the plasma chamber pressure to get to steady state as it took a long time

at a fixed flow rate for the foreline pressure to be raised or lowered to its new stable value.

→ In a later design the needle valve was eliminated from the system. Instead, a sand pipe was used between the mass flow controller and the plasma chamber (at 10^{-2} to 10^{-1} mbar). The sand pipe was a PTFE tube of 1.5 mm internal bore that was packed with glass spheres of 80 μm diameter. The sand pipe provided a low conductance gas path from the mass flow controller to the plasma chamber. In comparison to a foreline, this solution reduced the gas volume between the high pressure side (mass flow controller) and the low pressure side (plasma chamber). This allowed the plasma chamber pressure to reach steady state much faster (in a few minutes). At the same time it avoided voltage breakdown without the need for high pressure in the gas feed. This was because the distance between the glass spheres was very short, making the *pd* product too low to allow breakdown.

The plasma pressure was a key parameter that affected the plasma characteristics, and thus the characteristics of the electron beam generated. The pressure in the plasma chamber was both measured and calculated. Measuring the plasma pressure was not a straightforward task, as the plasma chamber was inside a vacuum chamber, as showed previously in this chapter. Figure 5.5 shows a diagram of the pressure measurement setup.

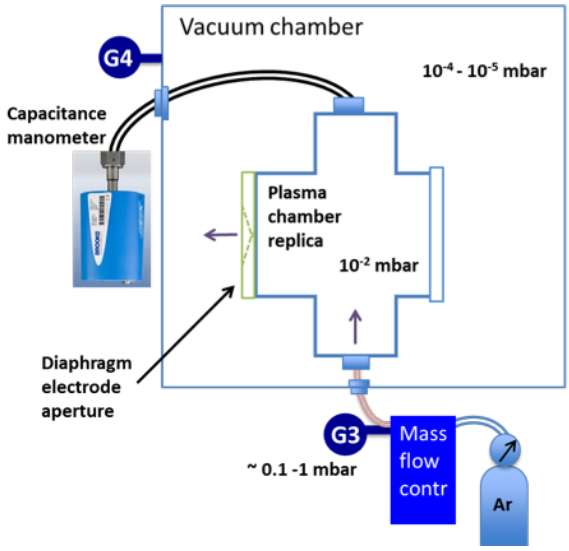

Figure 5.5 - Plasma chamber pressure measurements setup

The pressure in the plasma chamber was measured without generating a plasma. A capacitive gauge was used for the measurements. A capacitance manometer used (CMX2C0122), with an accuracy of 0.15% of the reading and 1.33 mbar full scale, operated across a range of four decades as shown in Figure 5.6.

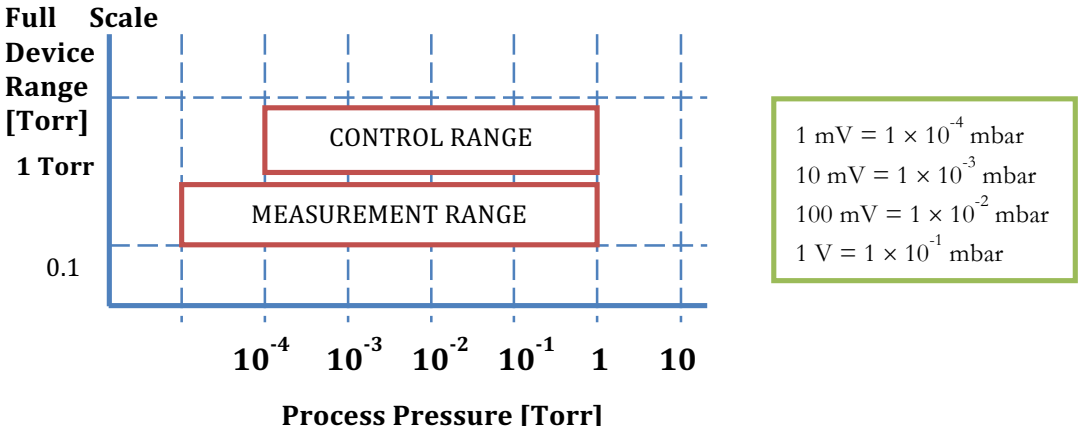

Figure 5.6 - Capacitance manometer (CMX2C0122) range

The plasma chamber pressure was measured at different gas flow rate values with diaphragm aperture diameters from 0.7 mm to 2 mm, which was the range used in the EB and plasma generation experiments. Foreline pressure (at the hose between mass flow controller and plasma chamber) and vacuum chamber pressure were monitored with gauges G3 and G4 respectively. Figure 5.7 is a graph with the pressure measurements at the different aperture diameters.

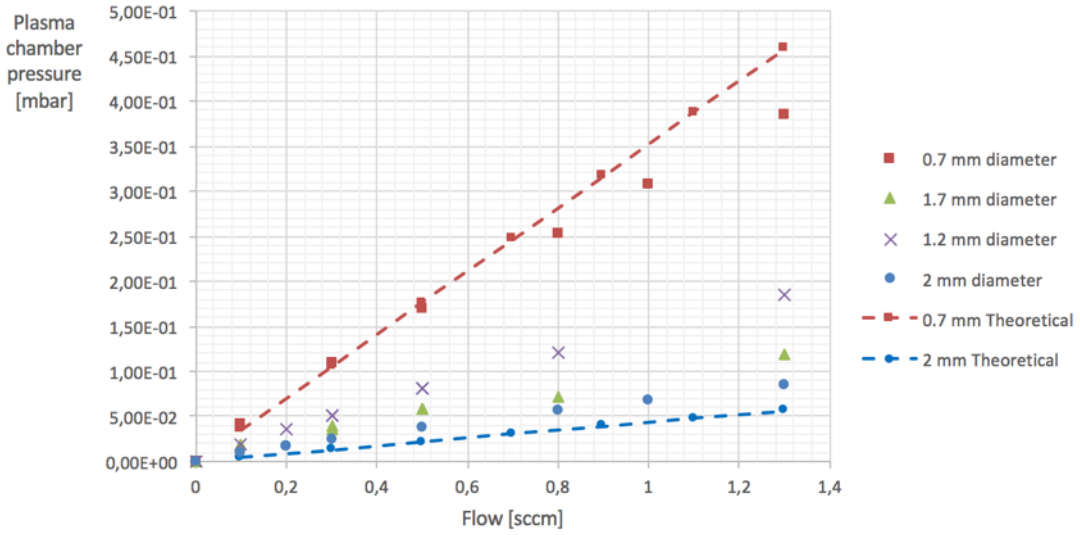

Figure 5.7 - Plasma chamber pressure as a function of gas flow for different diaphragm aperture diameters

The dotted lines in Figure 5.7 represent the calculated values for the indicated aperture diameters.

Summarising, the conclusions after the pressure measurements were the following:

- The plasma chamber pressure for a given flow value decreased with increasing aperture diameter.
- The vacuum chamber and foreline pressures remained unaffected by the aperture size.
- The pressure measurements and calculations were in agreement and within the same order of magnitude. The experimental values were higher, which can be explained as it was not just a circular aperture (as taken into account in the calculations), but had some length as well which would decrease the conductance.
- The plasma chamber pressure values obtained for given flow rates were used to estimate the plasma pressure during the experiments (when a gauge was not connected to the plasma chamber). The measured pressure values were also used as input in the CCP plasma model of the plasma chamber in VSim which is discussed in Chapter 7.

5.4. Plasma Gun Body

The plasma gun design has developed and changed during the work carried out. Figure 5.8 is a picture of the plasma gun body in the vacuum chamber as it was initially showing first antenna (1) and second antenna (2) in the RF coupled circuit, needle valve (3), anode (4), high voltage insulator (5), and parallel capacitor (6).

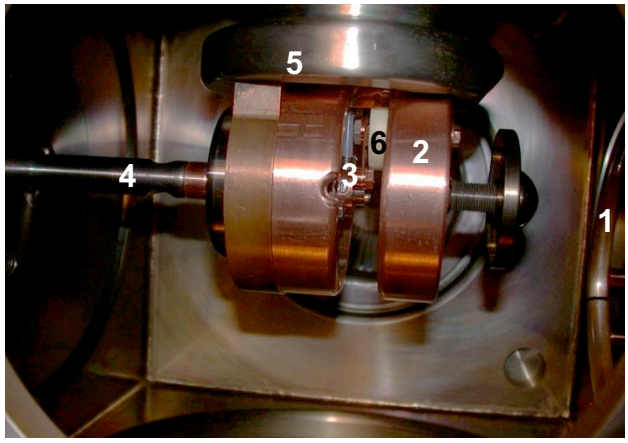

Figure 5.8 - Plasma gun body in EB vacuum chamber (del Pozo et al. 2014)

Figure 5.9 shows a 3D CAD model of the initial geometry of the plasma chamber, which had a 1 mm diameter hollow tube as the hollow electrode, in contrast to larger hollow electrode diameters in later designs.

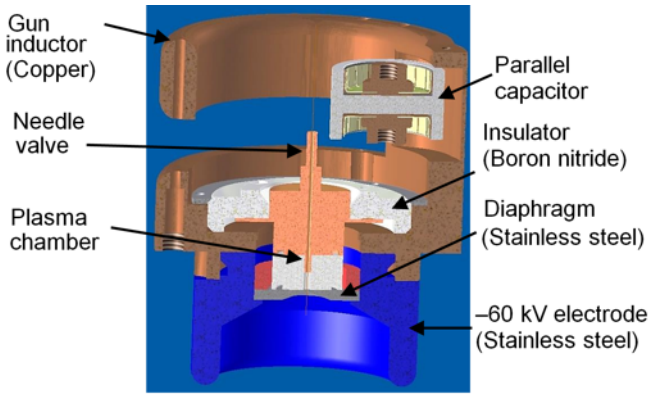

Figure 5.9 - 3D CAD model half section of the plasma gun body (Ribton, Sanderson 2015)

Preliminary plasma chamber designs used a parallel plate geometry but in later trials more complex electrode geometries were employed. The plasma chamber design was gradually modified for the following reasons:

- To add or modify the design features that would result in increasing electron density and thus electron beam power.
- To allow taking spectroscopic measurements and/or EB current measurements.

The main modifications were:

- Plasma chamber electrodes: flat vs. hollow – the first designs had flat electrode geometries with a hollow tube on the top electrode, as shown in Figure 5.10. However, the hollow tube diameter was 1 mm, which was not big enough for the hollow cathode effect to happen, thus this electrode geometry is referred to as a flat electrode geometry in this work.

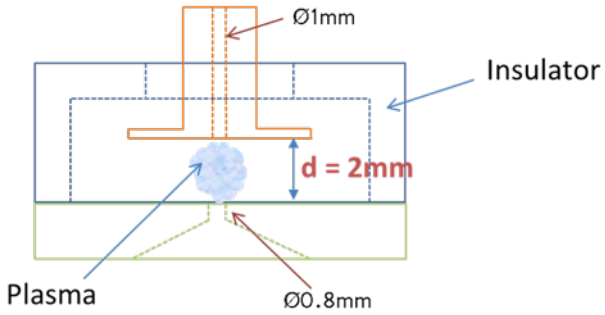

Figure 5.10 - Initial plasma chamber design with boron nitrade insulator

Later designs included larger diameter hollow cathodes, as shown in Figure 5.11:

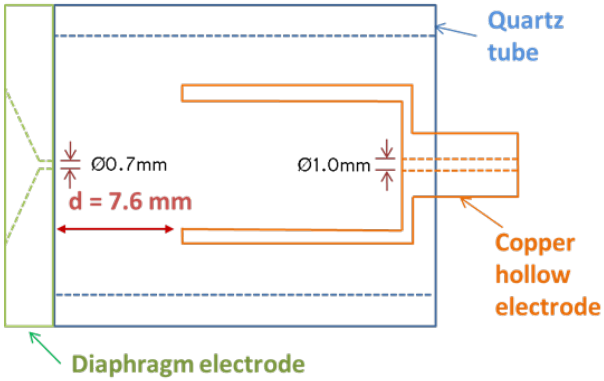

Figure 5.11 - Plasma chamber design with hollow electrode

Preliminary experiments showed that hollow cathodes produced higher EB currents than flat electrode geometries.

- Plasma chamber insulator – This part of the plasma chamber was modified in size and material. Figure 5.10 shows the plasma chamber with a boron nitrade insulator. This design was used with flat electrodes as a starting point. The short distance between the electrodes meant higher pressures were needed to strike a plasma than with the later design, and as a result, the boron nitrade piece would

often become coated with metal and needed cleaning. The diaphragm aperture had to be kept small (under 1 mm diameter) to maintain the high plasma chamber pressure. If the aperture diameter was increased above 1 mm the pump speed was insufficient to avoid the vacuum chamber pressure increasing to a level where high voltage breakdown between the gun body and the anode occurred.

Later plasma chamber insulators were made of quartz, so that the plasma could be observed through a hole in the gun body. One of the quartz plasma chamber designs is shown in Figure 5.12.

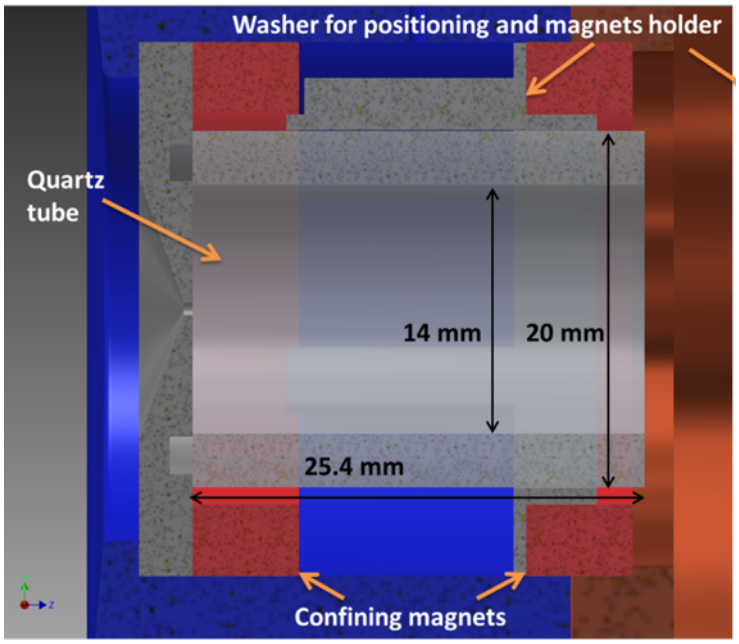

Figure 5.12 - Quartz plasma chamber design

Figure 5.13 shows the viewing aperture drilled on the HV electrode, to allow looking at the plasma through the quartz chamber with the optical spectrometer:

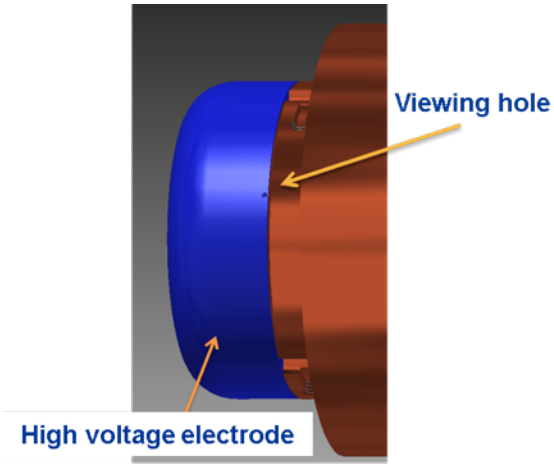

Figure 5.13 - Viewing aperture on HV electrode for plasma optical measurements

- Diaphragm aperture – Experimental work showed that increasing the aperture diameter generally resulted in higher EB currents extracted from the plasma chamber. However, there were limitations in the size of the aperture due to the following:
    - Increasing diaphragm aperture increased vacuum chamber pressure if the plasma chamber pressure was maintained by increasing gas flow. Thus, electrical breakdown was made more likely due to the penetration of plasma from the discharge region into the accelerating gap (Litovko 2008).
    - The pressure in the plasma chamber decreased with the size of the aperture for a given gas flow rate. Thus, a very large aperture may result in the plasma chamber pressure being not high enough to strike a plasma.
- Spacer for longer plasma chamber – Figure 5.14 shows one of the later plasma chamber designs, with a longer plasma chamber. This made the distance between the electrodes larger, which allowed, following Paschen's law, lower plasma chamber pressures to generate a plasma at the available excitation power. This was beneficial as it helped to keep the electrodes clean from metallic coatings and also allowed having larger diaphragm apertures without increasing the vacuum chamber pressure to values that may cause HV breakdown.

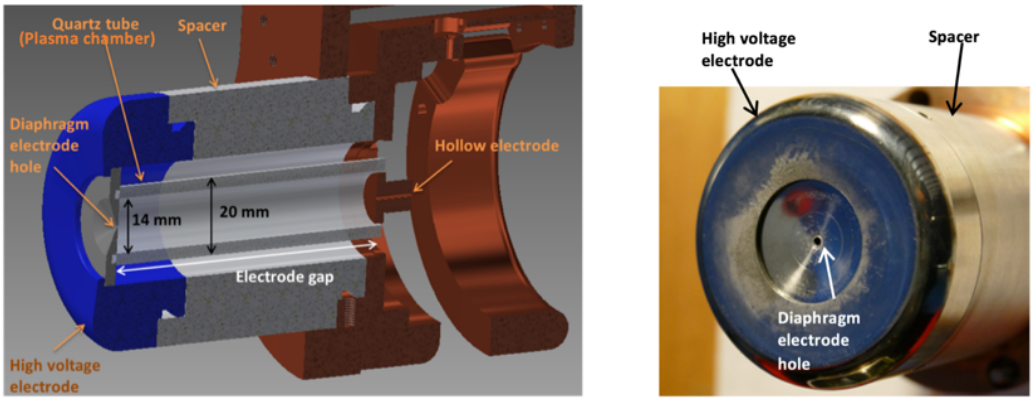

Figure 5.14 - Plasma cathode chamber CAD model and manufactured gun

- Magnets and magnet holder – The use of magnets increased the EB current extracted in most of the cases. However, optimising the value and position of the magnet was critical to achieve this. Figure 5.15 shows two ring magnets attracted to each other around a quartz plasma chamber, and a holder used to keep them apart.

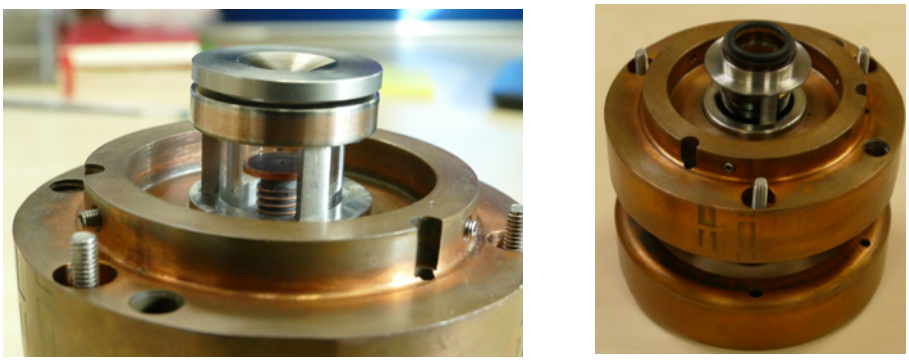

Figure 5.15 - Plasma chamber with magnets and magnets holder

The magnets used were sintered neodymium iron boron magnets with the following specification:

- 30 mm outside diameter × 22 mm inside diameter × 6 mm thickness
- The axial magnetic field is 1.32 – 1.37 T measured 5 mm from the magnet surface

5.5. Experimental Rig

In this work two main experimental rigs were used: the first one was used to look at the spectra of the plasma in a vacuum chamber (Figure 5.16), and the second one incorporated a HV PSU so that the plasma spectra was studied at the same time as an

electron beam was generated. The aim was to correlate optical emission spectroscopy with electron emission characteristics.

5.5.1. Test Rig 1 – Spectroscopic Measurements

The first experimental setup (Figure 5.16 and Figure 5.17) included a spectrometer and optical fibre that were used to record the emission spectrum of the plasma without generating an electron beam. The gas flow into the plasma chamber was kept constant by a mass flow controller. The gas pressure was dropped (P1 to the plasma pressure) across a needle valve (later substituted for a sand pipe). The plasma chamber was leaking gas through a 0.5 mm diameter aperture in the diaphragm into the vacuum chamber, which was at a pressure (Penning gauge P2) of 10^{-5} to 10^{-6} mbar. The pressure in the plasma chamber can be calculated from the monitored gas flow.

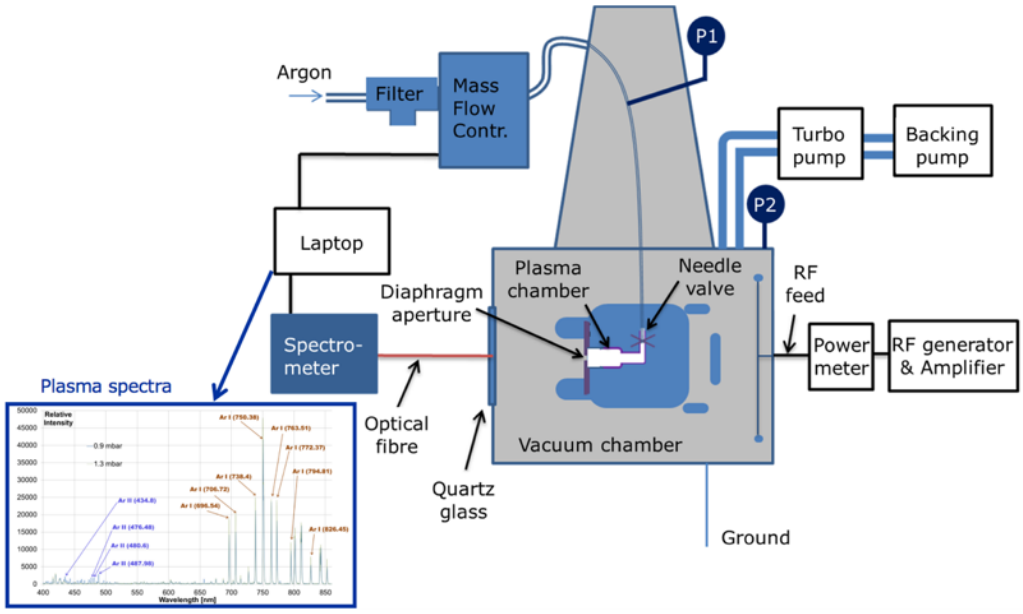

Figure 5.16 - Diagram of experimental setup for optical emission spectroscopy measurements

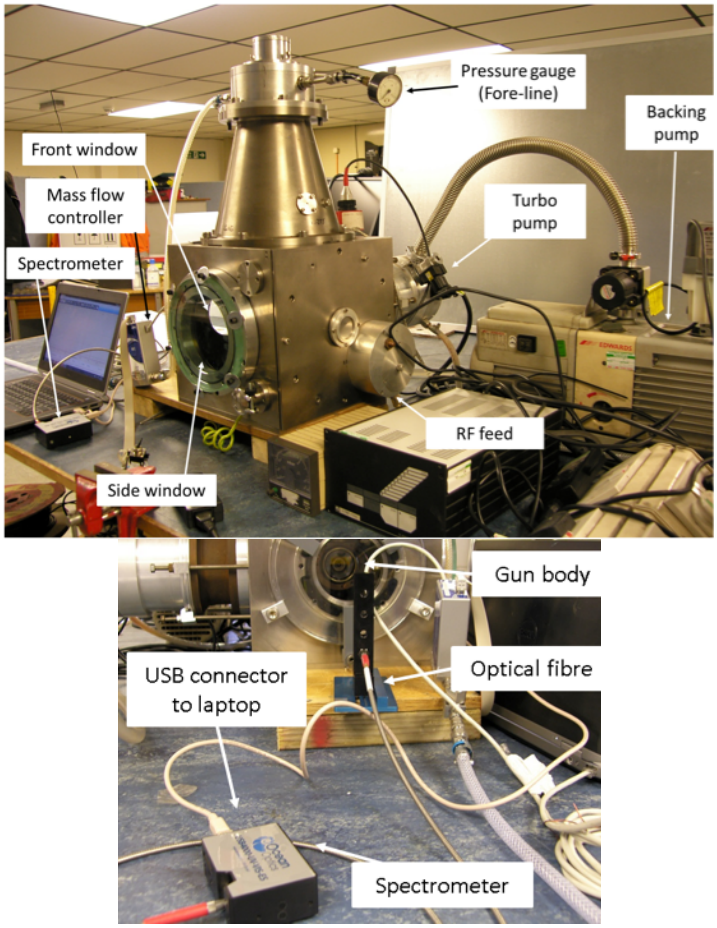

Figure 5.17 - Pictures of experimental setup for optical emission spectroscopy measurements

The radiation spectrum of the light emitted from the plasma was recorded. The optical fibre was pointing along the beam axis of the plasma chamber. With this set up, key plasma parameters could be monitored for different gases. Figure 5.18 shows an example of the measurements obtained in the experiments with argon. The relative intensities of the spectral lines from the argon plasma are shown in black. The red lines are a reference for argon spectral lines from the spectrometer software database.

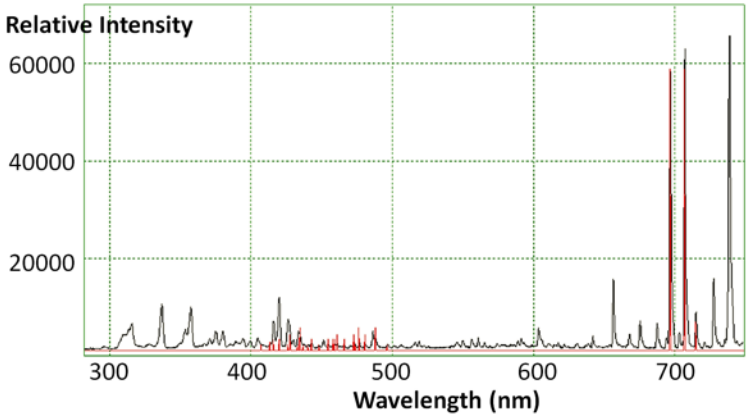

Figure 5.18 - Emission spectra of a plasma cathode in the plasma cathode gun

5.5.2. Test Rig 2 – EB Current Measurements Vs. Spectroscopic Measurements

In a second experimental rig a HV PSU of –30 kV to –60 kV was added to the first experimental setup and used to extract a beam from the plasma chamber. An anode with a Faraday cup attached to it was designed and manufactured, as detailed in Figure 5.19. The EB was generated from the front of the HV electrode (blue) and accelerated towards the anode (to the left in this diagram).

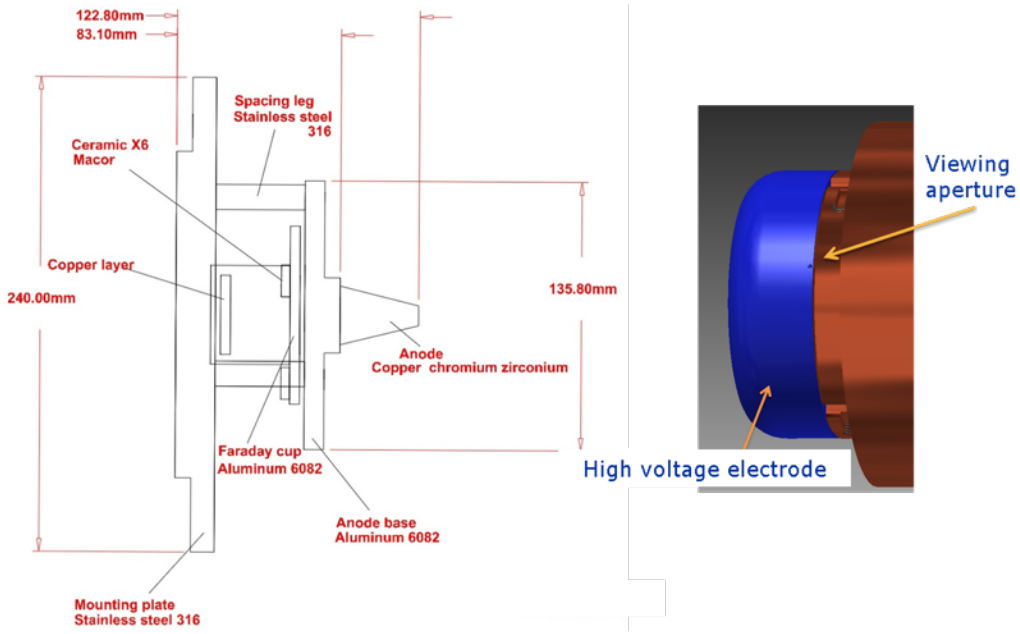

Figure 5.19 – Anode and faraday cup assembly (left) for EB current measurements and side aperture for spectroscopic measurements

In this setup the optical fibre was pointing at the side of the electron gun, so that the spectra measurements were collected looking at the side of the plasma chamber. Optical

emission spectroscopy and EB current measurements were carried out simultaneously. These experiments allowed evaluating the important plasma parameters that contribute to increasing EB current. Information included in the line spectra of optical emission can be used for calculating or inferring plasma parameters such as electron density and temperature (Fantz 2006).

5.5.3. Optical Spectrometer Calibration

The spectrometer used was an Ocean Optics USB4000-UV-VIS-ES model which has enhanced sensitivity. Table 5.1 and Table 5.2 show the optical spectrometer and optical fibre parameters respectively. A 5 mm diameter and 10 mm focal length collimating lens were used when the light emitted was too weak for the detectors.

Table 5.1 – Optical spectrometer USB4000-UV-VIS-ES model specifications

Wavelength range	200-850 nm (UV and visible measurements)
Integration time	3.8 ms-10 s
Optical resolution	1.5-2.3 nm FWHM
Fiber optic connector	SMA 905 to 0.22 numerical aperture single-strand fiber
Signal-to-noise ratio	300:1 (full signal)

Table 5.2 – Optical fiber specifications

Diameter	600 μm
VIS-NIR operating wavelengths	400-2200 nm
Numerical aperture	0.22 +/- 0.02
Full angle	25.4° (Acceptance angle = 12.7°)

The Oceans Optics spectrometer that was used for the spectroscopic measurements was supplied with wavelength calibration by default. A relative intensity calibration of the spectrometer was carried out to compensate for wavelength dependent CCD sensitivity and the effect of colour filters. This calibration was needed when comparing measured signal intensity at one wavelength with another. All the elements that were in the optical path in the experiments had to be present in the calibration test. Figure 5.20

shows a diagram of the elements that were used in the relative intensity calibration of the spectrometer for the RF plasma cathode setup.

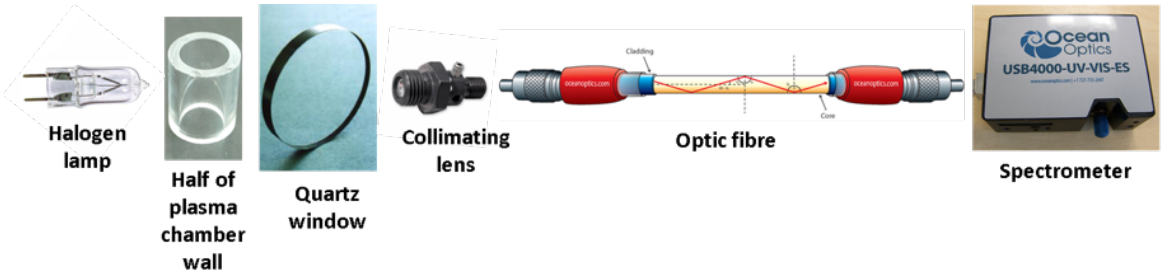

Figure 5.20 - Diagram of the elements in the optical path that were used in the relative intensity calibration

In order to carry out a relative intensity calibration a halogen lamp of a known colour temperature was used. The spectrum of the light emitted by the halogen lamp was collected in irradiance mode and a calibration file was generated by comparing the signal in scope mode to the shape of the spectroscopy curve emitted by the lamp with known colour temperature. Figure 5.21 shows the spectrum of the halogen lamp in scope mode (before an intensity calibration) and the spectrum after the relative intensity calibration.

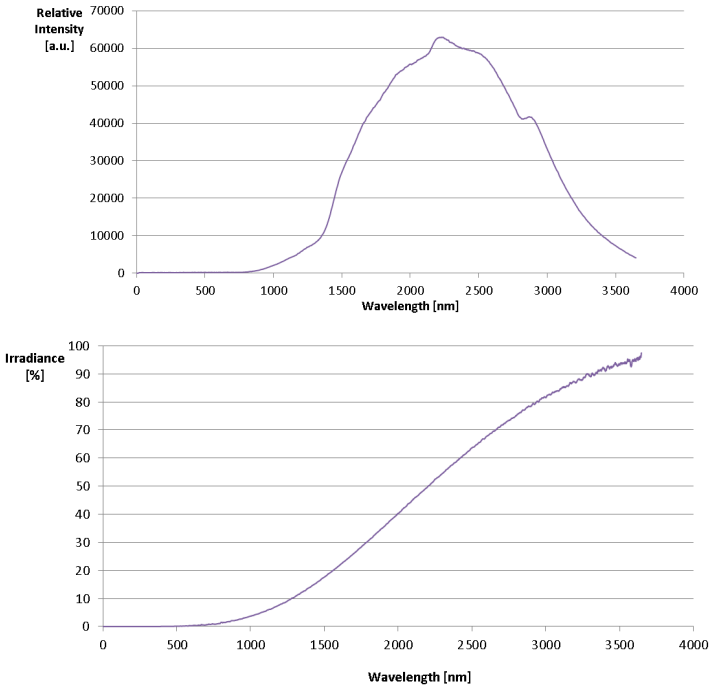

Figure 5.21 - Spectrum of a 2800 K colour temperature halogen lamp in scope mode before relative intensity calibration (top) and after calibration (bottom)

5.6. Summary

The plasma chamber design was modified to optimise the EB gun for maximum current generation. The later designs had a longer plasma chamber, hollow cathode geometry, large diaphragm aperture (up to 2 mm diameter) and magnets and magnet holder to locate them in an optimum position. The setup was also modified (adding a quartz chamber and viewing hole) in order to carry out spectroscopic measurements at the same time of generating an electron beam.

The plasma chamber pressure was accurately measured, which allowed choosing the right plasma model for experiments and also it was a vital input for the simulations. The measured values agreed with the calculated values.

Flat electrodes were used for comparison with plasma chamber simulations. However, the electron emissivity obtained with this design was limited.

In preliminary experiments some of the parameters that affected the plasma cathode were identified. These were plasma pressure, RF power, electrodes shape and gas type. In the following chapter these parameters are investigated further to find an optimum design.

Chapter 6 : Electron Gun Optimisation through Spectroscopic and EB Current Measurements

This chapter presents the experimental work carried out on the plasma cathode gun looking at the different parameters that affect the generated electron beam in order to optimise the plasma cathode electron gun. The important parameters are described in the introduction. The second section looks at each of the plasma parameters through spectroscopic measurements and electron beam current measurements. The results compare the DC plasma cathode to the RF plasma cathode and investigate the RF plasma cathode gun critical parameters.

6.1. Introduction

As described in Chapter 5, there are a number of parameters that influence the plasma behaviour, which need to be studied to enable optimisation of the plasma cathode gun:

- Accelerating voltage – As was shown in earlier chapters (Literature Review Chapter 2 and Case Study Chapter 3), the current extracted from thermionic electron guns increases with the accelerating voltage gradient in front of the cathode when they are space charge limited in emission – as is the case with the triode in Chapter 3. In the plasma cathode gun, the current extracted also increased with the accelerating voltage, which would not be expected for a diode gun of this type, and this chapter will describe how this increment of beam current with high voltage compared to thermionic guns in experiments
- Plasma chamber geometry – It was found that the geometry of the plasma chamber geometry had a strong influence on electron emission.
- Aperture diameter – In thermionic guns the electron current emitted from a cathode is related to the area, following the Richardson equation, as presented in Chapter 2. In plasma cathode guns, the current extracted also increased with the area of the cathode, in this case the aperture to the plasma chamber.

- Plasma pressure – As has been described within this thesis, plasma pressure is an important parameter which affects the plasma and thus the EB extracted from it. Plasmas of different pressure behave differently and thus the appropriate model should be chosen to study each plasma type. Zhu and Pu gave some guidelines on what model should be used depending on the plasma pressure and ionisation level. Figure 6.1 shows an example part of their work, in which they measured the electron density at pressures from 0.02 mbar (2 Pa) to 0.06 mbar (6 Pa) by using OES techniques and they validated their results by Langmuir probe measurements. The pressures in their experiments were in the pressure range of the plasma cathode gun studied in this work, which was measured for different flow rates and aperture diameters in Chapter 5.
- RF excitation power – The power used to generate a plasma has been shown to be another important plasma parameter. An example is shown in Figure 6.1, in which at any plasma pressure the electron density increases with RF power. The experiments in this chapter looked at whether increasing RF power increased electron density as well as the current of the EB extracted. In addition, the beam current – excitation power curve from the plasma cathode will be compared to the typical electron beam current curve from thermionic cathode guns.

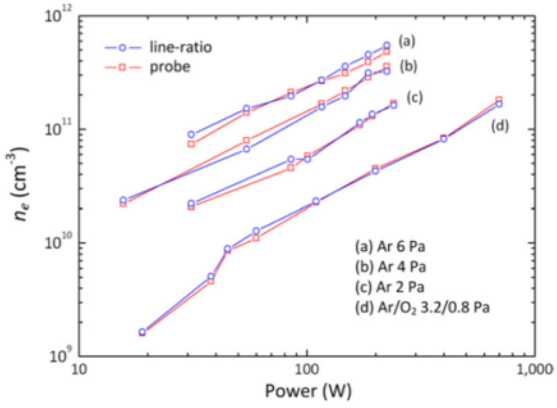

Figure 6.1 - Electron density (ne) as a function of RF power for different plasma pressures in an argon plasma (Zhu, Pu 2010)

- RF excitation frequency and DC – Zhu and Pu (Zhu, Pu 2010) showed in their experiments that both electron density and temperature change with plasma frequency, Figure 6.2 and Figure 6.3.

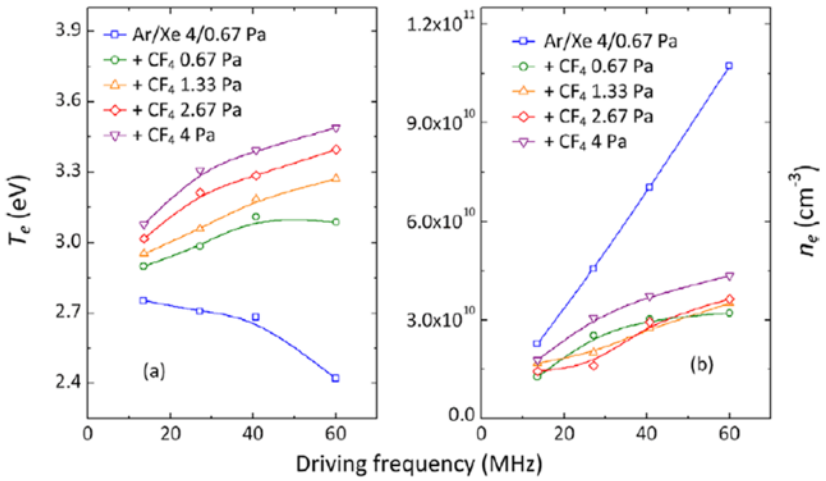

Figure 6.2 – T_e and n_e versus driving frequency (Zhu, Pu 2010)

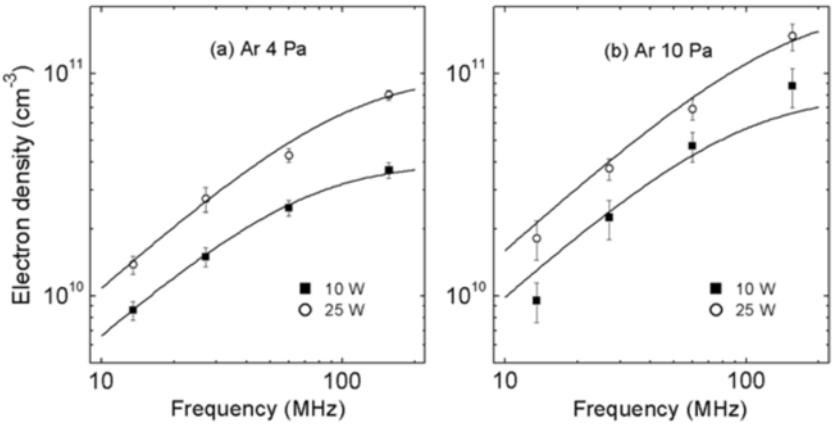

Figure 6.3 – Electron density versus driving frequency in argon CCP at a) 0.04 mbar b) 0.1 mbar. The values are experimental electron densities from the line-ratio techniques (Zhu et al. 2007)

In their experiments, (Zhu et al. 2007) showed that the electron density increases with the RF frequency at constant power. The experiments were carried out in the range of frequency from 13.54 to 156 MHz and it can be observed that the electron density graphs are tending towards a steady state at the upper end of the frequency range. The frequency of the plasma cathode in this thesis work was 80-84 MHz and the pressure and power conditions were similar. However, indications from the experiments and the simulation work (Chapter 7) showed that even though higher frequencies produce higher ionisation in general, the sheaths are larger, which may explain the low currents extracted from the RF plasma cathode gun in comparison to the DC plasma cathode.

- Use of magnets – Magnets were used in the experiments in order to reduce the number of electrons lost to the walls. As seen in the literature review (Chapter 4), the axial magnetic field confines the electrons around the magnetic field lines. In this work, permanent magnets with a ring shape were used around the plasma chamber in various positions along the plasma chamber x-axis (i.e. quartz cylinder axis).

6.2. Spectroscopic and Electron Beam Extraction Measurements

Spectroscopic and electron beam current measurements were carried out on the plasma cathode to understand the effect of the different the plasma parameters described in the previous section and to determine how the plasma gun could be optimised.

The beam currents were collected in a Faraday cup positioned beyond the anode, inside the vacuum chamber. Table 6.1 shows the main parameters involved in most of the tests carried out with the argon plasma cathode gun. The vacuum chamber pressure as well as the gas flow were monitored. The RF signal was between 80 – 84 MHz, depending on the best RF tuning given by the matching network and the resonant frequency of the gun. The flow rate (and thus plasma pressure) and excitation power were varied to see the effect in the plasma and beam current extracted. Any possible X-radiation was monitored and recorded with the time and date before and after each period of work requiring switching on the HV to generate an EB.

Table 6.1 - Plasma parameters in OES and EB generation tests

Vacuum chamber pressure [mbar]	Accelerating voltage to extract the EB [kV]	RF signal for plasma generation		Gas flow [sccm]
		Frequency [MHz]	Delivered Power [W]	
3×10^{-5}	30 - 60	80 - 84	5 - 100	0.1 - 1

In addition to the measurements taken on the RF plasma gun, a set of measurements were taken on a DC plasma cathode gun. The measurements of the RF plasma cathode gun optimised in this work were compared with data obtained from a DC plasma cathode gun at the Institut für Werkstoffkunde, Leibniz University, Hanover. This

involved using the same spectrometer to measure optical emission from the plasma. The results of the DC plasma cathode gun are also described in this section. A more detailed comparison of the DC plasma cathode and the RF plasma cathode is presented in subsection 6.2.6. Figure 6.4 is a picture of the experimental setup for the current measurements taken on the DC plasma cathode gun:

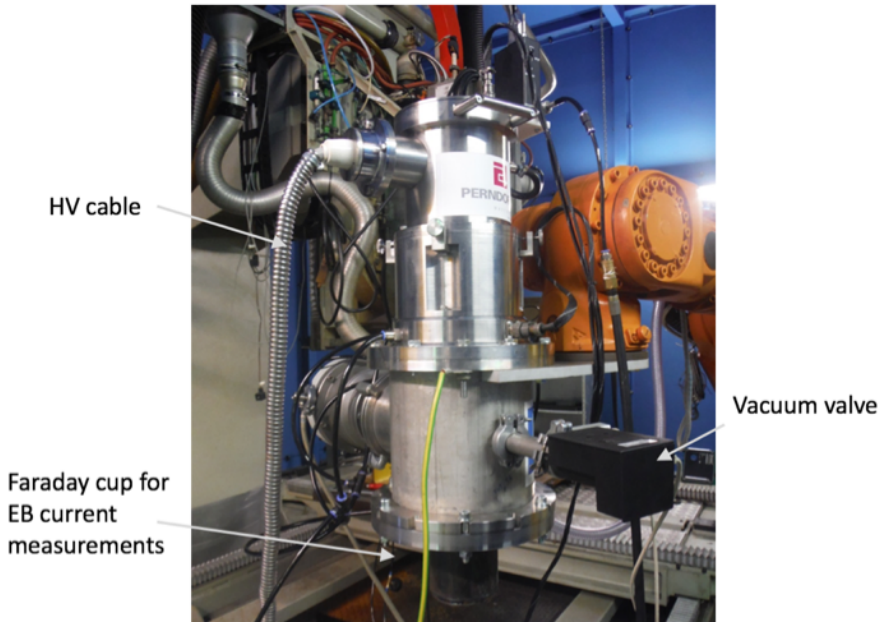

Figure 6.4 - DC plasma cathode gun at University of Hannover

Figure 6.5. shows the setup used for the OES experiments. In both setups used for collecting data with RF plasma and DC plasma cathodes, the optical fibre used to collect the light emitted was pointing along the axis of the plasma chamber. A collimating lens was attached to the end of the optic fibre when the signal was not intense enough to give a sufficient signal-to-noise ratio.

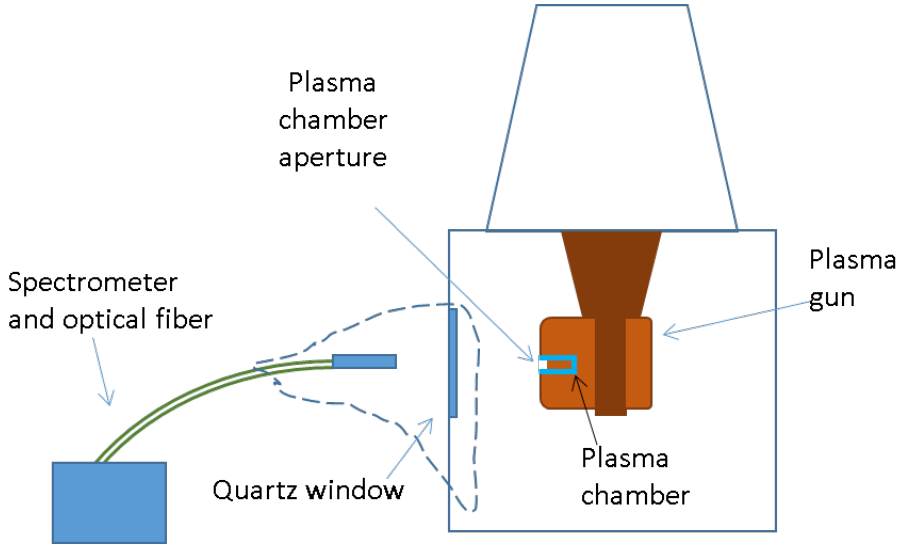

Figure 6.5 - Experimental test rig for OES experiments

The spectra range was collected with a USB4000 spectrometer with wavelength range 200 – 850 nm. The spectrometer was intensity calibrated and had an optical resolution of 1.5-2.3 nm FWHM. The fibre and holder were covered with a dark cover so that the background light did not interfere with the measurements. The plasma parameters for the DC plasma gun and the RF plasma gun are shown in Table 6.2.

Table 6.2 - Plasma parameters in DC plasma gun and RF plasma gun

Plasma parameters	**DC plasma cathode**	**RF plasma cathode**
Gas	Argon	Argon
Excitation power [W]	100 - 1000	5 - 100
Plasma frequency [MHz]	DC	80 - 85
Gas flow rate [sccm]	0.2	0.2
Plasma chamber pressure [mbar]	~ 2×10^{-2}	~ 2×10^{-2}
Aperture diameter [mm]	1.7	1.7
Electrodes shape	Hollow cathode	Hollow cathode
Aperture material	Iron or stainless steel	Iron or stainless steel
Electrodes materials	Copper	Iron or stainless steel

6.2.1. Accelerating Voltage and Electron Extraction

Preliminary experiments were carried out at –30 kV accelerating potential, even though –60 kV is currently being used as part of this work to generate more powerful EBs from

plasma. If all parameters were fixed and only the accelerating potential was increased, the measurements showed that beam current increased. Figure 6.6 shows that beam current increased with accelerating voltage with both the hollow cathode and flat electrodes designs. The measurements were taken with a –60 kV PSU for the hollow cathode design at 0.3 sccm and the flat design at 0.2 sccm, while the measurements taken for the hollow cathode design at 0.2 sccm the accelerating voltage was limited to a –30 kV PSU for that particular data set. In particular, in the hollow cathode design at 0.3 sccm, an increase of 50% in beam current from a beam generated at –30 kV to a beam generated at 60 kV at the same conditions can be observed. The dependencies of EB current with other plasma parameters such as pressure, geometry and aperture diameter can be appreciated and will be discussed in the following subsections.

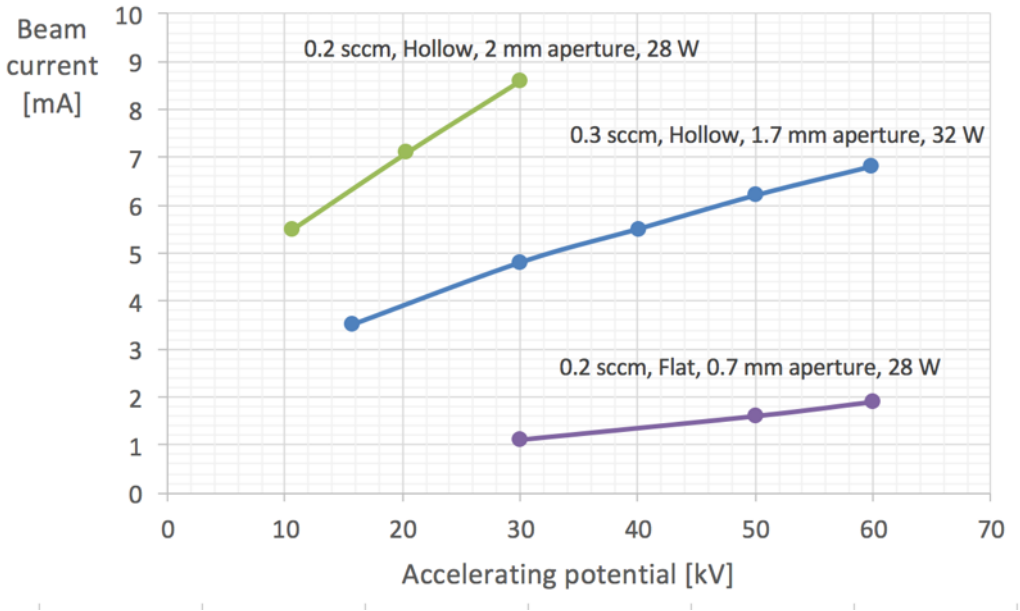

Figure 6.6 - Measured EB current vs. accelerating potential at ~30 W excitation power

The dependence of EB current with accelerating voltage can be also observed in the DC plasma gun. Figure 6.7 shows that the slope of the EB current curve as a function of the accelerating voltage is larger in the DC plasma cathode gun.

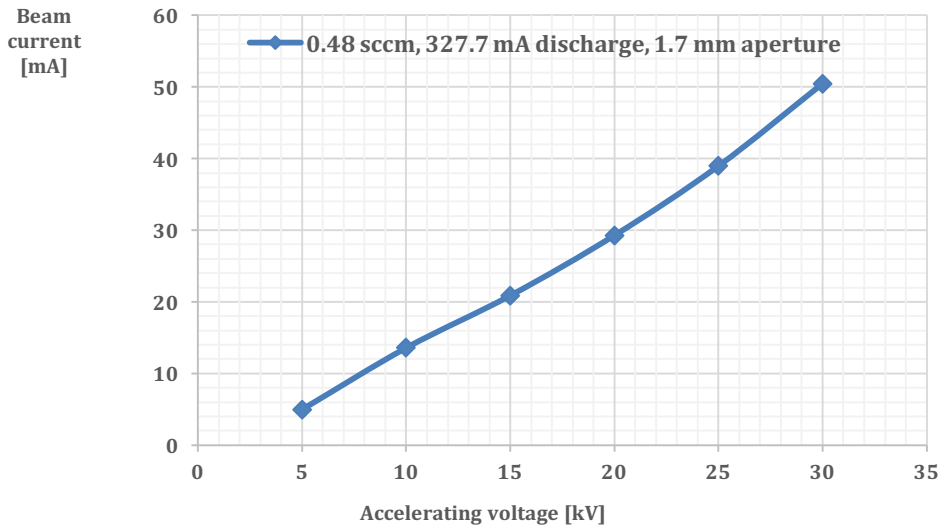

Figure 6.7 - EB current extracted from the DC plasma cathode at 327.7 mA discharge current as a function of the accelerating voltage

As both guns are diodes it was a surprising result to find the dependence of the beam current on the accelerating result. This would not occur for a thermionic diode where the emission would be dependent on the cathode temperature up to the saturated emission point where the gun becomes space charge limited. This dependence indicates that stronger electric field close to the boundary of the plasma causes higher electron emissivity.

It can be inferred that the sheath thickness has an effect on the level of current extracted. This was observed in the simulation work. Some authors (Goebel, Katz 2008) identified the limitations in beam current following Space Charge (ion beam current in this example) extracted from a plasma due to the sheaths effect.

6.2.2. Plasma Chamber Geometry: Flat Electrons Vs. Hollow Cathode

In this subsection, the EB current extracted as well as the spectroscopic lines emitted from hollow and parallel plate electrode designs are compared. As anticipated in Figure 6.6 in the previous subsection, the beam current extracted is affected by the geometry of the cathode, in this case the plasma chamber. Both of the hollow electrode geometries produced higher EB currents at the same plasma excitation power (~30 W) and at any accelerating voltage than the flat electrode geometry. A diagram of a hollow

cathode geometry used in the trials described in this subsection is presented in Figure 6.8. In this diagram, d is the electrode gap, which in the hollow cathode designs refers to the distance between the end of the hollow cylinder and the aperture electrode.

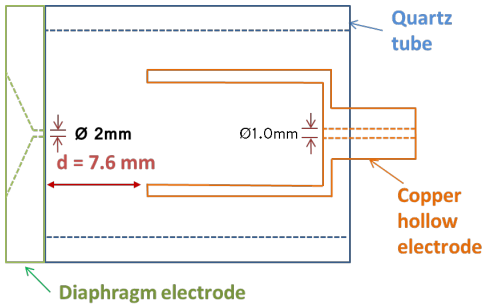

Figure 6.8 - Hollow cathode plasma chamber design

Figure 6.9 shows the beam extracted from a 0.7 mm diameter aperture in a parallel plate design as a function of the RF power. The electrode gap (d in the diagram) was 18.3 mm in both measurements. As seen in the plot, the beam current values both at 0.2 sccm and 0.4 sccm were only a few milliamps. It should be noted that the RF power applied was also very low (up to 18 W delivered power).

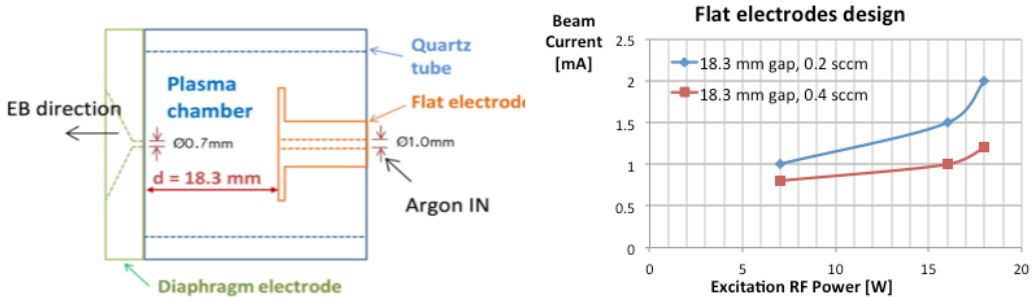

Figure 6.9 - EB current extracted at –30 kV from a flat electrode design at 0.2 sccm and 0.4 sccm flow rates

Figure 6.10 shows EB current measurements from both a hollow cathode and a flat electrode design, with all measurements taken at –30 kV and with a 0.7 mm diameter aperture. It can be seen that the curves are divided into two main groups in the plot: the solid lines which correspond to the hollow cathode currents and the dashed lines which correspond to the flat electrodes currents. The trials in the hollow cathode design were

carried out at 0.3 sccm gas flow and electrode gaps ranging from 4 to 7.6 mm. The trials in the flat electrodes design were carried out at 0.2 and 0.4 sccm and electrode gaps of 18.3 and 23 mm. In all cases, the hollow cathode design produced higher currents than the flat design. The dependence with pressure will be discussed in section 2.2.4.

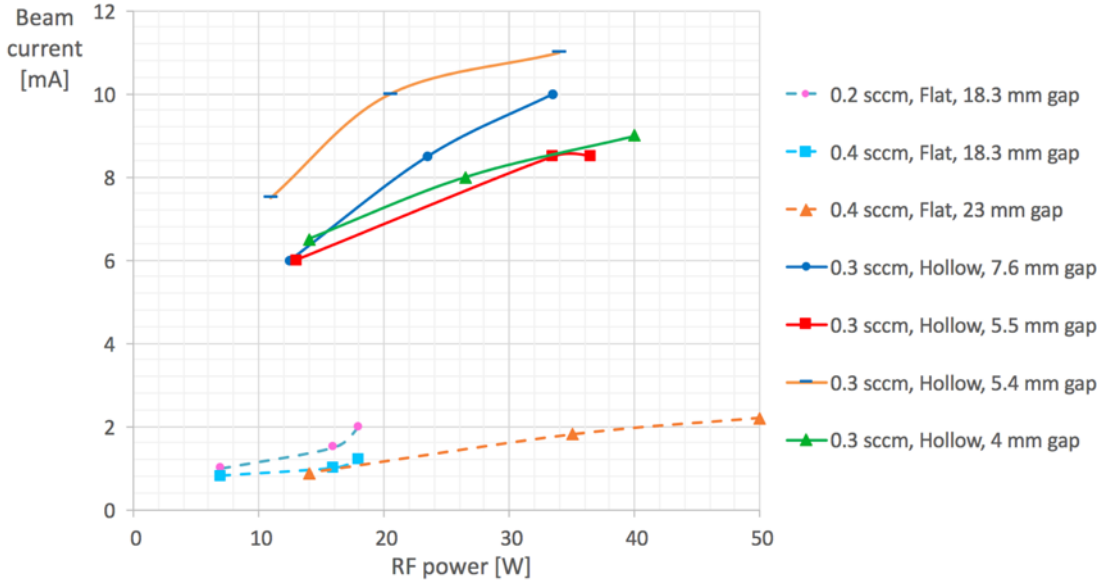

Figure 6.10 - EB current measurements from the hollow cathode and flat electrodes plasma chamber designs at –30 kV

Preliminary experiments with flat electrode plasma chamber geometries were useful for comparison with plasma chamber simulations. However, the ionisation density was limited by the mean free path, as this was longer, in low pressure plasmas, than the capacitively coupled flat electrode chambers. Thus, the main part of experiments in this chapter was carried out using hollow electrode geometries. The plasma cathode gun benefits from the "hollow cathode effect", described in Chapter 4, which produces higher ionisation levels as a result of a larger sheath area than the flat electrode design. The sheaths accelerate the electrons, giving them the necessary energy to cause ionisation through collisions.

6.2.3. Aperture Diameter

Figure 6.6 (subsection 2.2.1) shows that the current increased faster as a function of the accelerating voltage with the larger aperture design (2 mm diameter aperture). Figure

6.11 shows beam current measurements taken at 0.3 sccm flow rate and –30 kV acceleration voltage. The electrode gap and electrode geometry was almost identical: a hollow cathode type in both cases. However, the beam current extracted from the 2 mm diameter aperture is larger than the beams extracted from the 0.7 mm diameter aperture.

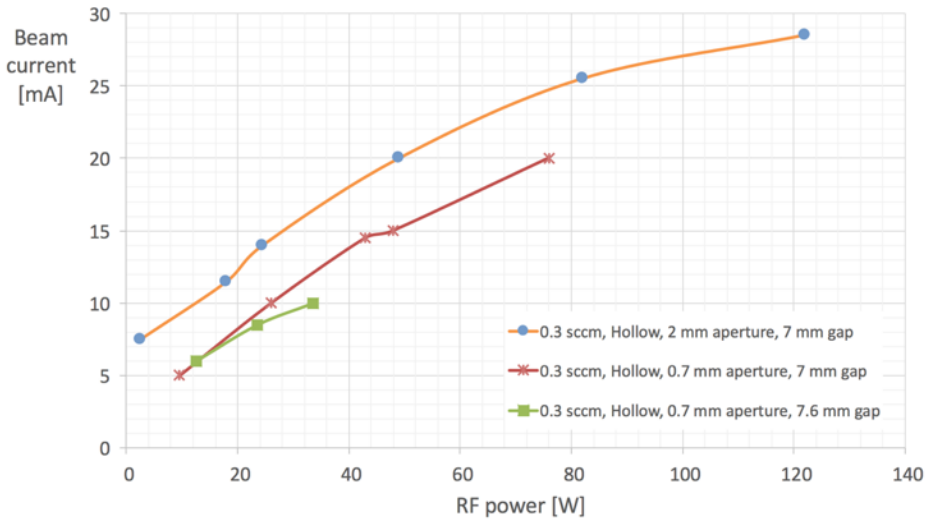

Figure 6.11 - EB current generated at –30 kV and 0.3 sccm flow rate from a hollow cathode with 0.7 mm and 2 mm diameter aperture

Increasing the aperture diameter required a higher gas flow in order to keep enough pressure in the plasma chamber to strike a plasma. As a result, the pressure in the gun vacuum chamber is higher. Thus there is a limitation on the largest aperture diameter than can be used, and this was found to be around 2 mm, as larger aperture diameters would cause a very large flow of gas to be leaked from the plasma chamber to the vacuum chamber and high voltage breakdown would occur between plasma chamber and anode. High voltage breakdown would be undesirable in operation as it interrupts the electron beam, and it also extinguished the plasma, thus this needed to be avoided.

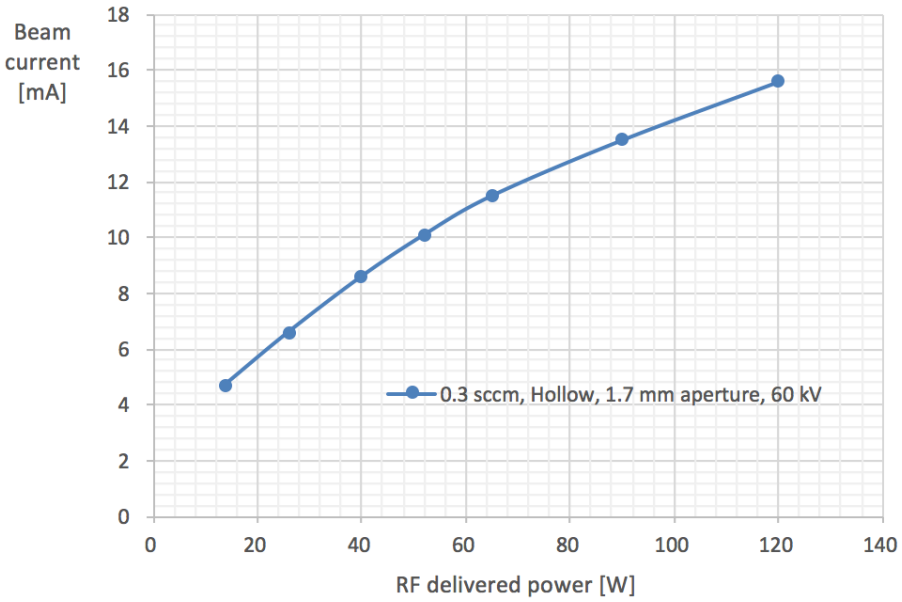

Figure 6.12 - EB current generated at –60 kV from a hollow cathode with 1.7 mm diameter aperture

6.2.4. Plasma Pressure

The pressure in the plasma chamber was measured for different gas flows (0.1 sccm to 1.3 sccm) and aperture diameters of the extraction electrode (0.7 mm to 2 mm), as presented in Chapter 5. Most of the OES and EB current measurement experiments were carried out at 0.2 – 0.3 sccm as this was found to produce the most stable plasmas. Some experiments were carried out at a lower and higher plasma pressures, most of them within the pressure range and aperture sizes shown in Figure 6.13.

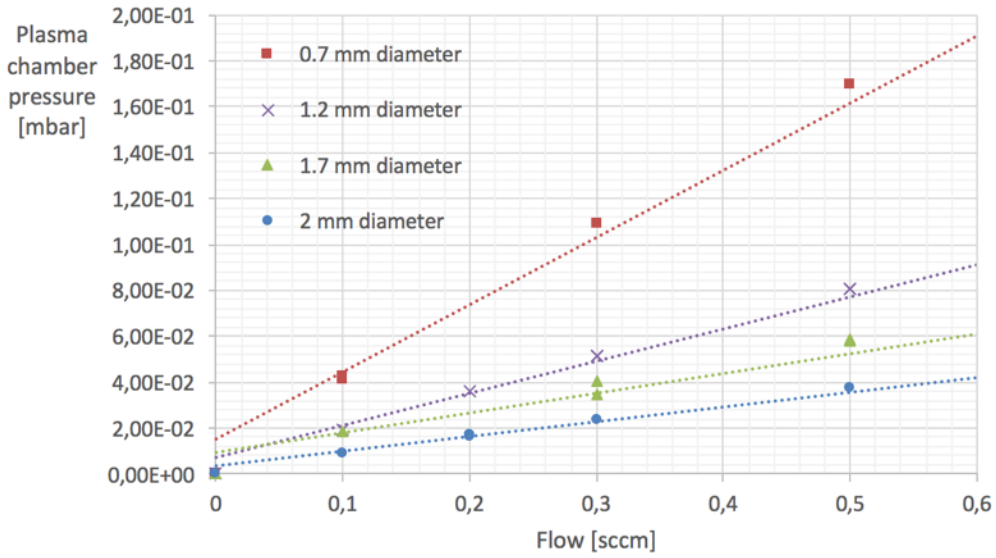

Figure 6.13 - Plasma chamber pressure as a function of gas flow for different aperture diameters

However, larger flow rates (i.e. 0.5 sccm at 1.7 mm or more) caused plasmas to be unstable. This may be due to the electron density distribution changing dramatically due to RF modes.

There were other reasons, in addition to the above, for which lower pressures were preferred. First, the sputtering inside the plasma chamber was reduced. Figure 6.14 (left) presents an example of a quartz plasma chamber coated at the inner wall after running at plasma chamber pressures above 0.2 mbar. Second, if the aperture diameter that leaks gas to the vacuum chamber is big enough, the pressure in the vacuum chamber can get high enough to strike a plasma outside the plasma chamber, as shown in Figure 6.14 (right). This causes obvious problems with HV breakdown in the vacuum chamber which switched off the EB. Finally, the EB current measurements carried out with this work showed that the lower pressure plasma tests generated larger beam currents at the same plasma conditions. An example can be seen in a previous section 2.2, in which Figure 6.6 showed that the plasma at 0.2 sccm produced larger currents than the plasma at 0.4 sccm at any RF power in a flat electrodes design.

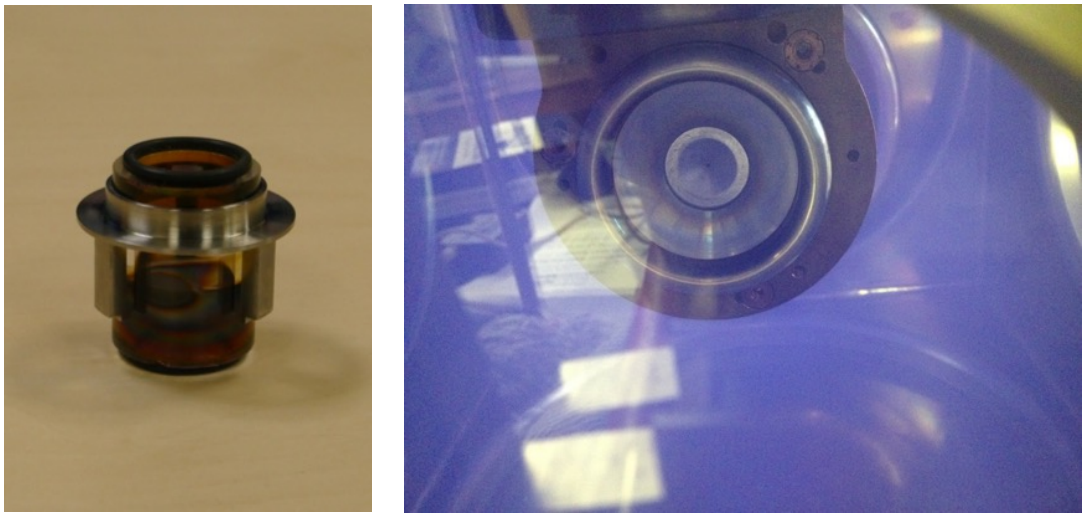

Figure 6.14 - Pressure limitations

Figure 6.15 presents the EB current measured from a hollow cathode design with a 2 mm aperture at –30 kV. As it can be observed, the lower pressure plasma (0.3 sccm flow rate) produced higher EB current at any RF power excitation.

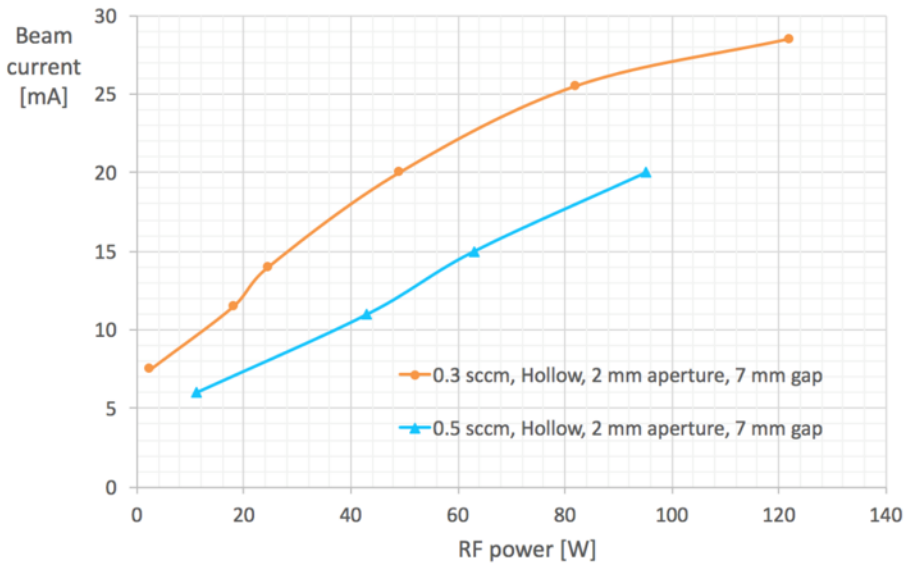

Figure 6.15 - EB current generated from a hollow cathode at –30 kV

Figure 6.16 shows the spectra of the spectra obtained from a hollow cathode design with a 7 mm gap between the hollow cylinder and aperture electrode for EB extraction. The measurements were taken at 42 W and 81 MHz for 0.1 sccm and 0.3 sccm flow rates.

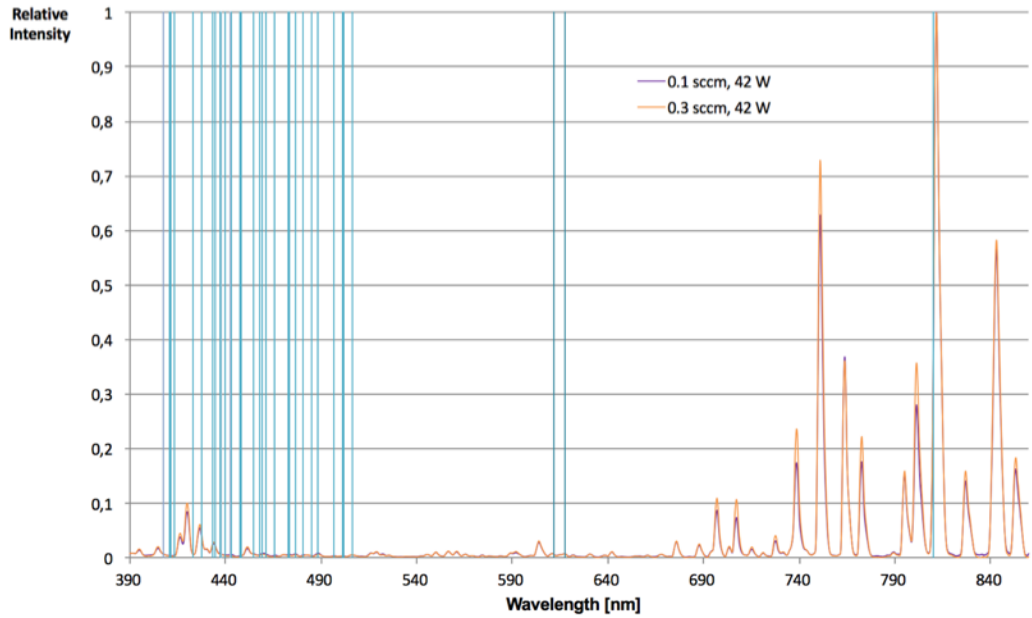

Figure 6.16 - RF plasma spectra at 0.1 sccm and 0.3 sccm

In order to see the changes in the main argon I and argon II lines and compare them with the current extracted in each case, a ratio of the spectra of the lines emitted from the hollow cathode at two different plasma pressures is presented. A comparison of a hollow cathode and flat electrode cathode was carried out by spectra lines ratios in other publications (Weinstein et al. 2010). The work concerned in this thesis looks at spectra ratios to compare not only hollow and flat electrode geometries, but also other parameters such as pressure, excitation power and DC vs. RF excitation. In addition to this, the spectra ratios are compared to the EB current extracted.

Figure 6.17 presents the spectra ratios of the argon II lines to compare the plasma generated in a hollow cathode design at 0.1 sccm and 0.3 sccm at a same RF power (42 W). Figure 6.18 shows the ratio of argon I lines.

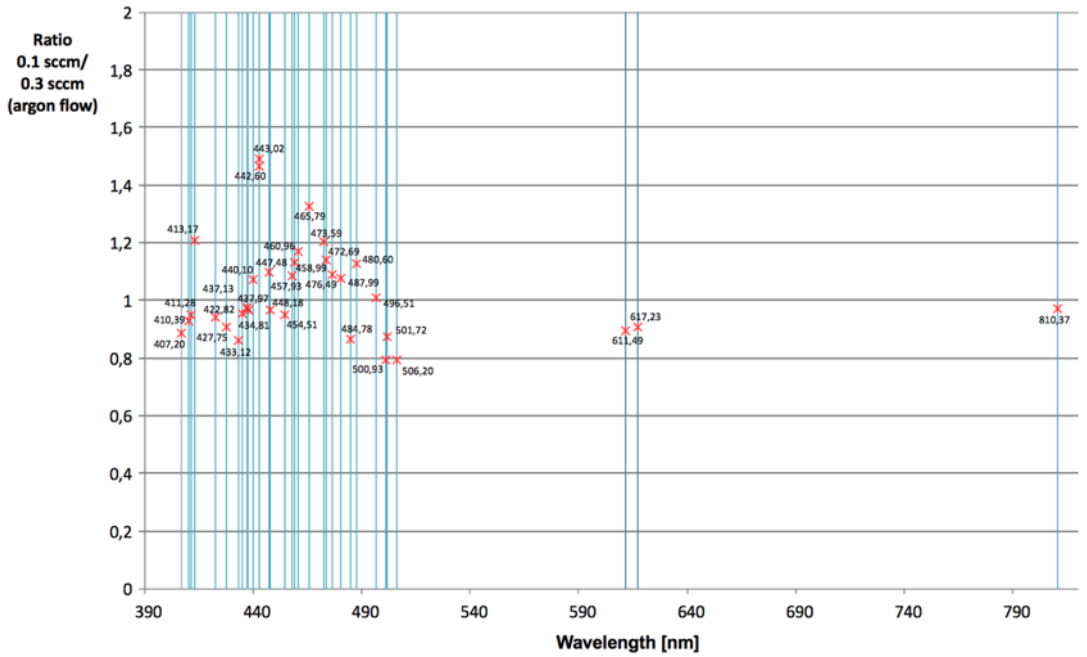

Figure 6.17 - Argon II lines ratio of the gas flows 0.1 vs. 0.3 sccm in the RF plasma cathode gun at a 42 W RF power

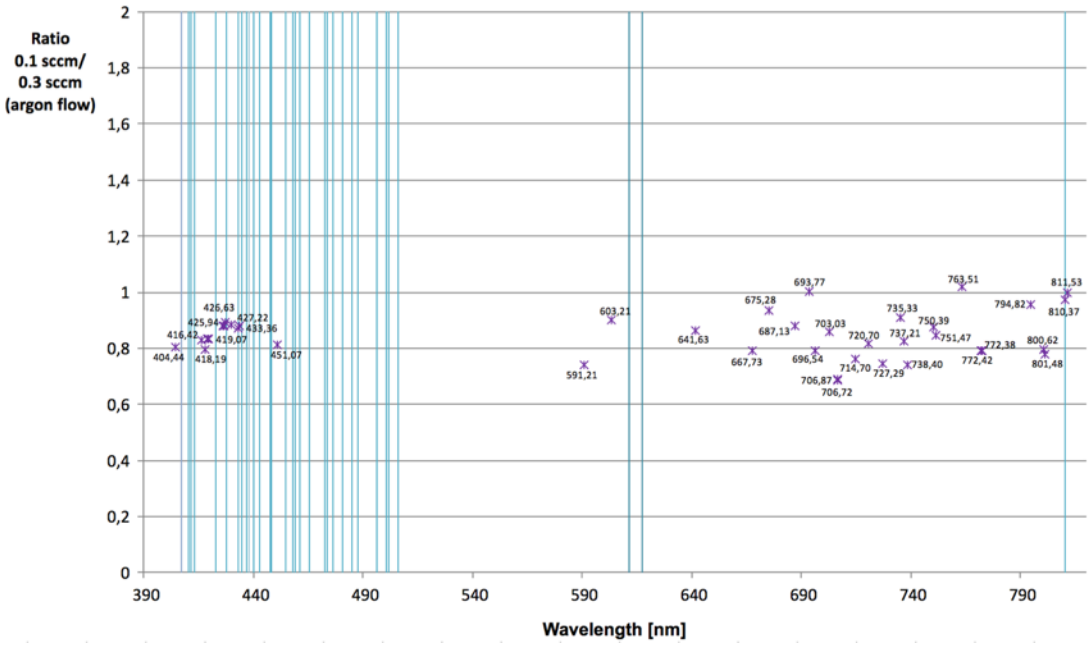

Figure 6.18 - Argon I lines ratio of the gas flows 0.1 vs. 0.3 sccm in the RF plasma cathode gun at a 42 W RF power

As it can be observed, argon II line intensities were larger at the 0.1 sccm than at the 0.3 sccm flow rate, indicating that the ionisation is larger at lower plasma chamber

pressures. This agrees with the EB current measurements, which were found to be larger at the lower plasma pressures (Figure 6.15).

Lower pressures also produced larger EB currents in the DC plasma cathode gun. Figure 6.19 presents the spectra of the DC plasma at 311.6 mA discharge current and compares a plasma generated at a flow of 0.16 sccm with 0.26 sccm.

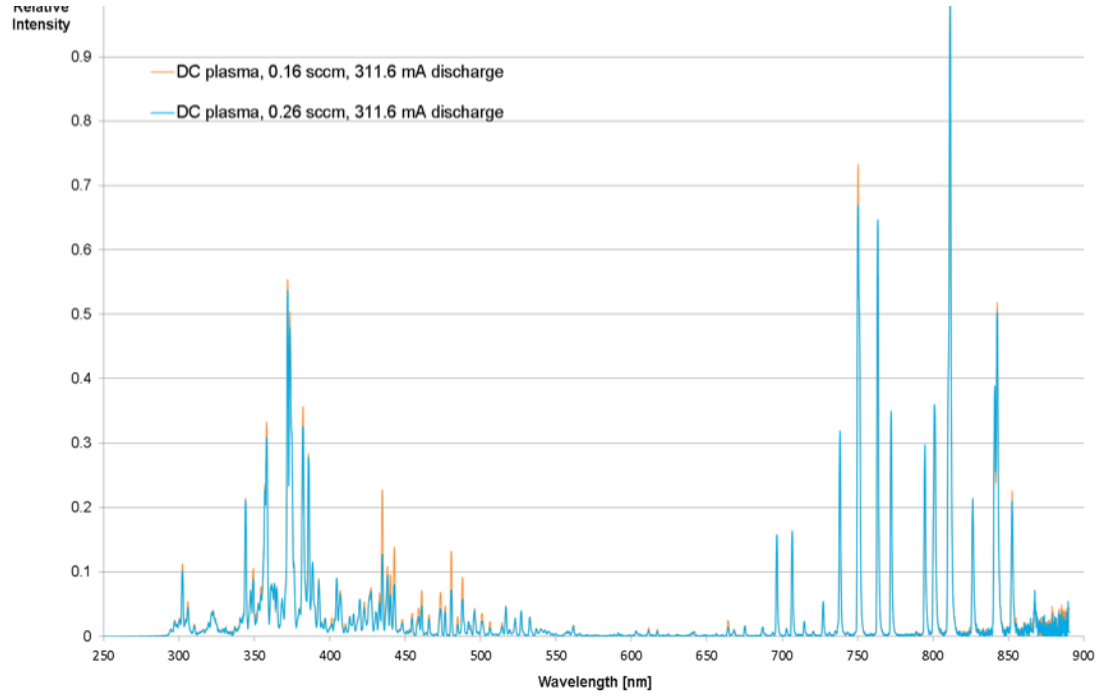

Figure 6.19 - DC plasma spectra at 0.16 sccm and 0.26 sccm

The main differences are observed at the lower wavelength values of the spectra. Figure 6.20 shows the ratio of argon II line intensities recorded at 0.16 sccm vs. 0.26 sccm.

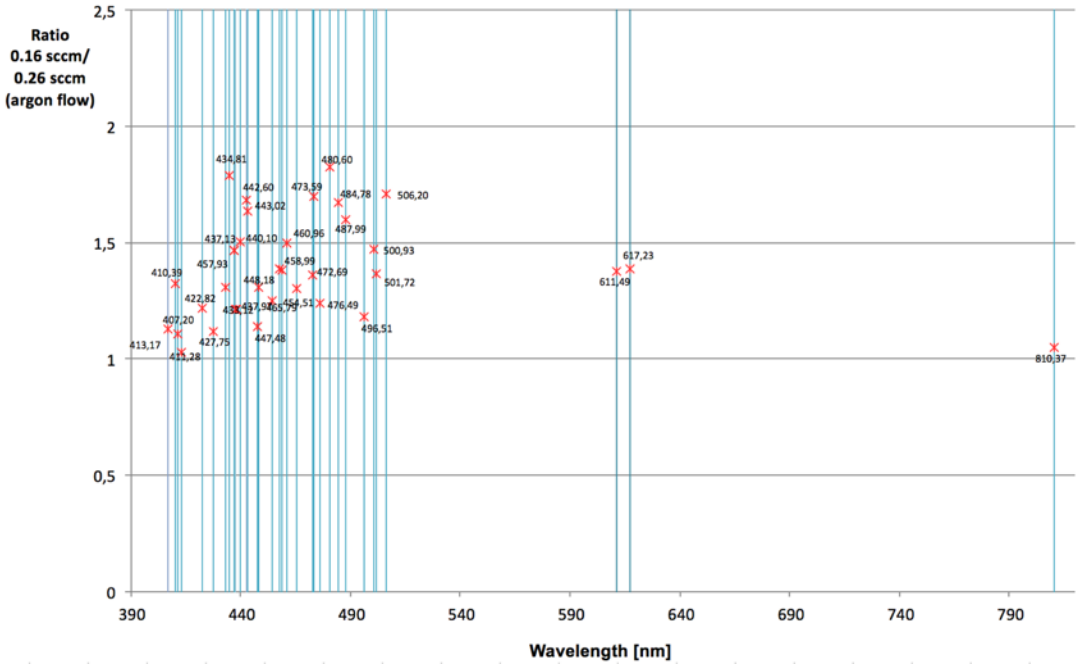

Figure 6.20 - Argon II lines ratio of the gas flows 0.16 vs. 0.26 sccm in a DC plasma cathode gun at a 311.6 mA discharge current

The effect of pressure was also looked at lower discharge currents. Figure 6.21 shows a comparison of the spectra argon II lines at 0.16 sccm vs. 0.48 sccm in a DC plasma generated at 126.2 mA discharge.

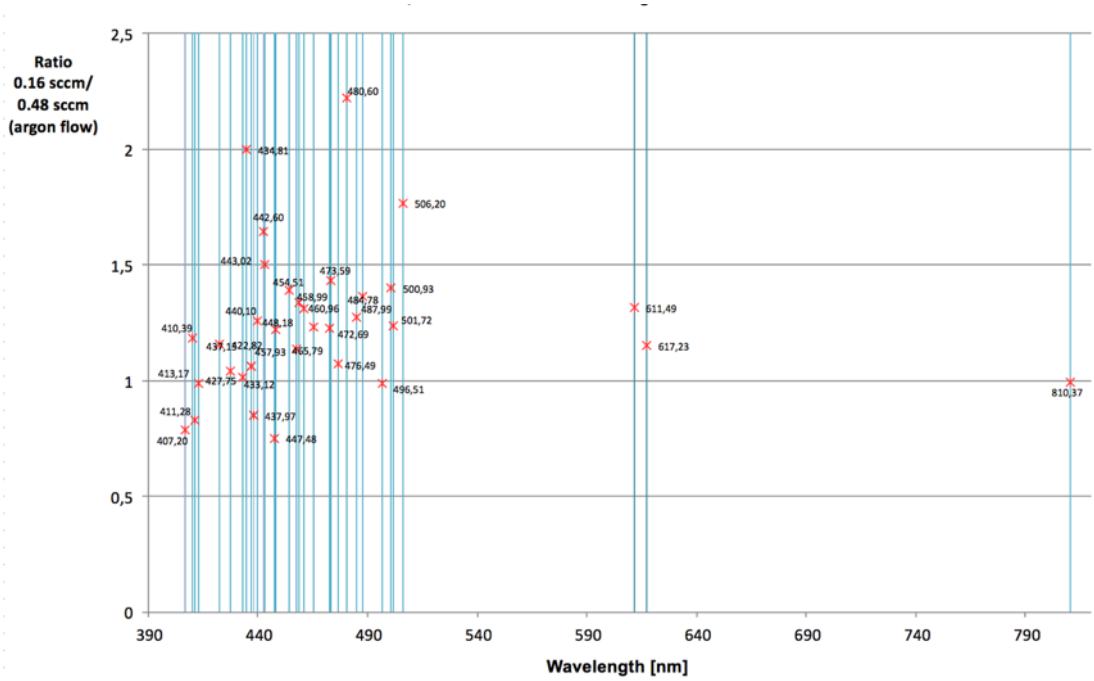

Figure 6.21 - Argon II lines ratio of the gas flows 0.16 vs. 0.48 sccm in a DC plasma cathode gun at a 126.2 mA discharge current

Figure 6.22 presents the ratios of the argon I lines for the 126.2 mA discharge. Figure 6.23 presents the argon I lines ratios for the 311.6 mA discharge.

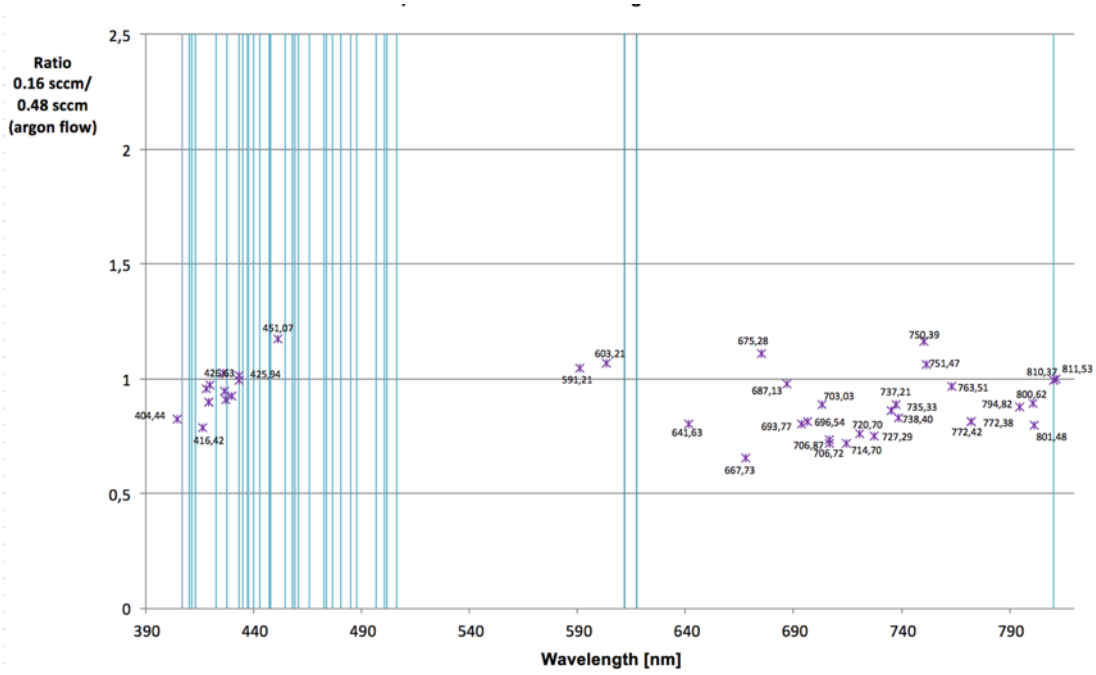

Figure 6.22 - Argon I lines ratio of the gas flows 0.16 vs. 0.48 sccm in a DC plasma cathode gun at a 126.2 mA discharge current

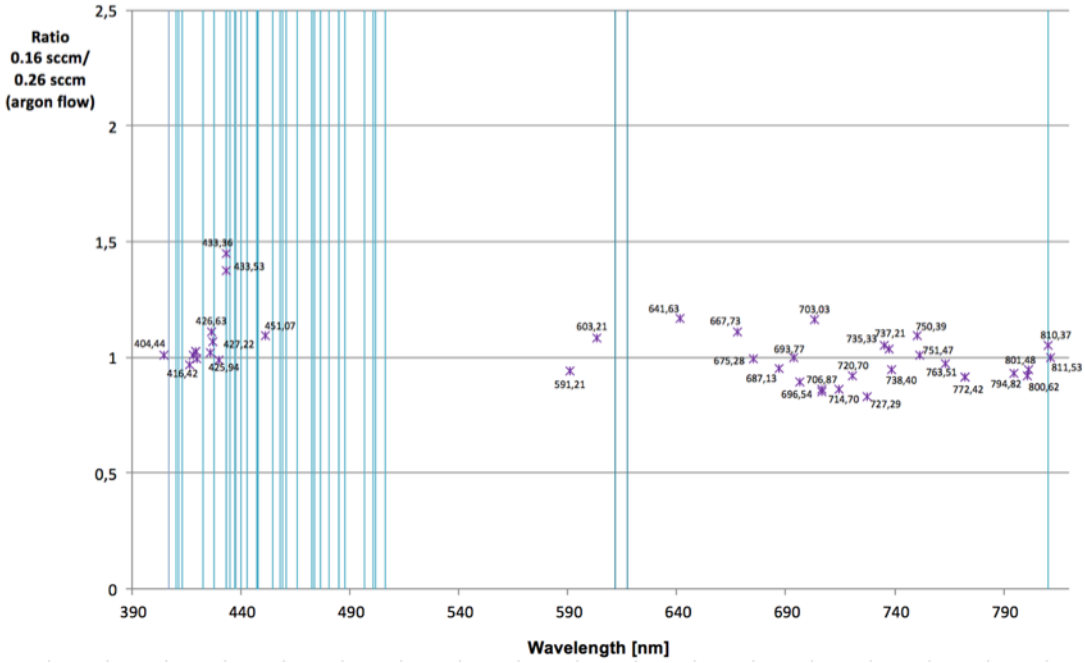

Figure 6.23 - Argon I lines ratio of the gas flows 0.16 vs. 0.26 sccm in a DC plasma cathode gun at a 311.6 mA discharge current

In summary, both the DC plasma cathode and the RF plasma cathode guns produced larger beam currents at lower plasma pressures. In addition, the spectra ratios indicate there is a higher ionisation (larger argon II intensities) in the lower pressure plasmas. The argon I intensities did not seem to have significant variations from one pressure to the other.

When comparing DC plasma and RF plasma, the intensity ratios of argon II lines were larger in the DC plasma with changes in pressure than the intensity ratios of argon II lines in the RF plasma. Argon II line ratios were similar (close to the unit) in the DC and RF plasmas.

6.2.5. RF Excitation Power

From the experiments it was observed that the EB current increased with RF excitation power in all cases. Figure 6.24 presents the largest EB currents extracted at –60 kV from the RF plasma cathode gun to date, using a hollow cathode design. The EB current curve increases with a larger slope up to 50 W excitation power, then the slope reduces but beam current continues to increase all times. The maximum current

extracted was about 38 mA in this case, as the maximum RF power that can be applied to the plasma chamber was limited to the power that the plasma gun could dissipate. On the other hand, Figure 6.25 shows the EB current extracted from a plasma at the same gas flow (and thus plasma pressure). The EB current extracted at 50 W is only 2 mA compared to the more than 20 mA extracted from the hollow cathode. In addition to this, the EB current extracted from the flat electrode design is at much lower values between 20 and 30 W. The reason for this was that flat electrode cathodes were found to be a lot more instable.

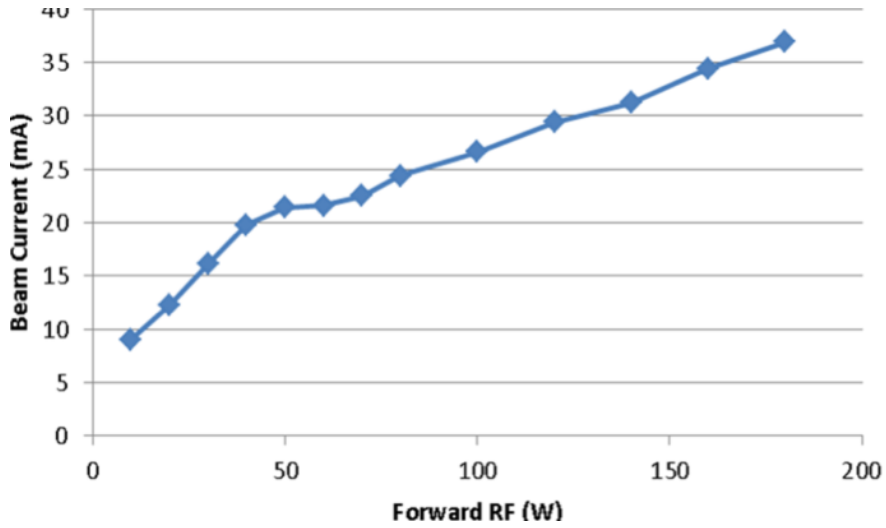

Figure 6.24 - High current trials with a hollow cathode design

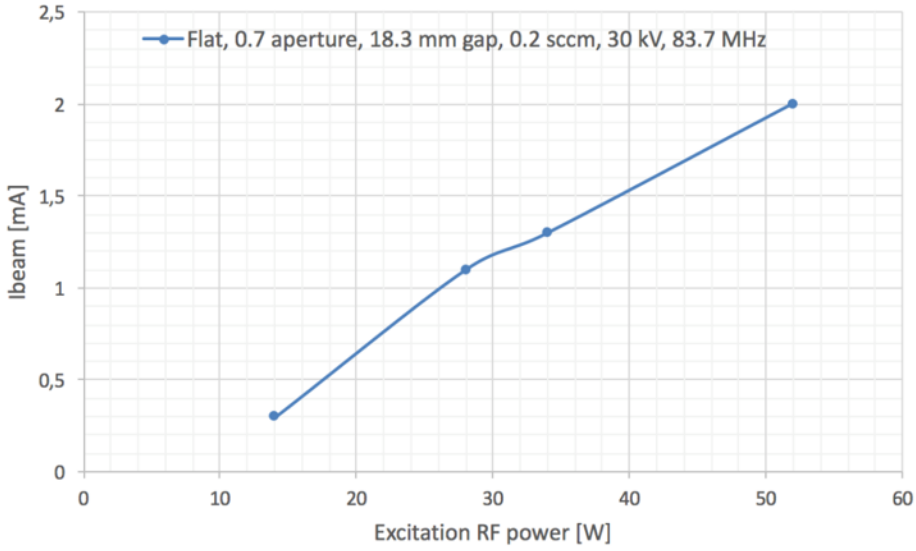

Figure 6.25 - EB current extracted from a flat electrodes plasma chamber design

However, the curve followed by the EB current is different to the typical thermionic gun characteristics, in which the current is eventually saturated by space charge. Space charge saturation was not apparent in the electron extraction measurements carried out in the RF plasma gun (nor in the DC plasma gun results which are presented in the following subsection), over the range of beam current examined.

Figure 6.26 shows the spectra recorded from a hollow cathode design at a 0.3 sccm while generating a beam from a 2 mm aperture. The beam current was presented in the previous subsection (Figure 6.15). In this subsection the spectra ratios compare the plasma at 2.5 W while generating an EB current of 7.5 mA vs. the spectra of the plasma at 122 W which generated 28.5 mA beam current. The spectra graphs are presented in Figure 6.26 with the argon II lines superposed. The intensity of the argon II lines is low due to the measurements were taken from the viewing hole on the side of the plasma chamber to be able to generate an EB at the same time.

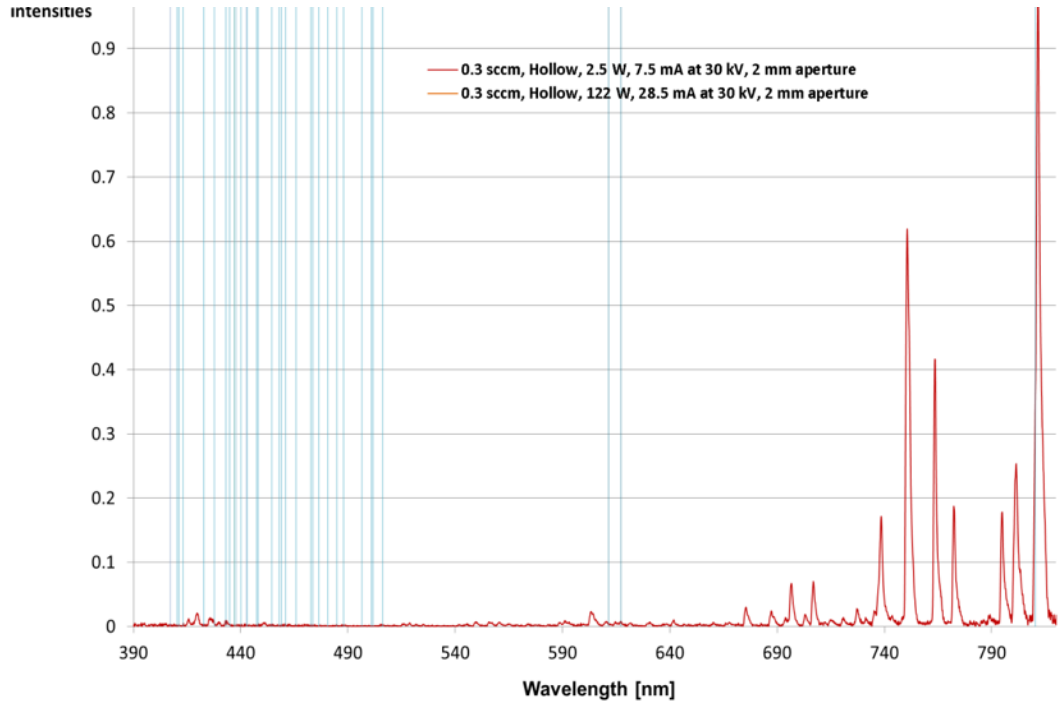

Figure 6.26 - Spectra of the plasma generated at 0.3 sccm from a hollow cathode while a beam current was extracted at –30 kV

The ratio of the spectra generated at the two power levels (2.5 W and 122 W) for argon II lines are presented in Figure 6.27. The ratio of the spectra for the argon I lines is

presented in Figure 6.28. All data was relative intensity calibrated and normalised for the most intense line (811.4 nm). As can be observed, most of the argon II lines are a few times larger (up to 4 times at line 476.49 nm) in intensity for the plasma generated at 122 W than the plasma generated at 2.5 W. However, when we look at the ratios of the argon II lines, the relative intensities seem to be very similar (the ratio is around 1 in most cases).

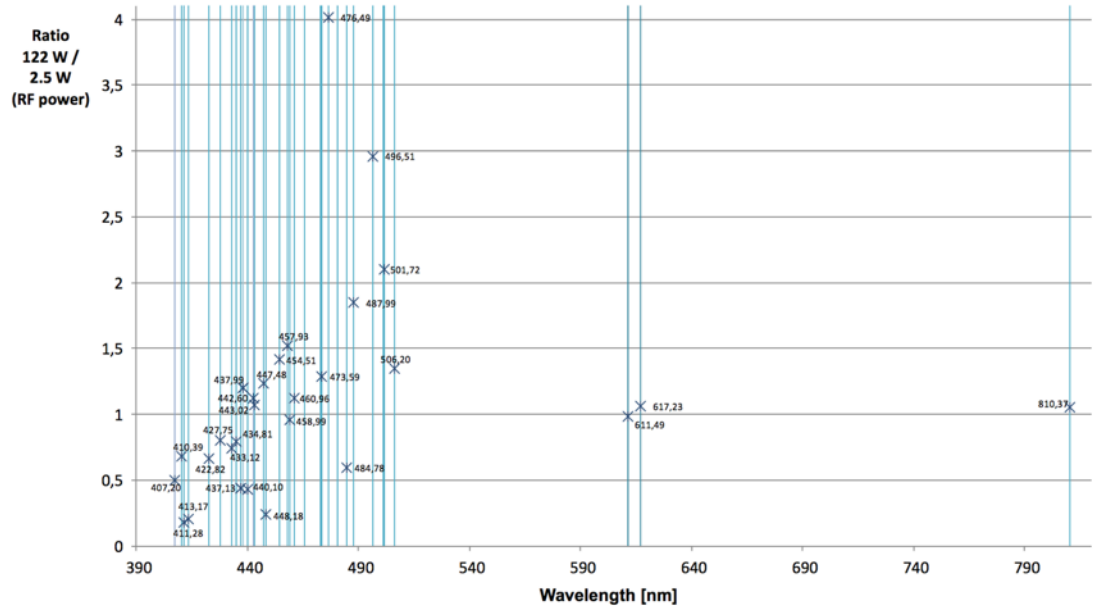

Figure 6.27 - Spectra ratio of argon II lines at 122 W / 2.5 W RF power

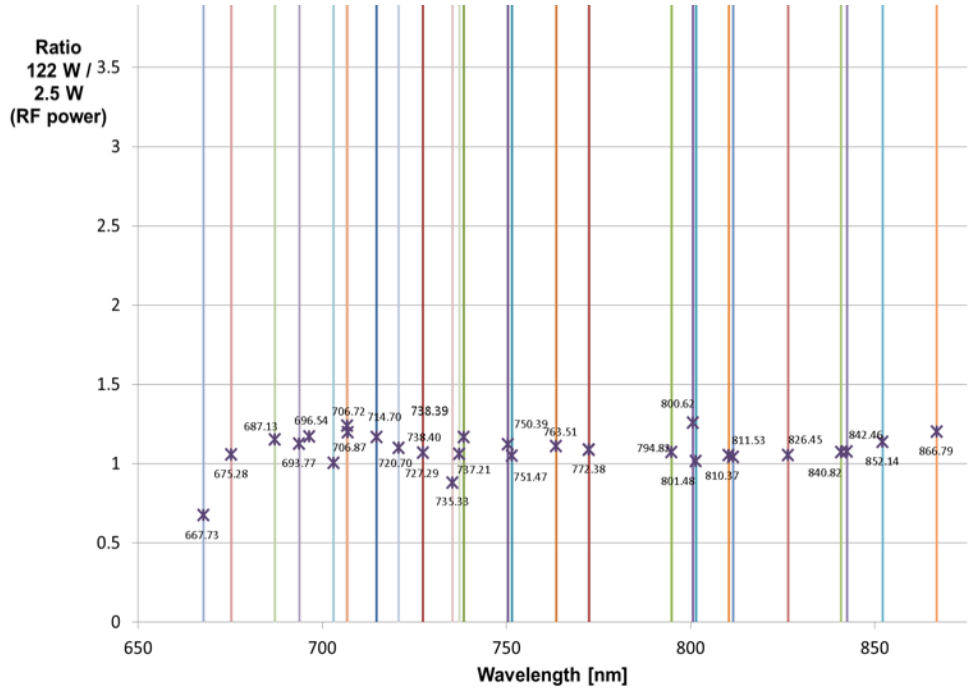

Figure 6.28 - Spectra ratio of argon I lines at 122 W/ 2.5 W RF power

The effect of the excitation power was also studied in the DC plasma cathode gun. Figure 6.29 shows a comparison of the spectral lines in a plasma generated at 126.2 mA and 311.6 mA discharge currents. In both cases, the gas fed was argon at a pressure of 0.26 sccm. The main differences in intensities can be observed at the lower wavelength side of the spectra range. Most of the argon II lines, which represent argon ionisation, are within this range.

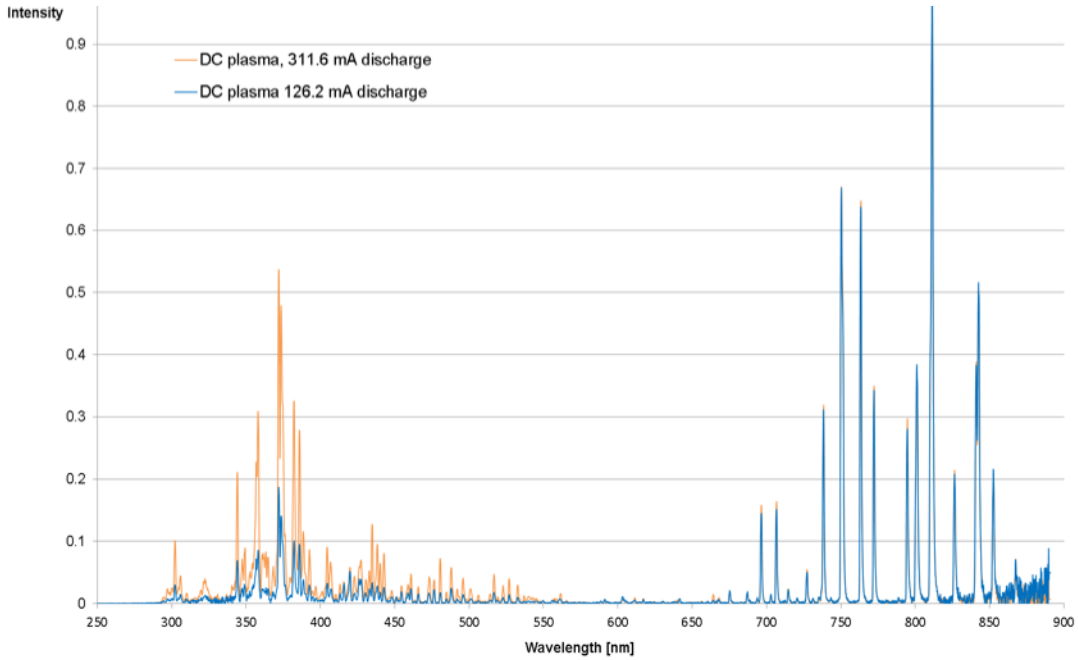

Figure 6.29 - DC plasma cathode spectra at 0.26 sccm comparing 311.6 mA and 126.2 mA discharge currents

Figure 6.30 shows the argon II lines superposed to the the DC plasma cathode spectra. It can be observed that all intensities corresponding to argon II lines are larger in the plasma generated at 126.2 mA than at 311.6 mA. The ratio of the argon II lines between the plasma at 311.6 mA and 126.2 mA is presented in Figure 6.31 and the ratio of the argon I lines is in Figure 6.32.

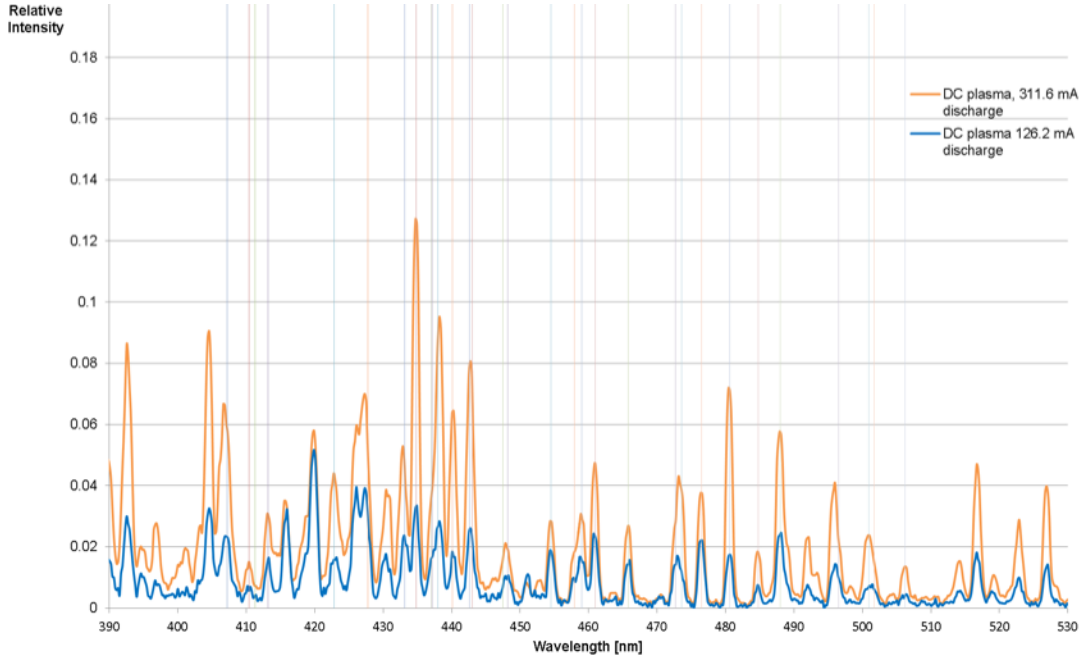

Figure 6.30 - Argon II lines in DC plasma at 0.26 sccm flow and 311.6 mA and 126.2 mA discharge current

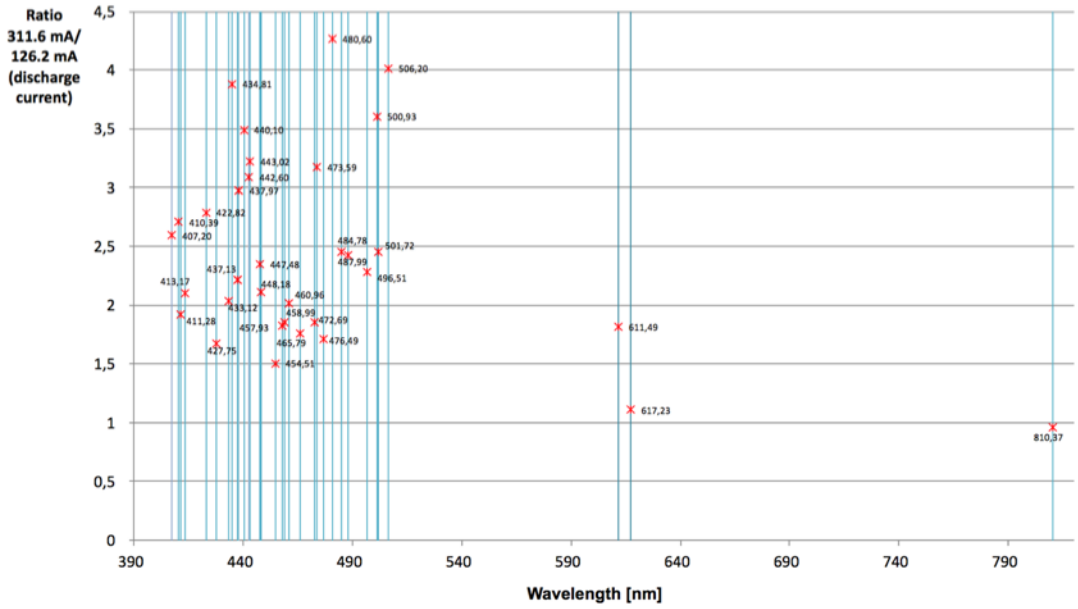

Figure 6.31 - Ratio of the DC plasma argon II lines generated at 311.6 mA / 126.2 mA

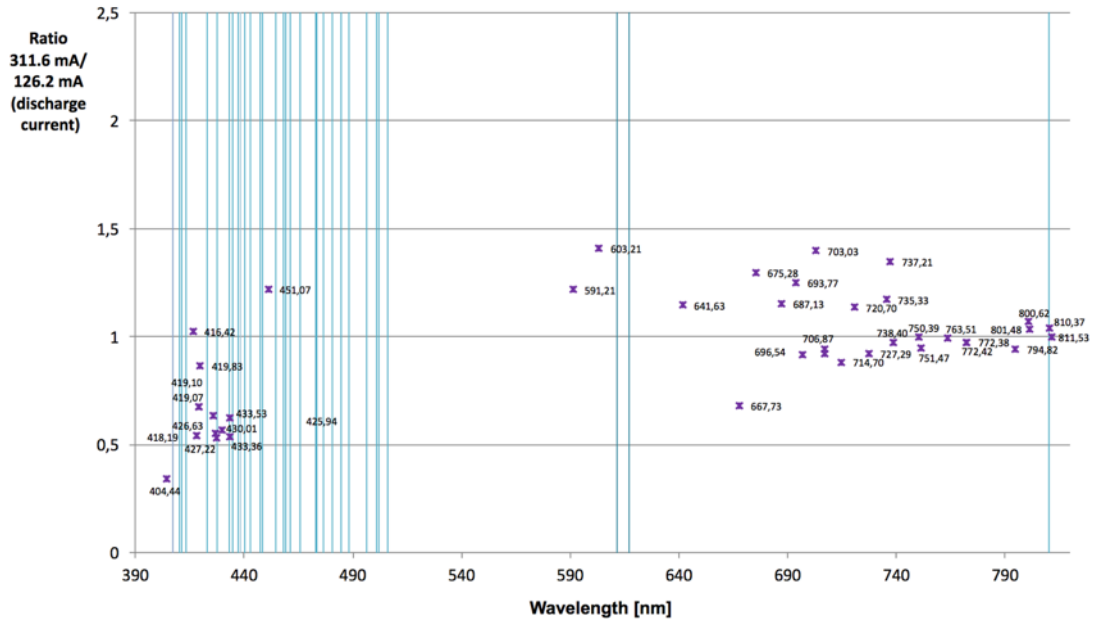

Figure 6.32 - Ratio of the DC plasma argon I lines generated at 311.6 mA / 126.2 mA

As seen in the results, the ratios comparing plasmas generated at different powers showed that the argon II lines were more intense for the larger excitation powers. This agrees with the EB current measurements, in which the EB current is larger at larger excitation power.

6.2.6. RF Excitation Frequency And DC

Figure 6.33 presents the beam currents extracted from the DC plasma cathode gun at different gas flows. The pressure estimated in the plasma chamber will be equivalent to the pressure measurements of the plasma chamber at those flow rates and 1.7 mm aperture diameter on the RF plasma cathode gun.

The continuous lines are the currents extracted at –60 kV, whereas the discontinuous lines are the currents extracted at –55 kV, except for the higher flow rate case (0.48 sccm), in which the high pressure made the plasma unstable and generated breakdown in the vacuum chamber which did not allow generation of EB current at a higher HV than –30 kV.

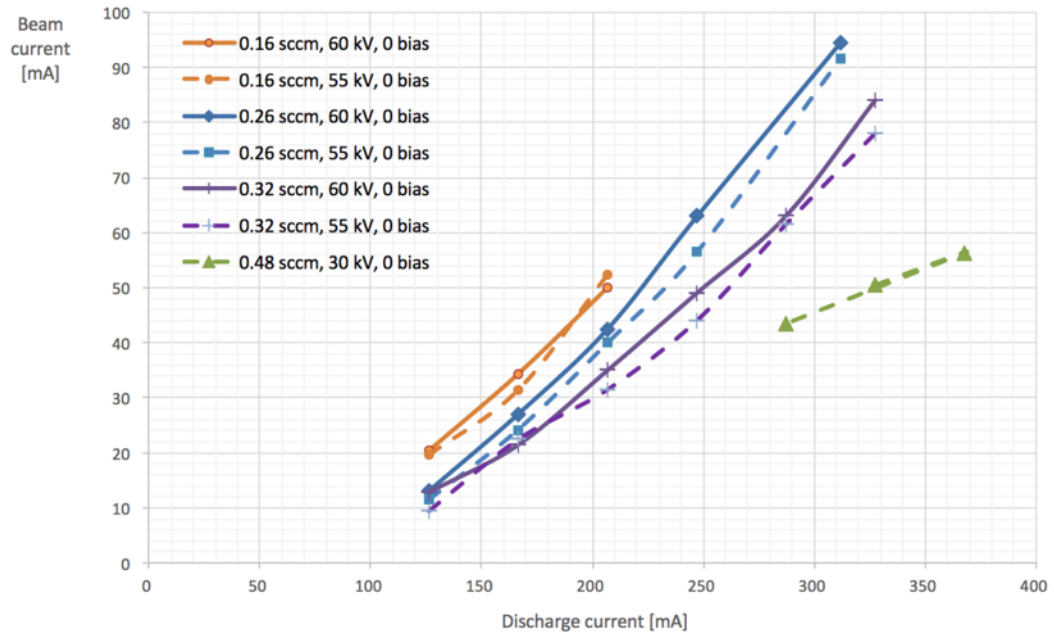

Figure 6.33 - EB current generated from the DC plasma cathode gun at different plasma pressures from a 1.7 mm aperture at –30 to –60 kV

Figure 6.34 shows a comparison of the DC plasma spectra (green) with an RF plasma spectra (red) at the same flow rate (0.2 sccm) and aperture diameter (1.7 mm) between the plasma chamber and vacuum chamber. The spectra was taken after a relative intensity calibration and the lines are normalised to the most intense line Ar-811 nm. The estimated plasma chamber pressure is in the 10^{-2} mbar range.

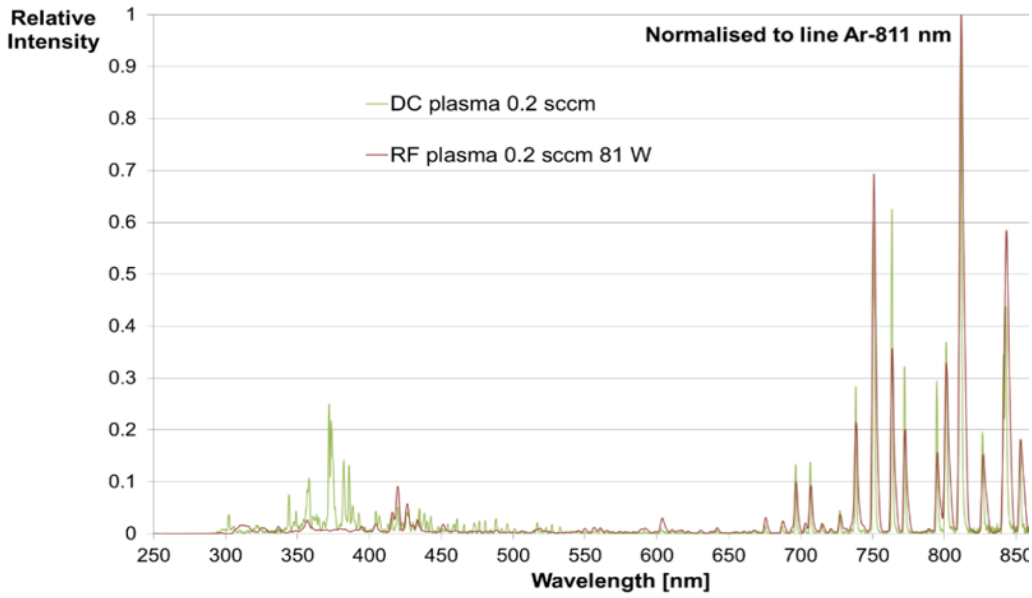

Figure 6.34 - Spectra of DC plasma (green) and RF plasma (red)

Some differences can be observed already between the DC and RF spectra, in particular in the lower wavelength range of the spectra. Figure 6.35 length range (650 – 850 nm) seem to match very well in wavelength number both for DC and RF plasma, however some differences in the relative intensities can be observed.

An analysis of the most intense argon I and argon II lines was undertaken. The most intense lines were selected from cross-sections from NIST databases (NIST ASD Team et al. 2013) and compared to the spectra recorded in this work.

Figure 6.35 shows a comparison shows the argon I lines superposed to the DC plasma and RF plasma. As it can be observed, the relative intensities of the argon I lines are very simmilar in both the DC and RF plasmas. identifies each of the argon I lines.

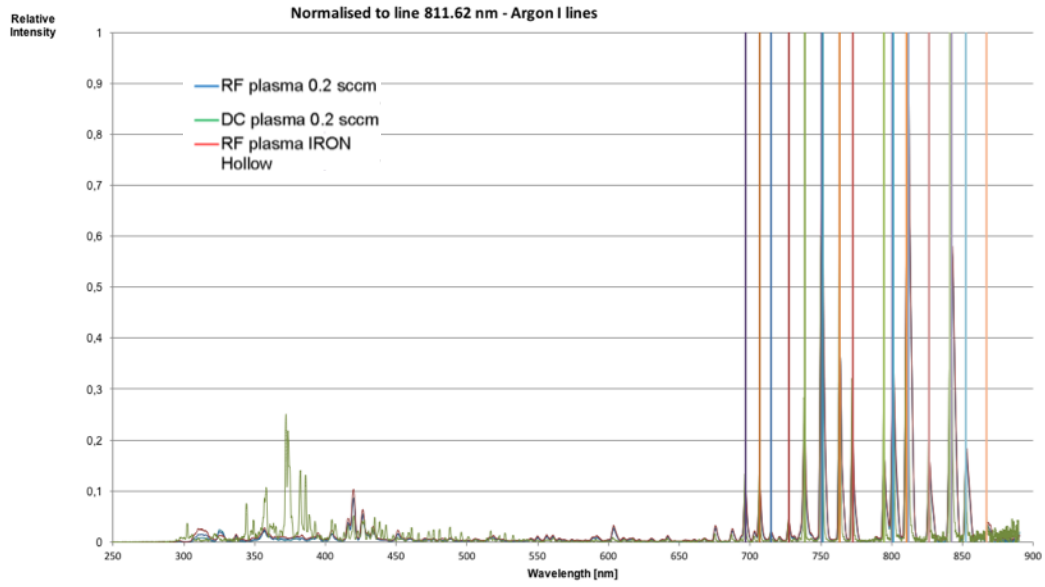

Figure 6.35 - Argon I lines on DC plasma and RF plasma comparison

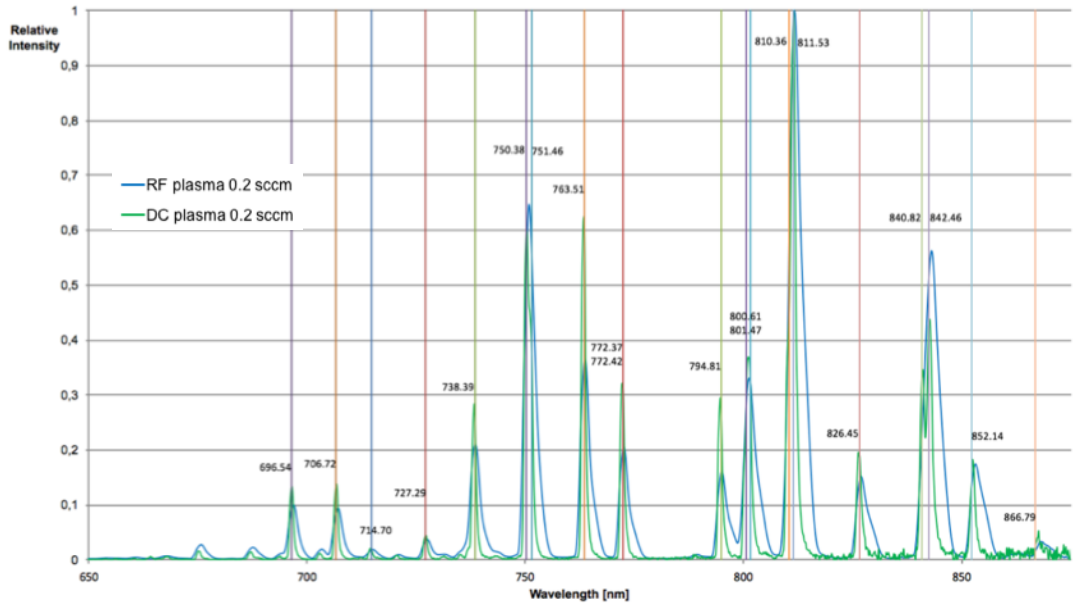

Figure 6.36 - Argon I lines identification in the DC and RF plasma cathodes within the 650 - 900 nm wavelength range

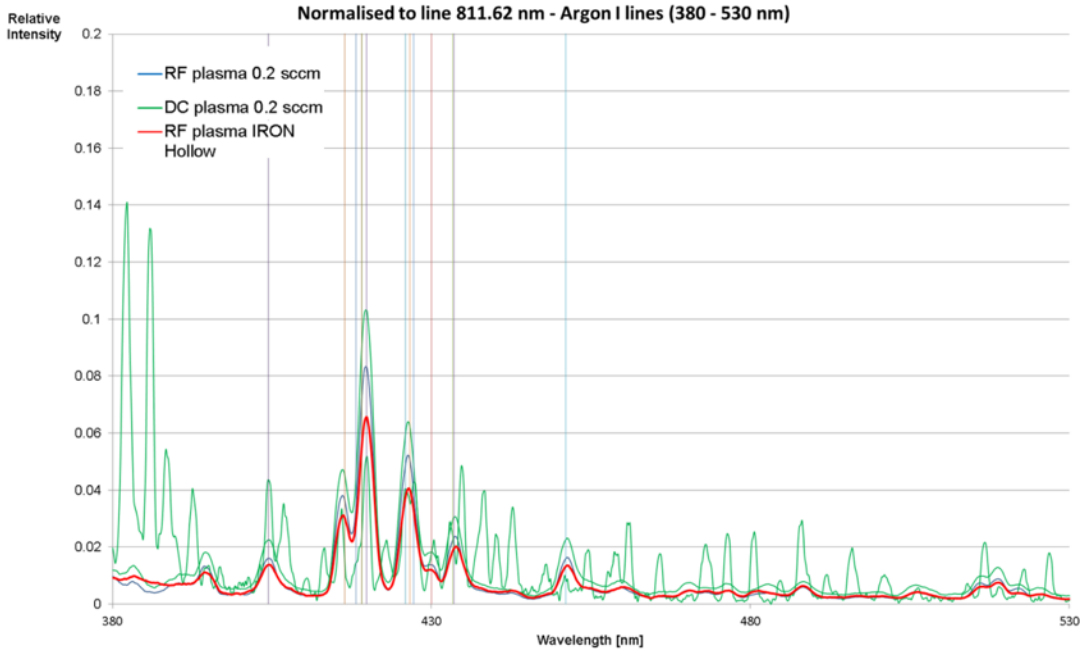

Figure 6.37 - Argon I lines identification in the DC and RF plasma cathodes within the 650 - 900 nm wavelength range

As expected, the argon I intensities were very similar in both the DC and RF plasma. In the following graphs, the argon II lines are studied. Figure 6.38 presents the DC plasma spectra compared to the RF plasma spectra and with argon II lines superposed.

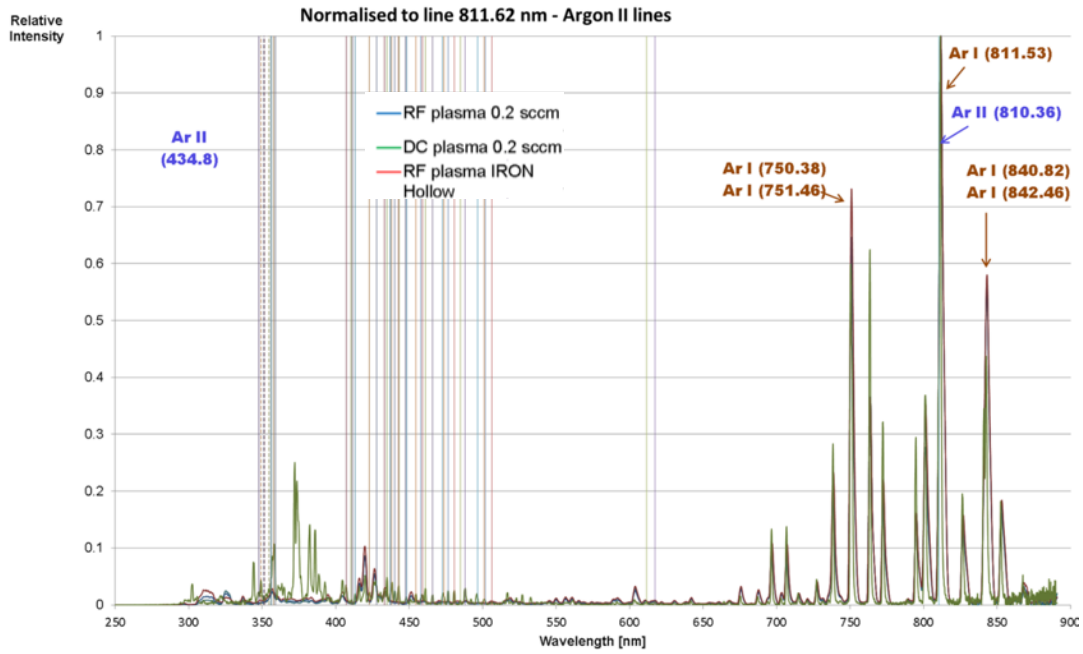

Figure 6.38 - Argon II lines on DC and RF plasma cathode spectra

Figure 6.38, Figure 6.39, Figure 6.40 and Figure 6.41 show the argon II lines superposed on a lower range of wavelengths each time.

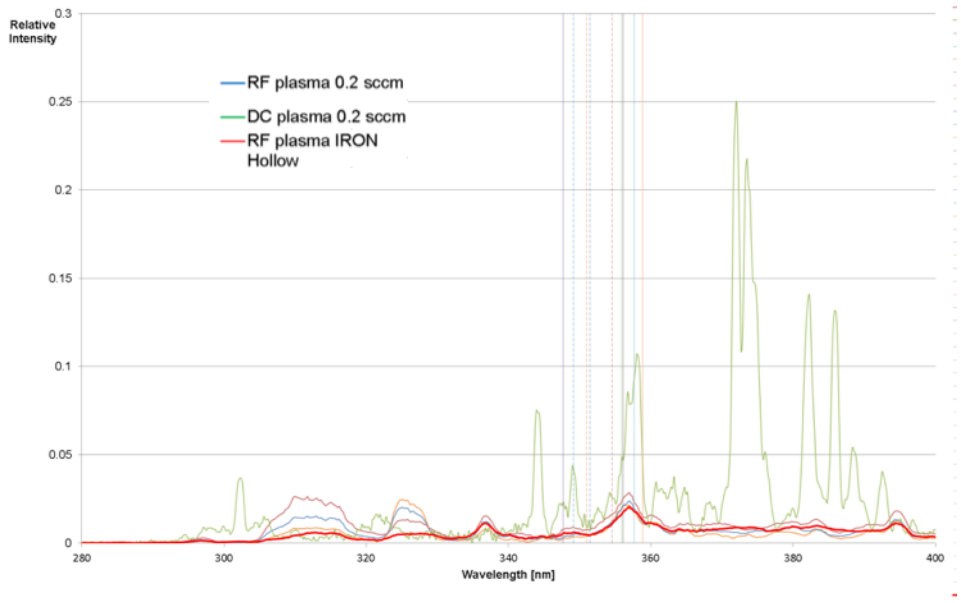

Figure 6.39 - Argon II lines identification on DC and RF plasma cathode spectra within 280 to 400 nm wavelenght range

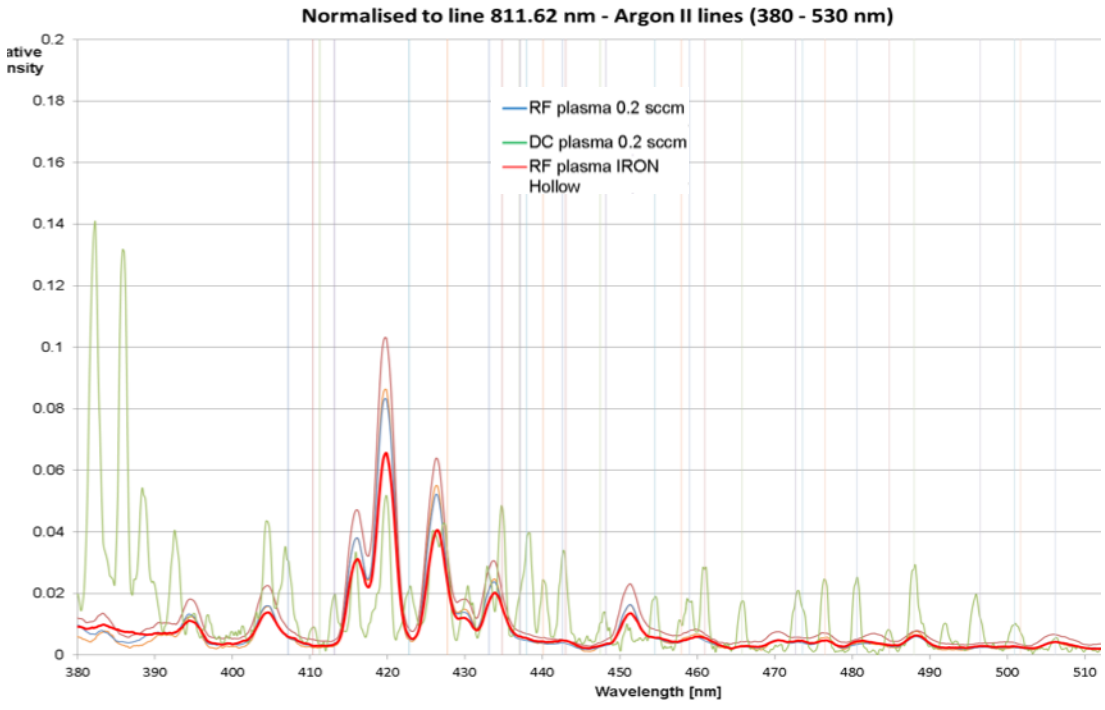

Figure 6.40 - Argon II lines identification on DC and RF plasma cathode spectra within 380 to 530 nm wavelenght range

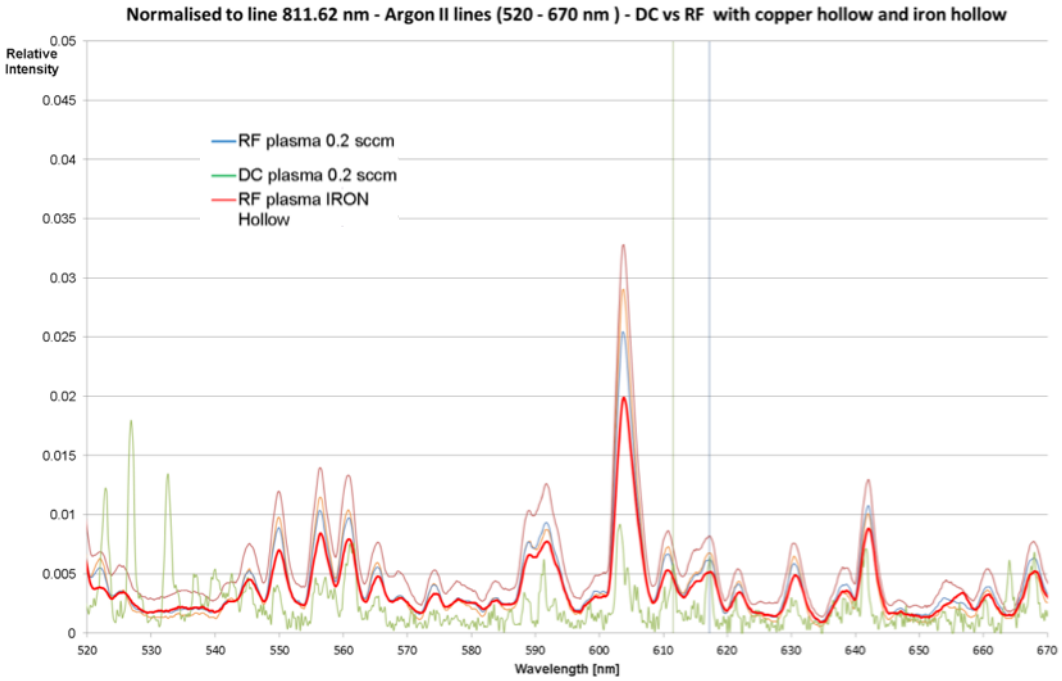

Figure 6.41 - Argon II lines identification on DC and RF plasma cathode spectra within 530 to 670 nm wavelength range

However, the lines that presented a larger intensity when comparing the DC plasma to the RF plasma were not identified as argon II lines. Thus, an analysis of other lines generated by the electrode materials present in the plasma chamber was carried out.

The hollow electrode of the RF plasma chamber is made of Cu. Thus, a search for Cu I and Cu II in the RF spectra was carried out. The aperture plates in both the DC plasma chamber and RF plasma chamber are made of iron. Fe I and Fe II lines were superposed to the DC and RF spectra. The closer identification was with the Fe I lines. Figure 6.42 shows the Fe I lines over the DC spectra (green) and RF spectra (red).

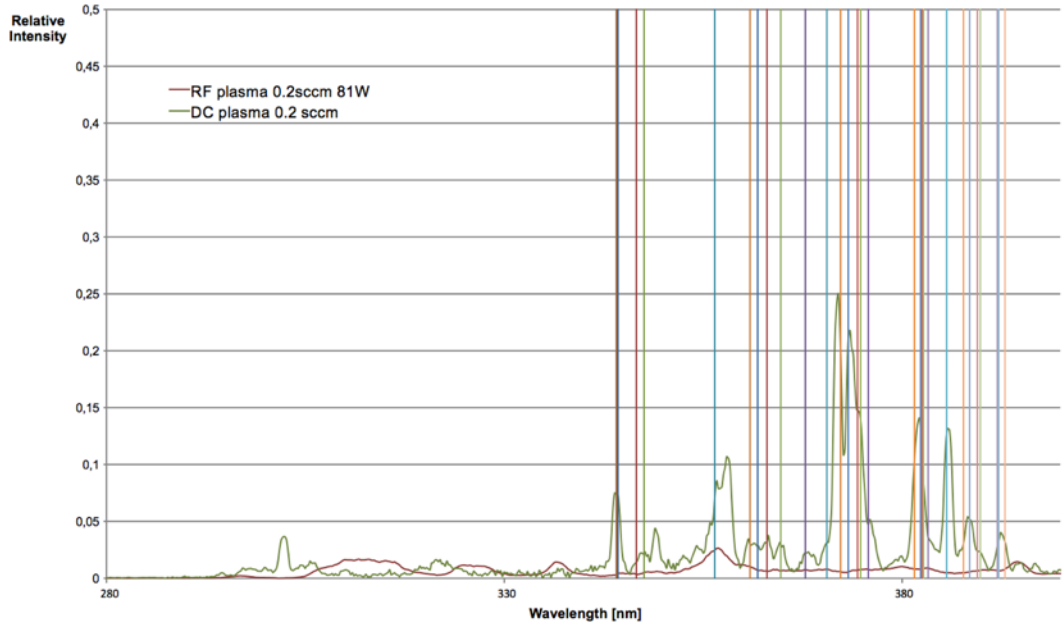

Figure 6.42 - Fe I line identification within wavelength rage from 280 to 400 nm

The Fe I lines seem to match the radiation emitted at the lower end of the spectra of the DC plasma. An iron hollow cathode was tested in the RF plasma cathode gun but no intense lines at the Fe I wavelengths were identified. The reason for this may be that the energy applied to the RF plasma chamber is much lower (RF power is limited) and thus is not enough to excite the Fe I lines and the argon II lines to the intensities that can be seen in the DC plasma cathode.

6.2.7. Use of Magnets

Permanent magnet rings were used while carrying out the spectroscopic measurements and EB current measurements. The results showed that magnets are needed to extract the maximum beam currents. The placement and B field magnitude of the ring magnets was found to be critical. The best configuration was found when using a permanent magnet of 0.6 T axial magnetic field or less around the middle of the plasma chamber axis. Higher magnitude magnets or magnets placed next to the aperture would not produce larger beam currents.

6.3. Summary

The gun has been tested by generating beams and characterising the optical emission spectra from the plasma. The different parameters were studied and the best configuration chosen from this work.

Increasing accelerating voltage increases EB current at any of the plasma cathode gun configurations investigated. The plasma cathode gun is a diode, and in contrast to thermionic diode guns which do not see this effect, its behaviour with accelerating voltage is closer to thermionic triode guns.

Flat electrodes (Parallel plate) were compared to hollow cathode designs. The results showed that hollow electrodes produced higher ionisation as expected. The flat electrodes design is limited and cannot generate a high density plasma. The reason is that the MFP is too long and there are not enough ionisation collisions. Inductively coupled plasmas can produce a higher electron density and this is an interesting topic to look at in future work.

The experiments showed that the EB current extracted - for a fixed accelerating voltage (-60 kV), plasma chamber design and pressure - increased with the area of the aperture. However, there was a limitation in the diameter of the aperture due to the amount of gas that leaked into the vacuum chamber and the risk of high voltage breakdown. As a result, for the pumps available, the maximum current was extracted with a 1.7 mm aperture with a flow rate of 0.3 sccm. It is recommended that more powerful pumps are used in order to allow opening the diaphragm aperture to a larger diameter and thus increasing the flow of gas to keep the plasma chamber pressure high enough for the plasma to strike.

Lower plasma pressure (produced by lower gas flow rate) is preferred as they produce higher EB currents. This was observed both in the RF and the DC plasma cathode guns. In addition, lower pressures reduced sputtering considerably on the plasma chamber and avoided HV breakdown in the vacuum chamber. The spectra ratios of the argon II lines showed that the intensities of the argon II lines was larger in compared to

lower pressures. Argon II lines indicate ionisation and thus larger beam currents as recorded in the lower plasma pressure measurements.

Electron beam current increases with excitation power. The EB current extracted so far is lower than the maximum beam current extracted from conventional thermionic guns. However, the power applied to the plasma chamber was limited by the heat dissipation. The beam current curve showed that as the power was increased, the EB current continued increasing, and no saturation point was reached in most cases as a result of space charge. In future developments the beam current could be increased further by increasing the amount of RF power applied to the plasma chamber further. In order to do this some cooling system would need to be included for the plasma chamber. The ratios of the argon II lines showed a higher ionisation at higher powers in comparison to lower powers, which were also the configurations generating the larger EB currents. Other lines showed contributions from other elements such as iron and copper. Copper electrodes were tested with RF and DC plasmas. However, the lines from Cu/Fe were more intense with the DC plasma in all cases. This may be due to the higher ionisation levels that occur in the DC plasma.

The plasma cathode gun design was optimised for maximum EB current with the available setup. The diaphragm aperture diameter was increased from less than 0.5 mm to 1.7 mm. The results agreed with the spectroscopic measurements: larger beam currents were produced from the larger plasma density cathodes. Within the experiments currents of 40 mA at –60 kV have been achieved. This power is significant and enough for material processing applications such as additive manufacturing, cutting or surface modification.

Chapter 7 : Simulation Work

The software package Opera-2d (Opera 2012) was used to simulate the electron acceleration in the plasma gun and the results of this are presented in section 7.2 of this chapter. This section also includes some simulations of electron beams extracted from a curved plasma boundary. The simulation work carried out on the cathode - the plasma chamber - is presented in section 7.3. The Opera-2d simulation package was introduced in Chapter 2.

7.1. Introduction

The plasma cathode electron gun has been described previously in this thesis (Chapter 4), and the main components are the electron source or cathode and the electron acceleration region. Optimisation of the beam intensity is important for many applications, and the plasma cathode electron gun was investigated for use at long projection distances from the lens, whilst retaining an intense spot.

7.2. Simulation of Electron Acceleration with Opera-2d

Chapter 3 presented a case study of a thermionic electron gun simulation, in which an emissivity value is given by the work function of the material and size. In the electron extraction simulation of the plasma cathode gun, the emissivity of the cathode was approximated by adding a surface to the model equivalent to a thermionic cathode.

The plasma cathode gun is a diode gun – there is no third electrode to control beam current as was the case in the simulation work carried out in Chapter 3. As a result, the design approach to produce a high brightness, high quality beam was different.

The simulation was setup as follows:

- The model was a diode gun design with the cathode at –60 kV and the anode at 0 V potential with no grid voltage. Figure 7.1 shows the high voltage (HV) electrode and aperture electrode geometry which were in contact and thus at

cathode potential. As the electron gun was axisymmetric, only the dashed area (orange) needed to be included in the simulation.

- The emitter material used was LaB_6 with a high emissivity value – as estimated for plasma cathodes. The cathode area was modelled to simulate the aperture area on the experimental plasma chamber, which was a 1.2 mm diameter circle.

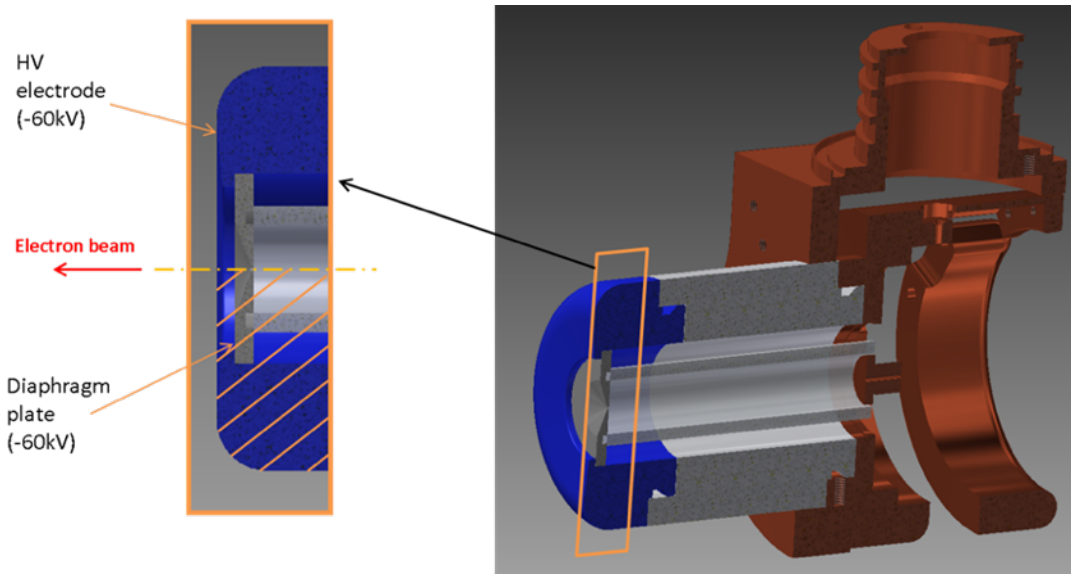

Figure 7.1 - 3D model of the plasma gun, showing the area that was used in the Opera-2d simulation with the HV electrode in blue and the diaphragm plate electrode at the front in grey

Figure 7.2 is a diagram of the Opera-2d axisymmetric model showing the HV and diaphragm plate electrodes (both shown as a single region in blue as they are at the same potential), as well as the anode (green).

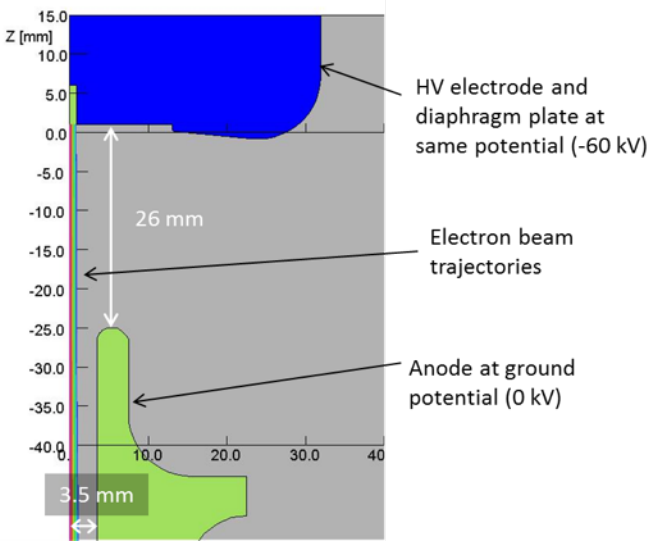

Figure 7.2 - Opera-2d model of the electron gun, showing the HV and diaphragm plate electrodes as a single region in blue at –60 kV, and anode at 0 kV in green

One of the problems found in the practical experiments was that the electron beam hit the anode bore. The anode bore diameter was opened to a larger diameter to avoid this. The Opera-2d model was updated with the corresponding larger size of the anode bore, which was Ø7 mm. Figure 7.3 shows the anode damage after a) 20 mA and b) 37 mA were generated from the plasma cathode and c) is the Ø7 mm bore anode.

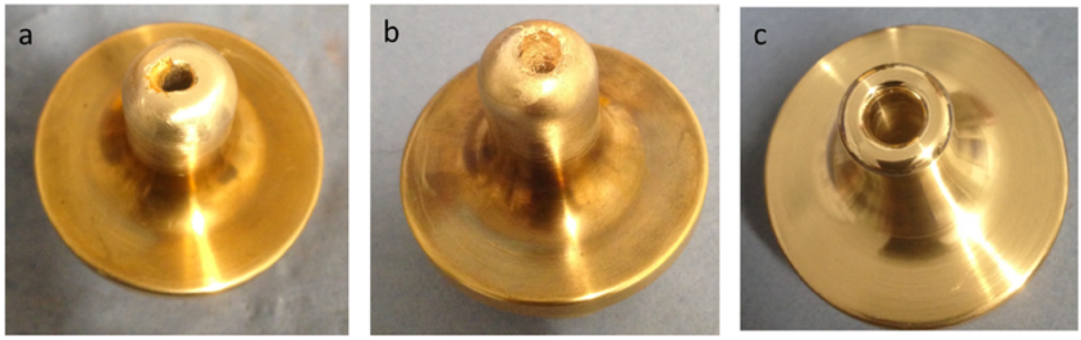

Figure 7.3 - Anode after generating beams from the plasma cathode at a) 20 mA b) 37 mA and c) anode after increasing the bore diameter

Additional changes were made to the diaphragm plate in order to keep the thickness of the flat front diaphragm plate at the aperture the same as in the original design. The simulation work was conducted in parallel with real world experiments to verify the design. From practical experiments, the flat front diaphragm electrode gave more beam current than the design with the angle at the aperture.

The aim of this set of simulations was to optimise the gun electrodes in order to increase the beam angle and thus beam diameter at the lens position. Generally, the larger the beam diameter is at the lens, the smaller the spot size that can be achieved at the focus position. However, this also depends on other parameters such as beam brightness as described in Chapter 2. The simulations were carried out with a flat front diaphragm electrode and the original HV electrode shape (as shown in Figure 7.2) which was gradually modified during several iterations. The simulations were run for cathode temperatures from 1500 K to 1800 K in 100 K temperature steps. The HV electrode was at –60 kV while the anode was at 0 V. The working distance was set at = –600 mm. The beam trajectories intersection was at –40 mm and lens position at = –200 mm.

The simulations were carried out for a range of beam currents from ~10 to 40 mA. The results presented below show the beam trajectories for 23 mA beams, as this was the closest to the beam current value generated during the practical experiments. The simulation results showed that currents of 23 mA would be generated from a cathode of 1.7 mm diameter hole.

Figure 7.4 shows the beam trajectories generated from the flat front aperture and the original HV electrode. It can be observed that the beam trajectories form a divergent beam but the angle is small. The HV electrode was modified to increase beam angle by two different approaches. The first approach was to try to produce a convergent beam that would crossover before the lens. This is easily achieved with triode guns. The second approach was to produce a divergent beam that would have a large diameter at the lens.

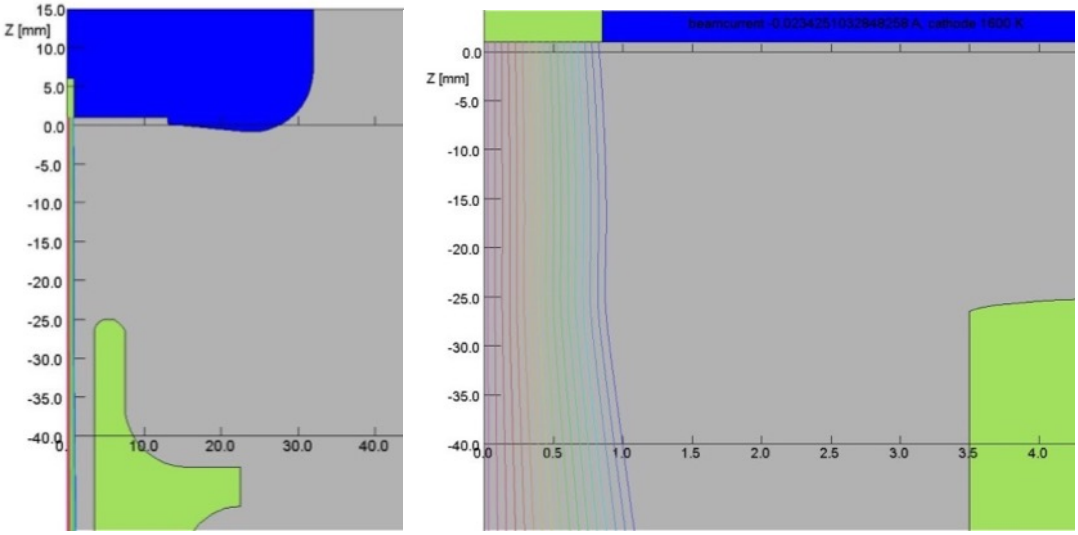

Figure 7.4 - Opera-2d model of the flat front diaphragm electrode with original HV electrode

First, the HV electrode was brought forward towards the anode, as shown in Figure 7.5. This design squeezed the trajectories towards a convergent beam. However, the HV electrode had to be brought forward a long way until the beam started to become convergent and the crossover did not happen as easily as with triode guns. In summary, changes in the HV electrode geometry away from the immediate region of the cathode had to be very large in order to influence the beam shape.

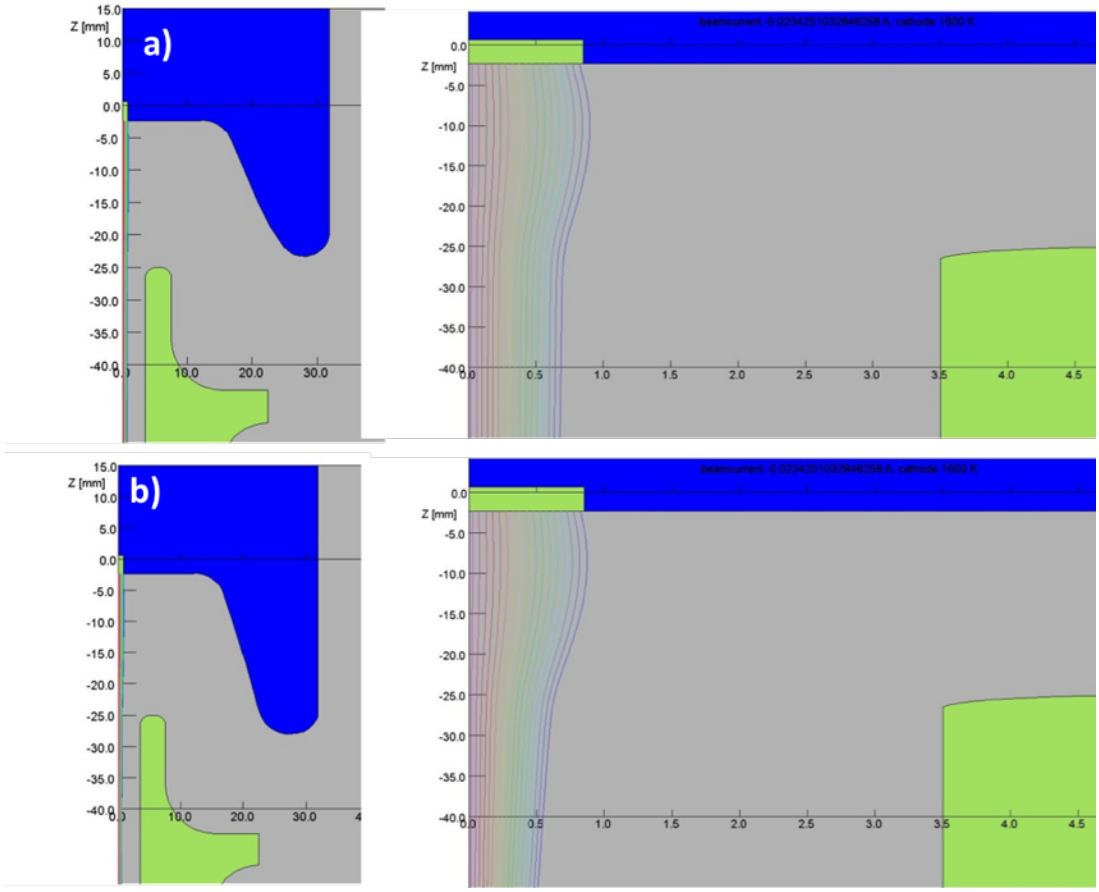

Figure 7.5 - Opera-2d simulation model of flat front diaphragm electrode with HV towards anode to produce convergent beam

Second, a divergent beam was generated by moving the HV electrode backwards. Figure 7.6 shows the results of the simulations with a flat front diaphragm plate and different HV electrode geometries. From a) to b) and from c) to d), the HV electrode was brought backwards with reference to the cathode. The beam angle increased in both cases but the spot size was not reduced as would be expected. Again, changes to the edges of the HV electrode did not affect the beam envelope or only affected the electron trajectories at the edges of the beam.

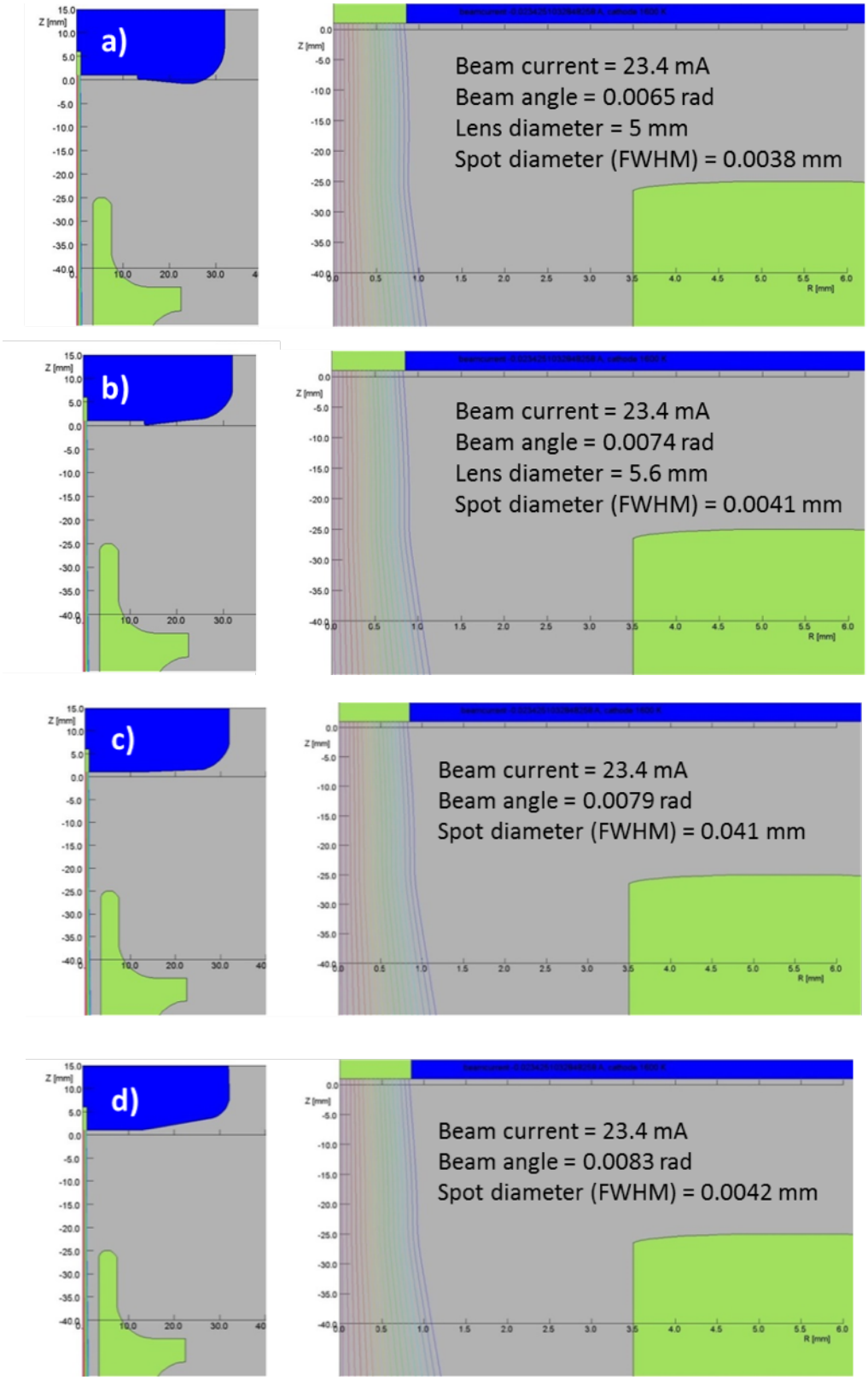

Figure 7.6 - Opera-2d model of the flat front diaphragm electrode generating a divergent beam

Changes in the area of the diaphragm plate closer to the aperture were modelled. Figure 7.7 a) shows a diaphragm plate design with round edges. Figure 7.7 b) shows a diaphragm plate design with set back on the area around the aperture. In both cases the beam angle was increased more readily than with the flat front plate. In general terms, changes in electrode geometry in areas close to the aperture made a large impact on beam shape.

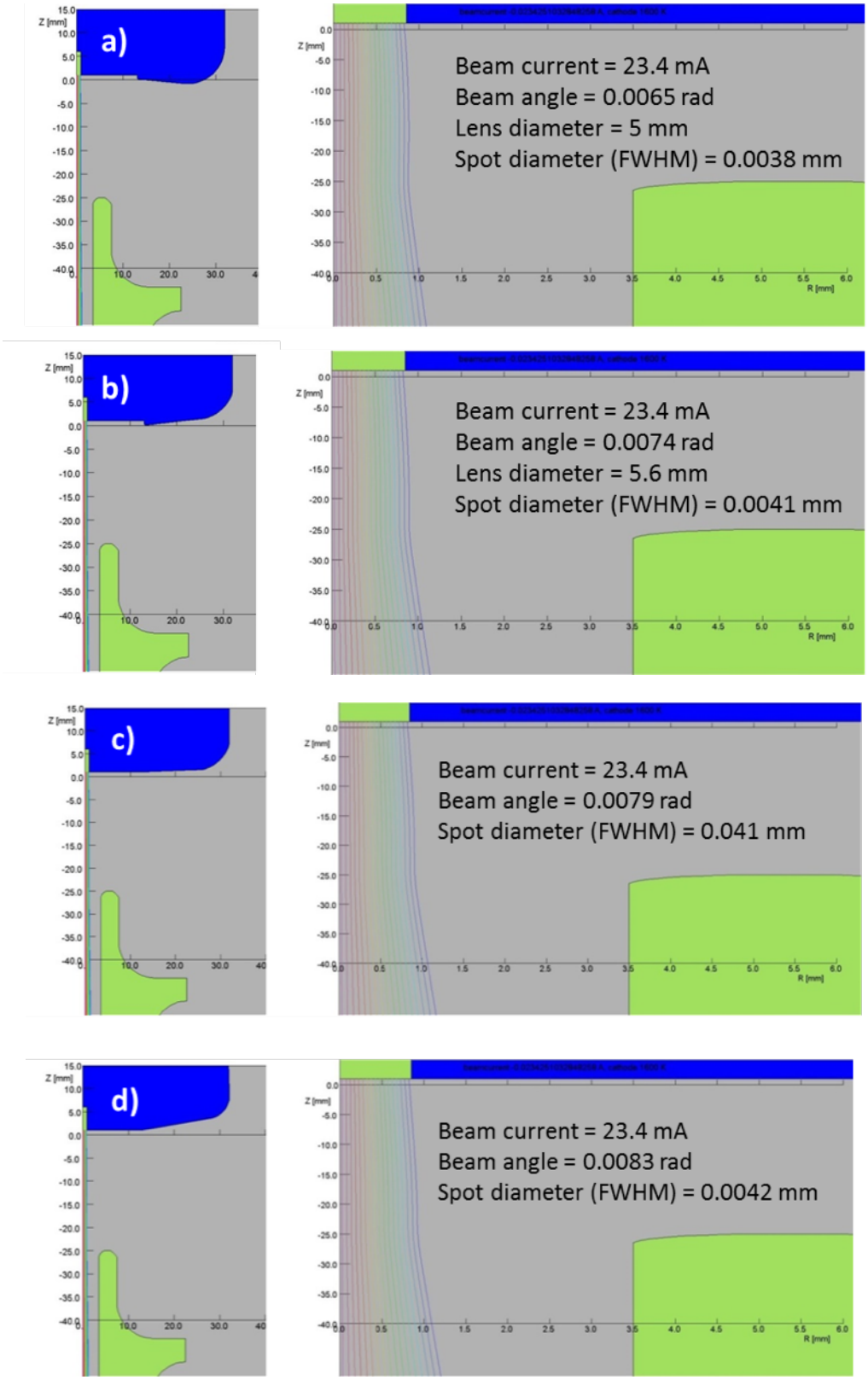

Figure 7.7 - Opera-2d simulation model of modified front diaphragm electrode

Figure 7.8 shows the different iterations in design carried out for the diaphragm plate with a bump on the front. First, the bump plate was modelled with a larger area anode (design a). Second, the bump was brought forward towards the anode (design b). This change increased the beam angle as well as reducing the beam spot diameter. Design c) was an extension of model b) with a smaller anode area (as in the original anode in Figure 7.5), and showed a reduction of the beam angle and thus an expected increase in the beam spot size. The next iteration of the design d), was developed from model c) with the HV electrode moved backwards. The outcome of this modification produced similar results to those shown in Figure 7.6, where changes in the edge area of the HV electrode increased the beam angle but did not decrease the beam spot size. Thus, in the final design, which was chosen for manufacturing and testing, the original HV electrode was tested with the bump electrode which gave a larger beam angle and a smaller spot size in the simulation results. This design e) showed an increase in beam angle and decrease in beam spot diameter.

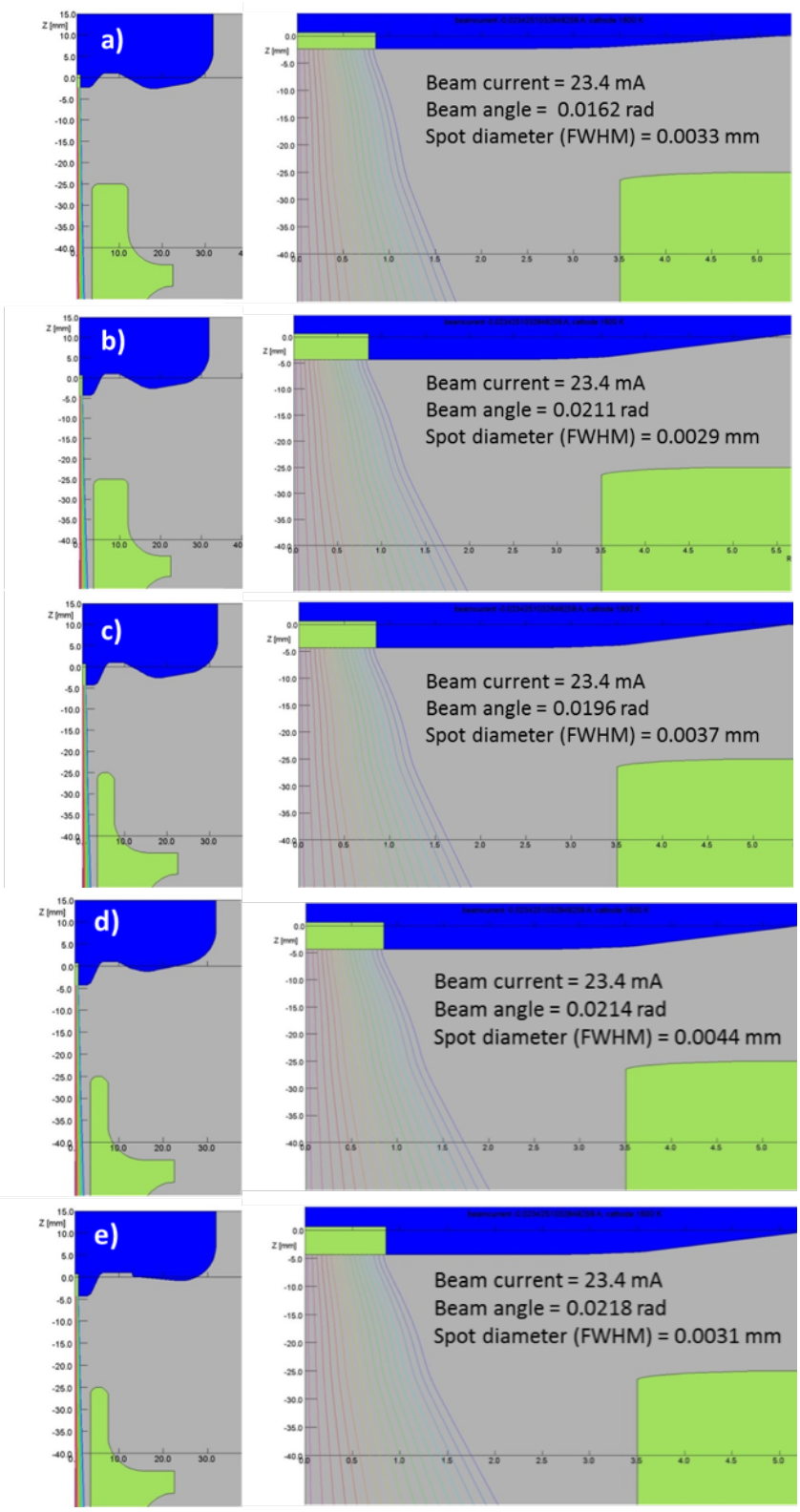

Figure 7.8 - Opera-2d simulations of the bump front diaphragm plate and different geometry iterations: a) Larger anode area; b) Bump brought forward; c) Bump brought forward and small anode area; d) HV electrode brought backwards; e) Bump plate and original HV electrode

Two ways of generating higher angle beams that give higher diameter in the lens were investigated and carried out with the simulations. However, the divergent design gives a more intense beam than the crossover design. This is because the brightness is better, and the magnification is less, because of the apparent electron source position. Brightness may be better for divergent guns generally because of the lower influence of space charge giving less aberration.

The bump design was manufactured and tested in the plasma cathode gun to extract beams at 60 kV. Figure 7.9 shows bump front diaphragm plate design that was chosen from the Opera-2d simulations:

Figure 7.9 - Forward bump diaphragm plate manufactured according to design from Opera-2d simulations

Beam shape can be optimised in conventional thermionic electron guns by modifying the gun electrode geometry –changing the cathode (or grid cup if the electron gun is a triode) and anode. In the plasma cathode gun the beam shape cannot be controlled in the same way as with conventional or triode guns. The beam shape was improved in the simulation as the angle was increased and thus the spot size has been reduced to less than 50 μm. However, when the diaphragm plates have been manufactured and tested in the gun, the beam diameter was not smaller than 0.7 mm.

Other possible causes and ways to reduce beam diameter were explored:

- Space charge in the vacuum chamber environment – Pressure in a plasma cathode gun is higher than in conventional guns (~10^{-4} mbar). It was observed that the vacuum chamber lit up in the dark when the RF power was increased sometimes. The pressure decreased in the vacuum chamber after some leaks were found and fixed. However, even with a pressure of order 10^{-5} mbar no significant changes in beam diameter were observed.
- Aperture diameter – Beams were generated with aperture diameters of 0.5, 0.7, 1 and 1.2 mm but no substantial change in beam diameter was found.
- Magnetic field effects – It was observed that the ring permanent magnets were needed to produce the maximum electron beam current from the plasma cathode. However, in the practical experiments it was also noticed that having the permanent magnets too close to the aperture or having a magnet with a very high value of magnetism would affect the beam trajectories and make the beam wider.
- Plasma boundary – The effect of the plasma boundary on the beam quality was studied and conclusions are presented below.
- RF cycle – The effect of the RF cycle in the generated beam quality is discussed later in this chapter (section 7.3).

Until now the electron beams had been generated and simulated from a flat cathode surface. This cathode shape is comparable to the shape of a metallic filament which has a flat surface. However, this may not be the case with plasma cathodes. When looking at the plasma chamber aperture from the side, the plasma is seen to extend outside the plasma chamber, appearing as a round shaped flame extending into the vacuum chamber.

In order to get an estimate of the plasma boundary shape, different plasma boundaries were modelled and the beams extracted from them were simulated and compared to the practically observed beam diameters. Figure 7.10 below shows some examples of the range of plasma boundary shapes simulated.

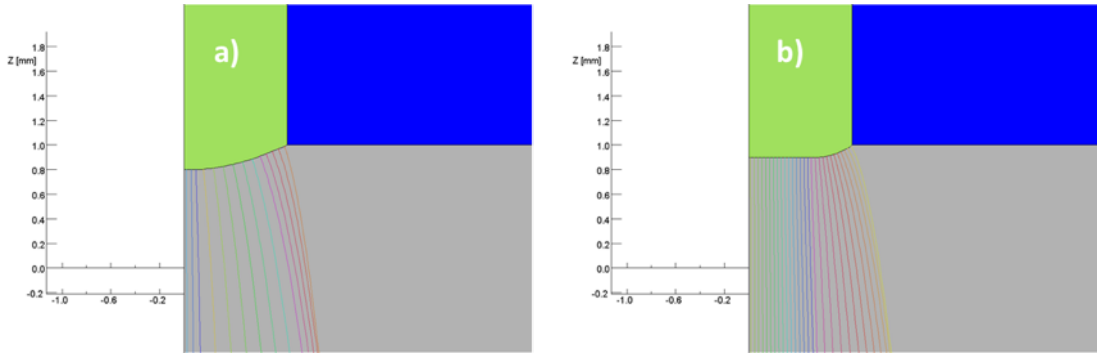

Figure 7.10 - Opera-2d simulations showing electron trajectories extracted from two different cathode boundaries

Figure 7.11 shows the range of cathode boundary simulations that were carried out. Except for the top simulations shown which have zero curvature – flat cathode surface; the simulations on the left have a negative curvature –concave cathode surface, whereas the simulations on the right have a positive curvature –convex cathode surface. The range of simulations simulate beam trajectories from plasma boundaries with an offset relative to the flat surface of 0.02 mm to 0.5 mm.

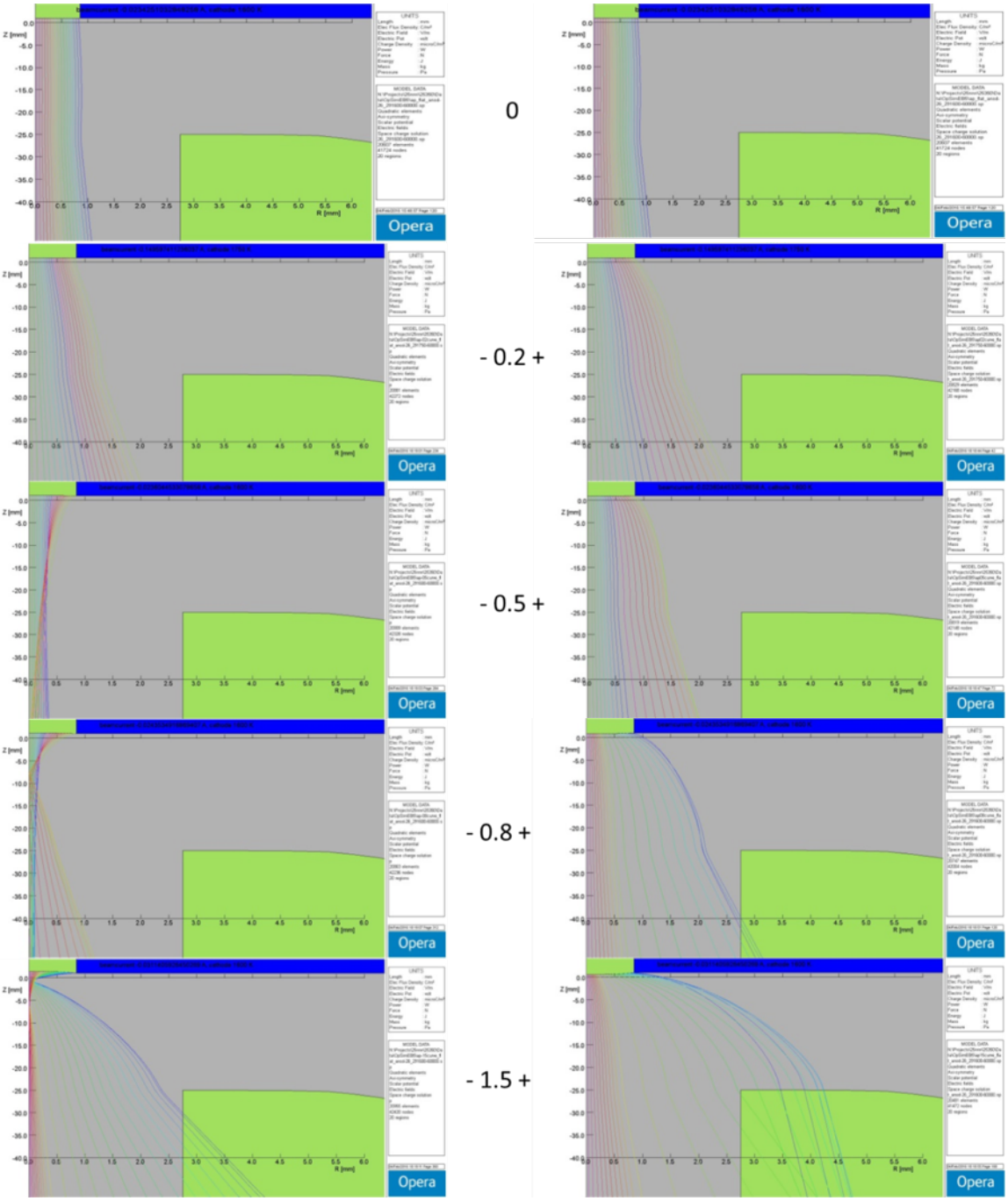

Figure 7.11 - Opera-2d simulation showing electron trajectories of beams generated from cathode surfaces with different curvatures. Top figures are for the original flat cathode surface, negative curvatures (on the left) indicate concave cathode surfaces and positive curvatures (on the right) indicate convex cathode surfaces

The results show that even for the smallest curvature, the beam trajectories were highly affected. The changes observed were larger than the changes resulting from modifications to the electrode geometry. This would explain why the beam diameter did not seem to be reduced in the practical experiments with the optimised electrode geometry that was designed in the simulations to give a small spot size. Further work is needed to investigate ways to reduce the curvature of the plasma boundary and its effect on beam quality.

7.3. Simulation of the Plasma Cathode With Vsim: A Model for Low Temperature, Low Pressure Plasma

As described in the literature review chapter of this thesis, low temperature low pressure plasmas are in non-thermal equilibrium. This means that the electrons have much higher energies than the other particle species in the plasma (ions and neutrals). In order to model the electrons, a particle in cell (PIC) model was used. The software VSim developed by Tech-X was found to be suitable for this type of plasma simulation. VSim uses a fluid model for the heavy and slow particles such as ions and neutral atoms, whereas the faster species such as electrons are modelled by PIC simulations (Tech-X Corporation 2016).

Electron collisions are relevant and for this Monte Carlo simulations are used to model the most relevant mechanisms occurring in argon low pressure low temperature plasmas:

- Ionisation: $e + Ar \rightarrow Ar^{+} + 2e$
- Excitation: $e + Ar \rightarrow e + Ar^{*} \rightarrow e + Ar + photon$
- Elastic scattering: $e + Ar \rightarrow e + Ar$

Modelling of complex geometries is possible with VSim, however, the model in this work was simplified due to limitations in computer power and processing time. Thus, even though the plasma chamber geometry in the real experimental setup is a hollow cathode, a parallel plate simple geometry was used in the VSim model. Some measurements were taken with a practical parallel plate plasma chamber for comparison with the simulations.

The software runs in short time steps where the particles are moved according to fields and collisions. Data is not recorded for every time step but is written out of the simulation (data dumps) at regular intervals to be interrogated by the user.

The plasma chamber was simulated as a parallel plate, axisymmetric, capacitively coupled RF excited argon plasma, as presented in Figure 7.12. The *x* length (LX) is the plasma chamber electrode gap; the *y* length (LY) is the size of the simulated electrodes face in the simulation – note only a thin element of the plasma chamber is modelled; the z length is the depth of the plasma chamber – which is close to infinite compared to the plasma chamber LX and LY sizes. In this example, the model simulated a plasma chamber with an electrode gap (X direction) of 76 mm, which reproduced the largest electrode gap that was used in the practical experimental setup.

Once the size of the plasma chamber was defined, the number of cells for each direction (LX, LY, LZ) was defined in the simulation by NX, NY and NZ respectively. Figure 7.12 shows that the number of cells for that particular simulation model was 800 in the *x* direction, 2 cells in the *y* direction and 2 cells in the *z* direction.

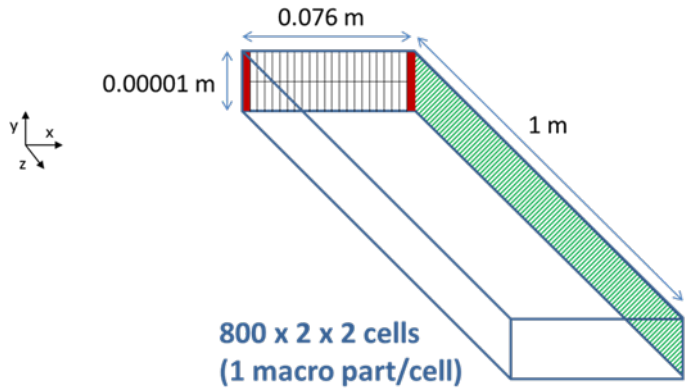

Figure 7.12 - RF plasma chamber quasi-2D model in VSim

The estimated particle density (nominal electron density) was defined in the model. Then the number of macroparticles per cell was specified. Each macroparticle contained a number of particles, and this number can be defined. The nominal particle density, the number of cells and initial number of macroparticles per cell determined the total number of particles per macroparticle.

The plasma was generated by an RF discharge at 84 MHz (each RF period taking 11.9 ηs). This means the plasma chamber electrodes changed their polarity each half cycle, thus the electrons in the plasma were attracted by a different electrode each half cycle. As the electrons were much lighter than the ions, they could reach the chamber walls sooner, whereas the heavy ions did not have time to move much before the polarity of the electrodes changed again.

Figure 7.13 is an example of a model with a 10 mm electrode gap and an RF discharge of 1000 V at 84 MHz. The nominal electron density was 5×10^{15} m^{-3}. The simulation was run with 12 data dumps per period (0.992 ηs per dump). The cloud of electrons (primaries in green and secondaries in blue) were attracted to the left wall electrode during dumps 250 to 252. At around that time the polarity changed and then the electrons were attracted to the right wall electrode during dumps 254 to 258. Around dump 258 the polarity changed again and the electrons went back towards the left wall to complete the RF cycle.

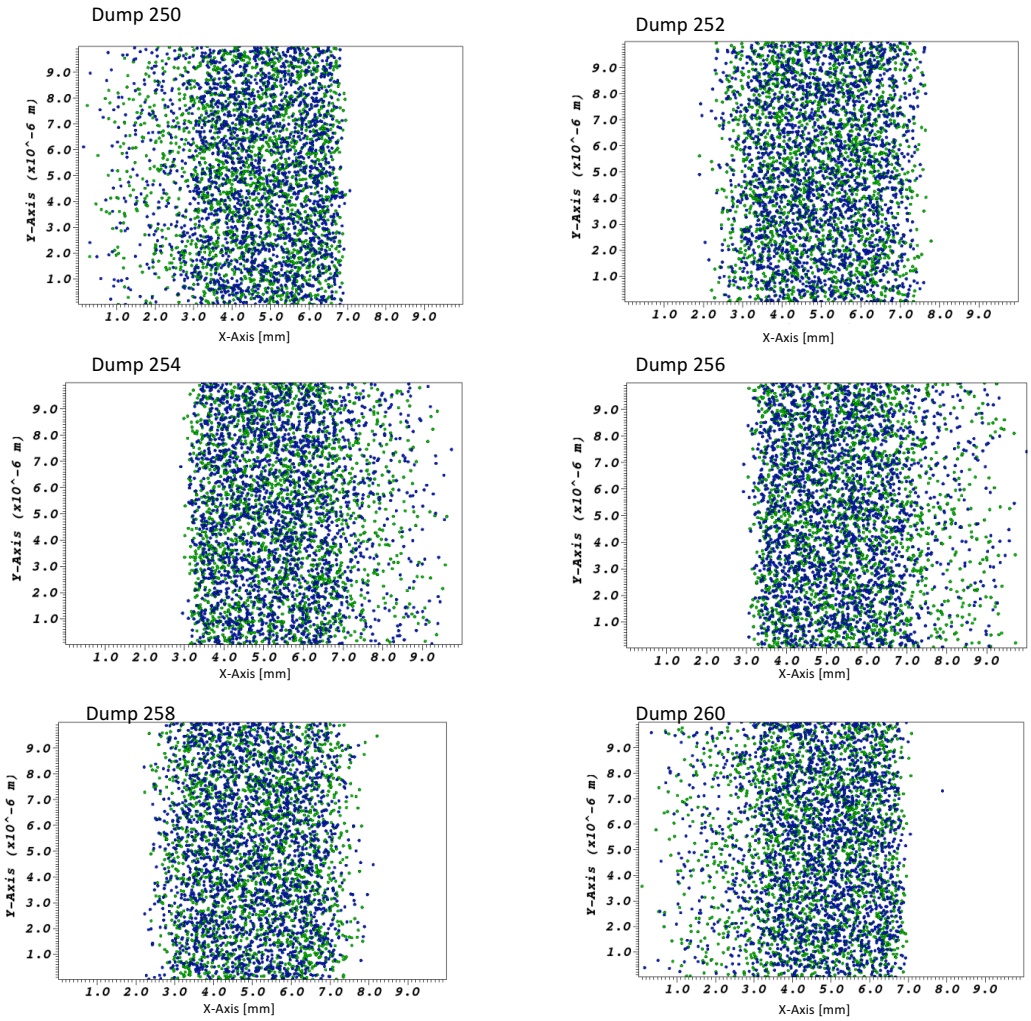

Figure 7.13 - Electron cloud (primaries in green and secondaries in blue) oscillating with RF cycle in a 10 mm electrode gap chamber (800 × 2 × 2 cells) at 0.02 mbar and 1000 V discharge voltage

However, the ions, shown in red in Figure 7.14, changed their position very little during the RF cycle. As a result, the area next to the discharge electrodes was less negatively charged than the centre of the plasma chamber where most of the electron cloud was concentrated. This less negatively charged area next to the plasma chamber electrodes oscillates with the RF cycle and constitutes the plasma sheaths.

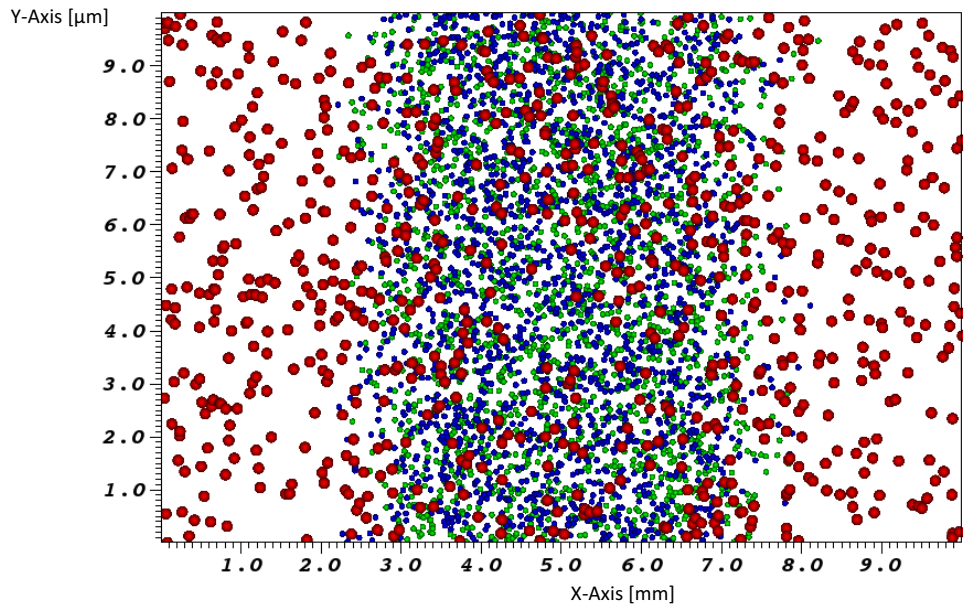

Figure 7.14 - Electron cloud (primaries in green and secondaries in blue) oscillating with RF cycle and heavy ions (red) unaffected by oscillating RF field

Figure 7.15 shows the history plot for the different particle species densities during a simulation that was run for 1 µs. First, all particles including ions (in red), primary electrons (in green) and secondary electrons (in blue) were gradually added to the model over a number of time steps (loaded) for about 0.04 µs. Then the different mechanisms (collisions of different species) occur, primary electron densities decrease as expected while secondary electrons densities increase, and the plot approaches steady state.

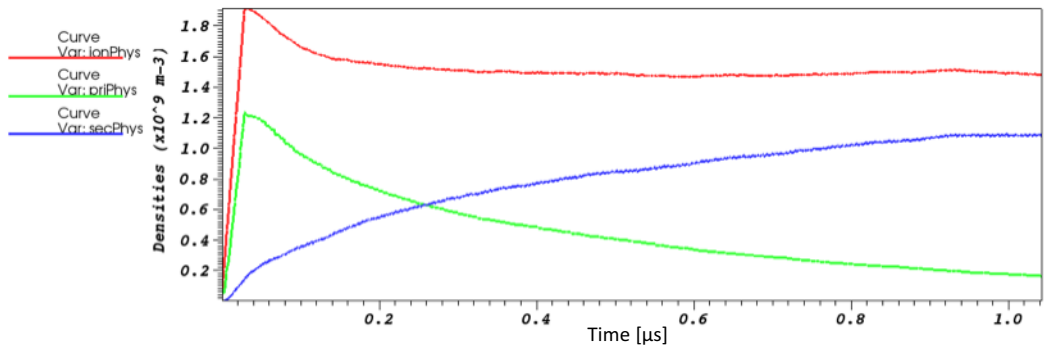

Figure 7.15 - Particle density plots over time showing heavy ions (red), primary electrons (green) and secondary electrons (blue)

The total current on each wall of the plasma chamber is shown in Figure 7.16. The resolution was low due to the number of macroparticles used in the simulation (1 macroparticle per cell in a 800×2×2 cell simulation), which was limited by the computer power and processing time available. The wall currents can be plotted in VSim and are given by the number of macroparticles hitting each wall (called ions, primaries and secondaries in VSim) or the number particles hitting each wall (called ion physics, primary physics and secondary physics in VSim). The graphs in Figure 7.16 plot the particle densities of the different particle species. The particle density is obtained by multiplying the number of macroparticles that hit each wall by the number of particles per macroparticle.

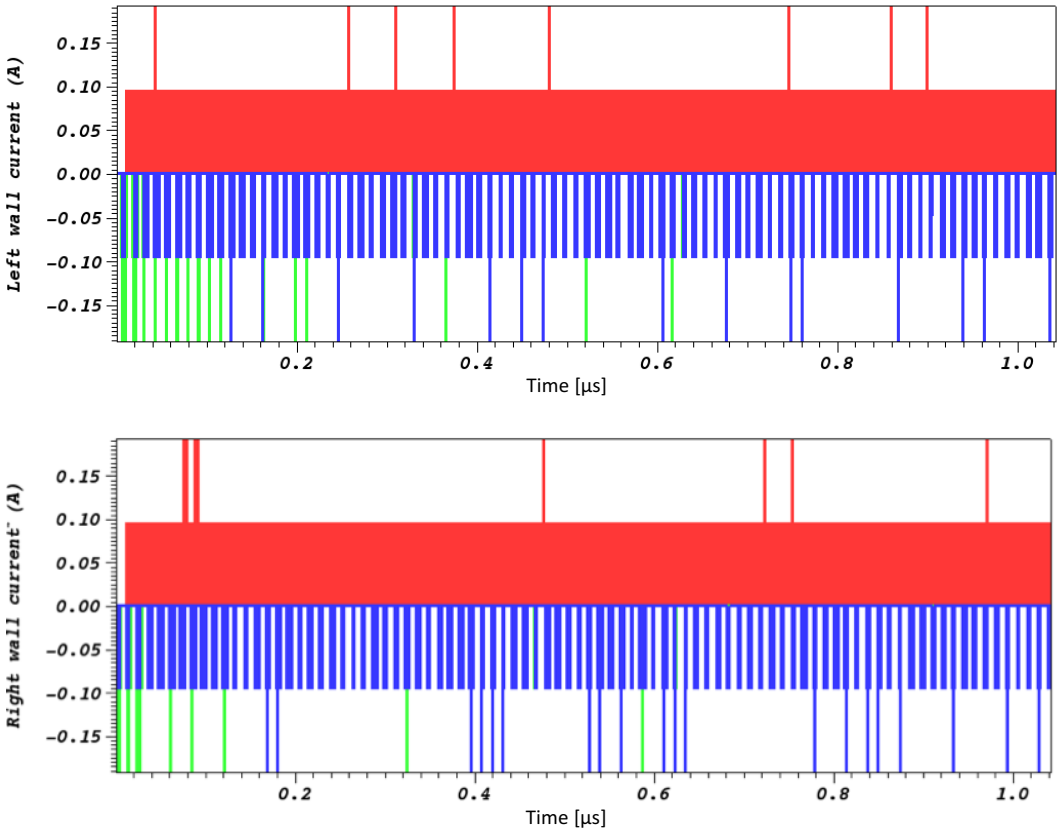

Figure 7.16 - Left and right wall currents showing heavy ions current (red), primary electrons (green), and secondary electrons (blue)

The charge equivalent to each macro particle can be calculated from $Q=I\times t$; where t is the time difference and I is the current from the graph, which has units of amps per

meter. Each of the current peaks corresponds to a differential of t. The average current over a time interval can be calculated by running a small file within the VSim software called analyser.

The current density on the right wall from which an electron beam was extracted can be calculated. This gives an estimate of the current that could be extracted from each plasma model that was simulated, and allows comparison of this value with the measured current extracted in the practical experiments.

The current density $\vec{J}$ can be calculated as the product of multiplying the charge of each carrier q (1.6×10^{-19} C), the number density n of the charges (n charge carriers per unit volume), and the charge carriers velocity $\vec{v}$ or drift velocity (*$\vec{v}$* and $\vec{J}$ point in opposite directions for negative charge carriers):

$$\vec{J} = -qn\vec{v}$$

One can consider, $\vec{F}$ is the electric force that an electron experiences:

$$\vec{F} = q\vec{E}$$

This force is also calculated as the product of the electron mass m multiplied by the acceleration $\vec{a}$. Thus the following expression can be derived containing w:

$$\left.\begin{matrix} \vec{F} = m\vec{a} = m\dfrac{d\vec{v}}{dt} = m(iw)\vec{v} = imw\vec{v} \\ \vec{F} = q\vec{E} \end{matrix}\right\} qE = -mwv;$$

From this expression the electron velocity can be calculated as:

$$v = -\frac{qE}{mw}$$

Thus, the current density $\vec{J}$ is:

$$\vec{J} = qn\vec{v} = -\frac{q^2nE}{mw}$$

In the 0.076 m electrode gap model, with a nominal electron density of 2.5×10^{15} m^{-3}, 1000 V discharge, and 84 MHz the current density per square meter will be:

$$J = \frac{(1.6\times10^{-19}\text{C})^2(2.5\times10^{15}\text{m}^{-3})\left(\frac{1000\text{ V}}{0.076\text{ m}}\right)}{(9.11\times10^{-31})(2\pi84\times10^{6}s^{-1})}$$

From calculations, the current density obtained per square meter was:

$$J = 1.8\times10^{3}\text{A/m}^2$$

The current over the area of one electrode (green area in Figure 7.12) in the VSim simulation would be:

$$I_{model} = \left(1.8\times\frac{10^3\text{A}}{\text{m}^2}\right)(0.00001\text{ m}\times 1\text{ m}) = 0.018\text{ A} = 18\text{ mA}$$

The current over the area of one of the electrodes in our real plasma chamber would be:

$$I_{real} = \left(1.8\times\frac{10^3\text{A}}{\text{m}^2}\right)(0.01\text{ m}\times 0.01\text{ m}) = 0.18\text{ A} = 180\text{ mA}$$

In addition, a particle sink macro was added in the RF CCP parallel plate simulation to model the electrons leaving the plasma chamber as an electron beam is extracted, as happens in the practical experiments.

However, as the simulation models only a 2D chamber with a 1 m z-axis, there were some adjustments that needed to be done when analysing the results. Figure 7.17 shows the equivalent of the particle sink area in the simulation compared to the aperture area in the practical plasma chamber.

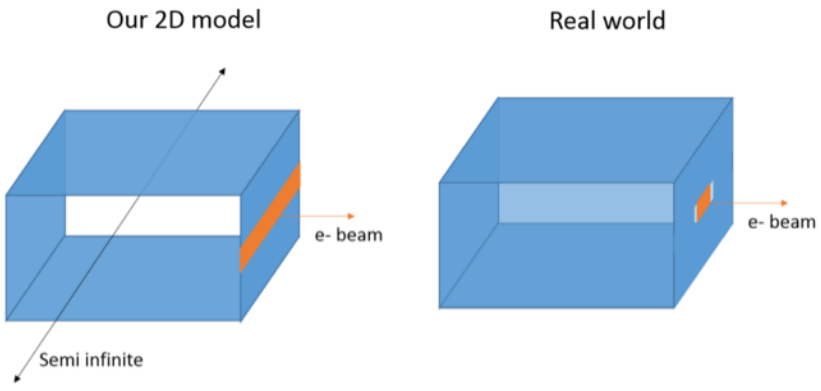

Figure 7.17 - Diagram showing comparison of EB current calculated from plasma chamber model in VSim and EB current extracted from real plasma chamber (Tech-X Corporation 2016)

The phase-space plots in Figure 7.18 show the momentum for the ions (red) and electrons (green) from data dumps 250 to 260. The x-axis is the *x* position of the

species and the y-axis indicates the x component of their velocity. The y-axis has been normalised to the unit cube so that the ions velocity is shown in the same plot as the electrons, but it should be noted that the scales are different: the ions velocity is a lot smaller than the electrons velocity, due to the ions being heavier and thus not following the RF cycle as the electrons do. It can be seen that the ions velocity is very uniform during the RF cycle. On the other hand, the electrons velocity is changing as the electrons oscillate from one wall to the other, following the changes in polarity dictated by the 84 MHz RF excitation signal, as well as a result of the collisions with other electrons or ions.

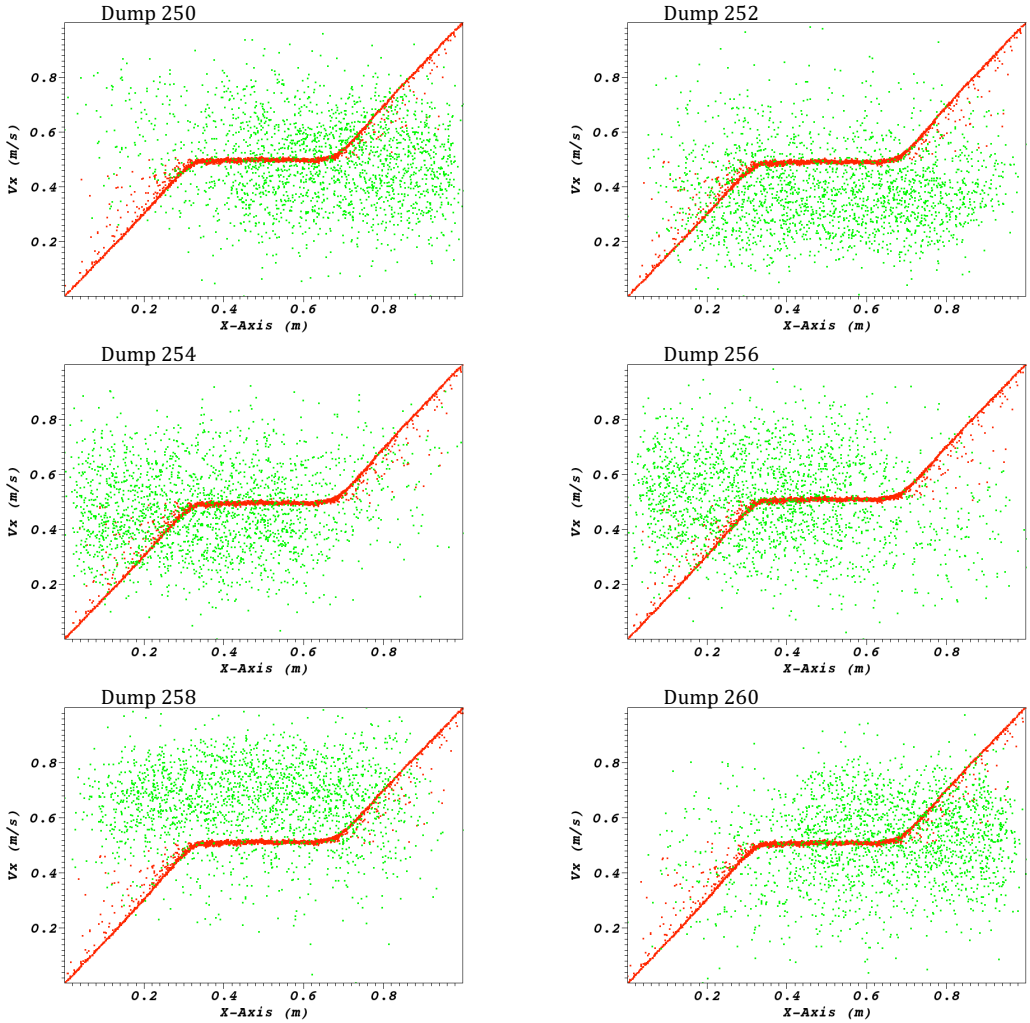

Figure 7.18 - Phase-space plots of the electrons cloud and ions (data dumps 250 to 260)

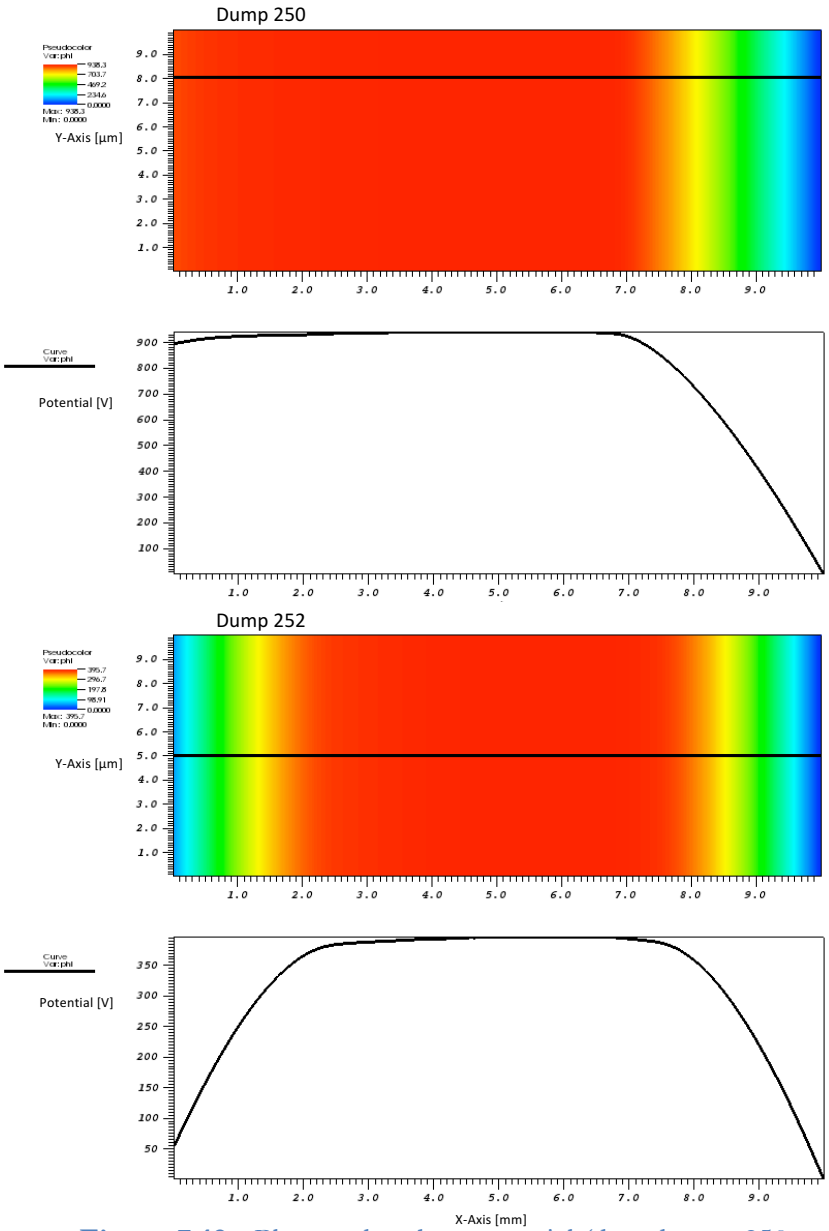

Figure 7.19 - Plasma chamber potential (data dumps 250 to 252)

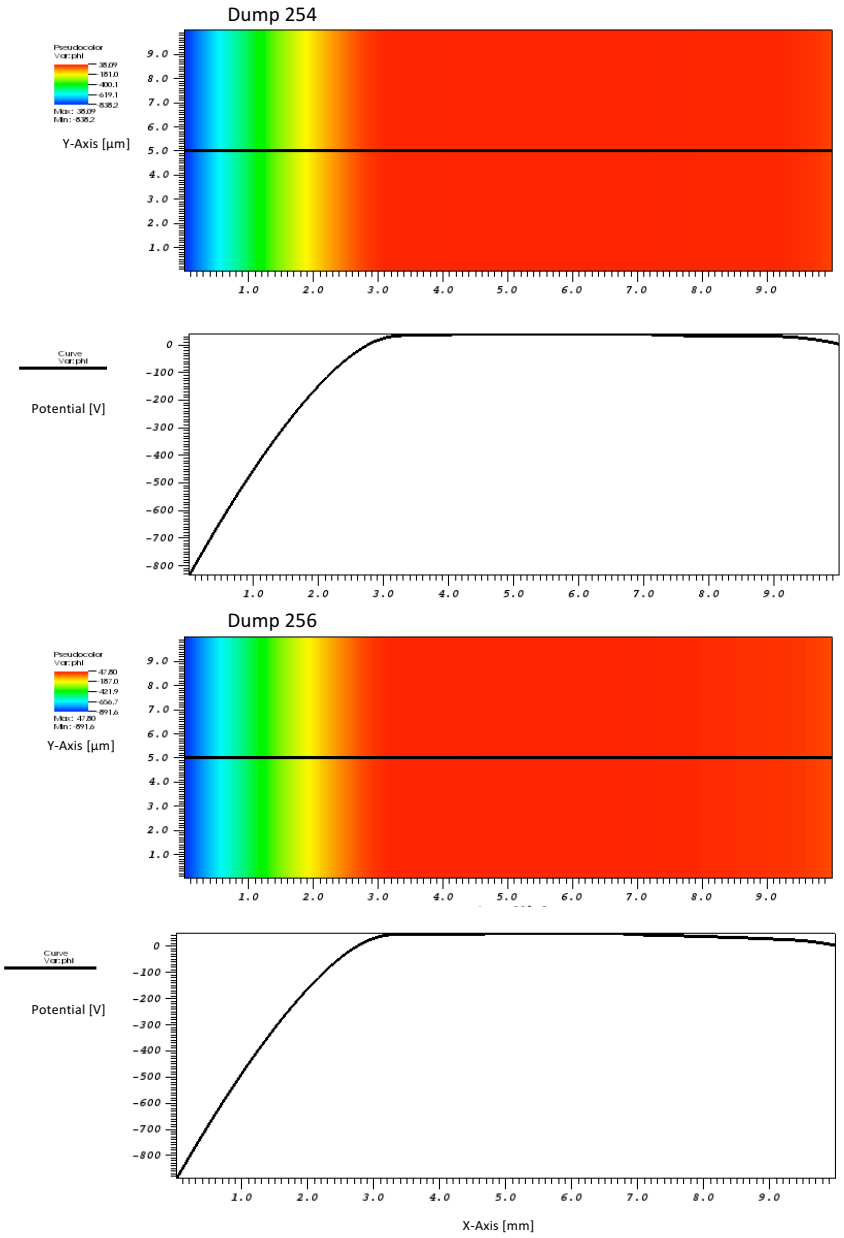

Figure 7.20 - Plasma chamber potential (data dumps 254 to 256)

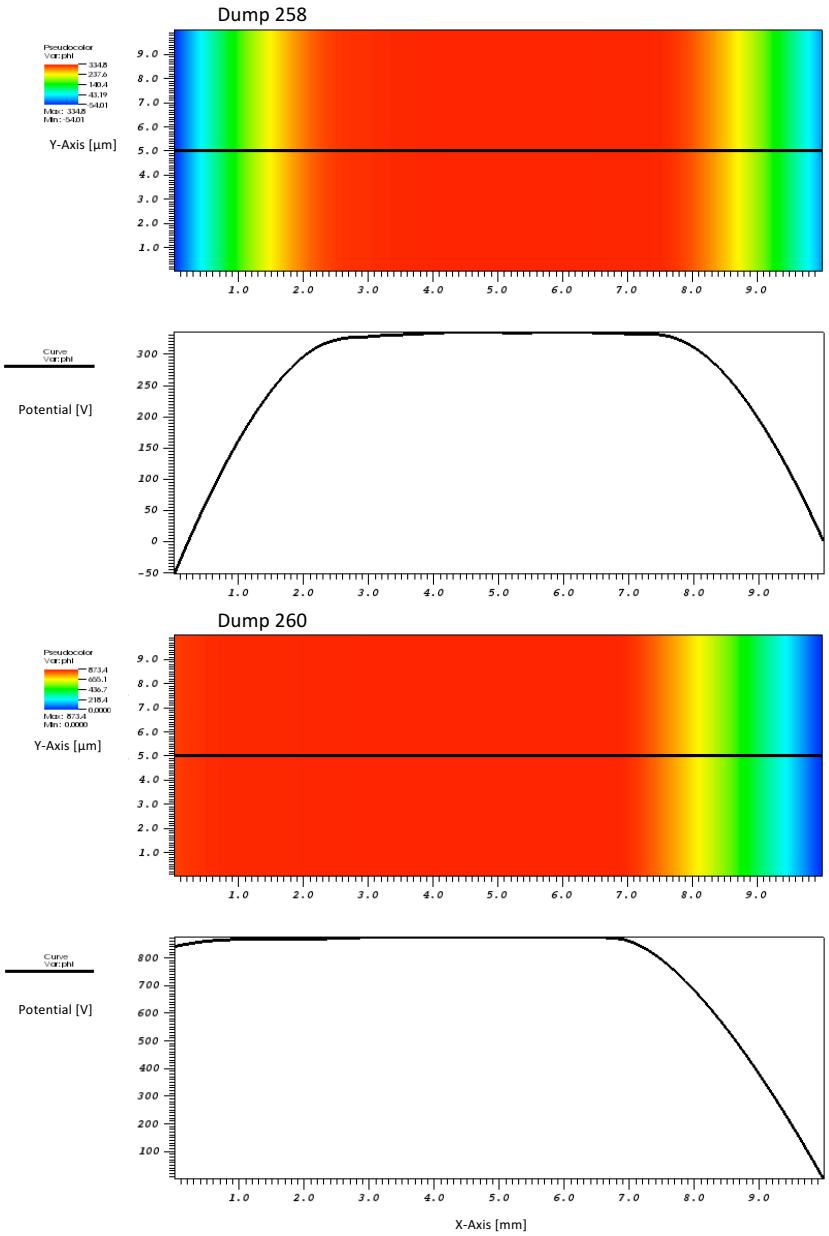

Figure 7.21 - Plasma chamber potential (data dumps 258 to 260)

Figure 7.22 shows the ion probability function of the plasma for data dumps 250 to 260. Figure 7.23 and Figure 7.24 show the electron (primaries and secondaries respectively) probability functions. It can be observed that the ion distribution has very similar shape during all the RF cycles. On the other hand, the electron distribution functions change shape with the RF cycle as the electron cloud moves from one electrode to the other.

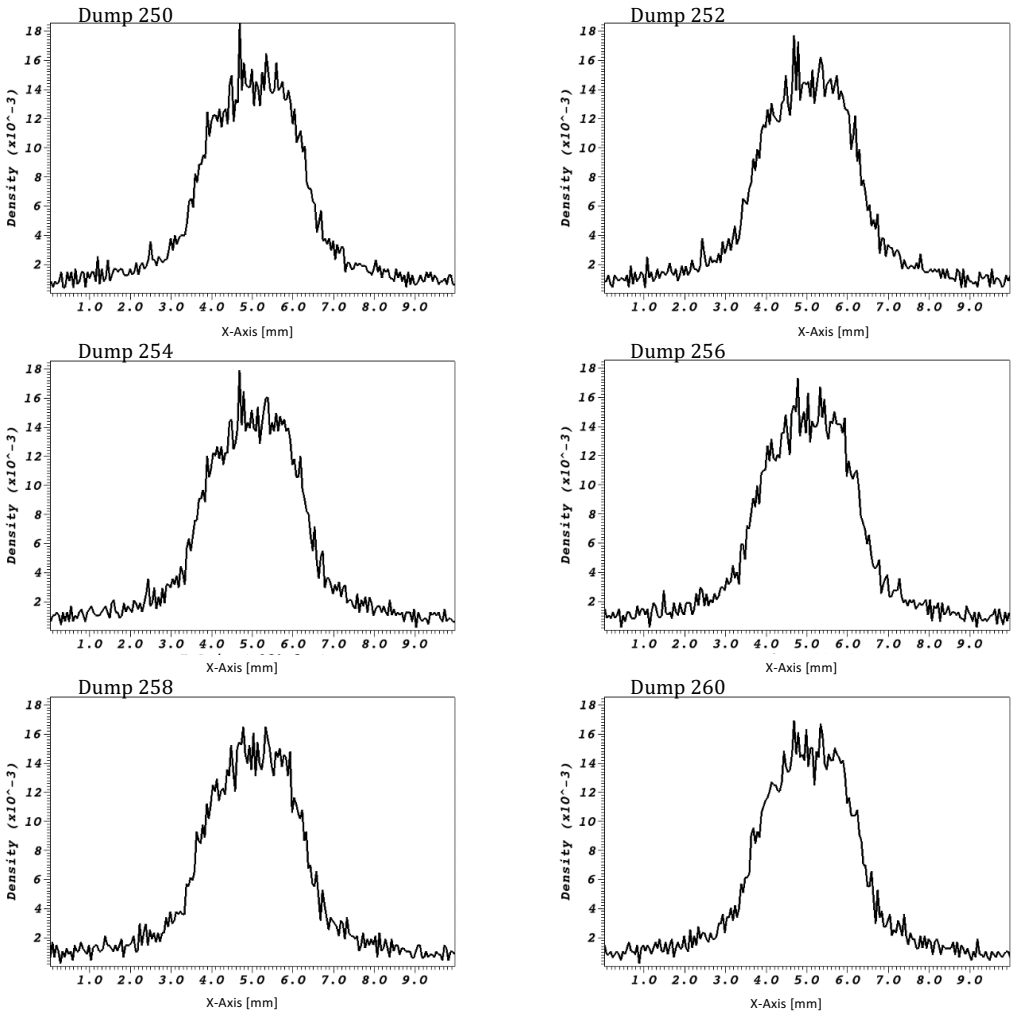

Figure 7.22 - Ions density probability function (data dumps 250 to 260)

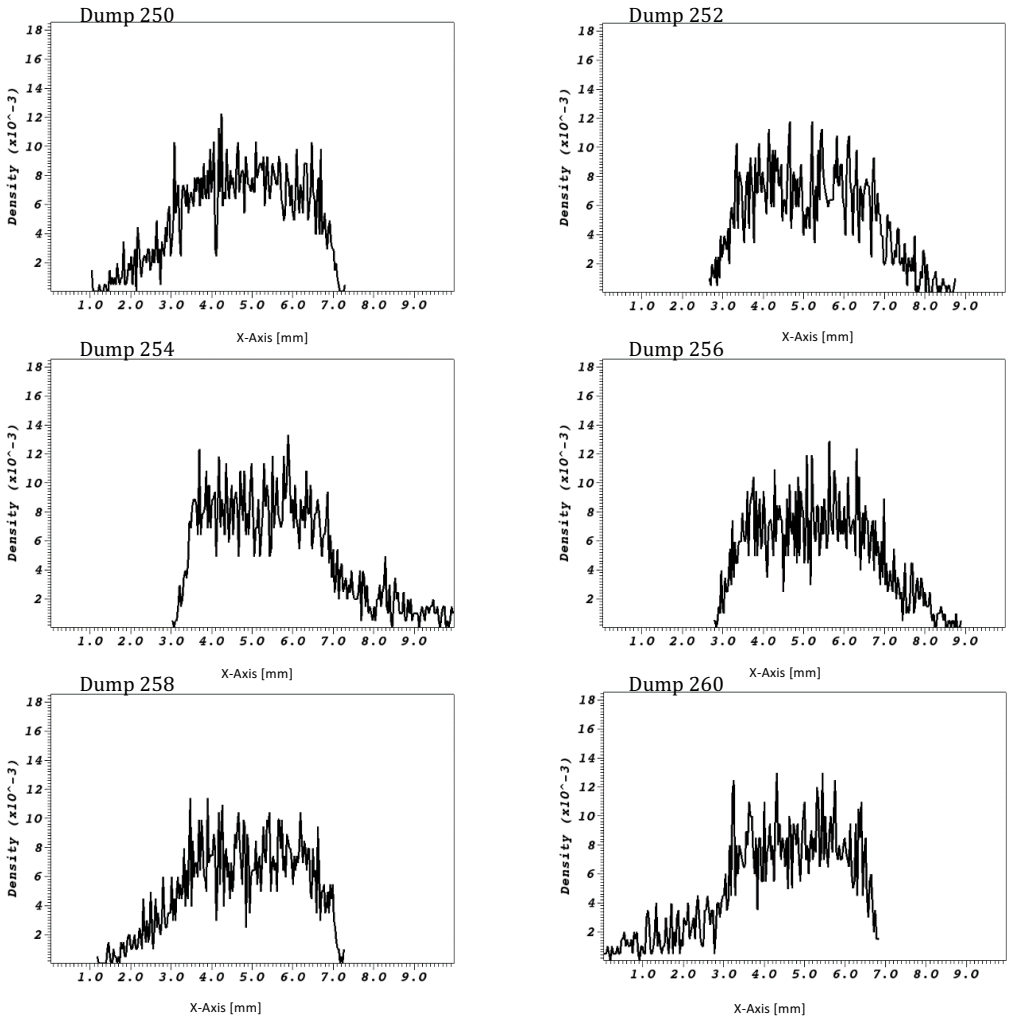

Figure 7.23 - Primary electron probability density function (data dumps 250 to 260)

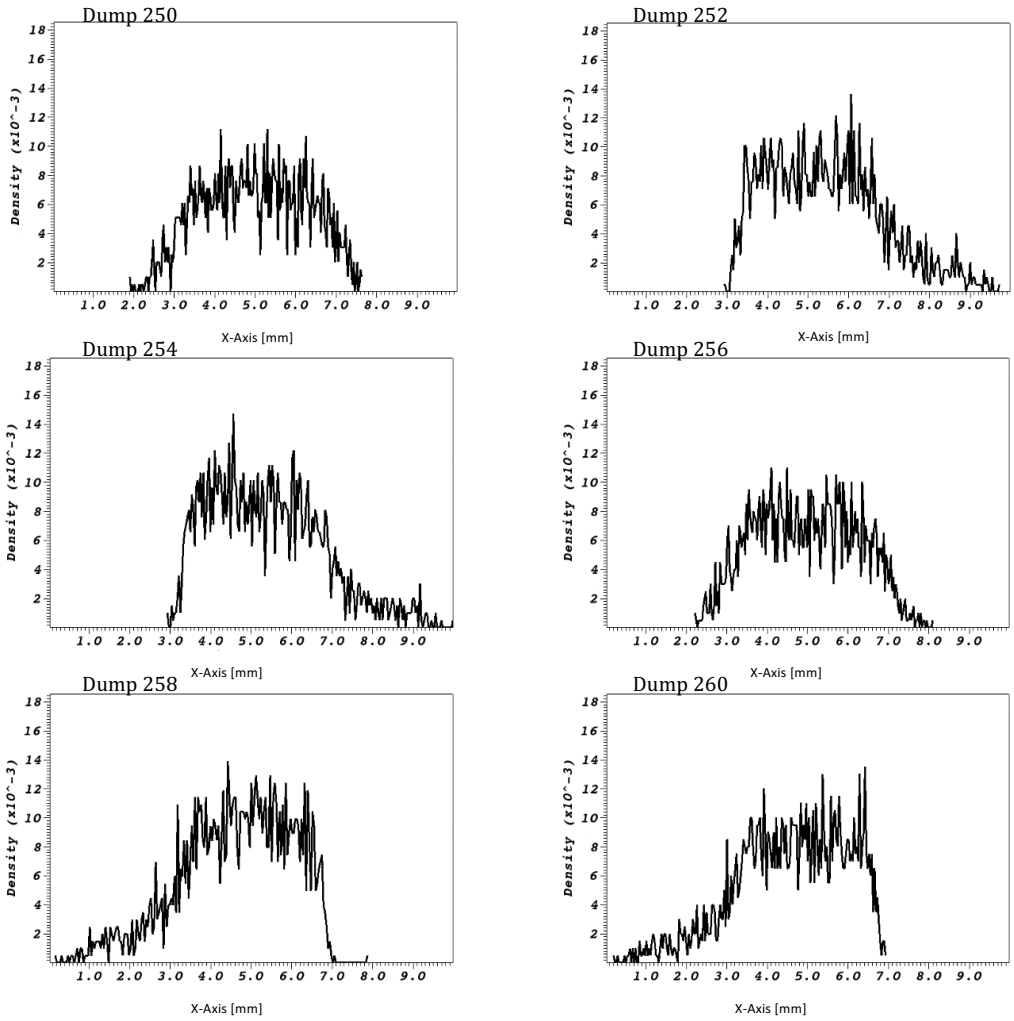

Figure 7.24 - Secondary electron probability density function (data dumps 250 to 260)

In summary, the results above showed thick plasma sheaths and a higher concentration of ions in the centre of the plasma chamber. Usually the ion distribution in typical RF discharges is more uniform across the plasma chamber gap. The reason for a higher concentration of ions in the middle of the chamber in this simulation might be due to the frequency being higher than in other typical RF discharges (84 MHz vs. 13 MHz) and the electrons being attracted for a shorter time to the same electrode before the electrode polarity changes. Thus, few electrons reach the plasma chamber walls and the electron cloud is concentrated in a small area in the middle of the chamber. As a result, the ions are also concentrated in this area.

Large plasma sheaths are not desirable for the end application of the plasma chamber developed in this work, which is to be used as an electron source. Electrons are extracted from the plasma cathode through an aperture in one of the chamber electrodes. Thus if a thick plasma sheath is next to the extraction electrode the number of available electrons would be low. Lower RF frequencies than the 84 MHz used in this work may give higher EB currents.

Another way to reduce the sheath thickness is to increase the electrode gap. Figure 7.25 show the results obtained from a simulation with a 76 mm gap.

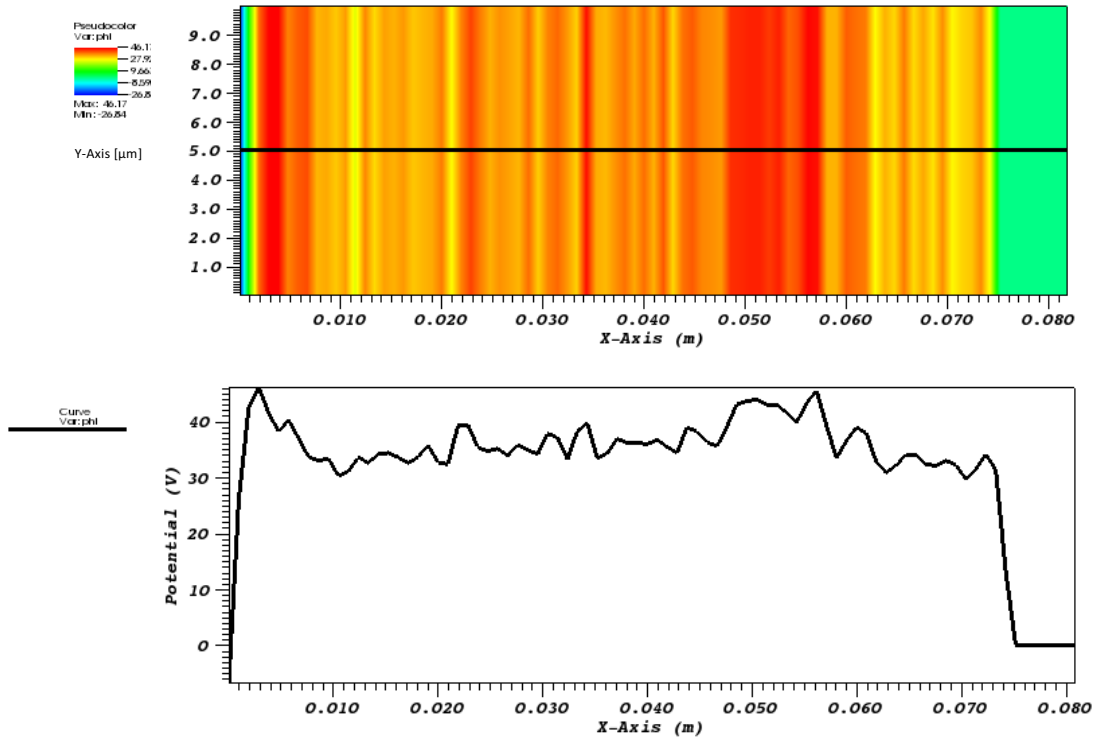

Figure 7.25 - Potential plot in 2D (top) and 1D (bottom) in a 76 mm electrode gap with an RF discharge at 84 MHz

The results shown until now were for a model with a 0.010 m gap. In order to study the effect of the electrode gap on the plasma parameters, simulations were carried out for three different electrode gaps: 10 mm, 23 mm and 76 mm; following the measurements taken from the practical plasma gun experimental setup. Table 7.1 shows the typical plasma parameters used in the VSim simulations:

Table 7.1 - 0.010 m and 0.023 m electrode gap simulation parameters

LX [m]	Pressure [mbar]	RF freq. [MHz]	Discharge volts [V]	Ne [m^{-3}]	Te [eV]	LY [m]	NX, NY cells	Macro /cell	Bx [T]
0.010	0.02	84	1000	5E15	2.5	0.00001	800, 2	1	0
0.023	0.02	84	100	2.5E16	2.5	0.00003	800,3	1	0.6
0.023	0.01	42	100	2.5E16	2.5	0.00003	800,3	1	0
0.010	0.02	84	100	2.5E16	2.5	0.00003	800,3	1	0.6
0.023	0.02	84	100	2.5E16	2.5	0.00003	800,3	1	0

7.3.1. Plasma Sheath Comparison in 10 mm Model Vs. 23 mm Electrode Gap Models

The observed plasma parameters for the models with 10 mm and 23 mm electrode gaps are compared in the results below to see the effect of electrode gap size on the plasma density and plasma sheath.

A steady state is reached at around 1 μs in both the 10 mm gap model (Figure 7.15) and in the 23 mm model (Figure 7.26).

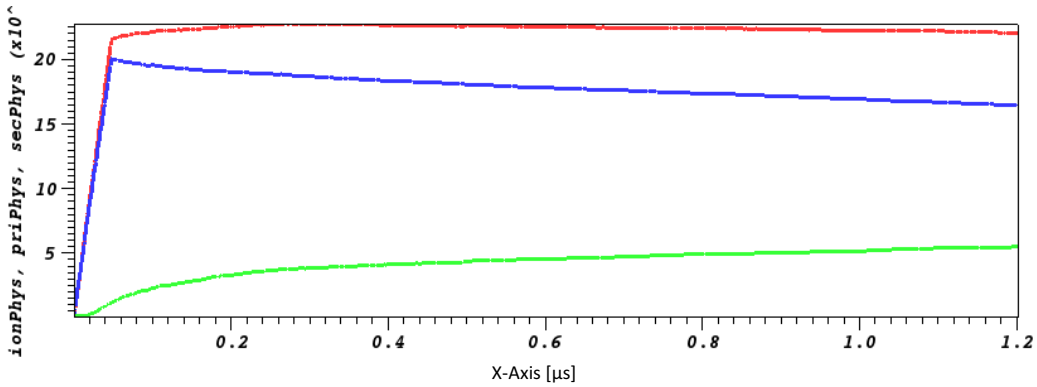

Figure 7.26 – Particle densities (ions in red, primaries in green and secondaries in blue) in a 0.023 m gap 100 V discharge at 84 MHz

The frequency was 84 MHz as in the previous models. The results showed that the sheaths become smaller with larger electrode gaps. Longer plasma chambers were also shown to be a better option to strike a plasma in the practical experiments at low pressures and for EB extraction when used in the experimental setup.

7.3.2. Plasma Sheath Comparison in 84 MHz Vs. 42 MHz RF Frequency Models

Plasmas generated at other frequencies were simulated to gain an understanding of how the excitation frequency affects the sheath thickness in the plasma chamber. The potential plots for a model run at 42 MHz was analysed. The RF cycle is longer (23.8 vs. 11.9 ηs) and the electrons have more time to reach the walls before the polarity changes. The number of dumps per period was still 12, thus 1.98 ηs/dump. In the simulation results, a higher number of electrons were observed to reach the plasma chamber walls at 42 MHz than at 84 MHz; thus the sheath thickness decreases.

The RF frequency used in the experimental setup was 84 MHz. Lower frequencies may be considered in future work to try to reduce the sheaths thickness further.

7.3.3. Effect of the Bx Field on the Plasma Distribution

The phase-space distribution in the plasma chamber was analysed from the simulation results. The electrons were confined along the axis, and even though some electrons reach the walls, less of them are lost compared to the model with no axial magnetic field along the plasma chamber. The ions were distributed around all the plasma chamber area, and seem to have a higher concentration in the middle.

7.4. Summary

Conclusion from gun electrodes and EB extraction simulation

The electrode shapes were optimised by using Opera-2d to improve beam quality. The optimum distance from the HV electrode to the anode must satisfy the compromise of avoiding HV breakdown between anode and cathode and at the same time keep a distance as small as is needed to extract the maximum electron beam current, i.e. to ensure that the beam current is not space charge limited, but rather limited by the emissivity of the plasma. The flat front diaphragm plate produced higher beam currents however the beam generated in the simulations showed a beam envelope which is very

close to parallel. As a result, the effect of the focus lens was minimum. The electrode geometries were modified to produce a beam with a larger angle. A beam with a large angle gave a large spot diameter at the lens, which enabled focusing of the beam to a small spot. The results showed:

- The flat front design with the HV electrode moved forward increased the beam angle and brought the crossover point close to the cathode in converging beams, and decreased the beam angle in diverging beams.
- The flat front design with round edges gave a convergent beam and the crossover point occurred closer to the cathode than in the flat front design.
- The setback diaphragm design produced a divergent beam and the angle increased more readily than in the other designs.

Even though Opera-2d predicted the beam shape and beam current in thermionic guns, there are other mechanisms governing these characteristics in plasma cathode guns which have been found to be more relevant. Several simulations were carried out with cathode surfaces with different curvatures (both convex and concave to the beam direction). The location of the plasma boundary was found to have a large effect on beam shape.

Conclusion from plasma chamber simulation

The VSim plasma simulations helped in understanding observations made using the practical plasma gun system in the laboratory and allowed for a comparison of simulation results with results obtained from practical experiments. Both simulation and experimental trials were carried out with 10 mm, 23 mm and 76 mm electrode gap for a parallel plate CCP discharge at 84 MHz.

The effect of the plasma parameters such as the frequency of the RF signal, the voltage of the discharge, the plasma pressure or the magnetic field confinement effect were investigated. One of the main concerns in some applications of the plasma cathode electron gun is the beam quality. The experiments in the lab indicated that the beam quality was governed by other parameters different to those in conventional thermionic guns. One of the causes investigated was the effect of the RF frequency on the electron beam being extracted. The VSim plasma simulations showed that the sheath of the

plasma moves with the RF cycle. Thus, even though the average current extracted is comparable to the current obtained in practical experiments, the fact that the sheath is alternating makes the plasma boundary vary, and therefore the quality of the beam extracted from the plasma cathode is variable.

The VSim simulation results gave an estimate of the plasma sheath thickness. This is also an important result for the plasma cathode gun as it has an effect on the EB current extracted from the plasma cathode. In summary, the plasma sheath thickness decreases when the electrode gap is increased. Longer electrode geometries were also used in the experimental setup and were demonstrated to be beneficial for the proposed application. The longer electrode gap allows for the generation of a plasma at lower chamber pressure. In addition to this, larger EB currents were extracted when using a longer electrode geometry, which may be due to the sheath thickness being thinner, as observed in the VSim simulations.

Chapter 8 : Conclusions and Future Work

This chapter is divided into three section according to the work carried out in this thesis: first, design and optimisation of the RF plasma cathode and development of the experimental setups; second, spectroscopic and beam current measurements; and third, simulation work. In each section, the main conclusions are drawn and the possible future work is presented at the end of each section.

8.1. Design Optimisation of the Plasma Cathode EB Gun and Experimental Setup Development

The following conclusions comprise the findings learnt during the development of the experimental setups used to carry out the experiments in this thesis, as well as the modifications done to the plasma chamber. Possible future work is outlined at the end of this section.

- At the beginning of this work, a mass flow controller was added to accurately control the plasma chamber pressure. In addition, the pipe through which the gas was fed to the plasma chamber was substituted by a sand pipe, which gave a finer and faster control of the plasma pressure. Accurate control of plasma pressure was found to be key, as it was one of the main parameters that affected the generated EB. The plasma pressure was measured with a capacitance gauge at different flow rates and apertures so that this parameter was known during the experiments. Even though the plasma cathode had been operated at higher pressures (in the order of a few mbar), low pressures (within the tenths of mbar range) were found to be the most appropriate for this application. The main reasons for this were reduced sputtering of the plasma chamber electrodes, the capability for extracting higher beam currents and a lower amount of gas needed and as a result better vacuum levels in the vacuum chamber which avoided HV breakdown.

- The literature was reviewed in order to find the plasma models that represented the type of plasma concerned in this work: low-temperature, low-pressure, RF excited plasma. A dedicated experimental setup was developed allowing OES measurements of the plasma chamber inside the vacuum chamber of the EB gun system. A second setup allowed generation of Ebs and monitoring of beam current at the same time as taking OES measurements. The beam current extracted from the plasma chamber aperture was collected in a Faraday cup, while the light emitted from the plasma was observed through a hole on the side of the electron gun body.

- The plasma chamber design evolved during this thesis work. The initial electron beam gun used had a small plasma chamber (about 4-5 mm electrode gap). The latest design operates with a larger plasma chamber with electrode gaps of up to 76 mm possible. The plasma chamber, originally made of Boron Nitride, was made in quartz in order to be able to measure the plasma optical radiation for spectroscopic measurements. The plasma chamber design allows for different chamber geometries (hollow and flat electrodes from 4 mm gaps to 75 mm gaps), different electron extraction apertures, the inclusion of permanent magnet configurations, along with other design variations while using a single electron gun body.

Future work could look at developing an experimental setup with a higher HV PSU, i.e. –150 kV. This would potentially increase the beam current extracted from the plasma, as it was observed in this work that this occurred when the accelerating voltage was increased from –30 to –60 kV.

8.2. Spectroscopic and EB Current Measurements

During this thesis work, the current extracted from the plasma cathode electron gun has been increased through design optimisation from a few mA to up to some 38 mA at –

60 kV with a plasma excitation power of only 100 W or less. Even though the maximum power achieved with the RF plasma cathode gun is still lower than that generally achieved with conventional thermionic guns, 38 mA at –60 kV is sufficient for low power EB material processing industrial applications such as 3D printing in metal or cutting. In addition, the EB current extracted from the plasma cathodes tested does not seem to saturate with space charge over the observed range and it may therefore be possible to extract higher current through further design optimisation of the plasma chamber.

- Accelerating voltage – The experimental work showed that increasing the accelerating voltage increased the amount of current extracted from a given plasma cathode gun design. In particular, the EB current increased by 50% in a hollow cathode design when the accelerating voltage was increased from –30 kV to –60 kV.

- Plasma chamber geometry – Hollow cathode geometries produced higher beam currents (up to 38 mA at –60 kV) than flat electrodes. The distance between the hollow cathode cylinder and the aperture electrode was found to be critical for beam current extraction.

- Aperture diameter – This work demonstrated that larger apertures in the RF plasma chamber produced larger beam currents. However, there was a limitation on the diameter of the aperture size due to the required low pressure in the vacuum chamber combined with an optimum pressure in the plasma chamber of the order 0.1 mbar. As the aperture size was increased, the gas flow into the plasma chamber had to be increased in order to maintain the optimum plasma chamber pressure. Consequently, more gas would flow out of the aperture, which would have to be pumped at a higher rate in order to maintain the vacuum level around the gun required for high voltage insulation. A 2 mm diameter aperture was found to be the maximum size that allowed the gun to generate beams without causing HV breakdown in the vacuum chamber due to pressure rise. However, increased pumping of the vacuum chamber would allow

a greater aperture size. An optimum was found at an aperture of 1.7 mm diameter, which allowed higher pressures in the plasma chamber making the plasma ignition easier.

- Plasma pressure – In general, low pressures were found to produce more stable electron beams. Low pressure plasmas gave higher beam currents in most cases and produced less sputter of the plasma chamber electrodes. However, there was a limitation at the low pressure end, as larger electrode gaps are needed to strike plasmas at lower pressures.

- RF excitation power – Another key parameter determining the EB current extracted from plasma cathodes is the power applied to the plasma. The results showed that EB current increased at any pressure, chamber geometry and accelerating voltage when the RF power was increased. However, limitations were found due to the matching network and the maximum reflected power taken by the RF amplifier. Even with efficient RF matching (~5% reflected power), the maximum RF power delivered was 100 W due to power dissipation limits of the plasma chamber and surrounding elements (i.e. O-rings).

- RF excitation frequency and DC – Most of the experiments with the RF plasma gun were carried out in the frequency range 80 – 85 MHz, depending on the resonant frequency of the system, which varied when the plasma was on or off. Spectroscopic and EB current measurements from the RF plasma were compared to measurements taken from a DC plasma gun, both used an argon plasma at 0.16 to 0.3 sccm gas flow. The EB current extracted from the DC plasma was larger (up to 65 mA at –60 kV), however, the discharge currents were also larger (about an order of magnitude larger than in the RF plasma cathode gun) compared to the RF plasma which would only need a few mA to be ionised. The spectra collected from the DC plasma also indicated a higher ionisation than in the RF plasma, which was probably due to the higher energy

applied (higher discharge current) than in the RF plasma. In addition, modelling has shown that the sheaths in the RF plasma oscillated as the excitation voltage polarity changed. This does not occur in DC plasmas, in which the sheaths would be static.

Future work would look at generating EB currents at higher discharge currents with the RF plasma. This would allow comparison of the EB current extracted from a DC and an RF cathode in similar conditions. A cooling system would be required. In future work collisional radiative models could be applied to calculate electron temperatures and densities if a higher resolution spectrometer were used.

EB current measurements from a DC plasma cathode with different electrode shapes would be useful to determine whether the changes in electrode geometry govern the EB quality in DC plasma cathodes, in contrast to the findings in RF plasma cathodes in which other parameters govern EB quality.

To ignite a plasma, RF is a better option as a few tenths of a watt were needed to start it and a few watts were enough for keeping the plasma alive. A combination of a DC and RF plasma chamber could be a solution. Inductively coupled plasmas could also be a solution for extracting higher EB currents as these are usually sources of higher ionisation.

8.3. Simulation Work

The conclusions from the simulation work are divided into the findings from the FEA modelling work and findings from the PIC simulations. Future lines of work are suggested at the end of this section.

- The use of an FEA model to simulate electron beams demonstrated that a divergent gun design gave a better quality beam and more intense beam spot.
- Observation showed that the plasma boundary did not appear flat, thus different curvatures were modelled for the plasma boundary. Model results showed that the emitter shape was very significant for the beam trajectories

extracted, and in curved plasma boundaries the electron beam trajectories were not very laminar. This was a possible explanation for the large beam diameters obtained in the experiments.

- PIC simulations were carried out for a parallel plate geometry with electrode gaps of 10 mm, 23 mm and 76 mm, as per the plasma chamber in the practical experiments. The simulations looked at different plasma pressures, discharge currents, and excitation frequencies. The use of VSim showed that the plasma sheaths were significant and move around with the RF phase. The emission shape or plasma boundary oscillates with the RF cycle.

- The VSim simulations showed that lower frequency excitations would reduce the sheath thickness, and therefore increase emissivity.

Oscillating sheath shapes and thickness may be the reason why a lower intensity spot is measured from the RF plasma cathode in the experiments instead of the intense spot predicted from the model simulations. DC excitation would not have oscillating sheaths and might give the optimum beam intensity. For future work, simulations of a DC plasma cathode with the same parameters as the RF simulations in this work (such as lower discharge current) would help to understand how much the sheaths contribute as a limitation in EB extraction. Additionally, PIC results showed that higher discharge currents produced higher ionisation. The next step would be to add an electron acceleration region to the model, which would allow for a direct comparison of simulation output with the actual beam current extracted in the practical experiments.

Bibliography

ADDITIVELY, 2016-last update, Electron Beam Melting (EBM). Available: https://www.additively.com/en/learn-about/electron-beam-melting 2016].

ALVES, L.L., 2015. *Plasma modelling: electron kinetics.* ISPC Summer School, Eindhoven, The Netherlands.

ANDERSON, S., ROSENZWEIG, J., LESAGE, G. and CRANE, J., 2002. Space-charge effects in high brightness electron beam emittance measurements. *Phys.Rev.ST Accel.Beams,* **5**(1), pp. 014201.

ARCAM AB, 2016-last update, 3D Printing Metal Interview with Arcam CEO Magnus René. Available: https://3dprintingindustry.com/news/3d-printing-metal-interview-magnus-rene-arcam-group-ceo-83724/2016].

ATTAR, E., 2011. Simulation of selective electron beam melting processes.

AUSTRALIAN MICROSCOPY AND MICROANALYSIS RESEARCH FACILITY, 2014-last update, The electron gun. Available: http://www.ammrf.org.au/myscope/sem/practice/principles/gun.php.

BAKISH, R.A., 1965. *Handbook of electron beam welding.* New York: Wiley.

BALACHANDRAN, W., BELECA, R., MANIVANNAN, N. and ABBOD, M., 2014. Non-thermal plasma system for marine diesel engine emissions control, *Industry Applications Society Annual Meeting, 2014 IEEE* 2014, pp. 1-9.

BARNARD, H., 2014-last update, Beam Dynamics Simulations (doctoral thesis). Available: http://science.haroldbot.com/beam-simulation/ [09/23, 2015].

BELYUK, S., OSIPOV, I. and REMPE, N., 2001. Industrial use of plasma-emitter electron sources. *Russian physics journal,* **44**(9), pp. 987-995.

BOFFARD, J.B., JUNG, R.O., LIN, C.C., ANESKAVICH, L.E. and WENDT, A.E., 2012. Argon 420.1–419.8 nm emission line ratio for measuring plasma effective electron temperatures. *Journal of Physics D: Applied Physics,* **45**(4), pp. 045201.

BOFFARD, J.B., LIN, C.C. and CHARLES, A.D.,Jr, 2004. Application of excitation cross sections to optical plasma diagnostics. *Journal of Physics D: Applied Physics,* **37**(12), pp. R143.

BOGAERTS, A., 2015. *Plasma Modeling I: General.* ISPC Summer School - Eindhoven, The Netherlands.

BOGAERTS, A. and GIJBELS, R., 2002. Numerical modelling of gas discharge plasmas for various applications. *Vacuum,* **69**(1), pp. 37-52.

BOGAERTS, A., NEYTS, E., GIJBELS, R. and VAN DER MULLEN, J., 2002. Gas discharge plasmas and their applications. *Spectrochimica Acta Part B: Atomic Spectroscopy,* **57**(4), pp. 609-658.

BRITISH STANDARDS INSTITUTION, 1971. *Recommendation for Data on Shielding From Ionizing Radiation, Part 2. Shielding from X-radiation.* London, UK: BSI.

BUCKMAN, S., 2014. *Low energy electron scattering cross sections: measurements and calculations.* International Plasma Summer School, Bad Honnef.

BUGAEV, A., VIZIR, A., GUSHENETS, V., NIKOLAEV, A., OKS, E., YUSHKOV, G.Y., BURACHEVSKY, Y.A., BURDOVITSIN, V., OSIPOV, I. and REMPE, N., 2003. Current status of plasma emission electronics: II. Hardware. *Laser and Particle Beams,* **21**(02), pp. 139-156.

CALABAZAS CREEK RESEARCH, I., 2010-last update, Beam Optics Analyzer (BOA). Available: http://calcreek.com/software.html#BOA [July, 2015].

CHABERT, P. and BRAITHWAITE, N., 2011. *Physics of Radio-Frequency Plasmas.* Cambridge University Press.

CHEN, F.F. and SMITH, M.D., 1984. *Plasma.* Wiley Online Library.

CHILD, C., 1911. Discharge from hot CaO. *Physical Review (Series I),* **32**(5), pp. 492.

CHUNG, H., LEE, R., CHEN, M. and RALCHENKO, Y., 2008. The How To For FLYCHK. *URL: http://nlte.nist.gov/fly/ [cit.2010-01-10],*

CONRADS, H. and SCHMIDT, M., 2000. Plasma generation and plasma sources. *Plasma Sources Science and Technology,* **9**(4), pp. 441.

COTHRAN, C.D., BORIS, D.R., COMPTON, C.S., TEJERO, E.M., FERNSLER, R.F., AMATUCCI, W.E. and WALTON, S.G., 2015. Continuous and pulsed electron beam production from an uninterrupted plasma cathode. *Surface and Coatings Technology,* **267**, pp. 111-116.

CPO LTD, 2015-last update, Charge Particle Optics. Available: http://www.electronoptics.com/index.html [July, 2015].

DANCE, B. and BUXTON, A., 2007. An introduction to Surfi-Sculpt technology–new opportunities, new challenges, *Proceedings of the 7th International Conference on Beam Technology* 2007, pp. 75-84.

DEL POZO, S., RIBTON, C.N. and SMITH, D.R., 2014. A Novel RF Excited Plasma Cathode Electron Beam Gun Design. *Electron Devices, IEEE Transactions on,* **61**(6), pp. 1890-1894.

DEL POZO, S., RIBTON, C. and SMITH, D.R., 2014a. Characterisation of an RF excited argon plasma cathode electron beam gun, *Vacuum Electron Sources Conference (IVESC), 2014 Tenth International* 2014a, pp. 1-2.

DEL POZO, S., RIBTON, C.N. and SMITH, D.R., 2014b. Spectroscopic characterization of a novel RF excited plasma cathode electron beam gun design, *Vacuum Electronics Conference, IEEE International* 2014b, pp. 169-170.

DRUYVESTEYN, M. and PENNING, F.M., 1940. The mechanism of electrical discharges in gases of low pressure. *Reviews of Modern Physics,* **12**(2), pp. 87.

EICHMEIER, J.A. and THUMM, M., 2008. *Vacuum electronics: components and devices.* Springer.

FANTZ, U., 2006. Basics of plasma spectroscopy. *Plasma Sources Science and Technology,* **15**(4), pp. S137.

FIKSEL, G., ALMAGRI, A., CRAIG, D., IIDA, M., PRAGER, S. and SARFF, J., 1996. High current plasma electron emitter. *Plasma Sources Science and Technology,* **5**(1), pp. 78.

FRIEDEL, K. and FELBA, J., 1994. Measurements of beam emittance in electron beam welding. *Welding International,* **8**(3), pp. 176-180.

GEWARTOWSKI, J.W. and WATSON, H.A., 1965. Principles of electron tubes.

GODYAK, V., 2011a. Probe diagnostics of RF plasmas for material processing, *Plasma Science (ICOPS), 2011 Abstracts IEEE International Conference on* 2011a, IEEE, pp. 1-1.

GODYAK, V.A., PIEJAK, R.B. and ALEXANDROVICH, B.M., 1992. Measurement of electron energy distribution in low-pressure RF discharges. *Plasma Sources Science and Technology,* **1**(1), pp. 36.

GODYAK, V. and DEMIDOV, V., 2011. Probe measurements of electron-energy distributions in plasmas: what can we measure and how can we achieve reliable results? *Journal of Physics D: Applied Physics,* **44**(23), pp. 233001.

GODYAK, V. and PIEJAK, R., 1990. Abnormally low electron energy and heating-mode transition in a low-pressure argon rf discharge at 13.56 MHz. *Physical Review Letters,* **65**(8), pp. 996.

GODYAK, V., 2011b. *Capacitive and Inductive RF plasma sources for industrial applications.* NCCAVS Plasma applications group meeting, SEMICON West.

GODYAK, V. and ALEXANDROVICH, B., 2015. Langmuir paradox revisited. *Plasma Sources Science and Technology,* **24**(5), pp. 052001.

GODYAK, V.A., PIEJAK, R.B. and ALEXANDROVICH, B.M., 1991. Electrical characteristics of parallel-plate RF discharges in argon. *Plasma Science, IEEE Transactions on,* **19**(4), pp. 660-676.

GOEBEL, D.M. and KATZ, I., 2008. *Fundamentals of electric propulsion: ion and Hall thrusters*. John Wiley & Sons.

GOEBEL, D.M. and WATKINS, R.M., 2000. High current, low pressure plasma cathode electron gun. *Review of Scientific Instruments,* **71**(2), pp. 388-398.

GOEDDE, C.G., LICHTENBERG, A.J. and LIEBERMAN, M.A., 1988. Self-consistent stochastic electron heating in radio frequency discharges. *Journal of Applied Physics,* **64**(9), pp. 4375-4383.

GOEDHEER, W.,J., 2000. Lecture notes on radio-frequency discharges, dc potentials, ion and electron energy distributions. *Plasma Sources Science and Technology,* **9**(4), pp. 507.

GOLDSTON, R.J. and RUTHERFORD, P.H., 1995. *Introduction to plasma physics*. CRC Press.

GOZADINOS, G., TURNER, M.M. and VENDER, D., 2001. Collisionless Electron Heating by Capacitive rf Sheaths. *Phys.Rev.Lett.,* **87**(13), pp. 135004.

HARRIS, N.S., 1989. Modern vacuum practice. *London: McGraw-Hill, c1989,* **1**.

HOFMANN, S., VAN GESSEL, A. F. H., VERREYCKEN, T. and BRUGGEMAN, P., 2011. Power dissipation, gas temperatures and electron densities of cold atmospheric pressure helium and argon RF plasma jets. *Plasma Sources Science and Technology,* **20**(6), pp. 065010.

HOWARD, J.A., LANGMUIR, I. and MACKAY, G.M.J., 1927. The Rates of Evaporation and the Vapor Pressures of Tungsten, Molybdenum, Platinum, Nickel, Iron, Copper and Silver. *Phys.Rev.,* **30**(2), pp. 201-214.

HUMPHRIES, S., 2013. *Charged particle beams*. Courier Corporation.

HUTCHINSON, I.H., 2005. *Principles of plasma diagnostics*. Cambridge university press.

IIT KHARAGPUR, 2009-last update, Electron beam and laser beam machining. Available: http://www.nptel.ac.in/courses/112105127/40 [08/14, 2015].

IIYOSHI, R., SHIMOYAMA, H. and MARUSE, S., 1996. A Comparison of Thermionic Emission Current Density and Brightness against Evaporation Loss for LaB_6 and Tungsten. *Journal of electron microscopy,* **45**(6), pp. 514-517.

IOP, 2013-last update, Plasma Physics Group. Available: http://www.iop.org/activity/groups/subject/pla/index.html [04/17, 2013].

JAWOREK, A., SZUDYGA, M., KRUPA, A., CZECH, T., SOBCZYK, A.T., MARCHEWICZ, A., ANTES, T., BALACHANDRAN, W., BELECA, R. and DI NATALE, F., 2014. Technical issues of PM removal from ship diesel engine exhausts, *Transport Research Arena (TRA) 5th Conference: Transport Solutions from Research to Deployment* 2014.

KANG, E., KIM, J., LEE, S., MIN, B. and LEE, S., 2015. Emission characteristics of high-voltage plasma diode cathode for metal surface modification. *International Journal of Precision Engineering and Manufacturing,* **16**(1), pp. 13-19.

KOLOBOV, V. and METEL, A., 2015. Glow discharges with electrostatic confinement of fast electrons. *Journal of Physics D: Applied Physics,* **48**(23), pp. 233001.

KORNILOV, S.Y., OSIPOV, I. and REMPE, N., 2009. Generation of narrow focused beams in a plasma-cathode electron gun. *Instruments and Experimental Techniques,* **52**(3), pp. 406-411.

KOU, S., 2003. Frontmatter. *Welding Metallurgy, Second Edition*, pp. i-xiv.

KOVAL, N., OKS, E., SCHANIN, P., KREINDEL, Y.E. and GAVRILOV, N., 1992. Broad beam electron sources with plasma cathodes. *Nuclear Instruments and Methods in Physics Research Section A: Accelerators, Spectrometers, Detectors and Associated Equipment,* **321**(3), pp. 417-428.

LASSNER, E. and SCHUBERT, W., 1999. *Tungsten: properties, chemistry, technology of the elements, alloys, and chemical compounds*. Springer.

LAWSON, J.D., 1988. The physics of charged-particle beams. 2.

LEE, Y., HWANG, K., LEE, M. and CHUNG, C., 2008. Spectroscopic measurement of the electron temperature and the metastable densities by using a simple collisional-radiative model in a low-pressure inductively-coupled argon plasma. *Journal of the Korean Physical Society,* **52**(6), pp. 1792-1799.

LIEBERMAN, M., BOOTH, J., CHABERT, P., RAX, J. and TURNER, M., 2002. Standing wave and skin effects in large-area, high-frequency capacitive discharges. *Plasma Sources Science and Technology,* **11**(3), pp. 283.

LIEBERMAN, M.A., 2007. *A mini-course on the principles of low-pressure discharges and materials processing*. 12th European Summer School on Low Temperature Plasma Physics, Bad Honnef, Germany.

LIEBERMAN, M.A., 2003. *A mini course on the principles of plasma discharges*. Berkeley.

LIEBERMAN, M.A. and LICHTENBERG, A.J., 1994. Principles of plasma discharges and materials processing. *Published by A Wiley-Interscience Publication*, pp. 388.

LIEBMANN, G., 1955. The field distribution in asymmetrical magnetic electron lenses. . *Proc. Phys. Soc.*, pp. 679-681.

LI, X., LI, M., DAN, L., HE, T., LIU, Y., XU, Z. and TANG, C., 2015. A double-frequency rf gun for field emission. *Nuclear Instruments and Methods in Physics Research Section A: Accelerators, Spectrometers, Detectors and Associated Equipment,* **783**, pp. 1.

LIEBMANN, G., 1955. A unified representation of magnetic electron lens properties. *Proceedings of the Physical Society.Section B,* **68**(10), pp. 737.

LIEBMANN, G., 1955. The field distribution in asymmetrical magnetic electron lenses. . *Proc. Phys. Soc.*, pp. 679-681.

LIEBMANN, G. and GRAD, E.M., 1951. Imaging Properties of a Series of Magnetic Electron Lenses. *Proceedings of the Physical Society.Section B,* **64**(11), pp. 956.

LITOVKO, I., 2008. Simulation of the extraction of a strongly focused electron beam from a plasma electron gun.

LIU, Y., JIANG, W., LI, X., LU, W. and WANG, Y., 2012. An overview of diagnostic methods of low-pressure capacitively coupled plasmas. *Thin Solid Films,* **521**, pp. 141-145.

LONGMIER, B., BAALRUD, S. and HERSHKOWITZ, N., 2006. Nonambipolar electron source. *Review of Scientific Instruments,* **77**(11).

MANIVANNAN, N., BALACHANDRAN, W., BELECA, R. and ABBOD, M., 2014. Non-Thermal Plasma Technology for the Abatement of NOx and SOx from the Exhaust of Marine Diesel Engine. *Journal of Clean Energy Technologies,* **2**(3), pp. 233-236.

MOLOKOVSKIY, S.I. and SUSHKOV, A., 2005. *Intense electron and ion beams.* Springer.

NEEF, D., 2009. The Development of a Global Maritime Emissions Inventory Using Electronic Monitoring and Reporting Techniques, *18th Annual International Emission Inventory Conference "Comprehensive Inventories-Leveraging Technology and Resources* 2009, pp. 14-17.

NIST ASD TEAM, A.KRAMIDA, YU.RALCHENKO and J.READER, 2013-last update [Homepage of NIST Atomic Spectra Database], [Online]. Available: http://physics.nist.gov/asd.

NOVA ADMIN, 2013-last update, Gas Discharge Physics. Available: http://www.szfki.hu/EN/gdp [01/09, 2015].

OKS, E., 2006. *Plasma Cathode Electron Sources: Physics, Technology, Applications.* John Wiley & Sons.

OKS, E.M. and SCHANIN, P.M., 1999. Development of plasma cathode electron guns. *Physics of Plasmas (1994-present),* **6**(5), pp. 1649-1654.

OKS, E.M., 2015. Special features of plasma generation and beam formation for fore-vacuum plasma electron sources, *Plasma Sciences (ICOPS), 2015 IEEE International Conference on* 2015, pp. 1-1.

OLSCHEWSKI, E.S., 2015. Aplicaciones de la física de plasmas en la industria. *Ingeniería Industrial,* (28), pp. 195-210.

OPERA, V.F., 2012. *Opera-2d reference manual.*

PAL, U.N., 2015. Particle-in-cell simulation study of PCE-gun for different hollow cathode aperture sizes. *Indian Journal of Pure & Applied Physics (IJPAP),* **53**(4), pp. 225-229.

PASCHEN, F., 1889. The potential difference necessary for the Passage of sparks in air, hydrogen and carbon dioxide at different pressure. *Ann.Phys.,* **37**, pp. 69-76.

PERRET, A., CHABERT, P., BOOTH, J., JOLLY, J., GUILLON, J. and AUVRAY, P., 2003. Ion flux nonuniformities in large-area high-frequency capacitive discharges. *Applied Physics Letters,* **83**(2), pp. 243-245.

PIERCE, J.R., 1954. Theory and design of electron beams.

RAYTEK CORPORATION, 2007. *Operating Instructions Raytek XR.*

REISER, M., 2008. *Theory and design of charged particle beams.* John Wiley & Sons.

RIBTON, C., DEL POZO, S. and SMITH, D.R., 2015. *Characterisation of a Novel Electron Beam Gun Design with a Radio Frequency Excited Plasma Cathode.* 1056/2015.

RIBTON, C. and SANDERSON, A., 2015. Plasma Source Apparatus and Methods for Generating Charged Particle Beams. *Plasma Source Apparatus and Methods for Generating Charged Particle Beams.*

RICHARDSON, O.W., 1913. The Emission Of Electrons From Tungsten At High Temperatures: An Experimental Proof That The Electric Current In Metals Is Carried By Electrons. *Science*, pp. 57-61.

RICHARDSON, O.W., 1916. *The electron theory of matter*. The University Press.

SANDERSON, A., 1978. Electron beam welding generators. *Electron beam welding generators*.

SCHILLER, S., HEISIG, U. and PANZER, S., 1982. *Electron beam technology*. John Wiley & Sons.

SCHULTZ, H., 1994. *Electron beam welding*. Elsevier.

SCHULZE, M., YANGUAS-GIL, A., VON KEUDELL, A. and AWAKOWICZ, P., 2008. A robust method to measure metastable and resonant state densities from emission spectra in argon and argon-diluted low pressure plasmas. *Journal of Physics D: Applied Physics,* **41**(6), pp. 065206.

SCHULZ-VON DER GATHEN, V., 2013. *Basics of Plasma Spectroscopy*. Bad Honnef - European Summer School on Low Temperature Plasmas.

SHOHET, J., 2012. *The plasma state*. Elsevier.

SCIAKY INC., 2015-last update, Electron Beam Additive Manufacturing Technology. Available: http://www.sciaky.com/additive-manufacturing/electron-beam-additive-manufacturing-technology [08/13, 2015].

SCIAMMA, E.M., 2007. *Plasma spectroscopic diagnostic tool using collisional-radiative models and its application to different plasma discharges for electron temperature and neutral density determination*. ProQuest.

SERLES, C., 2015-last update, Electron Beam Welding. Available: http://blog.xiris.com/blog/topic/electron-beam-welding [08/12, 2015].

STECKELMACHER, W., 1996. Electron physics of vacuum and gaseous devices: Miroslav Sedlaček John Wiley & Sons Ltd., Chichester, 1996, 538 pp. (Printed by John Wiley & Sons Inc., New York, USA) ISBN 0-471-14527-0. *Vacuum,* **47**(10), pp. 1246.

STUPAKOV, G. and HUANG, Z., 2008. Space charge effect in an accelerated beam. *Physical Review Special Topics-Accelerators and Beams,* **11**(1), pp. 014401.

TAVAKOLI, M., BUXTON, A., JONES, I., DANCE, B., TAVAKOLI, M., BUXTON, A., JONES, I. and DANCE, B., 2007. The use of power beams in surface modification. *Medical device technology,* **18**(1),.

TECH-X CORPORATION, 2016-last update, VSim documentation. Available: http://www.txcorp.com/images/docs/vsim/latest/VSimDocumentation.html2016].

TECH-X CORPORATION, 2015-last update, Simulating NASA's Next Generation Xenon Ion Thruster (NEXT) Discharge Chamber Plasma Processes. Available: https://www.txcorp.com/success-stories/vsim/plasma-discharges/simulating-nasa-s-next-generation-xenon-ion-thruster-next-discharge-chamber-plasma-processes [09/21, 2015].

THOMSON, J.J., 1897. XL. Cathode rays. *The London, Edinburgh, and Dublin Philosophical Magazine and Journal of Science,* **44**(269), pp. 293-316.

TORRES, C., REYES, G., CASTILLO, F. and MARTÍNEZ, H., 2012. Paschen law for argon glow discharge. *Journal of Physics: Conference Series,* **370**(1).

TUOHIMAA, T., 2008. Liquid-Jet-Target Microfocus X-Ray Sources: Electron Guns, Optics and Phase-Contrast Imaging.

TURNER, M., 2015. *Plasma Sources II: Radio Frequency Discharges.* Summer School Plasma Processing Science and Technology - Eindhoven, Netherlands.

TURNER, M.M., 2012. *Global models.* European summer school "Low Temperature Plasma Physics", Bad Honnef.

TWI LTD., Electron Beam Technology. Available: http://www.twi-global.com/capabilities/joining-technologies/electron-beam-processing/ [08/11, 2015].

VOLKOV, L., PCHELKIN, R. and REMPE, N., 2001. Optimisation of the parameters of electron sources based on plasma emitters in the regime of multiple penetration of metals. *Welding international,* **15**(6), pp. 481-485.

VON KEUDELL, A., 2013. *Fundamentals of plasmas.* Bad Honnef - European Summer School on Low Temperature Plasmas.

VON PIRANI, M., 1907. *Production of homogeneous bodies from tantalum or other metals.*

WEON, B.M. and JE, J.H., 2005. Time-dependent current-voltage relation in electron guns. *Journal of Applied Physics,* **97**(3).

WEINSTEIN, V., STEERS, E., ŠMÍD, P., PICKERING, J. and MUSHTAQ, S., 2010. A detailed comparison of spectral line intensities with plane and hollow cathodes in a Grimm type glow discharge source. *Journal of Analytical Atomic Spectrometry,* **25**(8), pp. 1283-1289.

WORSTER, J., 1969. The brightness of electron beams. *Journal of Physics D: Applied Physics,* **2**(3), pp. 457.

WRIXON, A.D., 2008. New ICRP recommendations. *Journal of Radiological Protection,* **28**(2), pp. 161.

ZHU, X., CHEN, W., ZHANG, S., GUO, Z., HU, D. and PU, Y., 2007. Electron density and ion energy dependence on driving frequency in capacitively coupled argon plasmas. *Journal of Physics D: Applied Physics,* **40**(22), pp. 7019.

ZHU, X.M., PU, Y.K., BALCON, N. and BOSWELL, R., 2009. Measurement of the electron density in atmospheric-pressure low-temperature argon discharges by line-ratio method of optical emission spectroscopy. *Journal of Physics D: Applied Physics,* **42**(14), pp. 142003.

ZHU, X. and PU, Y., 2010. Optical emission spectroscopy in low-temperature plasmas containing argon and nitrogen: determination of the electron temperature and density by the line-ratio method. *Journal of Physics D: Applied Physics,* **43**(40), pp. 403001.

ZHU, X. and PU, Y., 2008. Using OES to determine electron temperature and density in low-pressure nitrogen and argon plasmas. *Plasma Sources Science and Technology,* **17**(2), pp. 024002.

ZHU, X. and PU, Y., 2007. A simple collisional–radiative model for low-pressure argon discharges. *Journal of Physics D: Applied Physics,* **40**(8), pp. 2533.

ZHU, X., PU, Y., CELIK, Y., SIEPA, S., SCHÜNGEL, E., LUGGENHÖLSCHER, D. and CZARNETZKI, U., 2012. Possibilities of determining non-Maxwellian EEDFs from the OES line-ratios in low-pressure capacitive and inductive plasmas containing argon and krypton. *Plasma Sources Science and Technology,* **21**(2), pp. 024003.